IMPERIAL COLLEGE LONDON

UNIVERSITY OF LONDON

INSPECTION OF PIPES USING LOW FREQUENCY FOCUSED GUIDED WAVES

by

Jacob Owen Davies

A thesis submitted to the University of London for the degree of

Doctor of Philosophy

Department of Mechanical Engineering

Imperial College London

London SW7 2AZ

April 2008

Abstract

In recent years there have been several examples of the successful commercial exploitation of guided acoustic waves for long range inspection of large structures. One such successful application of guided wave has been the screening of long sections of pipework. This application employs guided waves essentially as a screening tool, and hence research has been driven by the need to maximize coverage which has necessarily been achieved at the expense of sensitivity. However, there is a clear need for a high sensitivity guided wave technique that can perform accurate defect sizing while still being deployed some distance away from the inspected region. Such a system will be utilized for inspecting critical regions of a structure to which direct access, and hence inspection by conventional local NDE techniques, is not possible.

The aim of the work presented here is to develop a pipe inspection tool that is capable of detecting, locating and then sizing defects that may be present in the pipe section under test. The work is primarily directed towards quantifying any improvements that can be made to the current commercially available system by using synthetically focused imaging algorithms. All of the work presented here uses torsional type wave modes for inspection.

It is found that a version of the Common Source Method of imaging which has been modified to deal with cylindrical pipe geometry works well for imaging the reflectors in the pipe. The system has been rigorously tested using data from 3D finite element model predictions. The performance of the system is established in terms of detection sensitivity to circumferential cracks, resolution and robustness towards set up errors. It is found that cracks of circumferential extent larger than around $1.5\lambda_{SH}$ can be directly sized from the image. This result is valid for any inspection frequency, axial defect location and pipe size. Laboratory validation experiments give results which show excellent agreement with the finite element predictions. Amplitude gains of around 18 dB over an unfocused system have been observed experimentally in 8 inch pipe.

Acknowledgements

I would like to take this opportunity to thank my excellent supervisors Professor Peter Cawley, Professor Mike Lowe and Dr. Francesco Simonetti. Their discussions and unfaltering guidance has made this work possible and enjoyable. I would also like to thank Professor Chris Scruby who first introduced me to the NDT group at Imperial College. Also to the project collaborators Dr. Sasha Velichko and Dr. Paul Wilcox at Bristol University NDT group.

Thank you to all my colleagues in the NDT group, past and present. You have made this the most enjoyable working environment I could ever imagine and have also made some great travelling companions on our worldwide conference adventures. I have made great friends here who I hope will remain friends for life. I would especially like to acknowledge Daniel, Fred, Matt, Giuseppe, Tino, Tom, Pierre and Prabhu.

My thanks to all the people at Guided Ultrasonics Limited, especially David Alleyne, Brian Pavlakovic, Jimmy Fong and Tom Vogt. You have not only given me guidance and support but also helped me to see the real-life applications of this research.

Last but definitely not least, a huge thank you to my family who have always stood by me in whatever I have ever done. Mum, Dad, Jonathan, Alice, Melissa, Nan and Grandad, you could not have helped me more. Also a special thanks to Eliska.

This work was funded by BNFL, dstl, British Energy and EPSRC.

Contents

List of Figures

Chapter 1

Introduction

There are millions of kilometres of pipelines throughout the world. Many of these pipelines carry hazardous or valuable liquids such as nuclear reactor coolant or petrochemicals. The environmental and economic ramifications of any leakage of these substances are often very severe. Therefore, a clear need for defect detection exists to avoid the risk of failure and its consequences. Non-destructive testing of pipelines is used to detect defects that are smaller than a given critical size before they lead to failure and has become an important discipline for infrastructure management.

1.1 Guided Wave Pipeline Inspection

The use of ultrasonic guided waves is potentially an attractive method for the inspection of pipelines and has received considerable research interest and successful commercial exploitation. Inspection of structures with guided waves requires knowledge of how the waves propagate in the structure. The solution to wave propagation in cylinders was first obtained by Gazis in 1959 [1] and will be reviewed in chapter 2 of this thesis.

Guided waves can potentially propagate long distances axially from the excitation

area [2]. Changes in acoustic impedance in the structure, for instance a cross sectional area step caused by a weld cap or a crack in the pipe wall, will cause reflections of the guided waves. These reflections can be received by the same transducers used for excitation of the guided waves or another sensor. These scattered signals contain information about the size and location of the pipe features which caused the reflections. Heuristically, it is the reflection arrival time that gives an indication of the axial location of the reflecting feature and the amplitude of the reflection that gives an indication of the severity of the cross sectional area change. However, guided wave propagation in pipes and their interaction with defects is complex, making accurate information about defects difficult to extract from the reflected signals.

The first work on guided wave inspection of pipes was for small diameter heat exchanger tubes. Mohr and Höller [3] used axially symmetric (axisymmetric) longitudinal guided waves to detect transverse failures in ferritic tubes of diameter around 20 mm. Torsional guided waves were used to inspect for longitudinal defects. Excitation and reception of the guided waves was achieved with Electro-Magnetic Acoustic Transducers (EMAT) at around 500 kHz. They were able to detect flaws of around 5% of the wall thickness. Thompson *et al.* [4, 5] then suggested an EMAT device to inspect from the inside of the tubes and also a piezoelectric transduction system was proposed by Silk and Bainton [6]. There has also been more recent work on the inspection of tubes using guided waves [7, 8].

Following the initial work on small diameter tubes, research attention shifted to the inspection of larger diameter pipes. The main areas of research were guided wave mode choice, their excitation and the interaction of these guided waves with defects.

1.1.1 Axially Symmetric Mode Inspection

There has been successful commercial deployment of pipe guided wave inspection using axisymmetric guided wave modes [9–12]. Axisymmetric modes are generally easier to excite and are uniform around the pipe circumference allowing more even inspection. A more detailed discussion of guided wave modes follows in chapter 2.

The commercial systems were first developed for applications where the removal of all of the pipe insulation would be prohibitively expensive. Rapid screening of tens of metres of pipe in either direction is possible from a single test location where the insulation is removed [13, 14]. Subsequently, the system has been employed in other applications where external access to the pipe is limited, such as road crossings where the pipe is buried, or offshore risers where the some of the pipe is submerged in water.

The first axisymmetric mode used was the longitudinal L(0,2) mode [15]. More detail on the guided wave modes in pipes will be given in section 2.3. An advantage of the L(0,2) mode is that it achieves 100% pipe wall coverage since it is axisymmetric and has a near constant mode shape through the wall thickness at the frequencies used [16]. This means that defects at any circumferential position and anywhere through the pipe wall thickness can be detected. Heuristically, this method of inspection uses the time of arrival to estimate the defect axial location and the amplitude of reflection to roughly estimate the severity of the defect.

The L(0,2) mode is dispersive but has been employed in relatively non-dispersive frequency regimes around 50-100 kHz [9]. These low frequencies suffer little attenuation and hence can propagate for long axial distances without significant loss of signal strength. Another advantage of the low frequency regime is that far fewer propagating modes exist which makes excitation of the chosen guided wave mode much easier without exciting other unwanted guided wave modes which can significantly complicate signals [17, 18].

More recently, the fundamental torsional guided wave mode T(0,1) has received considerable research interest and has been employed at lower frequencies (10-50 kHz) [19,20]. This mode has similar advantages to the longitudinal L(0,2) mode in terms of ease of excitation and full pipe-wall coverage due to axisymmetry. T(0,1) is entirely non-dispersive making post-processing of signals less complex than for L(0,2).

The T(0,1) mode is significantly less sensitive to liquid loading of the pipe than the

L(0,2) mode, which can excite waves in the liquid. These waves carry energy away from the pipe causing 'leakage' of guided wave energy [21]. Since liquids cannot support shear waves, then there is no energy leakage into the fluid for the T(0,1) mode which consists of shear displacement only. However, both guided wave modes are susceptible to energy leakage into the surrounding medium if it can support shear waves, for example, if the pipe is buried in soil. The conditions for energy leakage in multi-layered systems are reviewed by Lowe [22]. In addition, there is only one torsional axisymmetric mode at these low frequencies and so the transduction is less complex than for an L(0,2) system where the transducer system must be carefully designed to suppress the unwanted concurrent excitation of the L(0,1) mode [20]. For these reasons, the work presented in this thesis will concentrate on the torsional type guided wave pipe modes.

There has been considerable effort to selectively excite a desired guided wave once an inspection mode has been chosen [18]. Alleyne *et al.* [23] suggested a transducer array of dry coupled piezoelectric shear transducers clamped around the outer pipe wall to excite the axisymmetric guided wave modes. The shear transducers could either be angled perpendicular to the pipe axis (*i.e.* in a circumferential direction) to excite a torsional mode, or parallel to the pipe axis to excite longitudinal modes. If the system is to excite a pure axisymmetric mode then the transducer spacing Δ around the pipe must satisfy the Nyquist-Shannon sampling criterion ($\Delta < \lambda/2$, where λ is the wavelength of the inspection mode) at the frequencies used for inspection.

The transducers are held in place and forced onto the pipe wall by either a fixed or flexible collar. The collar is designed to push each individual transducer onto the pipe with a comparable force thus allowing even coupling of the transducers' energy into the pipe wall. The transducers can be dry coupled to the pipe because of the low operating frequencies [23]. Defects that remove around 5% of cross sectional area (CSA) can be reliably detected using this method [9]. Recently, permanently installed transducer collars have been developed for long term integrity monitoring of pipelines [24].

Magnetostrictive sensors (MsS) have been suggested for excitation and reception of guided waves in pipes [12, 25] as well as electromagnetic transduction [5, 26]. Comb transducers and angle beam wedges have also been investigated for transduction of specific guided wave modes [27–29]. A phased piezoelectric transducer array for the excitation of certain modes was implemented by Li *et al.* [30].

In the torsional commercial systems that employ piezoelectric transducer collars as described above, two rings of transducers are arranged around the pipe, separated by a quarter of the wavelength to be used [20]. This allows the system to achieve directional control. A guided wave mode can be excited in only one axial direction by applying a phaseshift to the excitation of the two rings so that the energy is summed in one direction and cancels in the other. In reality, the two transducer rings are fired separately and the phase shifts are applied to the recorded data post-acquisition prior to summation to synthetically achieve the desired directionality control. The data is then analysed for each axial direction in turn.

The scattering of the longitudinal L(0,2) and torsional T(0,1) axisymmetric guided wave modes by defects has been well covered in the literature. Ditri [31] derived expressions for the modal backscattering amplitudes of any arbitrary mode incident on a circumferential crack in a pipe wall. It was found that non-axisymmetric features in the pipe wall will backscatter to non-axisymmetric modes even with axiymmetric incidence on the feature. There have also been finite element studies investigating the scattering from notches of varying circumferential extent, depth and axial extent with L(0,2) incidence [17, 32] and T(0,1) incidence [19] of varying frequency. The finite element studies showed that the scattering is extremely complex due to mode conversion at the defect. These findings will be discussed in more detail in chapter 4.

The guided wave screening tool is typically used as the first step in a two stage inspection procedure, since the defect information recovered is generally not accurate enough to make a decision as to the likelihood of pipeline failure. The second stage is to use a more local inspection technique such as Ultrasonic Thickness (UT) gauging in problematic areas which have been identified using the guided wave screening tool. However, these problematic areas of the pipe may still be inaccessible and

hence there has been considerable work to improve the defect sizing ability of the screening tool.

1.1.2 Measuring Mode Conversion

A major barrier to the effectiveness of pipe inspection using guided waves was the difficulty of differentiating between defect reflections and non-problematic pipe features such as weld caps. The reflection amplitude of the T(0,1) mode increases roughly linearly with the change in wall cross sectional area (CSA) [19]. A deep but circumferentially local crack will produce a comparable T(0,1) reflection to that from a shallow weld cap which covers the entire circumference. This had already been observed in site trials using the L(0,2) mode [33]. In order to distinguish between the two scenarios, one needs an estimate of the circumferential extent of the scattering feature. This would subsequently lead to a more accurate estimate of the depth of the feature.

The NDT group at Imperial College, London suggested that since defects are generally not axisymmetric they will scatter the incident axisymmetric mode into higher order modes and this could be used as an indicator to the presence of non-axisymmetric defects [17]. The torsional piezoelectric transducer collar was therefore segmented into four quadrants which meant that the received signals could be separated into an axisymmetric torsional mode T(0,1) reflection and an antisymmetric flexural F(1,2) mode reflection using a normal mode expansion concept [19].

Demma *et al.* [14] proposed that the ratio of the antisymmetric flexural reflection to the axisymmetric reflection could be used to estimate the circumferential extent of the defect. In a similar fashion, mode conversion to the flexural antisymmetric F(1,3) mode is observed from L(0,2) incidence [17]. However, for small circumferential defects, the flexural to axisymmetric mode ratio is not very sensitive to small changes of the circumferential extent for both the torsional and longitudinal systems. This means that it is difficult to determine whether a defect extends over 5% or 10% of the circumference. The subsequent depth estimate could then be incorrect by a

factor of two.

1.1.3 Focused Inspection

In addition to the axisymmetric mode excitation inspection systems described above, there has been considerable work on non-axisymmetric excitation. Ditri and Rose [27] employed a normal mode expansion method, similar to that initially used by Gazis [1], to explain the excited guided wave structure in a pipe as a function of the applied transduction. The excitation of various guided wave modes by specific non-axisymmetric loading was discussed [34]. From this, a natural focusing concept developed whereby a transducer with a given circumferential extent and axial length would naturally focus guided wave energy at a focal point some distance downstream of the transducer [28]. The concept of the angular profile of a transducer was introduced [35] which is the field at a given axial distance as a function of circumferential position. The transducer could be designed to physically focus energy at a given point on the pipe wall which would subsequently cause a larger defect reflection, if a defect is present at the focal point [36].

Arrays of transducers located around the pipe circumference have also been used to physically focus energy at a desired test location in the pipe wall. Amplitude coefficients and time delays are calculated prior to inspection using a deconvolution algorithm developed by Li [36, 37] and are then applied to the transducer array. The transmitted wave packets from each transducer then form a beam which sums coherently at the chosen focal point, thus increasing the probing signal at this point. This kind of phased array focusing has shown 7 dB defect reflection improvements over the unfocused system using four focused transducers on a 16 inch pipe [35]. However, it was found that good focusing only occurred at the design frequency and decreased significantly away from this frequency [38, 39]. Li [40] suggested that an array of wedge transducers placed around the pipe circumference could be used to find the circumferential disposition of defects by focusing at several points around the pipe circumference at a fixed axial distance. However, only 8 transducers were used and the circumferential resolution was not sufficient for reliable circumferential

defect sizing. Recent testing of a 12 transducer focused system showed only a 4.5 dB increase in defect reflection amplitude over an unfocused system [41].

The phased array concepts developed from the study of non-axisymmetric mode excitation show good potential for increasing the defect reflection amplitude from small defects [35,36]. However, the method has many problems. Firstly, the angular profile tuning design of transducers must be achieved at a given frequency and axial focal distance. This means that the field they produce will vary with excitation frequency and axial distance [34, 38]. Secondly, the hardware required to drive a phased array is costly since separate signal generation and amplification is required for each transducer in the array. Thirdly, the phased array system will produce wave packets other than the desired focused packet [38] due to the simultaneous excitation of unwanted modes. These other wave packets may reflect from other non-critical features such as welds. These spurious signals will be interpreted as defect reflections from the focal point. This may lead to false calls at the focal point. Lastly, and most importantly for practical inspection purposes, the focusing must be carried out physically for each axial and angular position of interest on the pipe wall. This will be extremely time consuming and will lead to very long acquisition times for full coverage of the pipe wall. The inspection time will be directly proportional to the area to be inspected. Thus, the initial advantage of guided waves to be able to inspect large areas of structure quickly and efficiently is lost. However, the phased array techniques are still remote techniques and should still work under insulation or pipe burial conditions, although this has yet to be proved.

One way of reducing the inspection time required for the phased array technique is to limit the inspection area to problematic areas where defects may be suspected. These problematic areas can be found using the simpler guided wave screening system described above. The combination of these two tools could be implemented using the same transducer ring. The pipe circumference would be inspected using the phased array process only at axial distances flagged by the screening tool. However, this method would not improve the likelihood of detection of small defects as the improved sensitivity of the phased array tool would not be afforded at the initial

screening stage.

More recently, data recorded from an array of transducers has been processed offline post-acquisition. The idea is that the beam-forming time delays and amplitudes used for physical focusing of the phased array system can be emulated in post-processing. The advantage of such methods is that the acquisition time is minimized since the data is only recorded once. The focusing laws are then applied to the recorded data set for every point of interest for inspection. This process is known as synthetic focusing since the focusing is carried out post-acquisition. If this synthetic focusing is carried out at each point of the object under inspection then the result is an image of the reflectivity of the object.

Post-processing of array data in this manner has received considerable interest in the NDE community due to the reduction in acquisition time over conventional phased array methods. Most of the previous work has employed bulk waves in the MHz frequency range, for example [42–44]. Synthetic focusing algorithms have also seen wide use in radar [45] and sonar [46] applications. Recently, Holmes *et al.* [47] investigated synthetic focusing of array data for imaging cracks in steel blocks using bulk waves. They found that the only disadvantage of the synthetic focusing compared to conventional phased array inspection was that there was a reduction in signal to random noise ratio. However, this could be improved through averaging of the data acquired. Despite increasing the acquisition time, the averaging still required significantly less time than phased array focusing at every point in the block.

Synthetic focusing has also been applied in guided wave applications for the imaging of defects in metal plates. Work by Wilcox [48, 49] used a circular array of EMAT transducers exciting the S0 Lamb mode. The phase shifts were calculated so that the array would synthetically focus in each direction in turn. A system using piezoelectric transducers exciting the A0 Lamb mode at frequencies of around 150 kHz and similar post-processing was also built [50].

Work by Sicard *et al.* [51, 52] used a single wedge transducer to excite S0 Lamb

waves in a plate at around 1 MHz. The transducer was then scanned linearly to create a synthetic aperture, recording a pulse-echo data set. The post-processing algorithm used was similar to that used by Busse [53] for bulk wave imaging but was successfully employed here for imaging using guided waves by adding dispersion compensation.

Work on synthetic focusing of guided waves for pipe inspection has been minimal so far but the improvements observed using phased array techniques make it an attractive possibility. Hayashi *et al.* [26] used an EMAT sensor to record back-scattered defect signals after excitation of the T(0,1) mode by a magnetostrictive transducer at frequencies of 30-70 kHz in 4 inch pipe. The EMAT was mechanically scanned around the pipe circumference and recorded signals at 8 different evenly spaced circumferential positions. The data from this circumferential synthetic array was processed using a time-reversal technique to form an image of the defects in the pipe wall. It was possible to identify holes of the order of 1.5% CSA in the reconstructed images under laboratory conditions. The resolution of the system improved with increasing frequency of inspection. The performance of the system was not fully defined but this appears to be a promising technique for higher resolution guided wave pipe inspection.

1.2 Motivation and Methodology

The work on guided wave pipe screening has, to date, been primarily devoted to maximising the coverage of the screening tool and this has necessarily been achieved at the expense of sensitivity. The screening tool works well but the flagged problematic areas are often still buried, inaccessible or heavily coated making local inspection impossible. There is therefore a clear need for the development of a pipeline inspection tool that is capable of sizing defects from a remote location. Recent attempts to improve sensitivity to small defects whilst retaining the remote inspection advantage of guided waves using phased arrays [35] are extremely time consuming for full coverage of the pipe.

The aim of the work presented in this thesis is to develop a guided wave inspection tool, based on the current guided wave hardware, that has improved sensitivity to defects and also improved sizing resolution. In this respect, the system must achieve three distinct targets:

- Detection of the defect
- Location of the defect
- Sizing of the defect

Here, it is proposed to use synthetic focusing techniques to create a representative reconstruction of the scattering features in the pipe wall. The imaging process will make use of all of the back scattered defect information available and this should improve the sensitivity and defect sizing ability. Information about the location and severity of the defect will be measured from the image itself. The ability to size defects from a remote location is of great importance and will be tested thoroughly.

In order to receive all of the back-scattered information, the transducers in the pipe transducer collar will be individually addressable. These transducers will form a circumferential array around the pipe circumference and enable the system to record all of the reflected defect information available. It is proposed to carry out the inspection at similar frequencies to the screening tool. The low frequency advantages of simple guided wave mode structure, low attenuation and fewer propagating modes will therefore remain.

The imaging of plates using synthetic focusing with a linear array of transducers will be investigated in chapter 3 following a discussion of guided waves in plates in section 2.2. Three synthetic focusing algorithms for use with a linear array of sensors will be introduced and evaluated. The algorithms differ only in the data that must be recorded for the reconstruction of the image. This affects the data acquisition time, the hardware complexity and the reconstructed image quality. The performance of the synthetic focusing algorithms is analysed using optics theory, data from finite element models and some simple plate validation experiments.

Guided waves in pipes and their similarities to certain guided wave modes in plates will be discussed in the following chapter. It is proposed that the plate imaging algorithms discussed in 3 are directly applicable to the imaging of pipes due to the similarity of wave propagation of the torsional-flexural guided wave modes in pipes with the shear horizontal modes in plates established in section 2.3.4. The synthetic focusing algorithms are thoroughly tested using extensive finite element modelling studies of circumferentially oriented cracks and notches in chapter 4. The performance of the most applicable focusing algorithm is defined with varying frequency of excitation, pipe size and defect axial location.

The robustness of the pipe imaging system to possible setup errors of the transducer ring is evaluated in chapter 5. An example of such errors is coupling variation around the pipe circumference. The robustness will be tested with synthetically corrupted finite element data.

After quantifying the likely performance of the pipe imaging tool built using a circumferential array of transducers, the real performance is experimentally tested in chapter 6. The defects are circumferentially oriented notches, of vary circumferential extent and through-wall depths. The experimental results are compared to the finite element predictions of chapter 4.

The thesis conclusions follow in chapter 7. Details of performance improvements over the current guided wave pipe inspection technology are given in terms of defect sensitivity and defect sizing ability. Some options for further work are also presented.

Chapter 2

Guided Waves

Prior to being able to image a structure using ultrasonic waves, a thorough understanding of how waves can propagate in the medium to be imaged is necessary. Bulk waves can only travel in regions away from any boundaries where the longitudinal and shear waves are uncoupled. At boundaries of the material, bulk waves will interact with these boundaries by means of reflection and refraction. Also, mode conversion between bulk longitudinal and bulk shear waves can occur. It is these interactions of bulk waves with the boundaries of the material that lead to the development of guided waves in the material structure.

The propagation of bulk waves is dependent only on the material properties. In contrast, guided waves are dependent on the material properties *and* the material boundaries. Therefore, the solution to any guided wave problem must satisfy the governing equations of motion and some physical boundary conditions, such as traction free surfaces of the bounded medium. There are generally an infinite number of solutions to the boundary conditions applied by a given finite material structure.

Historically, certain guided wave problems have been solved and the solution has taken the name of the investigator. *Rayleigh* waves are free waves on the surface of a semi-infinite solid [54]. The boundary conditions for this problem are a traction-free surface and the waves must decay with depth from the surface. *Lamb* waves are plane-strain solutions to the free plate problem [55]. The traction forces must

be zero on the top and bottom surface of the plate. *Stoneley* waves are the waves that occur at the flat interface of two media [56]. The solutions must match at the interface and waves must decay away from the interface.

The solution to the Shear Horizontal (SH) modes and Lamb modes in plates will be outlined in this chapter after briefly reviewing wave propagation in unbounded media. The standard method of solution for the pipe case, originally proposed by Gazis [1], will then be introduced. The resulting pipe dispersion curves are compared with the corresponding plate curves.

A method for simplifying the pipe problem is presented for the case of the torsional-flexural modes (F(n,2)) which involves unrolling the pipe and analysing it as a flat plate. The discrepancies between these two approaches are evaluated and the maximum error is quantified. The regime in which this simplified plate approach is valid is discussed.

2.1 Wave propagation in unbounded media

Wave propagation in elastic infinite media is well documented in textbooks, for example [57–59] and is merely briefly outlined here.

The equation of motion for an isotropic elastic medium in the absence of body forces (Navier's equation) is,

$$(\lambda + \mu)\nabla\nabla \cdot \mathbf{u} + \mu\nabla^2\mathbf{u} = \rho(\frac{\partial^2\mathbf{u}}{\partial t^2}) \tag{2.1}$$

where $\mathbf{u}$ is the three dimensional displacement vector, ρ is the material density, λ and μ are Lamé constants and ∇^2 is the three dimensional Laplace operator.

Using the Helmholtz decomposition, $\mathbf{u}$ can be expressed as the sum of a compressional scalar potential, ϕ, and an equivoluminal vector potential, $\mathbf{\Phi}$

$$\mathbf{u} = \nabla\phi + \nabla \times \mathbf{\Phi}, \tag{2.2}$$

with

$$\nabla \cdot \mathbf{\Phi} = 0. \tag{2.3}$$

Substitution of these potential functions into Navier's equation (2.1) means that the equation of motion can be separated into two equations for the two unknown potentials

$$\frac{\partial^2 \phi}{\partial t^2} = c_l^2 \nabla^2 \phi, \tag{2.4}$$

which governs longitudinal waves and

$$\frac{\partial^2 \mathbf{\Phi}}{\partial t^2} = c_s^2 \nabla^2 \mathbf{\Phi}, \tag{2.5}$$

which governs shear waves. c_l and c_s are the velocities of longitudinal and shear waves in the infinite isotropic medium.

$$c_l = \sqrt{\frac{\lambda + 2\mu}{\rho}}, \tag{2.6}$$

$$c_s = \sqrt{\frac{\mu}{\rho}}. \tag{2.7}$$

This reveals that there are only two types of wave which can propagate in an unbounded isotropic medium. Equations 2.4 and 2.5 are independent of each other meaning that longitudinal and shear waves can propagate without interaction in unbounded media. The general solution to equation 2.4 and equation 2.5 which fully describes the propagation of the the two waves is

$$\phi = \phi_0 e^{i(\mathbf{k}_l \cdot \mathbf{z} - \omega t)}, \tag{2.8}$$

$$\mathbf{\Phi} = \mathbf{\Phi}_0 e^{i(\mathbf{k}_s \cdot \mathbf{z} - \omega t)}, \tag{2.9}$$

where ϕ_0 and $\mathbf{\Phi_0}$ are arbitrary initial constants and $\mathbf{k_l}$ and $\mathbf{k_s}$ are the longitudinal and shear wavevectors.

2.2 Guided Waves in Plates

The solution to the free plate problem will now be briefly reviewed. The two most common methods of solution are the potential method and the method of superposi-

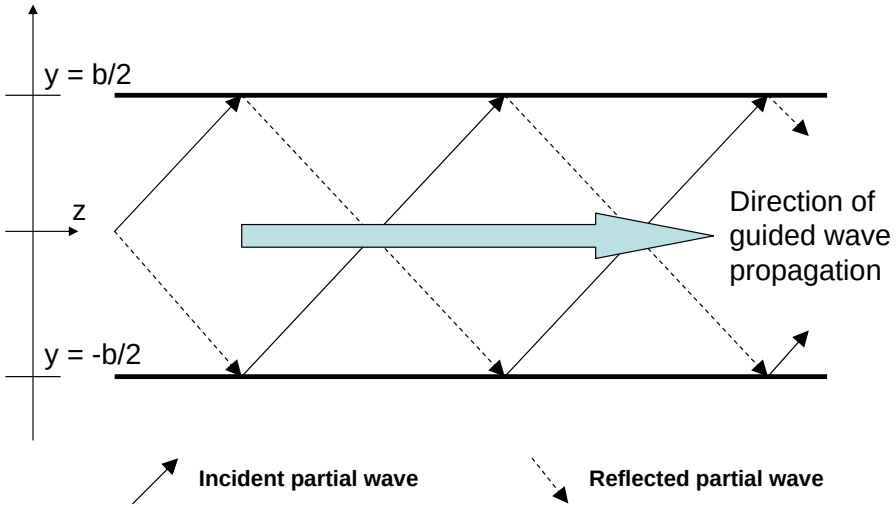

Figure 2.1: *Free-plate schematic showing geometry and internally reflecting bulk waves.*

tion of partial waves. For a more detailed insight into the methods see, for example, Auld [60] or Rose [59].

2.2.1 Shear horizontal guided waves in plates

The geometry of the free isotropic plate is shown in figure 2.1. The plate thickness is b. The surfaces at $y = b/2$ and $y = -b/2$ are considered to be traction free. These are the boundary conditions to the free plate problem. The solution to the free plate problem by the method of potentials is simple and seeks to solve equations 2.4 and 2.5 for the two potentials ϕ and $\mathbf{\Phi}$ respectively. This method is similar to that which will be outlined for the pipe case in section 2.3. Solutions when the scalar potential ϕ vanishes are known as Shear Horizontal (SH) plate modes.

If the assumption is made that the guided wave solution will propagate in the z direction then the solution to (2.5) will take the form

$$\mathbf{\Phi} = \mathbf{\Phi}_0(y)e^{i(k_z \cdot z - \omega t)} \tag{2.10}$$

The solution is constant across y and represents travelling waves in the z direction. Substitution of the assumed potential solution into (2.5) yields an equation for the

unknown potential in terms of through-thickness sinusoids

$$\mathbf{\Phi}_0(y) = \mathbf{A}\sin(k_y y) + \mathbf{B}\cos(k_y y) \tag{2.11}$$

where

$$k_y^2 = k_s^2 - k_z^2 \tag{2.12}$$

where $k_s = \omega/c_s$ is the bulk shear wavenumber and c_s is the bulk shear velocity defined by (2.7). The strain-displacement relations are used to find the strains in terms of the unknown vector potential Φ. Then Hooke's law is used to find the stresses in terms of the strains and hence in terms of the unknown potential. The boundary conditions state that the surfaces are traction free which leads to the condition that

$$(\lambda+\mu)\frac{\partial v_x}{\partial y} = (\lambda+\mu)\frac{\partial}{\partial y}(\frac{\partial}{\partial y}\Phi_z + ik_z\Phi_y) = 0 \tag{2.13}$$

at $y = b/2$ and $y = -b/2$. For a more thorough analysis see [60]. Substitution of the potential (2.11) shows that (2.13) is satisfied when

$$k_y = \frac{p\pi}{b}, \qquad \text{p = 0,1,2,3,...} \tag{2.14}$$

Substituting (2.14) into 2.12 gives the plate SH dispersion relation

$$k_z^2 = (\frac{\omega}{c_z})^2 = (\frac{\omega}{c_S})^2 - (\frac{p\pi}{b})^2 \tag{2.15}$$

The physical meaning of equation 2.15 is represented graphically in wavevector space in figure 2.2. The arrow represents the bulk shear wave inside the material. The plate boundary condition means that the through-thickness wavenumber k_y can only take discrete values (2.14). The propagation wavenumber k_z can therefore also only take discrete values as described by (2.15).

The SH mode dispersion curves for the first few modes generated using equation 2.15 are shown in figure 2.3 for mild steel ($c_S = 3260\ ms^{-1}$). Note from figure 2.2 that for $p = 0$ then $k_y = 0$ and $k_z = k$. Therefore the fundamental Shear Horizontal mode, SH_0, is non-dispersive as seen in figure 2.3. All higher order SH modes are inherently dispersive. It is also important to note that the number of propagating modes increases with the frequency-thickness product.

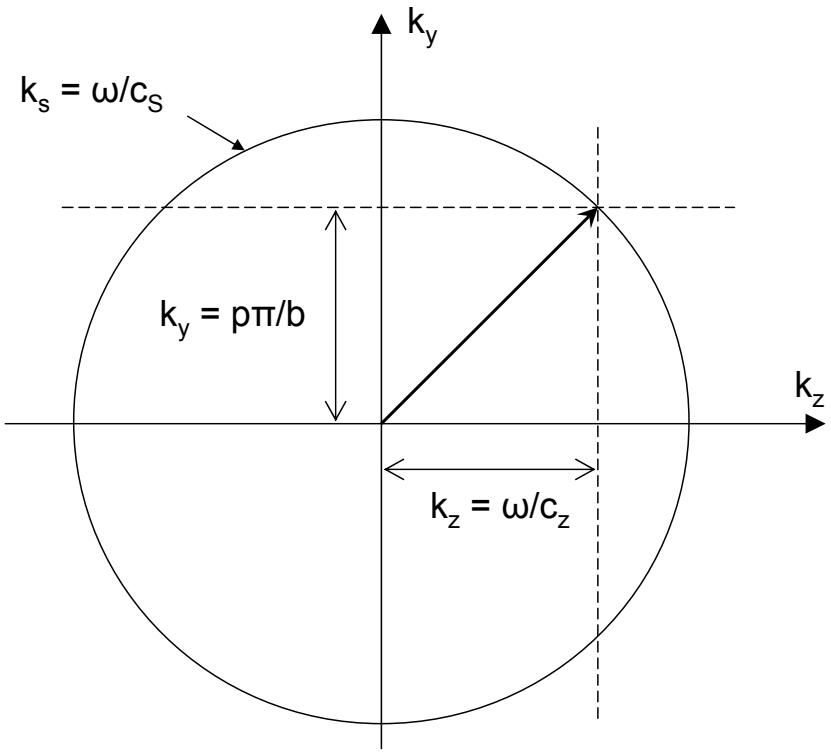

Figure 2.2: *Wavevector graphical representation of the free plate dispersion relation for SH modes.*

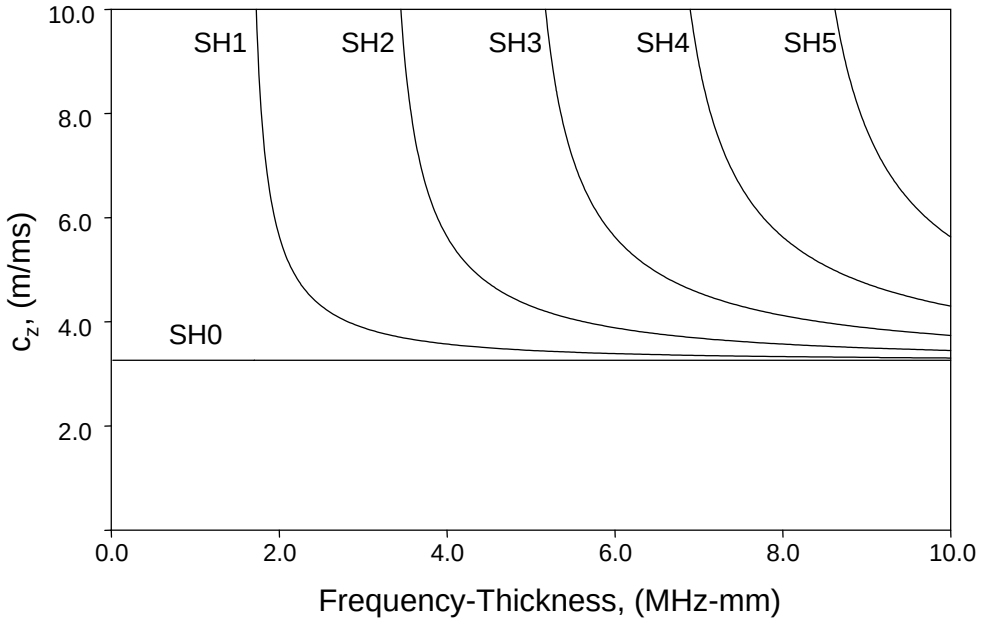

Figure 2.3: *SH mode dispersion curves for the mild steel isotropic free plate.*

2.2.2 Lamb modes in plates

Other guided wave modes can be formed from the combination of vertically polarised shear (SV) waves and longitudinal waves (P). SV and P waves cannot exist individually in the free plate case but are coupled, making the solution more complex. The stress-free surfaces at $y = \pm b/2$ on free-plate problem leads to the condition that both SV and P wave vectors must have the same wavevector component in the z direction $k_{z,s} = k_{z,l}$ [60]. The problem is illustrated graphically in figure 2.4. The two wavevectors prescribe two different circles of radii k_s and k_l whose axial component k_z must match for a propagating modal solution. Some geometric algebra, see for example [60], leads to the *Rayleigh-Lamb* frequency equations

$$\frac{\tan k_{ys} b/2}{\tan k_{yl} b/2} = -\frac{4k_z^2 k_{ys} k_{yl}}{(k_{ys}^2 - k_z^2)^2} \tag{2.16}$$

for the through-thickness symmetric solutions and

$$\frac{\tan k_{ys} b/2}{\tan k_{yl} b/2} = -\frac{(k_{ys}^2 - k_z^2)^2}{4k_z^2 k_{ys} k_{yl}} \tag{2.17}$$

for the antisymmetric solutions. The transverse wave vector components are linked to ω and the z component of the wave vector by

$$k_{ys}^2 = k_s^2 - k_z^2 = (\frac{\omega}{c_S})^2 - k_z^2 \tag{2.18}$$

and

$$k_{yl}^2 = k_l^2 - k_z^2 = (\frac{\omega}{c_L})^2 - k_z^2 \tag{2.19}$$

The dispersion relations for these *Lamb waves* can then be obtained by substituting (2.18) and (2.19) into (2.16) for symmetric solutions (S modes) or (2.17) for antisymmetric solutions (A modes). The dispersion relations are transcendental and are solved numerically, for example, using DISPERSE [61]. Figure 2.5 shows the Lamb wave dispersion curves for the symmetric and antisymmetric modes for

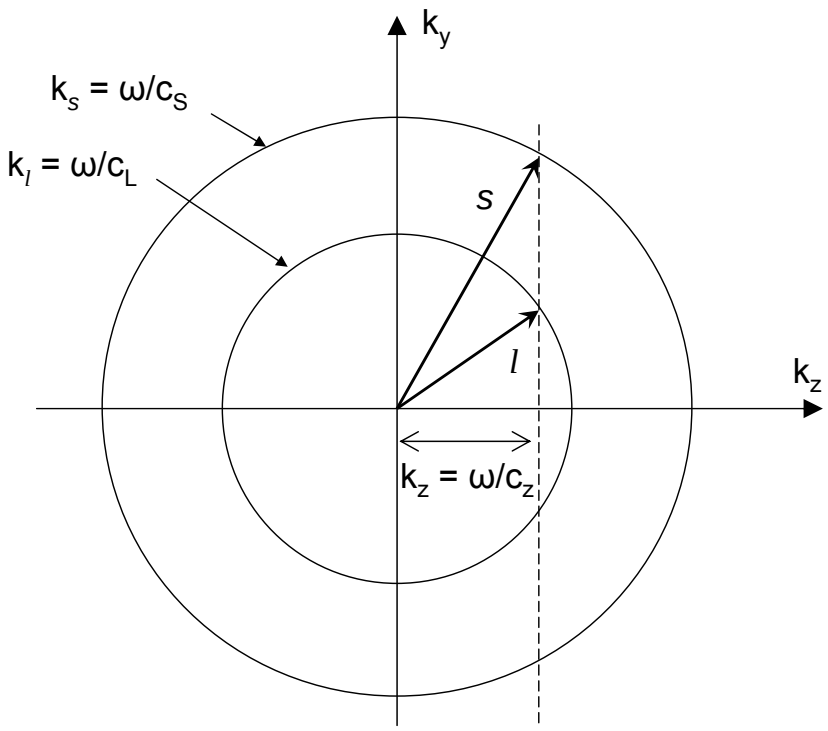

Figure 2.4: *Wavenumber graphical representation of the free plate dispersion relation for coupled SV and P partial waves.*

mild steel plate with $c_L = 5960\ ms^{-1}$ and $c_S = 3260\ ms^{-1}$ ($c_L/c_S = 1.83$) up to a frequency-thickness product of 10 MHz-mm. As with the SH modes, there exist more propagating modes with increasing frequency thickness. Note that all Lamb modes are dispersive but there are regions of frequency-thickness product which are comparatively non-dispersive.

2.3 Guided Waves in Pipes and similarities with the Plate case

The propagation of guided waves in pipes, or hollow cylinders, has been the subject of extensive investigation, for example [1, 62, 63] and the solution can be found in a variety of textbooks, for example [59, 60]. The problem was analytically formulated in three-dimensional cylindrical coordinates by Gazis in 1959 [1]. The method is broadly similar to the solution of the free-plate case of section 2.2 using a set of

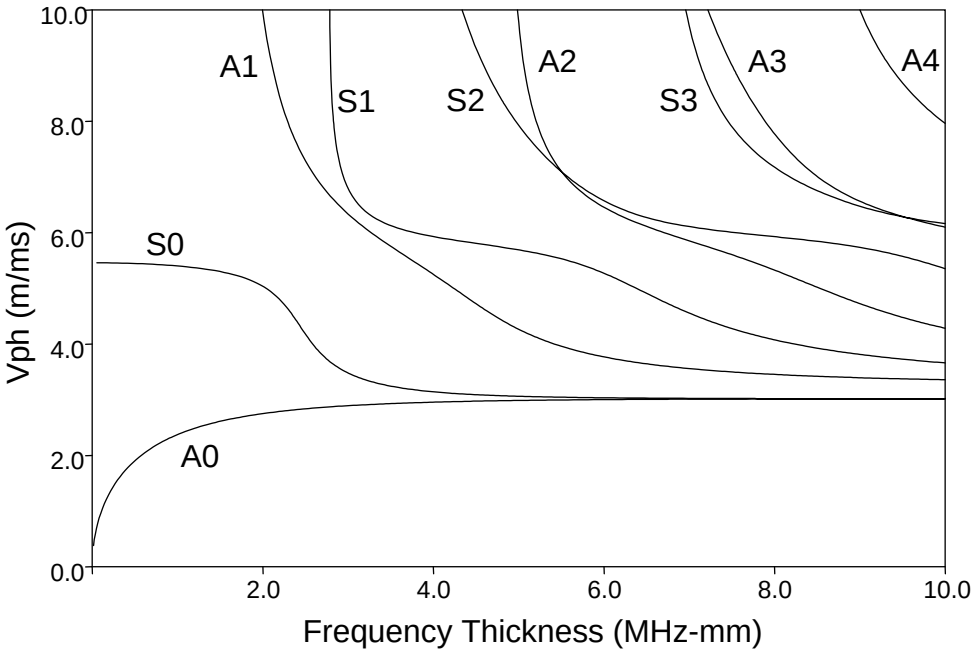

Figure 2.5: *Lamb wave phase velocity dispersion curves for mild steel plate.*

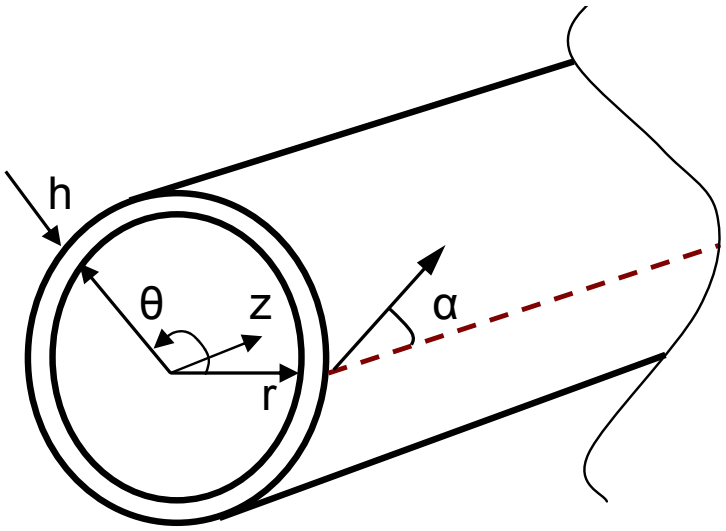

Figure 2.6: *Schematic of pipe geometry and cylindrical coordinate set.*

assumed potential functions for ϕ and $\mathbf{\Phi}$ (defined in equations 2.8 and 2.9). The geometry of the pipe case and the cylindrical coordinate set is shown in figure 2.6.

The propagation of waves in unbounded media was outlined in section 2.1. For the case of cylindrical geometry Gazis suggested the following form for the scalar potential ϕ and directional components of the vector potential $\mathbf{\Phi}$ defined by equations 2.8

and 2.9.

$$\begin{aligned} \phi &= f(r)\cos n\theta\cos(\omega t + k_z z) \\ \Phi_r &= g_r(r)\sin n\theta\sin(\omega t + k_z z) \\ \Phi_\theta &= g_\theta(r)\cos n\theta\sin(\omega t + k_z z) \\ \Phi_z &= g_z(r)\sin n\theta\cos(\omega t + k_z z) \end{aligned} \tag{2.20}$$

where k_z is the component of the wavevector in the axial direction and n is the circumferential order. Substitution of (2.20) into equations (2.8) and (2.9) results in solutions for the unknown potentials f, g_r, g_θ and g_z in terms of Bessel functions with arguments of either $k_{rl}r$ or $k_{rs}r$ where

$$\begin{aligned} {k_{rl}}^2 &= \frac{\omega^2}{{c_l}^2} - k_z^2 \\ {k_{rs}}^2 &= \frac{\omega^2}{{c_s}^2} - k_z^2 \end{aligned} \tag{2.21}$$

Expressions for the displacement field can be found by substituting 2.20 into (2.2). The strain-displacement relations for cylindrical coordinates are

$$\begin{aligned} \epsilon_{rr} &= \frac{\partial u_r}{\partial r} \\ \epsilon_{rz} &= \frac{1}{2}(\frac{\partial u_r}{\partial z} + \frac{\partial u_z}{\partial r}) \\ \epsilon_{r\theta} &= \frac{1}{2}[r\frac{\partial}{\partial r}(\frac{u_\theta}{r}) + \frac{1}{r}\frac{\partial u_r}{\partial \theta}] \end{aligned} \tag{2.22}$$

and Hooke's Law relates the stresses to the strains of equation 2.22

$$\begin{aligned} \sigma_{rr} &= \lambda\Delta + 2\mu\epsilon_{rr} \\ \sigma_{rz} &= 2\mu\epsilon_{rz} \\ \sigma_{r\theta} &= 2\mu\epsilon_{r\theta} \end{aligned} \tag{2.23}$$

where $\Delta = \nabla^2\phi$ is the dilation. The boundary conditions for the pipe geometry, for free motion are

$$\sigma_{rr} = \sigma_{rz} = \sigma_{r\theta} = 0 \quad \text{at} \quad r = r_i \quad \text{and} \quad r = r_o = r_i + h. \tag{2.24}$$

The stress components (2.23) in terms of the displacement potentials (2.2) and their derivatives are entered into the boundary condition equations (2.24) yielding a six by six characteristic, or dispersion equation, formed by the determinant of the amplitudes of the Bessel functions:

$$|c_{ij}| = 0 \quad \text{i,j} = 1 \text{ to } 6 \tag{2.25}$$

The components c_{ij} of equation 2.25 can be found in [1] and are coefficients of the circumferential order n and the radial components of the longitudinal and shear wavevectors k_{rl} and k_{rs}. For a hollow cylinder of given dimensions and fixed elastic constants, equation 2.25 is an implicit transcendental function of h/λ and $\frac{fh}{c_s}$, where λ is wavelength, f is frequency, h is wall thickness and c_s is the bulk shear velocity. The roots of the characteristic equation $\frac{fh}{c_s}$ can be computed by fixing h/λ or vice versa. The solution was achieved numerically by Gazis in 1959 [1]. For a detailed insight into the numerical issues of the pipe solution, see [64].

In order to determine the guided waves in arbitrary multilayered system, a general purpose software tool DISPERSE was developed by Lowe [22] and Pavlakovic [61, 65]. This uses the *global matrix method* proposed by Knopoff [66], later refined by Schmidt and Jensen [67].

There are certain cases where the six by six characteristic equation (2.25) degenerates to simpler, lower dimensional forms. These cases occur when the axial wavenumber k_z or the number of waves around the circumference n are equal to zero.

The case of k_z being equal to zero is equivalent to the motion being independent of z. The axial wavelength ($\lambda_z = 2\pi/k_z$) is infinite and the modes can either be plane-strain vibrations as discussed in [68] or longitudinal shear vibrations, involving only longitudinal displacements u_z.

The limiting case of $n = 0$ means that motion is independent of circumferential position θ and is axially symmetric. There are two types of pipe guided wave modes that have motion independent of circumferential position. These are longitudinal modes (L) and torsional modes (T).

2.3.1 Longitudinal pipe modes

Longitudinal modes can have displacements u_r and u_z which are independent of θ and are similar to the *Lamb* modes in plates discussed in section 2.2. The characteristic equation (2.25) to be solved for the longitudinal modes is now a four by four determinant [1]. The dispersion characteristics of the longitudinal pipe modes are similar to the Lamb-type plate modes described by equations 2.16 and 2.17.

The longitudinal dispersion curves are shown in figure 2.7 for a mild steel (c_L = 5960 ms^{-1} and c_S = 3260 ms^{-1}) pipe of 10mm internal radius and 1mm wall thickness. Also shown in the figure are the plate Lamb modes for a 1mm thick plate of the same material. Note that the pipe dispersion curves are almost identical to the Lamb mode dispersion curves with the exception of the very low frequency region where the pipe modes deviate from the plate modes. The Bessel functions which describe the pipe modes match the exponential functions which describe the plate modes for large frequency-radius product but differ more and more as the frequency-radius product is decreased and the wavelength becomes comparable to the circumference.

The longitudinal modes are numbered L(0,m) where m is the mode number and the zero refers to the fact that the modes have zero circumferential order (motion is independent of circumferential position). This is the notation of Silk and Bainton [6].

2.3.2 Torsional pipe modes

Torsional pipe modes involve displacements u_θ only and are similar to the Shear Horizontal (SH) plate modes discussed in section 2.2. The solution determinant is now two by two. The torsional dispersion curves are shown in figure 2.8 for a mild steel ($c_L = 5960\ ms^{-1}$ and $c_S = 3260\ ms^{-1}$) pipe of 10mm internal radius and 1mm wall thickness. The torsional dispersion curves are exactly identical to the Shear Horizontal dispersion curves for a 1mm thick plate of the same material since the torsional modes have particle displacement in the θ directions only. The modes are

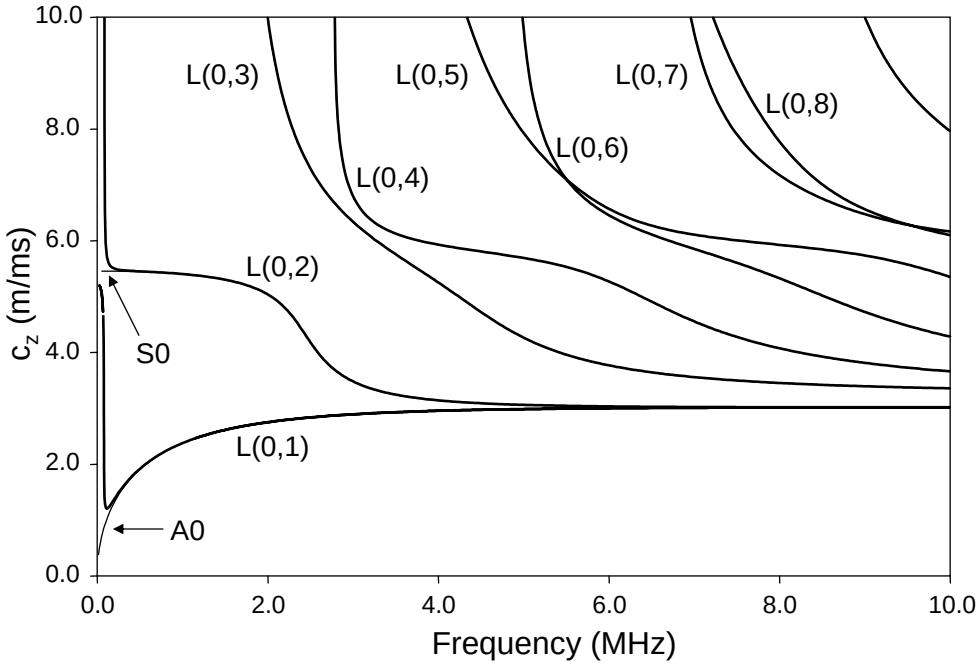

Figure 2.7: *Longitudinal mode dispersion curves for a mild steel pipe of 10mm internal radius and 1mm wall thickness.*

numbered T(0,m) where m is the mode number (which increases with the frequency at which the mode appears) and the zero refers to the fact that the modes have zero circumferential order.

2.3.3 Flexural pipe modes

The other family of modes which can exist in a pipe are called flexural modes, F(n,m). Flexural modes are not axisymmetric and hence have circumferential order n and mode family number m. The solution to flexural modes involves the full six dimensional determinant (2.25) since all three displacement components u_r,u_θ and u_z can exist. Flexural modes will converge to either a longitudinal or torsional mode at high frequencies where the wavelength to radius ratio is small. For example, F(n,1) modes converge to L(0,1), F(n,2) modes converge to T(0,1), F(n,3) converge to L(0,2) and so on. The phase velocity dispersion curves of these three mode families are plotted in figure 2.9 up to the 5^{th} order.

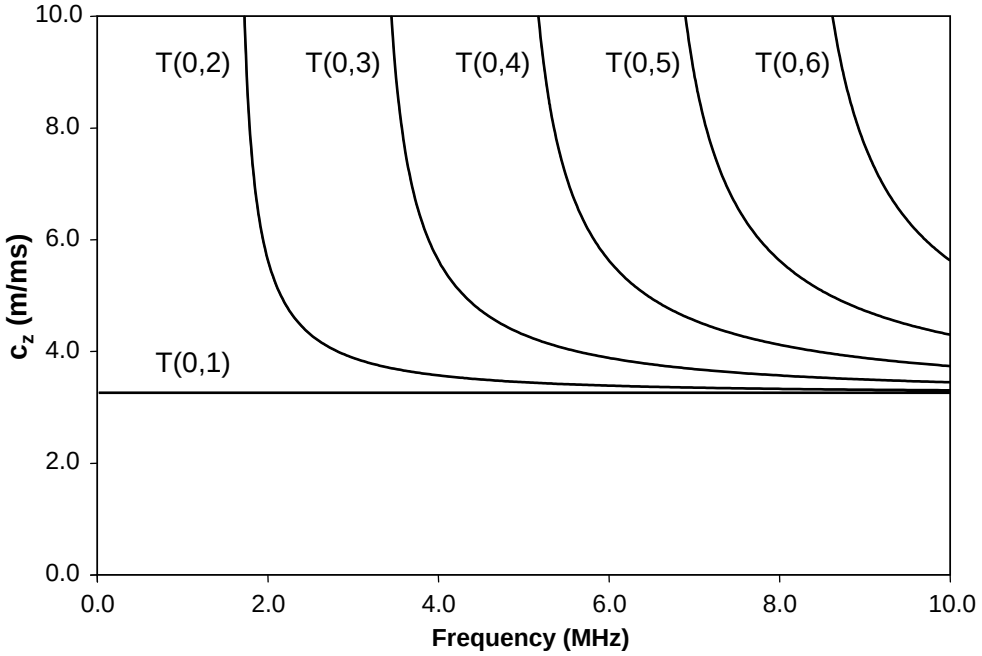

Figure 2.8: *Torsional mode dispersion curves for a mild steel pipe of 10mm internal radius and 1mm wall thickness.*

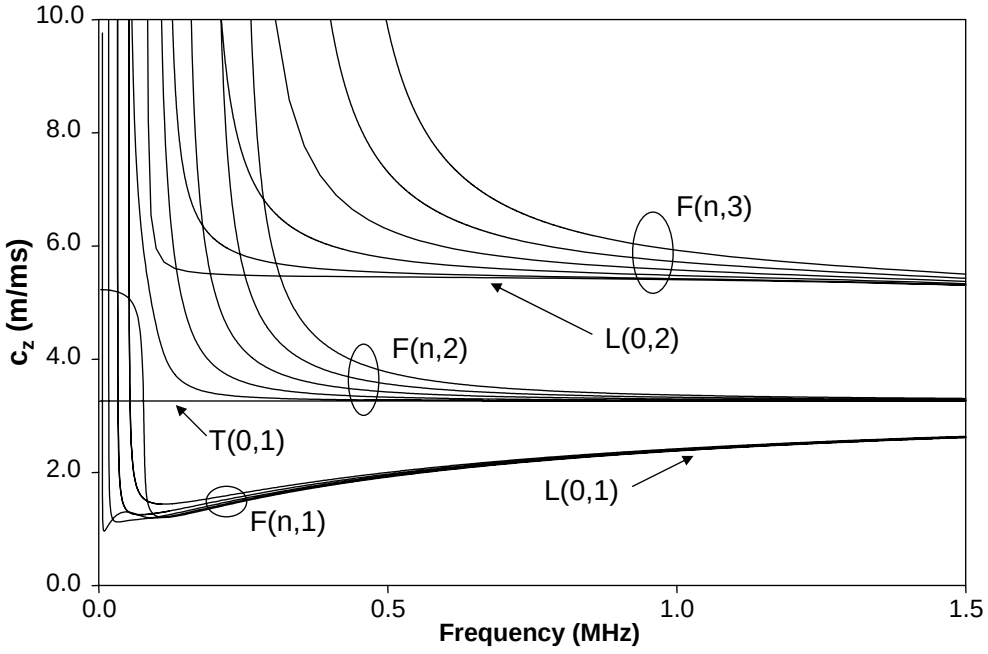

Figure 2.9: *All dispersion curves up to fifth circumference order for a mild steel pipe of 10mm internal radius and 1mm wall thickness.*

Pipe guided wave inspection typically operates at frequencies at which the wavelength is much larger than the pipe wall thickness. It was found in section 2.2 for plates that at these frequencies there exist only three fundamental guided wave modes, S0, SH0 and A0. In this frequency regime, only the modes which converge to the fundamental torsional mode (T(0,1)), the fundamental symmetric mode (L(0,2)) and the fundamental antisymmetric mode (L(0,1)) can propagate in the pipe, as was shown in figure 2.9. However, for reasons which were discussed in the thesis introduction, it is the torsional type modes which will be investigated here. Hence, the F(n,2) flexural mode family, which converges to the fundamental torsional mode T(0,1) which will henceforth be termed the torsional-flexural mode family will be investigated more thoroughly.

2.3.4 Torsional-Flexural pipe modes and their plate analogy

The following analysis aims to simplify the complex pipe guided wave solution for the torsional-flexural mode family by assuming plate-like behaviour. This is based on the assumption that the cylinder contour has negligible effect on the wave propagation. The SH0 propagation in a plate is described by the bulk shear wavenumber k_s in any direction of propagation. Therefore, the assumption for the plate-like pipe analogy is that the wavevector k_α for any direction of propagation α is equal to the bulk shear wavenumber k_s

$$k_\alpha = k_s = \frac{\omega}{c_s} \tag{2.26}$$

This allows one to unroll the pipe and think of it as an isotropic plate. The pipe and its plate-like unrolled surface are shown in figure 2.10. A similar simplification procedure for calculating the axial phase velocities of the longitudinal-flexural pipe modes based on their similarities with plate Lamb modes was presented by Li and Rose [37].

However, there is an extra boundary condition to be solved for this problem in addition to the traction free surfaces that were considered for the plate solution of section 2.2. This extra boundary condition occurs along the axial cut made in

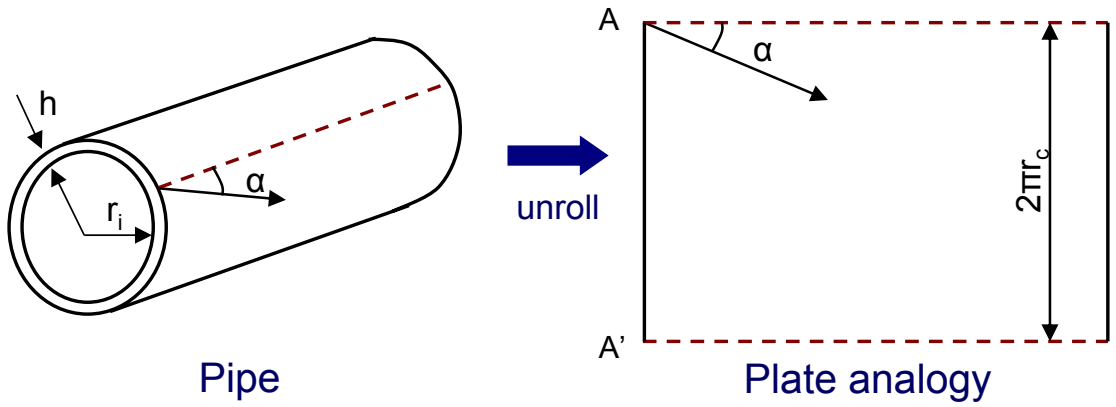

Figure 2.10: *Schematic showing the pipe and unrolled pipe analogy.*

the pipe in order to unroll it and states that the two solutions at either side of the unrolled plate (A and A' in figure 2.10) must match. Satisfying this condition means there are no discontinuities made by unrolling the pipe. A diagram of this situation is shown in figure 2.11a. The diagram shows the plane wavefronts propagating at angle α from the axial direction z. If the solution at A is to match that at A', then there must be an integer number of wavelengths $n\lambda_S$ between the matching wavefronts shown. Note that if the wavefronts are propagating with $\alpha = 0$ then there is no circumferential variation and the circumferential order is zero. In this case, T(0,1) is the axially propagating guided wave mode. If $\alpha = \pi/2$ then there is no variation in the z direction and $k_z = 0$.

Figure 2.11b shows the right-angled triangle used to find the possible solutions for propagating wave modes. Using simple trigonometry we get

$$\sin \alpha_n = \frac{n\lambda_s}{2\pi r_c} \tag{2.27}$$

where n is the mode order and r_c is the pipe wall centre radius. Assuming that the plane wavefronts are travelling with wavenumber $k_s = 2\pi/\lambda_s$ then the expression for the possible circumferential wavenumbers is

$$k_{circ} \;=\; k_s \sin \alpha_n = \frac{n}{r_c} \tag{2.28}$$

The partial wavevector components are linked by

$$k_s^2 = k_z^2 + k_{circ}^2 \tag{2.29}$$

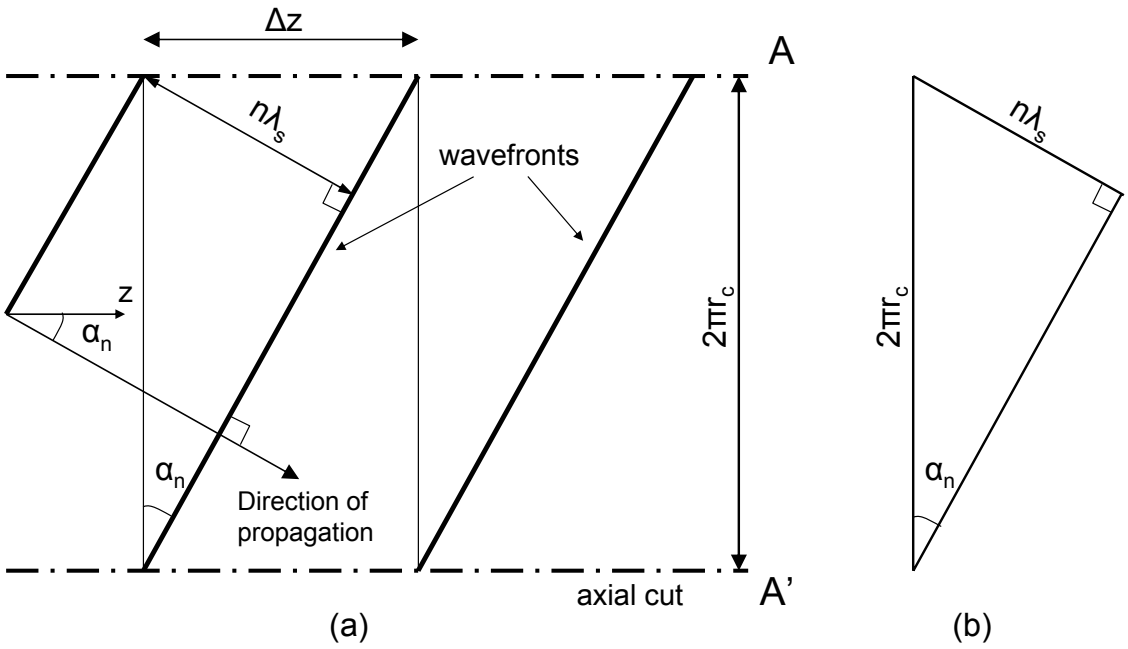

Figure 2.11: *Diagram showing the necessary boundary condition for modal propagation in the plate-like pipe analogy; (a) full schematic, (b) right-angled triangle used to find modal solutions.*

as demonstrated graphically for forward propagation (k_z is positive) in figure 2.12. Hence the axial wavenumber is

$$k_z \;=\; k_s \cos\alpha_n = \sqrt{k_s^2 - (\frac{n}{r_c})^2}. \tag{2.30}$$

Propagating solutions for k_z therefore require that $n/r_c < k_s$. This accounts for the finite discrete number of propagating modes at a given frequency. The axial phase velocity c_z is linked to the axial wavenumber (equation 2.30) by

$$c_z = \frac{\omega}{k_z} \tag{2.31}$$

where $\omega = 2\pi f$ is the angular temporal frequency of the wave. Substituting 2.30 into 2.31 gives the dispersion relation for the wave modes assuming isotropic plate-like behaviour

$$c_{z,n} = \frac{\omega}{\sqrt{k_s^2 - (\frac{n}{r_c})^2}} \tag{2.32}$$

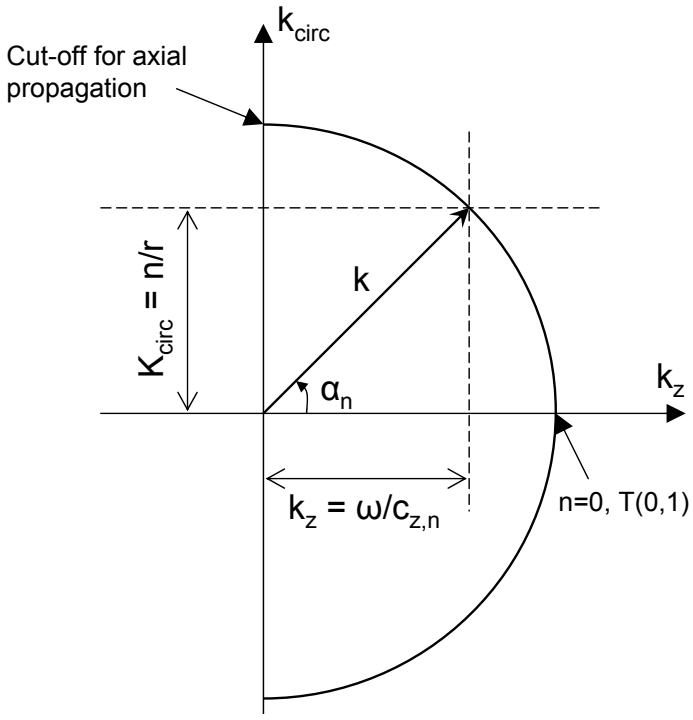

Figure 2.12: *Graphical representation of wavevector showing circumferential and axial wavevector components for pipe geometry.*

where $k_s = \omega/c_s$ is the bulk shear wavenumber. The resulting axial phase velocity dispersion curves for an 8 inch schedule 40 (r_c = 0.10546 m and t = 8.18 mm) mild steel pipe are plotted in figure 2.13 for the frequency region of interest for pipeline inspection. The dispersion curves calculated using DISPERSE [61,65] which numerically solves the six dimensional characteristic equation (equation 2.25) are also shown up to the 18^{th} order mode. It can be seen that there is generally very good agreement between the two methods apart from some differences for the lower order modes at low frequencies. These discrepancies can be quantified by calculating the difference in phase velocity between the two methods for each direction of possible propagation $\alpha_{n,D}$ where the subscripts refer to the circumferential mode order and the fact that the values are calculated using DISPERSE.

The direction of propagation α_n of each mode of order n can be calculated from the DISPERSE curves at a given frequency ω using

$$\alpha_n = \arctan(\frac{k_{circ}}{k_{z,n,D}}) = \arctan(\frac{n/r_c}{\omega/c_{z,n,D}}) \tag{2.33}$$

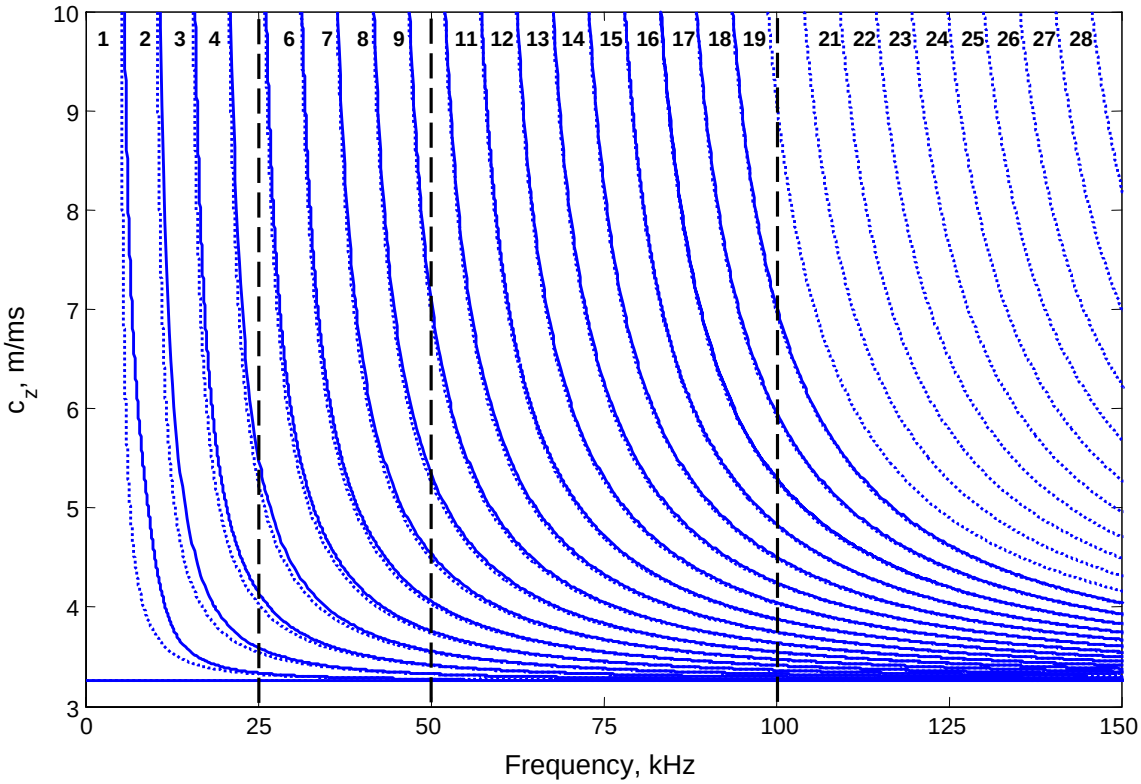

Figure 2.13: *Dispersion curves for the F(n,2) flexural mode family in an 8 inch schedule 40 mild steel pipe; solid lines: DISPERSE results; dotted lines: Results calculated using the simplified plate analogy.*

where $c_{z,n,D}$ is the axial phase velocity from DISPERSE for the n^{th} mode and $k_{z,n,D} = \frac{\omega}{c_{z,n,D}}$ is the axial wavenumber of that mode. Note that α_n is frequency dependent so a given mode will travel in different directions at different frequencies. The wavenumber of the n^{th} mode $k_{\alpha_n,D}$ in the direction of propagation α_n is

$$k_{\alpha_n,D} = \sqrt{k_{circ}^2 + k_{z,n,D}^2} \tag{2.34}$$

and so the phase velocity $c_{\alpha_n,D}$ in the α_n direction calculated using the Disperse software package is

$$c_{\alpha_n,D} = \frac{\omega}{k_{\alpha_n,D}} = \frac{\omega}{\sqrt{k_{circ}^2 + k_{z,n,D}^2}} \tag{2.35}$$

The assumption made when unrolling the pipe to the plate-like case was that the

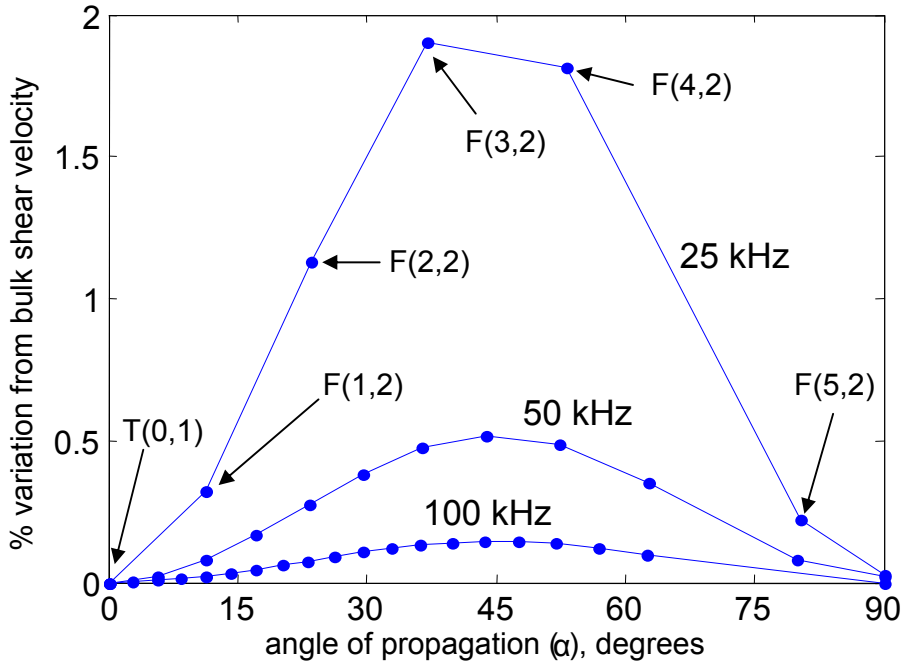

Figure 2.14: *% variation of the phase velocity calculated using DISPERSE from the bulk shear velocity against angle of propagation from the axial direction for an 8 inch schedule 40 mild steel pipe.*

phase velocity is equal in all directions (equation 2.26). This hypothesis can be tested for a given frequency by calculating the variation in phase velocity from the bulk shear velocity using equation 2.35 for all possible propagation directions defined by (2.33).

Figure 2.14 shows the percentage variation of the the phase velocity calculated using DISPERSE from the bulk shear velocity against angle of propagation from the axial direction at 25 kHz, 50 kHz and 100 kHz for the 8 inch pipe whose dispersion curves were shown in figure 2.13. At 25 kHz, up to the 5^{th} order mode exists. At 50 kHz, up to the 10^{th} order mode exists and up to F(20,2) exists at 100 kHz. Figure 2.14 shows velocity errors for each mode at the chosen frequencies apart from F(19,2) and F(20,2) at 100 kHz since DISPERSE [65] can plot up to the 18^{th} order mode only. Note that the maximum deviation from the bulk shear velocity occurs at around $\alpha = 45^o$ for all cases tested. The axial phase velocity ($\alpha = 0$) is simply the phase velocity of the T(0,1) mode and is the bulk shear velocity for the material.

At 25 kHz, $k_s = \omega/c_s = 48.18$ and there are 5 propagating modes of the torsional-flexural family. These are labeled in figure 2.14. The F(5,2) mode has $k_{circ} = 47.41$ and propagates at $\alpha_5 = 80^o$. The worst variation from the bulk shear velocity is +1.9% for the F(3,2) mode which propagates at 40^o from the axial direction. The data point in the circumferential direction, $\alpha = 90^o$ was found using Disperse for a SH wave propagating in a circumferential direction. The solution to the wave equation in the circumferential direction was studied in detail by Fong [69] and Gridin [70] and will not be covered here.

At 50 kHz, there are twice as many propagating modes since the wavelength has halved from that at 25 kHz. The bulk shear wavenumber is $k_s = \omega/c_s = 96.37$ and there exists up to the tenth order mode of the torsional-flexural family, F(10,2) for which $k_{circ} = 94.82$. This mode propagates at an angle of 80^o from the axial direction at this frequency. At 50 kHz, the mode with the largest variation from the bulk shear velocity is F(7,2) which propagates at 43^o from the axial direction. The velocity deviation is +0.52% from the bulk shear velocity.

At 100 kHz, the highest order propagating mode in the 8 inch pipe is F(20,2). However, the software package will calculate up to circumferential order $n = 18$ only. There are therefore no velocity predictions for $n = 19, 20$ available from Disperse. The largest velocity deviation is 0.14% at F(14,2) at $\alpha_{14} = 43.6^o$.

The same analysis was carried out for a 16 inch schedule 40 ($r_c = 0.19847$ m and $t = 9.53$ mm) mild steel pipe at 25 kHz and 50 kHz. 100 kHz analysis was not carried out due to the large number of modes (up to F(38,2)) that can propagate in this larger pipe at this frequency. The velocity deviation from the bulk shear velocity is plotted against propagation angle α for the 25 kHz and 50 kHz cases in figure 2.15. Also shown on the figure are the 50 kHz and 100 kHz cases for the 8 inch pipe from the above analysis. The velocity deviations for the 25 kHz 16 inch and the 50 kHz 8 inch cases are almost identical, as are the 50 kHz 16 inch and 100 kHz 8 inch cases. The maximum deviations from the bulk shear velocity $err_{\%}$ for each case studied are summarized in table 2.1.

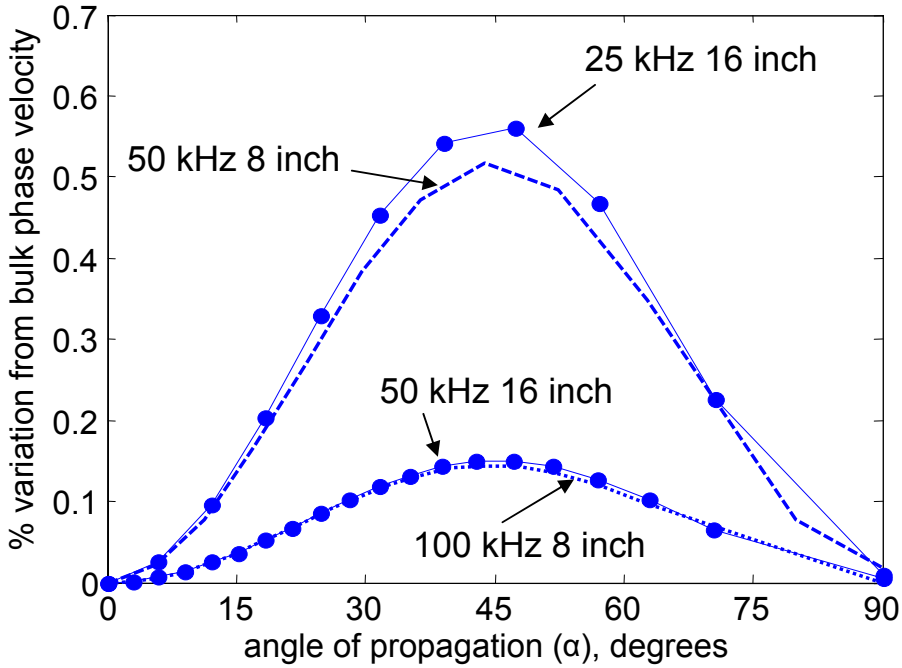

Figure 2.15: *% variation of the phase velocity calculated using DISPERSE from the bulk shear velocity against angle of propagation from the axial direction for a 16 inch schedule 40 mild steel pipe.*

The maximum velocity deviations are plotted against $(c_s/\omega r_c)^2$, which is a dimensionless parameter, in figure 2.16. The data points fit accurately to a line. The line of best fit is also plotted and has gradient of 49. The predicted maximum velocity error is therefore

$$err_{\%} = 49(\frac{c_s}{\omega r_c})^2 = (\frac{7}{k_s r_c})^2 \tag{2.36}$$

where $\omega = 2\pi f$. Note that this prediction is restricted to frequencies below the SH1 cutoff in a plate of thickness equal to the pipe wall thickness or below the T(0,2) mode cutoff in the pipe ($f > \frac{2c_s}{h}$). Equation 2.36 predicts that the velocity error will decrease with increasing frequency-radius product and will be zero for a pipe of infinite radius, which is effectively a plate. However, there will be a velocity error, albeit a small error, for all finite pipe sizes in the frequency region of interest for inspection purposes.

The maximum error prediction (2.36) is extremely useful since it can be used to

Table 2.1: Cases studied for the pipe-plate analogy and their respective maximum deviation from the bulk shear velocity

Pipe size	f, kHz	n_{max}	maximum $err_{\%}$
8 inch	25	5	1.9
	50	10	0.51
	100	20	0.144
16 inch	25	9	0.56
	50	19	0.149

define the frequency-radius (fr_c) region where the pipe-plate analogy can be used for a given maximum velocity error err_{MAX}

$$fr_c > \frac{7c_s}{2\pi\sqrt{err_{MAX}}}. \tag{2.37}$$

As an example, the lowest frequency f_{lim} for which the pipe-plate analogy can be used for an 8 inch pipe ($r_c = 0.10546m$) for a maximum allowable velocity error of $err_{MAX} = 1\%$ is

$$f_{lim} = \frac{7c_s}{2\pi r_c\sqrt{err_{MAX}}} = \frac{7 \times 3260}{2\pi \times 0.10546 \times \sqrt{1}} = 34.4 \text{ kHz} \tag{2.38}$$

2.4 Guided Wave Conclusions

Bulk waves can travel in two ways, as a shear wave and as a longitudinal wave; the two wave types are uncoupled in an infinite medium. In a finite medium the bulk waves will interact with the boundaries of the medium and these interactions give rise to the formation of guided waves. The guided wave solution can be found by assuming a certain type of solution and substituting it into the given boundary conditions to find the unknown coefficients in the assumed solution. This is known as solution by the method of potentials.

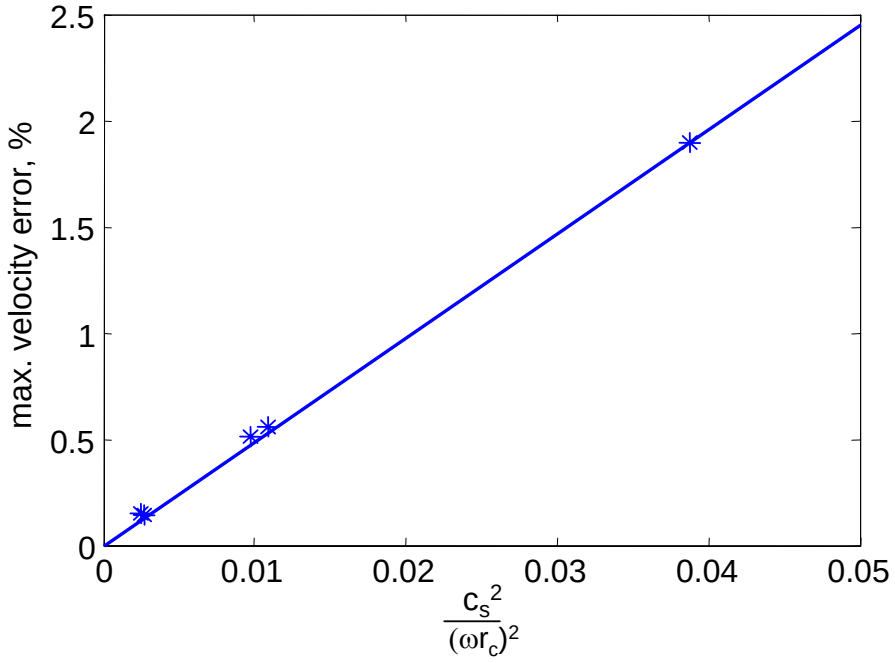

Figure 2.16: *Maximum velocity errors for all cases examined.*

A brief overview to the solution of the Shear Horizontal (SH) guided wave family in plates by the method of potentials was given in section 2.2.1. The solution for Symmetric and Antisymmetric plate modes was then outlined in section 2.2.2.

Wave propagation in pipes is complex but can be fully described by solving a six dimensional determinant (equation 2.25) whose solutions are described by Bessel functions. This can be solved numerically by, for example, DISPERSE [61]. There are various situations in which the pipe guided wave solution is simplified. These cases arise when there is either no variation along the pipe axial direction or no variation around the pipe circumference. The latter axisymmetric modes may be longitudinal or torsional in nature. The longitudinal modes can be either symmetric or antisymmetric through the pipe wall. These longitudinal modes are similar to the symmetric (S) and antisymmetric (A) plate modes with discrepancies at very low frequencies. The torsional (T) modes in a pipe correspond exactly to the shear horizontal (SH) mode solutions in a plate.

Flexural modes involve displacements in all directions and require solution of the full six dimensional pipe determinant. The flexural mode family whose dispersion curves

tend to the bulk shear velocity at higher frequencies (F(n,2)) have been thoroughly investigated. This family of modes is relevant for the torsional type inspection which is the main topic of this thesis.

It has been proposed, for this torsional-flexural family of modes, that one may think of the pipe as a plate-like structure whose solution is described by exponential functions instead of the Bessel functions. There is, however, an extra boundary condition over the isotropic plate case which states that the plate-like solution at the two edges which would be joined to form the pipe structure must match. It is this extra boundary conditions which accounts for the finite number of propagating modes at a given frequency in the pipe. Each mode, of circumferential order n, can be thought of as a plate plane wave propagating in a direction at a fixed angle α_n to the axial direction. It is important to note that the angle of propagation in a given pipe size will be different for each temporal frequency.

The extent to which the pipe modal solution for the torsional-flexural (F(n,2)) mode family converges to the plate SH0 case was investigated. The SH0 propagation in the plate case has phase velocity c_s in all directions. The phase velocity in all possible modal propagation directions α_n was found for 8 and 16 inch pipes at various frequencies of interest using DISPERSE [61, 65] which solves the full pipe guided wave problem. The maximum phase velocity deviation from the bulk shear velocity occurred at a propagation angle of $\alpha = 45^o$. The maximum velocity deviation was quantified and is proportional to $(c_s/\omega r)^2$. The pipe solution therefore tends to the plate-like solution with increasing frequency-radius product. The worst phase velocity errors occur at lower frequencies and were 1.9% at 25 kHz for an 8 inch schedule 40 pipe and 0.5% at 25 kHz for a 16 inch pipe.

The similarity of the results from the two methods of creating dispersion curves for the F(n,2) torsional-flexural mode family means that the plate imaging algorithms which will be introduced in the following chapter should be easily modified for use in pipe imaging over the frequency-radius product of interest for inspection. It also means that one can apply the extensive work which has been done for defect scattering in plates [71–78] to the case of defect scattering in a pipe, which is often

a difficult problem to analyse [14, 17].

Chapter 3

Plate Imaging

3.1 Synthetic Focusing

In this chapter, synthetic focusing algorithms will be derived and tested for imaging of plates using guided waves. The aim of the algorithms is to create a representative reconstruction of a real object space which contains local changes in acoustic impedance. These local changes will be referred to as scatterers and could be caused by, for example, changes in plate thickness due to corrosion. The reconstructed image is generally not a perfect reproduction of the object space due to diffraction effects of the wave propagation. This limits the resolution of the reconstruction as will be demonstrated in the following sections of this chapter. The steps for imaging are:

- Excite a known wavefield in the object space
- Record the scattered field from the object space
- Apply a reconstruction technique to image the object space

The first two steps are the acquisition or data-capture phase. For imaging using ultrasonic sound waves, the first step of exciting a probing wavefield is known as insonification of the object space. The third step is the reconstruction phase and

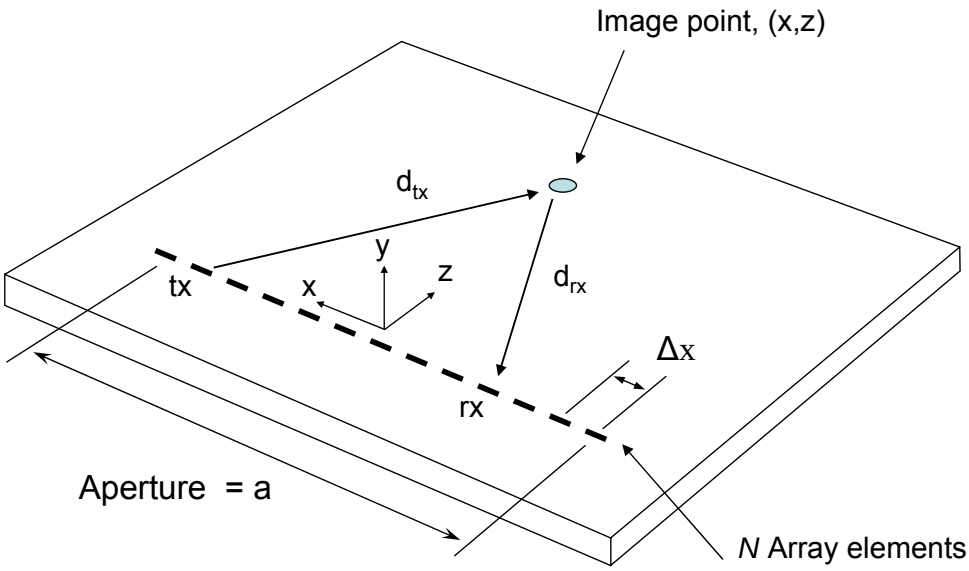

Figure 3.1: *Geometry of the plate case studied.*

aims to synthetically invert the wave propagation of the first two steps leading to coherent summation of recorded signals at the scatterer locations in the image. The image reconstruction is achieved for the entire object space post-acquisition and hence these methods can be termed synthetic focusing methods.

The geometry of the plate case studied is shown in figure 3.1. The z direction is perpendicular to a linear array, into the object space, and will be referred to as the axial direction. The x direction, or lateral direction, is parallel to the array, with the origin at the centre of the array. The aperture a has linear sampling Δx and contains $N = a/\Delta + 1$ sensors. The sensors, or transducers, are assumed to be able to excite and receive a chosen guided wave mode. The sensors are assumed to be phase sensitive, meaning they can record both amplitude and phase of the backscattered signal. This is not an unreasonable assumption since the measurement time is negligible compared to the temporal period of the wave fields considered. The object space is essentially two dimensional over (x, z) after the behaviour of the guided waves through the plate thickness (y) has been explained using the analysis of section 2.2.

The image reconstruction algorithms which will be investigated in this chapter for plate imaging and in the following chapter for pipe imaging differ in their transmit-

receive geometries. These differences arise due to the type of array architecture that is available and subsequently allows different data sets to be recorded. The different architectures require varying amounts of hardware and their data acquisition times vary significantly. Therefore, it is important to test the performance of the different options to ascertain whether more complex and expensive hardware or longer acquisition times is worthwhile.

The three transmit-receive geometries that will be considered here are shown in figure 3.2. They each require a different inversion algorithm to achieve the optimum synthetic focusing of the recorded backscattered data set and this will lead to differences in imaging performance [79]. Figure 3.2a shows the transmit-receive geometry used for the imaging algorithm which we have called the Common Source method (CSM). One transducer is fired and backscattered reflections from the object space are recorded at each sensor in the array in a pitch-catch arrangement [79]. Note that normally all of the transducers would be fired simultaneously to increase the input power into the object space during the acquisition phase.

The Synthetic Aperture Focusing Technique (SAFT) requires only the pulse-echo data set as shown in figure 3.2b. This means that the data set can be acquired using a single scanned transducer [44, 52, 80] or by individually addressing each sensor in the array in turn [42].

The Total Focusing Method (TFM) uses data from all possible transmit-receive combinations [47]. That is to say, that a time trace is recorded at each receiver for each firing transmitter. This is often referred to as Full Matrix Capture (FMC) since the transmit-receive matrix is filled. In fact, the matrix is symmetric due to reciprocity so only the lower or upper triangular part of the matrix need be recorded as shown in figure 3.2c. The rest of the data matrix can then be filled by symmetry [79]. The CSM and SAFT data sets are in fact, subsets of the full matrix. Various other subsets of the full matrix have been investigated using subapertures [43, 81, 82] but this will not be investigated here.

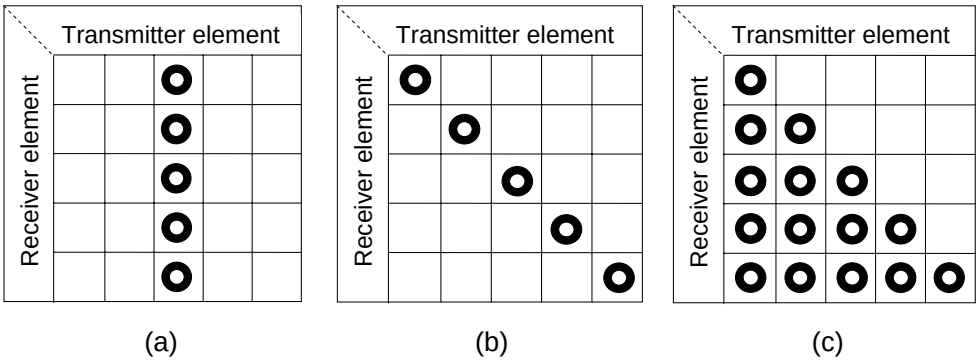

Figure 3.2: *Transmit-receive matrices for the imaging algorithms; (a) CSM; (b) SAFT; (c) TFM.*

Section 3.5 discusses the implementation of CSM, SAFT and TFM. Their data-capture complexity, hardware requirements and acquisition times are also discussed.

The inversion algorithms associated with each transmit-receive geometry of interest are derived in the following sections of this chapter. The analysis makes extensive use of the angular spectrum method which formulates diffraction theory into a form which resembles the theory of linear systems [83]. This approach involves analysing the complex field recorded across the sensor aperture at $z = 0$ in terms of its Fourier components. The Fourier transform of the recorded field is called the recorded angular spectrum. The Fourier components of the recorded angular spectrum can be identified as plane waves travelling in different directions away from the measurement plane (see appendix A for more detail). An extremely important property of this approach is that the angular spectrum at a plane which is parallel to the measurement plane can be calculated by adding the contributions of these plane wave components, taking due account of the respective phase shifts they have undergone during their propagation [83]. Similar approaches are used for imaging with radar, for example [84] and seismic imaging [85], where the algorithm are referred to as Fourier migration algorithms.

The monochromatic inversion algorithm for CSM will first be derived for an infinite aperture with continuous sampling in section 3.2.1. Its performance with the limiting case of a finite aperture with discrete sampling will then be investigated

in section 3.2.2. Sections 3.3 and 3.4 examine SAFT and TFM respectively and investigate their theoretical imaging performance.

The theoretical response to a point scatterer in the object space will be analysed for each algorithm. This response is called the Point Spread Function (PSF) which would ideally be a Dirac delta function in the image at the scatterer location having infinitesimal width and no sidelobes. In reality, the PSF has finite width and sidelobes due to diffraction and finite array aperture effects. The width of the main lobe of the PSF can be used as a measure of resolution of the imaging algorithm [80]. The width of the main lobe can be measured using the Full Width at Half Maximum (FWHM) which is also called the 6 dB Width (W_{6dB}) of the main lobe since the half maximum amplitude is at -6 dB. It is hoped that the width of the PSF main lobe will prove a useful measurable quantity to indicate the lateral size of a finite sized defect. The relative amplitude of the PSF sidelobes give useful information as to the coherent noise rejection of the algorithm.

The separation required between two point scatterers in order for them to be resolved is also evaluated for each algorithm presented. In the context of this plate imaging study, the amplitude of the defect response is not of interest. The amplitude of the defect response will be investigated in more detail in the following chapter for the imaging of pipes as a way of estimating the defect depth.

The algorithms are tested using data from a plate finite element model of a crack oriented parallel to the array using the SH0 guided wave mode in section 3.6.

Imaging results from simple validation experiments on a mild steel plate using the A0 guided wave mode are given in section 3.7. Conclusions for the imaging of plates using synthetic focusing of guided waves are given in the final section of this chapter.

3.2 Common Source Method (CSM)

3.2.1 CSM for a continuously sampled infinite aperture

The CSM involves firing all of the transducer elements simultaneously and then receiving at each sensor individually. In order to derive the algorithm to perform the inversion of this propagation, consider the simplified case of a continuously sampled infinite aperture along the x-axis ($z = 0$). The recorded angular spectrum $F(k_x, z = 0)$ of a monochromatic field $f(x, z = 0)$ recorded along the aperture is defined as

$$F(k_x, z = 0) = \int_{-\infty}^{\infty} f(x, z = 0) e^{-jk_x x} dx. \tag{3.1}$$

The recorded field can then be written as the inverse Fourier transform of the received angular spectrum

$$f(x, z = 0) = \int_{-\infty}^{\infty} F(k_x, z = 0) e^{jk_x x} dk_x. \tag{3.2}$$

Suppose a scattering distribution of $s(x, z_s)$, located along a line at axial distance $z = z_s$ away from the array in the object space, whose angular spectrum is $S(k_x, z_s)$. In this case, the scattering distribution refers to changes in local acoustic impedance which will cause scattering of probing wave. Changes in local acoustic impedance can be caused by deviations in density or compressibility [86]. For example, a hole is a sudden local change in density from that of the background medium to zero (strictly, the local density is that of the gas which occupies the hole but this will be significantly less than the background medium).

The recorded spectrum is the scattered spectrum $S(k_x, z_s)$ phase shifted to take account of the propagation of the probing plane wave from the array to the scattering plane and the scattered plane waves propagating in the background medium back to the array (see [83] or appendix A).

$$F(k_x, z = 0) = e^{-jkz_s} S(k_x, z_s) e^{-jk_z z_s}. \tag{3.3}$$

where $k = 2\pi/\lambda$ is the wavevector of the probing plane wave in the background medium and k_z are the wavevector components in the z direction of the returning plane waves and is given by

$$\begin{aligned} k_z &= \sqrt{k^2 - k_x^2} \quad k_x < k, \\ k_z &= i\sqrt{k_x^2 - k^2} \quad k_x > k, \end{aligned} \tag{3.4}$$

The condition $k_x > k$ in (3.4) corresponds to evanescent waves which decay within a few λ of propagation. The propagation in the background medium therefore acts as a low pass filter which suppresses spatial frequencies larger than $k = 2\pi/\lambda$. It is this low pass filtering which will limit the resolution of any conventional imaging system as only the propagating waves can be used for remote image reconstruction. The propagating solutions of k_z in (3.4) are illustrated in figure 3.3. $k_x = 0$ is the DC component of the angular spectrum which corresponds to $k_z = k$ and is a plane wave travelling perpendicular to the array, and hence has no variation across the aperture.

The first exponential terms of (3.3) accounts for the phase shift of the probing plane wave which travels from the aperture with $k_z = k$ to the scattering line at $z = z_s$. The probing plane wave is generated by exciting the entire aperture simultaneously. The second exponential term in (3.3) accounts for the phase shifting of the scattered plane waves as they travel back to the array at $z = 0$. Both positive and negative values of k_x must be propagated in order to account for all of the plane waves travelling from the scatterer. The propagation of the angular spectrum in (3.3) neglects any interaction of the propagating waves with other scatterers present in the medium. This is the Born approximation and assumes that the propagation is not distorted by the object structure as the waves travel through it.

Substituting (3.3) into (3.2) gives the recorded field in terms of the scattering spectrum

$$f(x, z = 0) = \int_{-\infty}^{\infty} \sqcap(k_x/k) e^{-jkz_s} S(k_x, z_s) e^{-jk_z z_s} e^{jk_x x} dk_x \tag{3.5}$$

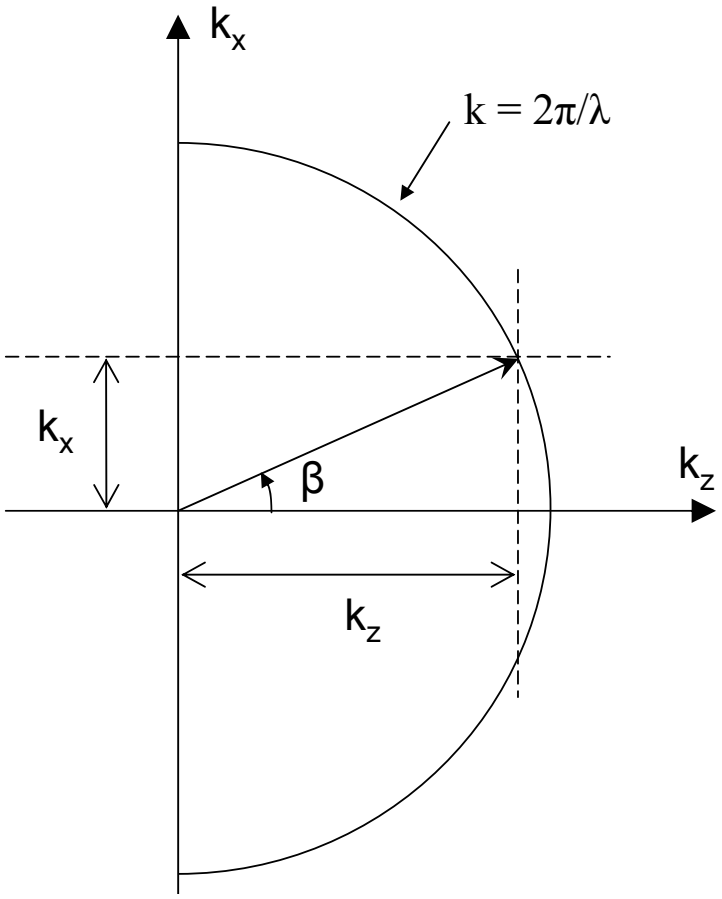

Figure 3.3: *Wavenumber graphical representation. β is the propagation angle.*

where $\sqcap(k_x/k)$ denotes a top hat spatial frequency filter over k_x which removes spatial frequencies for which $|k_x| > k$ and is shown in figure 3.4. This accounts for the spatial frequency filtering due to the propagation in the background medium discussed above.

The proposed imaging method is to use the angular spectrum method to backproject the recorded spectrum to lines parallel to the array aperture at axial distance $z = \zeta$. The lateral image $I(x, \zeta)$ is the inverse Fourier transform of the recorded angular spectrum phase shifted to take into account the propagation of the probing waves to $z = \zeta$ and the propagation of all of the scattered plane waves back to the array. For the plane wave insonification of CSM, the proposed lateral image slice at $z = \zeta$ is

$$I(x, \zeta) = \int_{-\infty}^{\infty} e^{jk\zeta} F(k_x, z = 0) e^{jk_z\zeta} e^{jk_x x} dk_x \tag{3.6}$$

The exponential phase shifting terms of (3.6) are chosen to cancel the effects of the propagation of the probing plane wave to the axial distance of interest and the scattered waves propagating back the aperture. Substituting (3.3) into (3.6) and taking account of the spatial frequency filtering of propagation in the background medium (3.4) gives

$$I(x,\zeta) = \int_{-\infty}^{\infty} e^{jk\zeta}[\sqcap(k_x/k)e^{-jkz_s}S(k_x,z_s)e^{-jk_z z_s}]e^{jk_z\zeta}e^{jk_x x}dk_x \tag{3.7}$$

$$= \int_{-\infty}^{\infty} \sqcap(k_x/k)S(k_x,z_s)e^{jk(\zeta-z_s)}e^{jk_z(\zeta-z_s)}e^{jk_x x}dk_x. \tag{3.8}$$

It is clear that the only axial distance ζ where there is coherent summation over all spatial frequencies k_x is at the scatterer axial location $\zeta = z_s$. At this axial location, synthetic focusing has been achieved. The algorithm of equation (3.6) will produce an image peak at the scattering location $\zeta = z_s$ where the lateral image slice will be

$$I(x,z_s) = \int_{-\infty}^{\infty} \sqcap(k_x/k)S(k_x,z_s)e^{jk_x x}dk_x \tag{3.9}$$

The integral over k_x can be identified as the inverse Fourier transform of the low-pass filtered version of the actual scattering object $S(k_x,z_s)$. The convolution theorem states that (3.9) can be written as

$$I(x,z_s) = s(x,z_s) \otimes h(x) \tag{3.10}$$

where $h(x)$ is the inverse Fourier transform of $\sqcap(k_x/k)$:

$$IFT_{k_x}[\sqcap(k_x/k)] = \frac{\sin kx}{x} \tag{3.11}$$

The image slice at the scattering axial location $z = z_s$ can then be written as

$$I(x,z_s) = s(x,z_s) \otimes \frac{\sin kx}{x}. \tag{3.12}$$

It is clear that the image $I(x,z_s)$ is not an exact representation of the scattering distribution $s(x,z_s)$ but is blurred by the removal of higher spatial frequencies ($k_x >$

k) by the background medium. The probing plane wave used for CSM provides no lateral resolving power and all of the lateral resolution obtained can be attributed to the focusing on reception.

If a point scatterer is located at $(x, z) = (0, z_s)$ then the scattering distribution is simply a Dirac delta function at $x = 0$ and $s(x, z_s) = \delta(0)$. The lateral image slice at the scatterer axial location is

$$PSF = \delta(0) \otimes \frac{\sin kx}{x} = \frac{\sin kx}{x}. \tag{3.13}$$

This is the Point Spread Function (PSF) for the CSM using an infinite aperture which is continuously sampled, the modulus of which is shown in figure 3.5. The FWHM and maximum sidelobe amplitude are marked on the figure. The first zero of equation 3.13 occurs when $kx = \pi$ or $x/\lambda = 0.5$ giving a main lobe width of 1λ. The Full Width at Half Maximum (FWHM) can be measured from figure 3.5 and is $\approx 0.6\lambda$. Another important factor in determining the performance of an imaging algorithm is the coherent noise rejection. This can be measured by the amplitude of the sidelobes of the PSF. Here, the amplitude of the first and largest sidelobe is measured relative to the scatterer peak and is 0.22 or -13 dB as marked on figure 3.5. The shape of the PSF is not dependent on axial location and is therefore space invariant for this infinite array case with a linear object $s(x, z_s)$ parallel to the aperture. The PSF would not be space invariant if the object function $s(x, z)$ was 2-dimensional.

The *Rayleigh criterion* [87] states that two separate scatterers will be resolved when the maximum response of one scatterer is at the same location as the first zero of the other PSF. This separation distance for the infinite aperture CSM case described above would be $\lambda/2$. However, for the case when the two scatterers are insonified in phase, as would be the case if they were both an equal distance from the array (*i.e.* the probing plane wave has the same phase $\vartheta = jkz_s$ at both scatterers) then the Rayleigh separation is not sufficient to be able to distinguish the two scatterers.

A more general resolution criterion is the *Sparrow separation* [88] which is the sep-

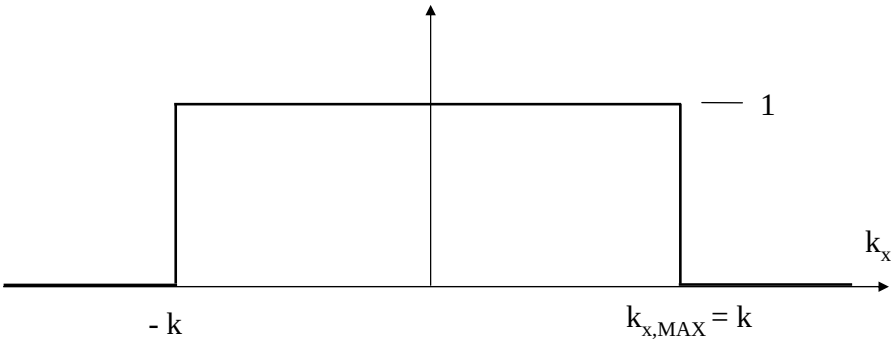

Figure 3.4: *Low-pass filtering of spatial frequencies above $k = 2\pi/\lambda$ by propagation in the background medium.*

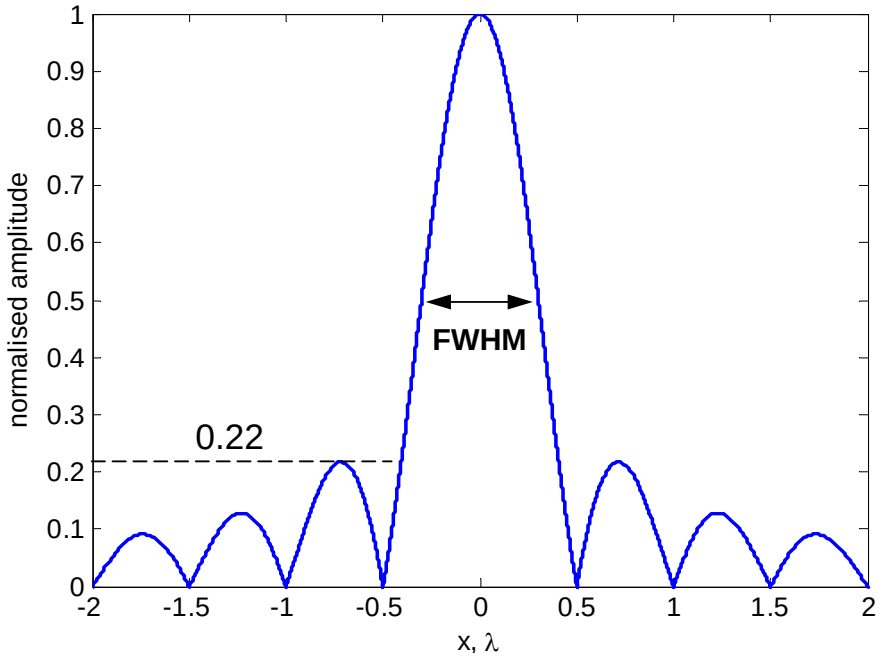

Figure 3.5: *CSM lateral Point Spread Function for infinite array and array sampling of $\Delta < \lambda/2$.*

aration distance between two point scatterers at which they just become resolvable and a dip appears between the two image peaks. Two point scatterers with coherent insonification, separated by the Rayleigh separation are shown in figure 3.6a and cannot be resolved. Figure 3.6b shows two scatterers separated by the Sparrow separation which can just be resolved. Figure 3.6c shows two scatterers separated by more than Sparrow separation which can clearly be resolved. The CSM Sparrow separation is $\delta_{res} = 0.7\lambda$ for the infinite aperture case.

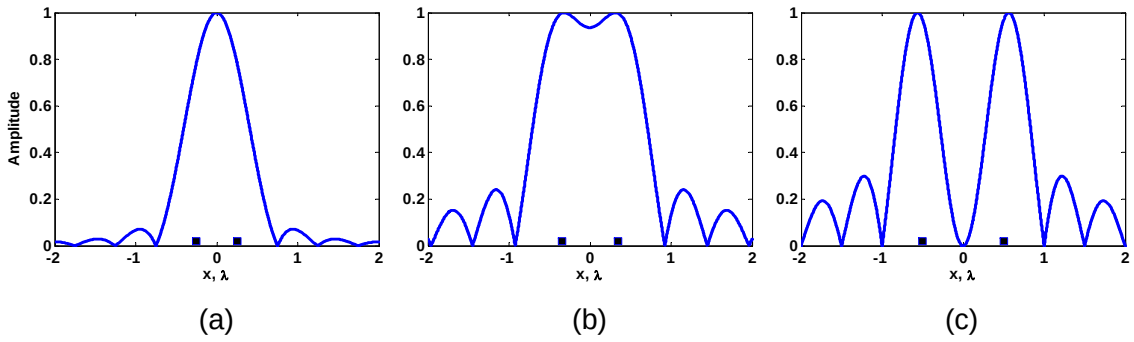

Figure 3.6: *The two-point resolution for CSM with coherent insonification. (a) Rayleigh separation of* 0.5λ*: unresolvable, (b) Sparrow separation of* 0.7λ*: peaks are just resolvable, (c) Separation of more than Sparrow separation* (1λ)*: peaks are clearly resolvable.*

3.2.2 CSM response with a sampled finite aperture

The imaging response for CSM was defined in the previous section for a continuously sampled infinite aperture along the x-axis at $z = 0$. Now the effects of a finite aperture of length a with a regular sampling step of Δ will be evaluated. Firstly, the response to a plane wave incident orthogonal to the aperture will be evaluated theoretically. Then the analysis will be extended to that of a plane wave incident at any angle β to the aperture; the PSF for the finite array case will also be examined.

The imaging performance can be studied by analysing the angular spectrum $F(k_x, z = 0)$ of the measured field $f(x, z = 0)$. The measured field can be expressed as $f(x, z = 0) = s(x, z = 0)p(x)g(x)$, where $s(x, z = 0)$ is the backscattered wave field along the x-axis, $p(x)$ is the aperture pupil function and $g(x)$ is a sampling function which is periodic with Δ such that

$$g(x) = \delta(x - n\Delta) \tag{3.14}$$

where n is an integer, Δ is the array sampling interval and $\delta(.)$ denotes the Dirac delta function. The spatial spectrum $F(k_x)$ of $f(x)$ is the convolution of the Fourier transform of the pupil function $p(x)$, $P(k_x)$, with that of the sampling function $g(x)$,

$G(k_x)$ with the incoming wave spectrum $S(k_x, z = 0)$

$$F(k_x, z = 0) = S(k_x, z = 0) \otimes P(k_x) \otimes G(k_x). \tag{3.15}$$

Since $g(x)$ is periodic with period Δ, it can be written as a Fourier series

$$g(x) = \sum_{n=-\infty}^{+\infty} e^{i\frac{n2\pi}{\Delta}x} \tag{3.16}$$

whose Fourier transform is a simple summation of delta functions

$$G(k_x) = \sum_{-\infty}^{+\infty} \delta(k_x - n\frac{2\pi}{\Delta}). \tag{3.17}$$

If the aperture is a square pupil function defined by

$$\begin{aligned} p(x) &= 1 \quad |x| < a/2, \\ p(x) &= 0 \quad |x| > a/2, \end{aligned} \tag{3.18}$$

then the Fourier transform of $p(x)$ is a sinc function

$$P(k_x) = \frac{2\sin(\frac{a}{2}k_x)}{k_x}, \tag{3.19}$$

whose main lobe width (to first zero) is $4\pi/a$. $P(k_x)$ will tend to a Dirac delta function for an infinite array.

In order to evaluate the array response, consider a plane wave field impinging on the linear aperture at normal incidence. The angular spectrum $S(k_x, z = 0)$ of the incoming plane wave is a Dirac delta function centred at $k_x = 0$, *i.e.* there is no variation across the aperture. Therefore, the recorded spectrum is now simply

$$F(k_x) = \delta(0) \otimes P(k_x) \otimes G(k_x) = P(k_x) \otimes G(k_x). \tag{3.20}$$

The convolution of $P(k_x)$ with $G(k_x)$ leads to periodic repetitions of the sinc functions (3.19) separated by $2\pi/\Delta$. Figure 3.7 shows the recorded angular spectrum

(3.20) for an incident wave orthogonal to the aperture of length a, uniformly sampled by Δ. Note that the ideal recorded angular spectrum would be a delta function at $k_x = 0$. The width of the sinc functions depends on the size of the aperture a only, whereas the position of the repeated peaks is defined by the sampling interval Δ only. In order to approach the ideal case of $F(k_x) = \delta(0)$, it is clear that the aperture size a must tend to infinity and the aperture sampling Δ must tend to zero.

The repeated peaks in $F(k_x)$ caused by convolution with $G(k_x)$ shown in figure 3.7 will amplify any plane waves associated with $k_x = n2\pi/\Delta$. It is these undesired amplifications of certain plane waves in the backprojection procedure that leads to *grating lobes* in the reconstructed image. Since waves with $k_x > k$ are evanescent, the condition for no grating lobes in the reconstructed image is that no extra peaks can exist in $F(k_x)$ in the range $k < k_x < k$, where $k = 2\pi/\lambda$. Therefore, for no grating lobes, the aperture sampling should satisfy

$$\Delta < \lambda, \tag{3.21}$$

which holds for an incident plane wave orthogonal to the aperture. In the more general case, with a plane wave incident at an angle β to the normal of the aperture, the incoming scattered spectrum $S(k_x)$ becomes a Dirac delta function at $k_x = k\sin\beta$. Therefore, $F(k_x)$ is shifted by $k\sin\beta$. This leads to the condition for no grating lobes to become

$$2\pi/\Delta > k + k\sin\beta \tag{3.22}$$

$$\Delta < \frac{\lambda}{1 + sin\beta} \tag{3.23}$$

which, to be satisfied for all β, requires

$$\Delta < \frac{\lambda}{2} \tag{3.24}$$

which is the standard Nyquist-Shannon sampling theorem and must be observed to avoid grating lobes in the reconstructed image. If this sampling criterion is met then the sampling spectrum $G(k_x)$ of (3.20) can be ignored.

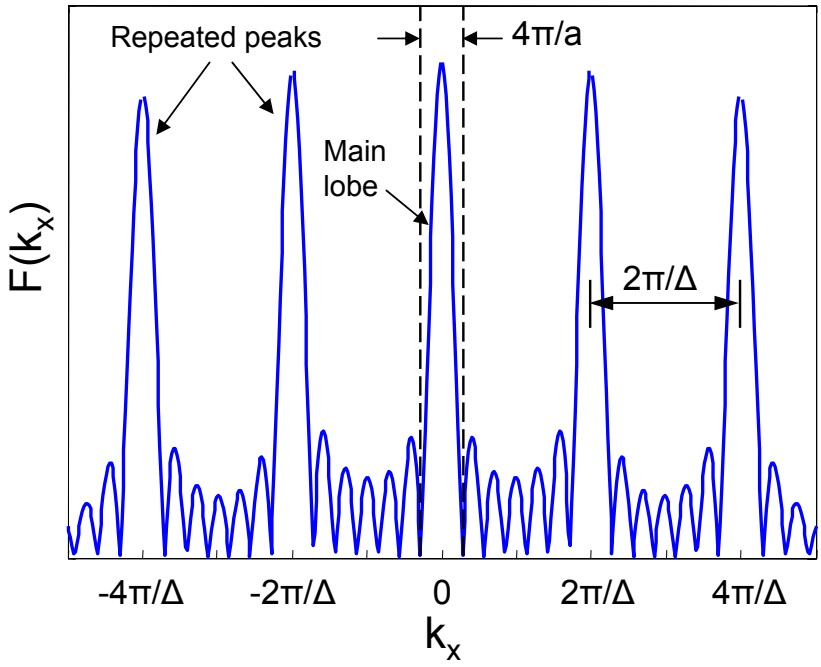

Figure 3.7: *The recorded angular spectrum $F(k_x) = P(k_x) \otimes G(k_x)$ for a plane wave incident orthogonal to the aperture.*

For the more general case of a linear scattering distribution at axial distance z_s whose spatial Fourier spectrum is $S(k_x, z_s)$, the recorded spectrum, assuming sufficient array sampling, is

$$F(k_x, z = 0) \quad = \quad P(k_x) \otimes [e^{-jkz_s} S(k_x, z_s) \sqcap (k_x/k) e^{-jk_z z_s}] \tag{3.25}$$

where the two exponential terms account for the phase shifting due to the propagation of the probing plane wave and the backscattered plane waves respectively.

In order to assess the effect of the finite aperture, consider a finite sized array and a point scatterer located at $(x, z) = (0, z_s)$, as shown in figure 3.8. The maximum angle β_{max} of plane wave that can be received by the finite-sized array is the angle between the aperture normal and the ray path to the scatterer

$$\beta_{max}(z_s, a) = \arctan(\frac{a/2}{z_s}) \tag{3.26}$$

where a is the aperture of the array and z_s is the distance of the scatterer from the array. In this case the received angular spectrum $F(k_x)$ is limited to components of

k_x such that $|k_x| < k \sin \beta_{max}$, where $\sin \beta_{max}$ is known as the numerical aperture [83]. The lateral spatial frequencies available for imaging are shown in figure 3.9. In this respect, the finite aperture $p(x)$ has the effect of further low pass filtering the lateral spatial frequencies k_x which is more severe than the low pass filtering as a result of propagation in the medium, and even less of the backscattered information can be received by the aperture. The expression for the recorded angular spectrum becomes

$$F(k_x) \quad = \quad \sqcap(\frac{k_x}{k \sin \beta_{max}}) e^{-jkz_s} S(k_x, z_s) e^{-jk_z z_s} \tag{3.27}$$

where the top hat function $\sqcap$ accounts for the limited lateral spatial frequencies that can be received ($|k_x| < k \sin \beta_{max}$) by the finite aperture.

Substituting (3.27) into the CSM (3.6) leads to the image at axial distance ζ

$$I(x, \zeta) \quad = \quad \int_{-\infty}^{\infty} \sqcap(\frac{k_x}{k \sin \beta_{max}}) e^{jk(\zeta - z_s)} S(k_x, z_s) e^{jk_z(\zeta - z_s)} e^{jk_x x} dk_x \tag{3.28}$$

As for the infinite array case (3.7), coherent summation over all spatial frequencies occurs only at the scattering axial location, $\zeta = z_s$ where the lateral image is

$$I(x, z_s) = \int_{-\infty}^{\infty} S(k_x, z_s) \sqcap (\frac{k_x}{k \sin \beta_{max}}) e^{jk_x x} dk_x. \tag{3.29}$$

Recognising the integral over k_x as an inverse Fourier transform, the image slice at $z = z_s$ can be written in a similar form to (3.12) for the infinite array

$$I(x, z_s) = \frac{sin([k \sin \beta_{max}]x)}{x} \otimes s(x, z_s) \tag{3.30}$$

where the sinc function is the inverse Fourier transform of the top hat function $\sqcap(\frac{k_x}{k \sin \beta_{max}})$.

The PSF is the lateral image for the case of a point scatterer at $(x, z) = (0, z_s)$. Setting $s(x, z_s) = \delta(0)$ gives

$$PSF_{\beta_{max}} = \frac{\sin ([k \sin \beta_{max}]x)}{x}. \tag{3.31}$$

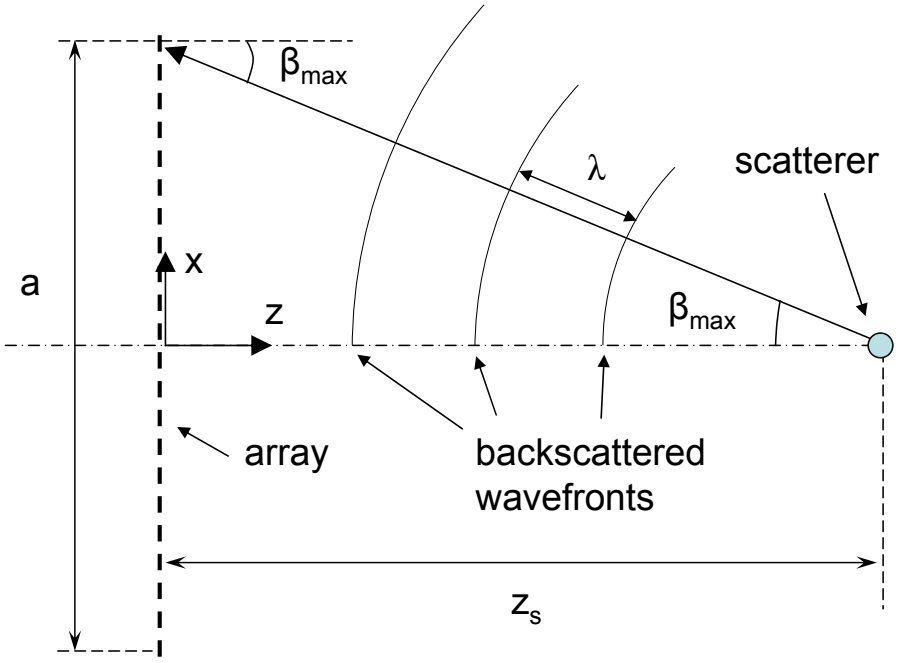

Figure 3.8: *Geometry of finite-sized array situation showing maximum recordable angle, β_{max}.*

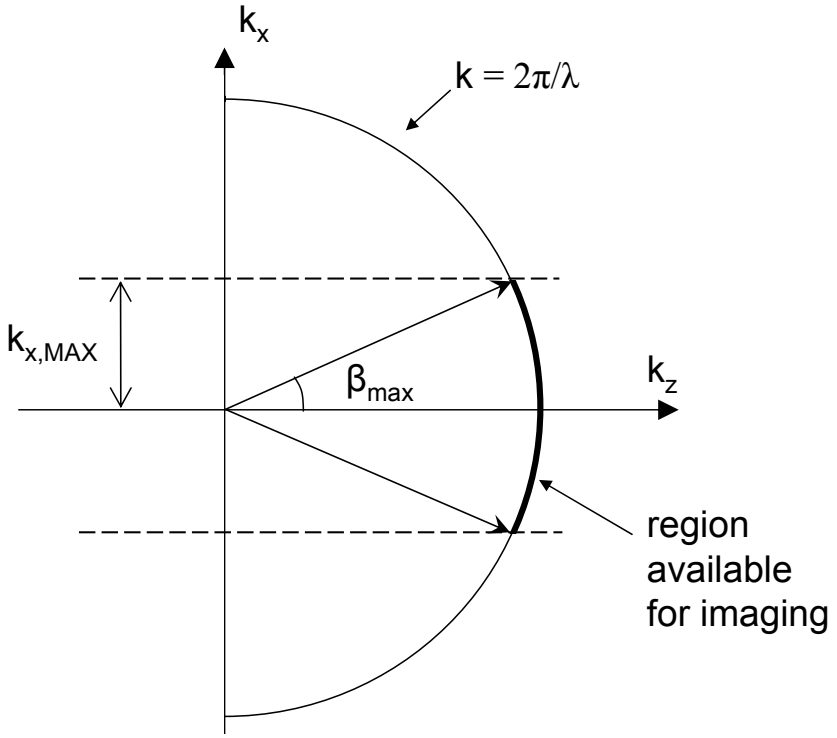

Figure 3.9: *Wavenumber graphical representation of limited array aperture limiting the maximum recordable lateral wavenumber k_x.*

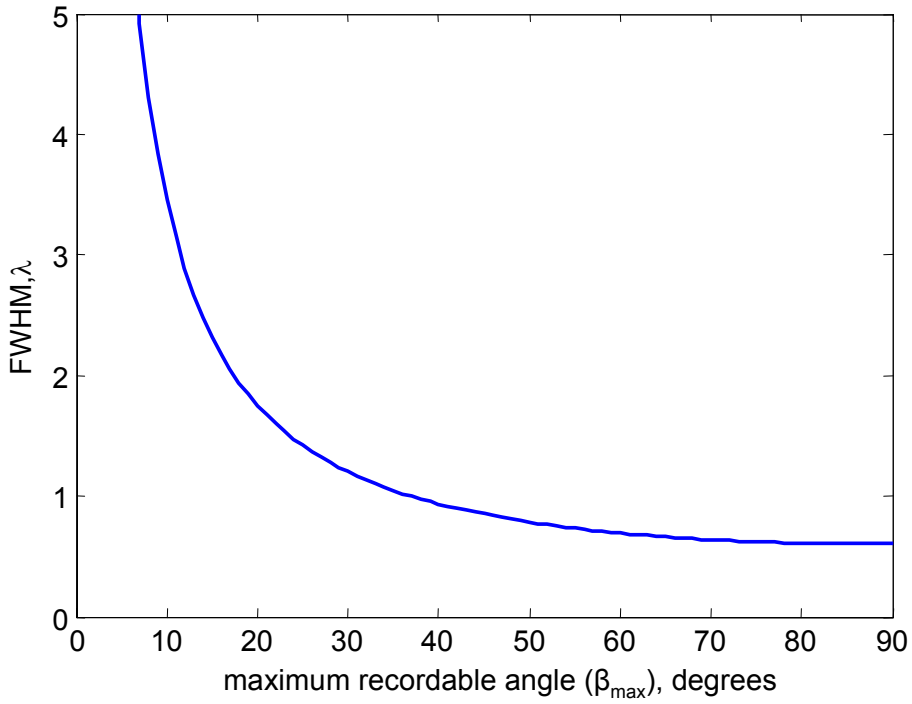

Figure 3.10: *CSM FWHM against maximum recordable angle, β_{max}.*

The first zero of the PSF occurs at $x = \frac{\lambda}{2 \sin \beta_{max}}$. The sidelobe amplitude remains unchanged from the infinite aperture case of equation (3.13) and is 0.22. The FWHM for the finite array case is

$$FWHM_{\beta_{max}} = \frac{0.6\lambda}{\sin \beta_{max}}. \tag{3.32}$$

The FWHM is plotted against β_{max} in figure 3.10. Note that the FWHM will change with axial scatterer position z_s and aperture size a as described by (3.26). The limiting case of $\beta_{max} = 90^o$ corresponds to an infinite aperture and the resulting PSF is the same as (3.13) shown in figure 3.5.

Consider a specific array setup with aperture $a = 20\lambda$ and a point scatterer located 10λ from the array at $(x, z) = (0, 10\lambda)$. The maximum receivable angle, using equation (3.26) is $\beta_{max} = \arctan(\frac{20/2}{10}) = 45^o$ and the numerical aperture is $\sin \beta_{max} = \frac{1}{\sqrt{2}}$. The resulting PSF for this situation is shown in figure 3.11. The sidelobes are the same amplitude as those predicted for the infinite array case shown in figure 3.5. The FWHM for this case can be measured from figure 3.11 to be 0.85λ

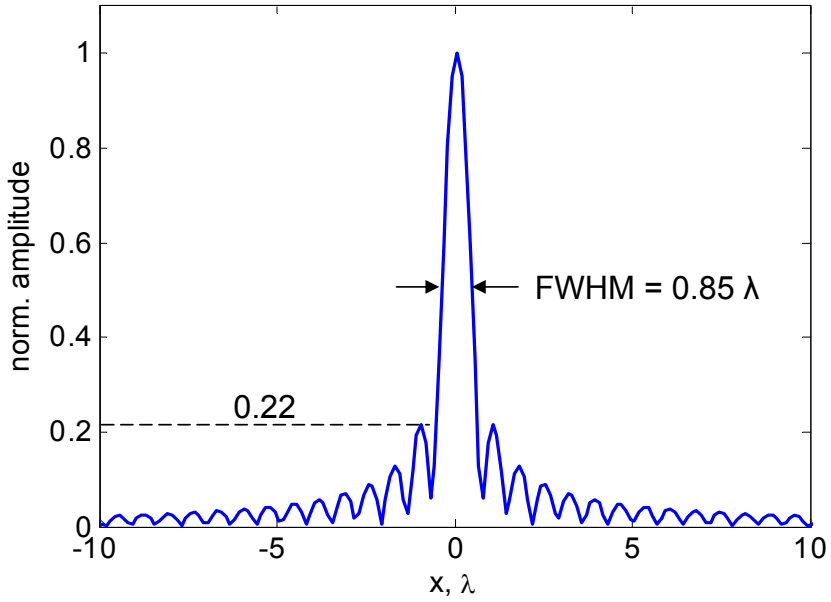

Figure 3.11: *The CSM PSF for aperture $a = 20\lambda$ and distance to scatterer $d = 10\lambda$.*

which is equal to that predicted using (3.32).

The Sparrow 2 point separation for the finite array case, assuming sufficient aperture sampling and plane wave probing signal, is

$$\delta_{res}(\beta_{max}) = \frac{0.7\lambda}{\sin \beta_{max}}. \tag{3.33}$$

3.3 Synthetic Aperture Focusing Technique (SAFT)

It was shown in section 3.2.1 that the optimal monochromatic synthetic focusing phase shifts for image reconstruction with plane wave insonification was $F(k_x, \zeta) = e^{jk\zeta}F(k_x, z = 0)e^{jk_z\zeta}$ which forms the CSM (3.6). The $e^{jk\zeta}$ term simply accounts for the probing plane wave and provides no lateral resolving power. The second phase shifting term accounts for the propagation of all spatial frequencies $k_z = \sqrt{k^2 - k_x^2}$ from the scattering location back to the array. Note that a propagator of $e^{jk_z\zeta}$ used alone gives synthetic focusing onto a source in the object space since no probing wave is required to insonify a source.

The Synthetic Aperture Focusing Technique (SAFT) only records the pulse-echo data set, as shown in figure 3.2b. The CSM monochromatic imaging algorithm of (3.6) can be modified to account for this pulse-echo data set by removing the probing plane wave propagator ($e^{jk\zeta}$) and modifying the scatterer backpropagator term ($e^{jk_z\zeta}$) to account for propagation of the outgoing probing waves and the returning backscattered waves.

The distance from a point on the array to any point in the object space and back to the aperture is simply double the distance from the aperture to the object point. Therefore, the pulse-echo nature effectively doubles the distance travelled. This has the effect of halving the apparent propagation velocity which doubles the effective wavenumber (k_{eff})

$$k_{eff} = \frac{\omega}{c/2} = 2k, \tag{3.34}$$

the SAFT partial wavevector relation is

$$k_{eff}^2 = (2k)^2 = k_x^2 + k_{z,SAFT}^2 \tag{3.35}$$

and hence

$$k_{z,SAFT} = \sqrt{(2k)^2 - k_x^2} \tag{3.36}$$

The monochromatic algorithm of SAFT is therefore

$$I(x,\zeta) = \int_{-\infty}^{\infty} \sqcap(\frac{k_x}{2k}) F(k_x, z=0) e^{jk_{z,SAFT}\zeta} e^{jk_x x} dk_x \tag{3.37}$$

Note that only one phase shifting operator is required to synthetically focus on transmission and reception. The low pass filtering of the SAFT algorithm $\sqcap(\frac{k_x}{2k})$ allows spatial frequencies up to $|k_x| = 2k$ which is double those allowed by CSM (3.9).

The PSF of SAFT for a continuously sampled infinite array will therefore be

$$PSF = \delta(0) \otimes \frac{\sin 2kx}{x} = \frac{\sin 2kx}{x}. \tag{3.38}$$

and is shown in figure 3.12. Note that the effective doubling of spatial frequencies available for image reconstruction halves the width of the CSM PSF. The sidelobe amplitude is equal to the CSM sidelobe amplitude of 0.22 or -13 dB.

It can readily be shown that the effects that were seen in section 3.2.2 for the CSM with a linearly sampled finite array will be comparable for SAFT. Therefore, assuming sufficient aperture sampling, the PSF for the finite array case is

$$PSF_{\beta_{max}} = \frac{\sin\left([2k\sin\beta_{max}]x\right)}{x}. \tag{3.39}$$

where β_{max} is defined by (3.26). The SAFT main lobe is half the width of that of CSM (3.31) giving a Full Width at Half Maximum (FWHM) of

$$FWHM_{\beta_{max}} = \frac{0.3\lambda}{\sin\beta_{max}}. \tag{3.40}$$

The predicted Sparrow 2 point separation for SAFT with a finite aperture is

$$\delta_{res}(\beta) = \frac{0.35\lambda}{\sin\beta_{max}}. \tag{3.41}$$

which is half that of the CSM (3.33).

3.4 Total Focusing Method (TFM)

The Total Focusing Method (TFM) uses the full matrix of data and every transmit-receive combination is recorded (figure 3.2c). In this respect it is possible to synthetically focus the received backscattered waves on transmission and reception to produce coherent summation at scatterer locations. Assuming transmission from point $x = x_T$ and reception at $x = x_R$ the recorded angular spectrum $F(k_{x_T}, k_{x_R}, z = 0)$ is 2 dimensional over k_{x_T} and k_{x_R}

The elemental plane waves associated with all combinations of k_{x_T} and k_{x_R} of the recorded angular spectrum must be backpropagated to account for both transmission

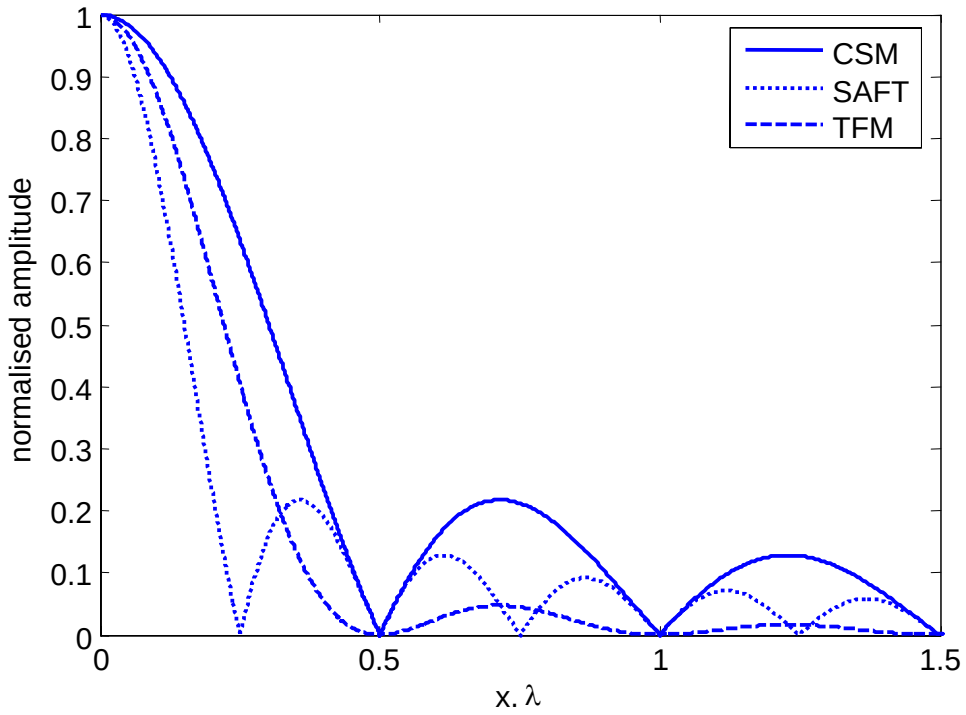

Figure 3.12: *Point Spread Functions for a continuously sampled infinite aperture, solid line: CSM; dotted line: SAFT; dashed line: TFM.*

and reception. The propagator $e^{jk_z\zeta}$ with $k_z = \sqrt{k^2 - k_x^2}$ was used in CSM to synthetically focus the backscattered waves at an axial location ζ after that location had been insonified with a probing plane wave. The same propagator can be used to synthetically focus on transmission due to reciprocity of the system.

The proposed TFM algorithm is therefore

$$F(k_{x_T}, k_{x_R}, \zeta) = e^{jk_{z_T}\zeta} F(k_{x_T}, k_{x_R}, z = 0) e^{jk_{z_R}\zeta} \tag{3.42}$$

The first exponential propagator synthetically focuses over spatial frequencies associated with transmission (k_{x_T}) where $k_{z_T} = \sqrt{k^2 - k_{x_T}^2}$. The second exponential propagator of (3.42) synthetically focuses over spatial frequencies associated with reception (k_{x_R}) where $k_{z_R} = \sqrt{k^2 - k_{x_R}^2}$. Both transmission propagation and reception propagation will remove spatial frequencies above $|k_{x_T}| > k$ and $|k_{x_R}| > k$ respectively. It can be shown that the phase shifts of (3.42) will produce coherent summation at the scatterer locations using a similar argument used in the preceding sections of this chapter for CSM and SAFT. Assuming the phase shifts invert the

propagation correctly, the image at $\zeta = z_s$ is the 2D inverse Fourier transform of (3.42) which leads to

$$I(x_T, x_R, z_s) = \frac{\sin kx_T}{x_T}\frac{\sin kx_R}{x_R} \otimes s(x_T, x_R, z_s) \tag{3.43}$$

Noting that for the geometry under consideration $x_R = x_T = x$ the lateral image for TFM is simply

$$I(x, z_s) = (\frac{\sin kx}{x})^2 \otimes s(x, z_s) \tag{3.44}$$

Therefore, a point scatterer at $(x, z) = (0, z_s)$ giving $s(x, z_s) = \delta(0)$ will give the PSF for TFM

$$PSF = (\frac{\sin kx}{x})^2 \tag{3.45}$$

The TFM PSF is therefore the CSM PSF (3.13) squared. This has the effect of narrowing the main lobe and reducing the relative sidelobe amplitude. The TFM PSF is shown in figure 3.12 for the infinite aperture case along with the those of CSM and SAFT. The TFM PSF main lobe is clearly narrower than that of CSM but not as narrow as that of SAFT.

The finite aperture case with maximum recordable angle β_{max} as defined by (3.26) will give a TFM PSF of

$$PSF_{\beta_{max}} = (\frac{\sin([k\sin\beta_{max}]x)}{x})^2. \tag{3.46}$$

The Full Width at Half Maximum (FWHM) of the TFM finite aperture case is

$$FWHM_{\beta_{max}} = \frac{0.44\lambda}{\sin\beta_{max}}. \tag{3.47}$$

The predicted Sparrow 2 point separation for TFM with a finite aperture is

$$\delta_{res}(\beta_{max}) = \frac{0.45\lambda}{\sin\beta_{max}}. \tag{3.48}$$

The TFM sidelobe amplitude is just 0.048 or -26 dB, compared to -13 dB for CSM and SAFT, making the two point resolution comparable to the FWHM due to the reduced coherent noise in the image.

3.5 Implementation of Imaging Algorithms and their complexity

The imaging algorithms used to reconstruct the image along a line parallel to the array aperture have been derived in the previous sections of this chapter; (3.6) for CSM, (3.37) for SAFT and (3.42) for TFM. In order to build the full image the recorded angular spectrum must be backprojected to each axial slice of interest for each temporal frequency of interest.

The Common Source Method (CSM) is the simplest of the three imaging algorithms studied here since there is only one firing during the acquisition phase. This makes the data capture very fast. Subject to sufficient parallel receiver amplifier channels, backscattered reflections are recorded at each transducer in the array simultaneously. If parallel reception is not possible then the receiver amplifier channel can be multiplexed across the array, requiring N firings for an N element array. The number of separate transducer firings required for each algorithm are listed in table 3.1.

The SAFT requires only the pulse-echo data set which can be acquired by scanning a single transducer to synthetically create the full aperture. For N transducer locations there are N recorded time traces. For a fixed array, the acquisition is achieved by addressing each transducer in turn.

The recorded data set for CSM and SAFT is a set of N time traces for an array of N transducers, $f(x, z = 0, t)$. These traces form a two dimensional data set sampled over x and t with sampling steps of Δ and δt respectively. Here, x represents the positions of the transducer along the aperture, $z = 0$ indicates that the data are recorded along the x-axis and t is the time.

Performing a 2D Fourier Transform over x and t of the recorded data set gives the recorded Angular Spectrum, $F(k_x, z = 0, \omega)$. More detail on the angular spectrum can be found in appendix A or [83]. For each frequency, ω, The Angular Spectrum is a superposition of plane waves with component wavenumbers k_x in the x direction

$$F(k_x, z = 0, \omega) = FT_{x,t}[f(x, z = 0, t)]. \tag{3.49}$$

The Fourier transform is a Discrete Fourier Transform since the aperture is sampled with N points. The number of discrete values of lateral spatial frequencies k_x is N. k_x will take N discrete values between $-\pi/\Delta$ and π/Δ where Δ is the aperture sampling interval. Note that the largest value of recordable k_x must be larger than k to accurately measure all backscattered waves. This leads to the same sampling criterion derived earlier (3.24)

$$\begin{aligned} k_{x_{max}} = \frac{\pi}{\Delta} &> k = \frac{2\pi}{\lambda} \\ \Delta &< \frac{\lambda}{2} \end{aligned} \tag{3.50}$$

The recorded angular spectrum is then backprojected into the object space in order to find the angular spectrum at each axial slice ($z = \zeta$) of interest for each frequency $\omega \in \Omega$ where Ω is the chosen bandwidth. The total angular spectrum $\bar{F}(k_x, \zeta)$ at $z = \zeta$ is the summation of all the angular spectra within the chosen temporal frequency bandwidth

$$\bar{F}(k_x, \zeta) = \sum_{\omega \in \Omega} F(k_x, z = 0, \omega) e^{jk_z \zeta} \tag{3.51}$$

where $k_z = k + \sqrt{k^2 - k_x^2}$ for CSM, where the k accounts for the probing plane wave, and $k_z = \sqrt{(2k)^2 - k_x^2}$ for SAFT and $k = \omega/c$ is the wavenumber of the guided wave in the background medium. For certain guided wave modes, the phase velocity is not constant as was discussed in chapter 2. This dispersion can be accounted for automatically by using $k(\omega) = \omega/c(\omega)$ where $c(\omega)$ is the frequency dependent phase velocity of the guided wave mode being used for inspection.

Table 3.1: Acquisition and image reconstruction complexity as functions of the number of transducers in the array N

Complexity	CSM	SAFT	TFM
Acquisitions with multiplexed reception	N	N	$(N-1)N/2$
Acquisitions with parallel reception	1	N	N
imaging formation using DFTs	$\propto N^2$	$\propto N^2$	$\propto N^3$
imaging formation using FFTs	$\propto N \log N$	$\propto N \log N$	$\propto 2N^2 \log(N)$

The final image at $z = \zeta$ is the inverse discrete Fourier transform of (3.51) over k_x

$$I(x, \zeta) = IFT_{k_x}[\bar{F}(k_x, \zeta)]. \tag{3.52}$$

The complexity of the image reconstruction process as a function of the number of transducers in the array N is listed in table 3.1 for each algorithm.

Since the TFM uses the full data matrix (FMC) then the data acquisition is necessarily more complex. It was shown in figure 3.2c that due to reciprocity, only $(N-1)N/2$ time traces need to be acquired for an N element array. The rest of the data matrix can then be filled by symmetry. If N parallel receiver amplifier channels are available then the acquisition can be achieved with N firings and hence the acquisition time is comparable to that of SAFT but at the expense of the extra receiver channels. Without parallel reception capabilities, FMC will take significantly longer than SAFT or CSM acquisition.

The FMC is a set of N^2 time traces for an array of N transducers, $f(x_T, x_R, z = 0, t)$. These traces form a three dimensional data set sampled over x_T, x_R and t with sampling steps of Δ over the array and δt over time. Here, x_T is the transducer position and x_R is the receiver position, $z = 0$ indicates that the data are recorded at $z = 0$ and t is the time. Performing a 3D discrete Fourier transform over x_T, x_R and t of the recorded data set gives the TFM Angular Spectrum

$$F(k_{x,T}, k_{x,R}, z = 0, \omega) = FT_{x_T, x_R, t}[f(x_T, x_R, z = 0, t)] \tag{3.53}$$

For each temporal frequency ω the Angular Spectrum is two-dimensional over k_{x_T} and k_{x_R}. The angular spectra for each frequency within the chosen bandwidth $\omega \in \Omega$ must be backpropagated to each axial slice of interest at $z = \zeta$. The total angular spectrum $\bar{F}(k_{x_T}, k_{x_R}, \zeta)$ is the summation of all the angular spectra within the temporal frequency bandwidth

$$\bar{F}(k_{x_T}, k_{x_R}, \zeta) = \sum_{\omega \in \Omega} F(k_{x_T}, k_{x_R}, z = 0, \omega) e^{jk_z\zeta} \tag{3.54}$$

where $k_z = \sqrt{(k)^2 - k_{x_T}^2} + \sqrt{(k)^2 - k_{x_R}^2}$.

Taking the 2D inverse Fourier transform of (3.54) over k_{x_T} and k_{x_R} gives an image matrix over x_T and x_R for the axial slice at $z = \zeta$. The physically meaningful solution occurs when $x_T = x_R = x$ and so the image for the axial slice at $z = \zeta$ is simply the leading diagonal of this matrix

$$I(x, \zeta) = diag(IFT_{k_{x_T}, k_{x_R}}[\bar{F}(k_{x_T}, k_{x_R}, \zeta)]). \tag{3.55}$$

3.6 Imaging of Cracks in Plates with Finite Element Data

A simple plane stress finite element model of an aluminium plate was made using Abaqus software [89] in order to test the imaging algorithms derived in the previous sections of this chapter. Membrane elements were used, assuming infinitesimal plate thickness. The plate model was evenly meshed with square elements. A schematic of the FE model is shown in figure 3.13.

The excitation signal was a 5 cycle Hanning-windowed toneburst centred at 100kHz. The excitation was applied to individual nodes at the locations of the transducers int he array in a direction parallel to the array. This type of source excites both compressional S0 and shear horizontal SH0 in the plate model. Both modes are non-dispersive due to the membrane elements used. The peak S0 wave is in the

direction of excitation and the peak SH0 wave is perpendicular to the direction of excitation. It is therefore mainly the SH0 mode that travels in the direction of the crack. Note that membrane elements cannot support antisymmetric wave modes and hence there is no A0 mode. The phase velocity of the S0 wave is

$$c_{S0} = \sqrt{\frac{E}{\rho(1-\nu^2)}} \tag{3.56}$$

and the phase velocity of the SH0 wave is

$$c_{SH0} = \sqrt{\frac{E}{2\rho(1-\nu)}} \tag{3.57}$$

where E is the Young's modulus, ν is the Poisson's ratio and ρ is the density of the material. For aluminium, $c_p = 6320\ ms^{-1}$ and $c_s = 3130\ ms^{-1}$. The overall plate model size was chosen so that the earliest edge S0 reflection arrived after the slowest SH0 crack reflection, and hence could be time-gated out. The wavelength of the SH0 mode at the excitation centre frequency of 100 kHz is 31.3mm.

A crack of length $l_{crack} = 2.06\lambda_{SH}$ oriented parallel to the array was modelled by disconnecting adjacent elements at a distance of $d = 5\lambda_{SH}$ from the array. 33 nodes were used to model the array of aperture $a = 8\lambda_{SH}$ giving a transducer separation of $\Delta x = 0.25\lambda_{SH}$ which satisfies the sampling criterion of (3.24). The element size was 2mm which is $\lambda_{SH}/16$ at 100 kHz.

Full Matrix Capture (FMC), which is required for TFM (see figure 3.2c), was achieved by running 17 separate finite element jobs of the same FE model but with individual excitation at each of the transducer nodes on one side of the array in turn. The backscattered waves from the crack were received across the entire array ($N = 33$) for each of the 17 transducer locations. Only 17 runs were necessary since the model is symmetric about the z-axis as shown in figure 3.13. The SAFT data set (pulse-echo only, figure 3.2b) is the leading diagonal of the FMC. The CSM data set (pitch-catch) is the summation of columns of the FMC which is equivalent to firing all of the transducers simultaneously.

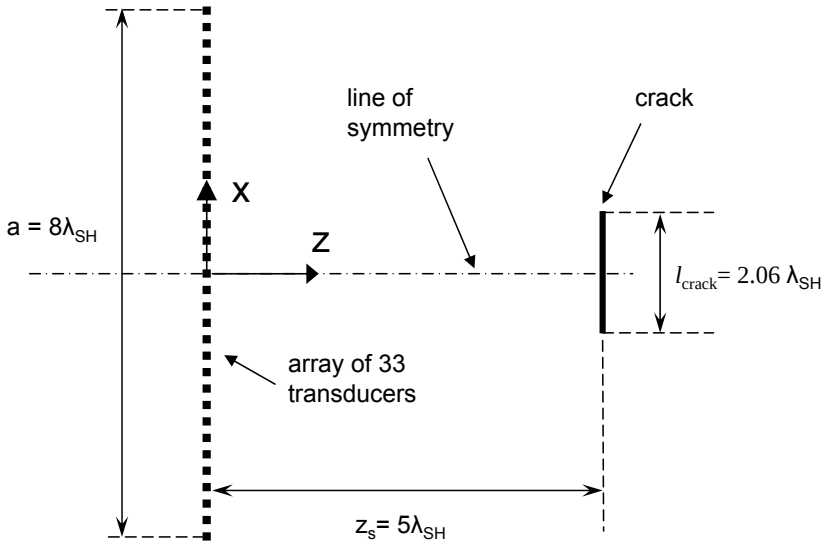

Figure 3.13: *Plate finite element model schematic.*

The time domain data set was processed using CSM, SAFT and TFM with the processing described in section 3.5 and phase velocity equal to that of the SH0 wave mode (3.57). The temporal frequencies used for processing were 80 kHz to 120 kHz, which is roughly the bandwidth of the excitation toneburst. In order to model different aperture sizes, varying subsets of the full data set were processed. The array aperture was varied from $a = 1\lambda_{SH}$ using the centre 5 transducer elements to the maximum available $a = 8\lambda_{SH}$ using all 33 transducer elements in $1\lambda_{SH}$ increments. Varying the aperture changes the maximum recordable reflection angle from the crack, β, as defined by equation 3.26. From the theoretical analysis of the finite array case of the preceding sections of this chapter, the resolution is expected to be better for larger apertures for all of the imaging algorithms.

Figure 3.14 shows the computed finite element crack FWHM against the aperture used for CSM. Also shown are the actual crack length and the theoretical FWHM of a point scatterer (3.32). The FWHM obtained from processing the finite element data is a reasonable estimator of the actual crack length when the point scatterer FWHM is less than the actual crack length. This means that when the main lobe of the PSF (3.31) is smaller than the actual crack size, accurate size estimates for cracks can be obtained. Therefore, equation (3.32) can be used to define the smallest sizable crack using CSM for a given array setup. This sizeable crack length decreases

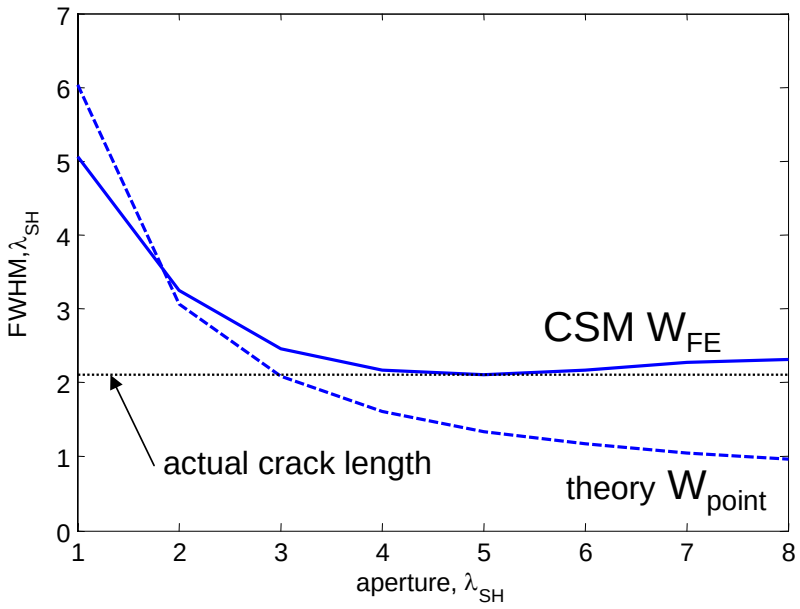

Figure 3.14: *FWHM for plate finite element study using CSM; solid line: measured from FE image; dashed line: point scatterer prediction from theory .*

as the aperture is increased or when the crack is closer to the array.

Figure 3.15 shows the measured finite element crack FWHM against the aperture used for SAFT. Also shown are the actual crack length and the theoretical FWHM of a point scatterer using SAFT (3.40). The predicted point scatterer FWHM is half that predicted for CSM. As was observed for CSM, the measured FWHM is a reasonable estimator of actual crack length when the predicted point scatterer FWHM is less than the actual crack length. However, this occurs for a smaller aperture than CSM since the predicted FWHM of SAFT is smaller, as defined by (3.40) which can be used to calculate the minimum sizeable crack size for a given array setup. Note that the FWHM curve for the finite element data does not monotonically decrease. This occurs since the crack does does reflect the probing waves equally in all directions and may exhibit reflectivity peaks in certain directions [76,77]. As the aperture size is increased, these peaks will be received by the array and will cause distortions in the shape of the crack image, leading to variations in the measured crack FWHM. The ripple effect is more pronounced for SAFT than CSM since the probing signals are incident on the crack at different angles and hence there are larger variations in

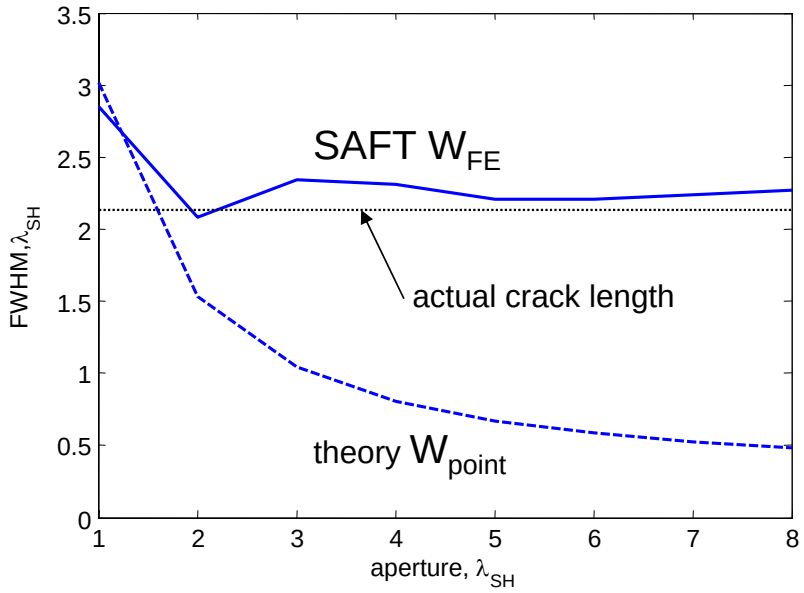

Figure 3.15: *FWHM for plate finite element study using SAFT; solid line: measured from FE image; dashed line: point scatterer prediction from theory .*

directional reflectivity than for the simple probing plane wave of CSM.

Figure 3.16 shows the measured finite element crack FWHM against the aperture used for TFM. The predicted point scatterer FWHM (3.47) is between those of CSM and SAFT as can be seen from the PSFs of figure 3.12. Once again, the measured FWHM is a reasonable estimator of the actual crack length providing the predicted point scatterer FWHM is smaller than the crack length. Equation 3.47 can be used to define the smallest sizable crack length using TFM for a given array setup. It should be noted that the TFM image FWHM overestimates the actual crack length for all apertures considered here. However, using the FWHM to estimate crack length is arbitrary and another measure of the width of the crack image may give a more accurate estimate of the actual crack length.

3.7 Validation Experiments

Experiments were carried out in order to validate the theoretical and finite element results of the preceding sections. The results of imaging of finite element data agreed

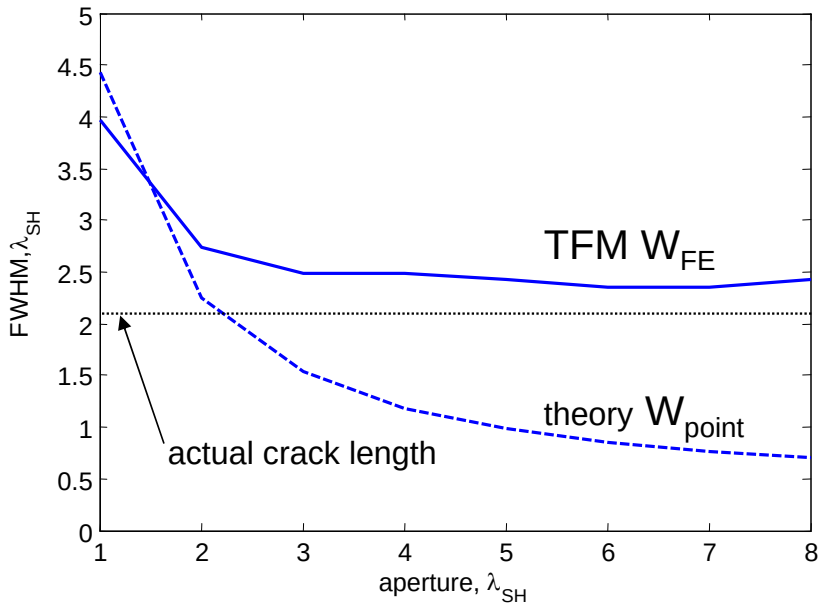

Figure 3.16: *FWHM for plate finite element study using TFM; solid line: measured from FE image; dashed line: point scatterer prediction from theory .*

well with the theoretical predictions of sections 3.2 to 3.4 for the SH0 mode. The theoretical predictions should be valid for any guided wave mode and will now be compared with experimental results using the A0 mode. The A0 mode was chosen due to its ease of excitation and reception using simple transduction methods. Also, the A0 mode is dispersive in this frequency region (see figure 2.5) which will give the opportunity to test the ability of the imaging algorithms to deal with this common guided wave phenomenon.

A single PZT disc was used for transduction and was manually scanned across a 0.9mm thick mild steel plate to simulate an array. The transducer disc was 2mm thick, had a diameter of 5mm and was bonded to a 6mm thick brass backing mass of the same diameter to increase input power to the plate. The transducer was held in place on the plate by a light spring. The PZT disc acts as an omni-directional point source for the fundamental antisymmetric guided wave mode (A0). The Poisson effect in the PZT disc may also cause some excitation of the S0 extensional mode but this is greatly reduced by gel-coupling the transducer to the plate since the fluid does not support shear forces.

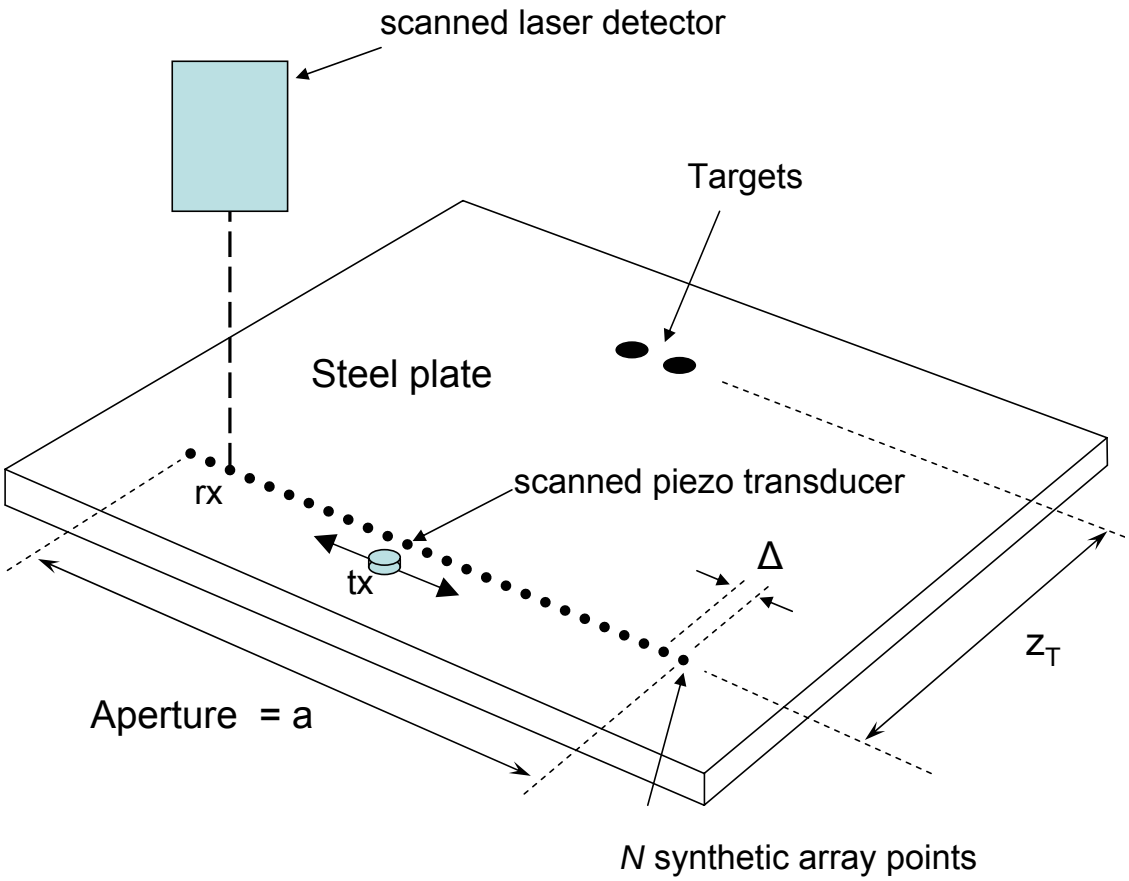

Figure 3.17: *Plate experimental setup.*

The reflected field was measured using a Polytec [90] OFV505 heterodyne laser interferometer with a Polytec OF5000 vibrometer controller. The laser was mechanically scanned across a line in front of the transduction line to simulate a receiver array. The receiver laser was angled perpendicular to the plate so it only recorded out-of-plane movement which greatly reduced its sensitivity to the S0 wavemode which has very little out-of-plane motion at the frequencies used here. The reflected signal was recorded at all receiver locations for all source locations for Full Matrix Capture (FMC) meaning that all three imaging algorithms could be used to process the experimental data. The experimental setup is illustrated in figure 3.17. Each time trace was recorded several times and averaged to sufficiently remove random noise. A five cycle Hanning-windowed toneburst centred at 50 kHz was used for the excitation signal and is shown with its frequency spectrum in figure 3.18. At 50 kHz, the A0 wavelength is 13.1mm. All dimensions quoted in λ are in λ_{A0} at 50 kHz.

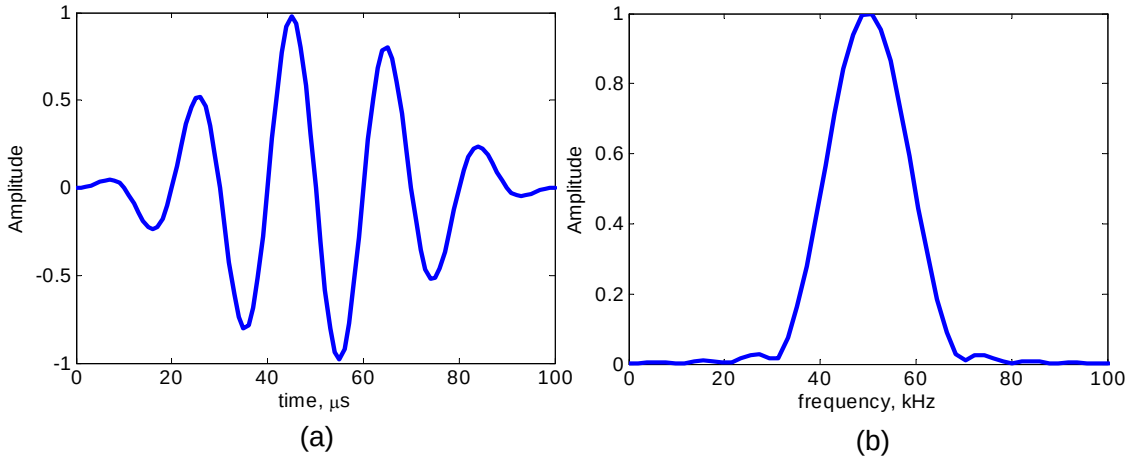

Figure 3.18: *Excitation signal for plate experiments: (a) 5 cycle Hanning-windowed toneburst centred at 50 kHz; (b) Its frequency spectrum.*

In order to validate the theoretical results for the point spread functions a single brass rod of diameter 5mm (0.38λ) was bonded to the surface of the plate. The rod creates a local change in acoustic impedance and hence causes a reflection of some of the incident wave. Measurements were taken 108mm ($z_T = 8.24\lambda_{A0}$ at 50 kHz) from the target using an aperture of 56mm ($a = 4.27\lambda$) and aperture sampling of 7mm ($\Delta = 0.53\lambda$) using 9 transducer locations ($N = 9$). In the second experiment, two 5mm (0.38λ) holes were drilled through the steel plate to test the 2 point resolution of the imaging algorithms. The centres of the holes were separated by 11mm (0.84λ). Another experiment was carried out with a 35mm (2.67λ) slit at 140mm (10.7λ) cut parallel to the array aperture . The slit was 1mm wide (0.08λ). Table 3.2 shows the setup of each of the three experiments. Note that the size of the plate was sufficiently large to be able to time gate out any edge reflections which arrive after the backscattered target reflections.

The time domain data from the experiments was transformed into the temporal frequency ω and lateral spatial frequency k_x domains and used to create images of the targets as described in section 3.5. The temporal frequencies processed were 40-60 kHz which is comparable to the bandwidth of the input toneburst as shown in figure 3.18b. The phase velocities used for processing at these frequencies were calculated using DISPERSE [61, 65] which solves the dispersion relation for the

Table 3.2: Plate Experimental Setup

Target	a, λ	Δ, λ	N	z_T, λ	β_{max}, deg
1 brass rod	4.27	0.53	9	8.24	14.6
2 drilled holes	10.7	0.53	21	7.7	33.0
2.5 λ slit	10.7	0.38	29	10.7	26.6

fundamental antisymmetric guided wave mode (equation 2.17) as described in section 2.2.2.

Figure 3.19 shows the CSM image around the single rod scatterer and its lateral image slice. There is excellent agreement with the theoretical CSM PSF evaluated using (3.31) at 50 kHz which is also shown on the lateral image slice. The main lobe is almost identical to the prediction but the sidelobes of the experimental image are slightly smaller than the prediction. This is due to the broadband processing employed which effectively increases the coherent summation of the main lobe whilst reducing the coherent summation of the sidelobes. This occurs because the wavelength varies with frequency and hence the sidelobes are not in the same position at every frequency in the bandwidth ($\omega \in \Omega$) used to create the image.

Figures 3.20 and 3.21 show the images and lateral image slices around the brass rod location for SAFT and TFM respectively. Also shown are the theoretical PSF predictions evaluated using (3.39) and (3.46) at 50 kHz. There is excellent agreement between the predictions and the experimental PSF for both SAFT and TFM. Once again, the amplitude of the experimental sidelobes are slightly less than the monochromatic prediction due to the broadband processing. Note that the experimental CSM and SAFT have similar amplitude sidelobes but those of the TFM are significantly reduced in amplitude as was predicted.

The axial extent of the main lobe of the image of the rod, which was not evaluated analytically, appears to be comparable for all algorithms at around 2.5λ. It is interesting to note that the axial sidelobes are small compared to the lateral side-

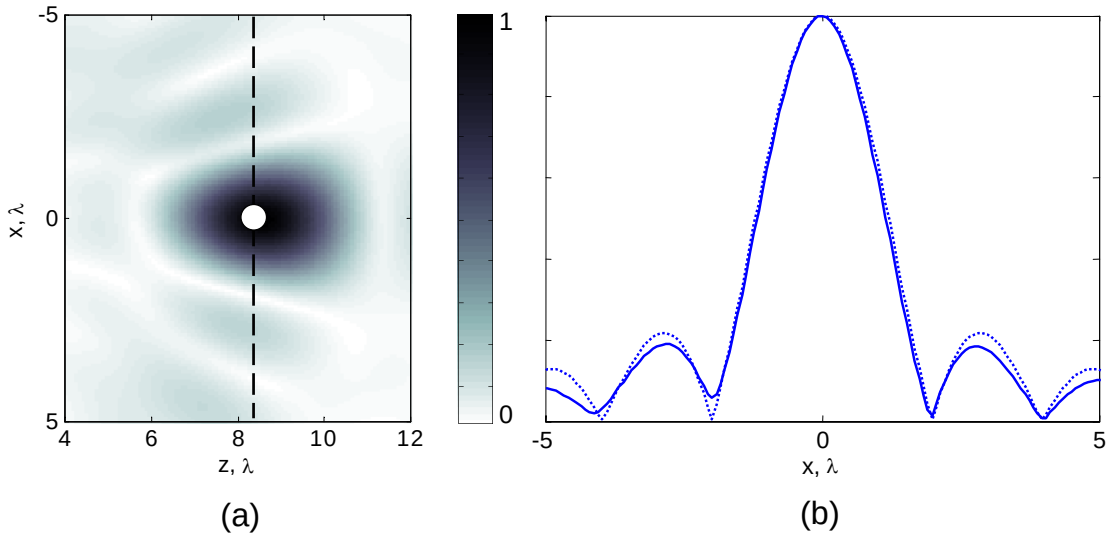

Figure 3.19: *CSM for single rod scatterer plate experiment; (a) CSM image, circle denotes scatterer location; (b)lateral CSM PSF; solid line: experimental PSF; dotted line: theoretical PSF.*

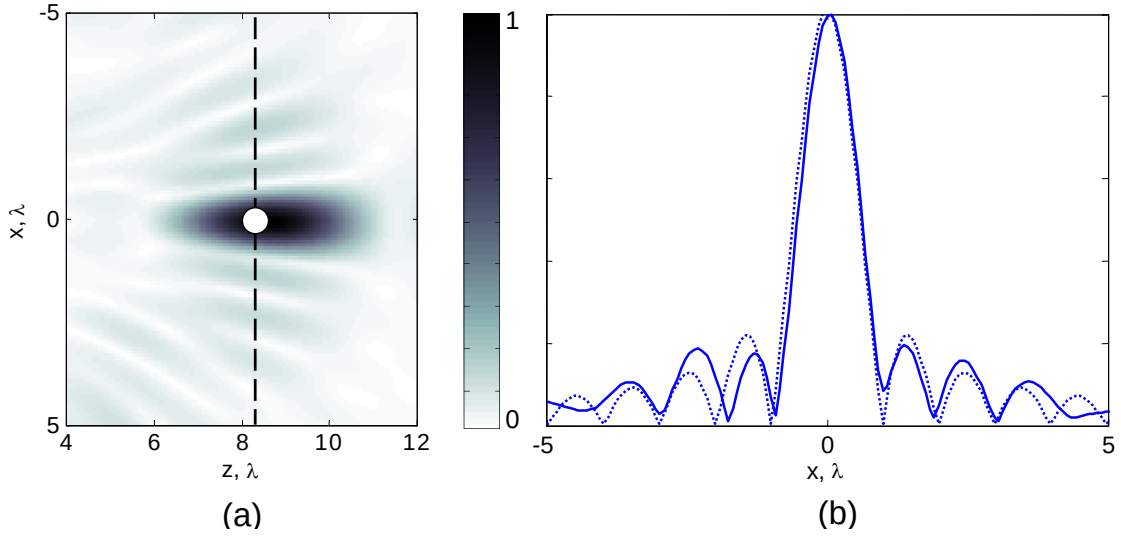

Figure 3.20: *SAFT for single rod scatterer plate experiment; (a) SAFT image, circle denotes scatterer location; (b)lateral SAFT PSF; solid line: experimental PSF; dotted line: theoretical PSF.*

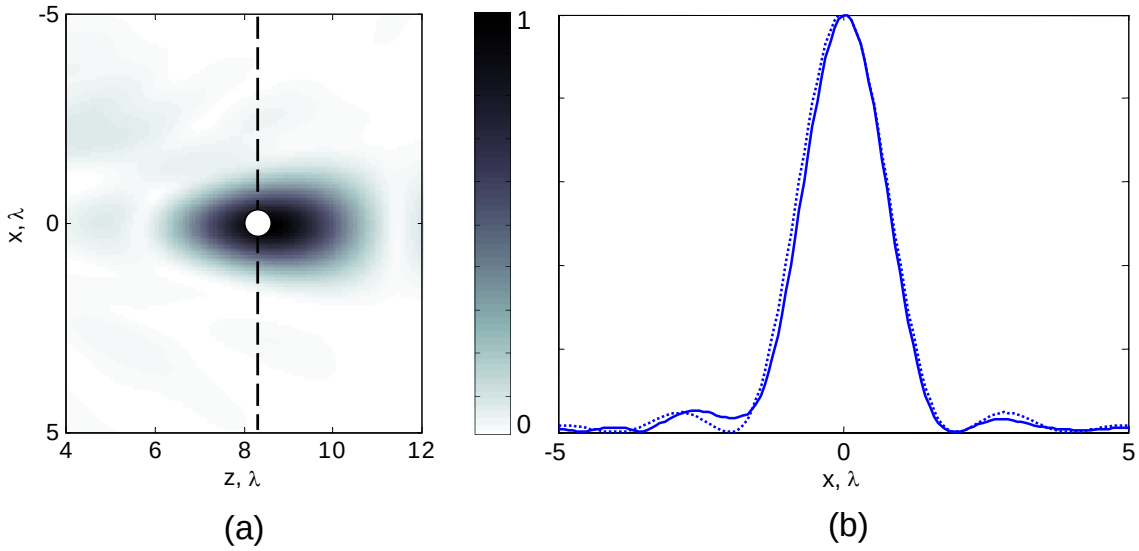

Figure 3.21: *TFM for single rod scatterer plate experiment; (a) TFM image, circle denotes scatterer location; (b)lateral TFM PSF; solid line: experimental PSF; dotted line: theoretical PSF.*

lobes. This is due to the input toneburst, and hence also the frequency spectrum available for image reconstruction, being Hanning-windowed as shown in figure 3.18. The windowing of temporal frequencies reduces the axial sidelobe amplitude. The theoretical Sparrow two-point separations δ_{res} for the array setup of the two-hole experiment can be calculated using equations (3.33), (3.41) and (3.48) for the CSM, SAFT and TFM respectively. The maximum recordable angle β for the two-hole experiment was 33^o giving separation distances of 1.29λ for CSM, 0.64λ for SAFT and 0.83λ for TFM. Therefore, the actual holes, separated by 0.78λ, should be easily resolvable with SAFT, just resolvable with TFM and not resolvable with CSM. Figures 3.22, 3.23 and 3.24 show a section of the processed images around the two holes for the CSM, SAFT and TFM respectively. The lateral PSF are shown in figure 3.25 and it is clear that the resolvability predictions were correct.

It was shown in the previous section that, for finite element data, the FWHM of the crack image could provide a reasonable estimate of the crack length, providing the crack was larger than the theoretical point scatterer FWHM. The theoretical PSFs for the geometry of the slit experiment have FWHM of 1.56λ,0.78λ and 1λ for the CSM, SAFT and TFM respectively using (3.32),(3.40) and (3.47). The experimental

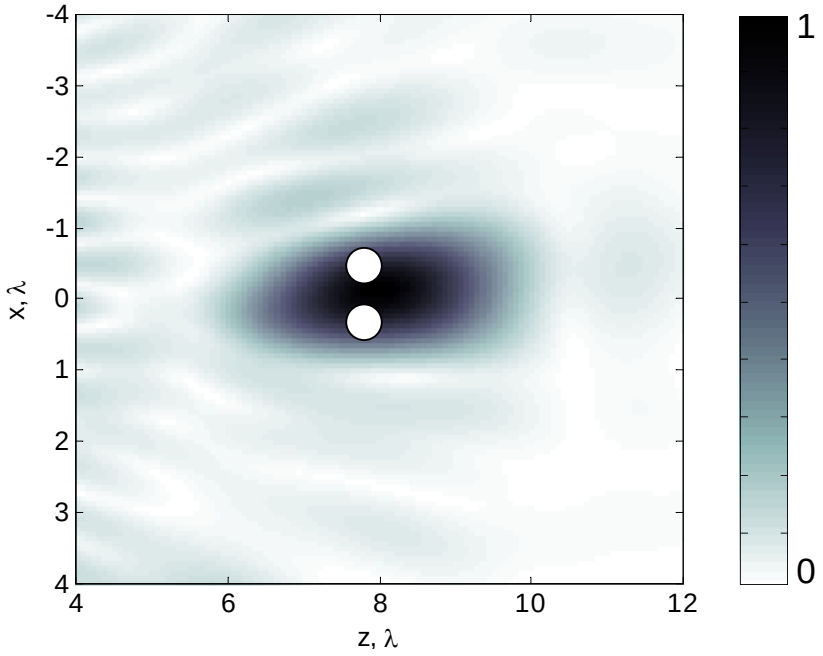

Figure 3.22: *Experimental CSM image around two holes.*

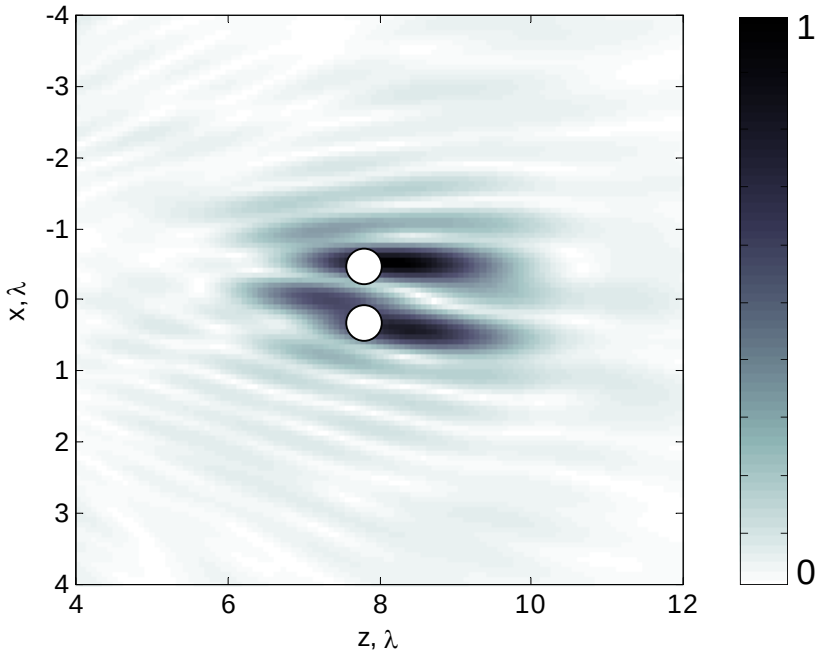

Figure 3.23: *Experimental SAFT image around two holes.*

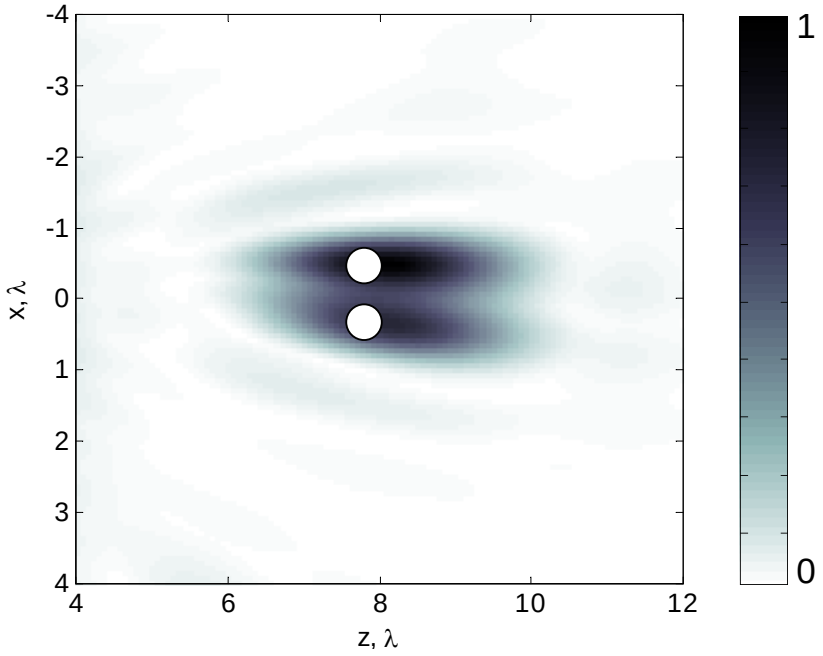

Figure 3.24: *Experimental TFM image around two holes.*

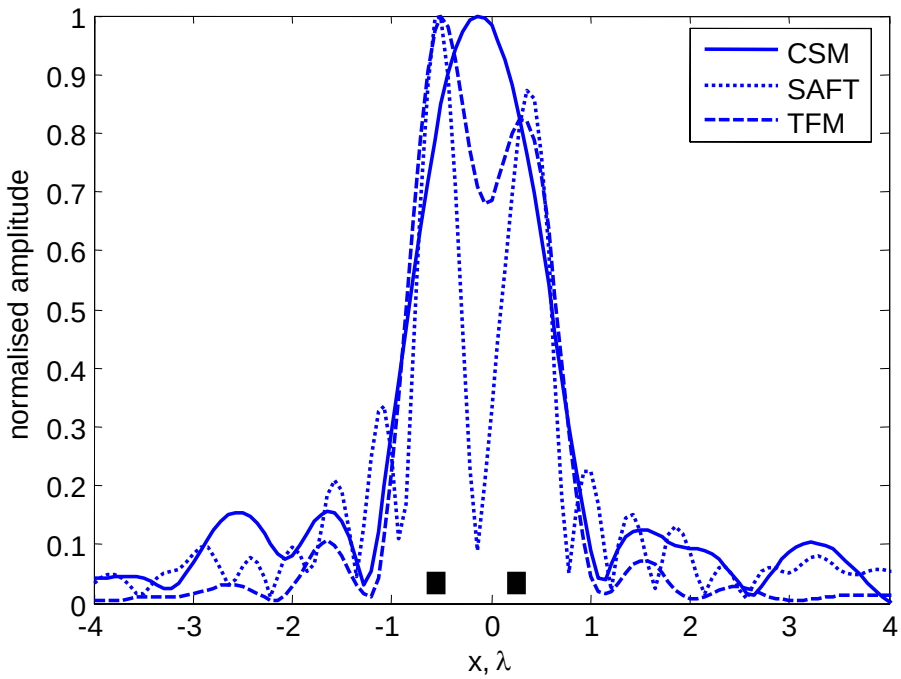

Figure 3.25: *Two hole experimental PSF; solid line: CSM; dotted line: SAFT; dashed line: TFM.*

slit is larger than the PSF FWHM for each algorithm and hence the experimental FWHM should estimate the actual slit length accurately. The measured experimental FWHM from the images produced using the three imaging algorithms were 2.3λ,2.3λ and 2.5λ for the CSM, SAFT and TFM respectively. Therefore, all the algorithms provide a slight underestimate of the actual slit length with the exception of TFM which exactly estimates the lateral extent.

3.8 Plate Imaging Conclusions

Three synthetically focused imaging algorithms have been introduced within the context of plate imaging: Common Source Method (CSM), Synthetic Aperture Focusing Technique (SAFT) and Total Focusing Method (TFM). The performance of the three algorithms was investigated theoretically and it was found that SAFT produced the narrowest Point Spread Function (PSF), half that of the CSM, and hence achieved the best two-point resolution. However, SAFT and CSM both suffer from substantial sidelobes in the image. The TFM has significantly smaller sidelobes and FWHM between those of CSM and SAFT. Table 3.3 shows the image quality metrics for the three algorithms for the infinite aperture case.

It should be noted that TFM requires significantly more complex acquisition and subsequent image formation time. This means that, if the acquisition time for TFM is to be comparable with CSM or SAFT then parallel reception of the backscattered waves at all sensors will be required, necessitating a more expensive hardware architecture. However, for plate imaging, it appears that TFM would be worth the extra acquisition time or hardware expense due to the significantly reduced sidelobe amplitude and a two-point separation criterion which is comparable with that of SAFT.

The lateral crack sizing ability of the imaging algorithms was tested using data from a finite element model using the SH0 guided wave mode at 100 kHz for inspection. It was found that all of the algorithms were capable of reliably estimating the crack length so long as the crack size was larger than the width of the theoretical PSF.

Table 3.3: Image quality metrics for the infinite aperture case

Metric	CSM	SAFT	TFM
shape of PSF	$sinc(kx)$	$sinc(2kx)$	$sinc^2(kx)$
FWHM, λ	0.6	0.3	0.44
$\delta_{Sparrow}$, λ	0.7	0.35	0.45
Sidelobe amplitude, dB	-13	-13	-26

The width of the theoretical PSF can therefore be used to define the smallest sizable crack.

Several plate experiments using the A0 guided wave mode at 50 kHz were carried out. The image results of the experimental data showed excellent agreement with the theory and the finite element study. It was found that broadband processing slightly reduced the sidelobe amplitude. The experimental results also showed the ability of the imaging techniques presented to deal with dispersion effects.

The results for lateral sizing of cracks and slits using synthetic focusing techniques is encouraging for the goal of circumferential sizing of defects in pipes, which will be investigated in the following chapter.

Chapter 4

Pipe Imaging

4.1 Pipe Imaging Introduction

Three synthetic focusing algorithms were evaluated in detail for plate imaging in chapter 3. It was found that the Total Focusing Method (TFM) had excellent coherent noise rejection but required more extensive data acquisition than the Common Source Method (CSM) or Synthetic Aperture Focusing Technique (SAFT). All of the imaging algorithms were capable of estimating the lateral extent of cracks parallel to the array aperture if the crack was larger than the predicted Full Width at Half Maximum (FWHM) of a point scatterer at the crack location. SAFT had the smallest point scatterer FWHM, followed by TFM, and CSM had the largest point scatterer FWHM. In this chapter, the three algorithms will be tested for use with pipe geometry.

The analogies between the propagation of guided waves in plates and the propagation in pipes was discussed in chapter 2. It was noted that the complex wave propagation of torsional-flexural (F(n,2)) pipe modes of interest here can be adequately approximated by assuming plate-like behaviour. This simplified approach allows one to assume constant phase velocity equal to the phase velocity of the corresponding plate Shear Horizontal guided wave mode in all directions of propagation α. An extra boundary condition along the axial cut made in the pipe in order to

unroll it means that the pipe guided waves can only propagate at fixed angles which can be found using (2.27).

If the wavefield $f(circ, z = 0, t)$ around the pipe circumference at $z = 0$ is sampled with N transducers with equal spacing of Δ such that $N\Delta = 2\pi r$, then the two dimensional discrete Fourier transform over circumferential location ($circ$) and time (t) yields the angular spectrum at each temporal frequency ω

$$F(k_{circ}, z = 0, \omega) = FT_{circ,t}[f(circ, z = 0, t)]. \tag{4.1}$$

the components of the recorded angular spectrum at any temporal frequency have circumferential wavenumbers k_{circ} of $-N/2r$ to $N/2r$ in steps of $1/r$. Note that these values of circumferential wavenumber correspond exactly to the propagating solutions for the torsional-flexural guided wave modes which were analysed in section 2.3.4 where $k_{circ} = n/r$ where n is the circumferential order of the mode. If all of the propagating modes are to be received without aliasing then twice as many transducers as propagating modes are required $N > 2n_{max}$. This is equivalent to sampling of $\Delta < \lambda/2$ where λ is the wavelength of the SH0 plate mode at the highest excitation frequency. If this circumferential sampling criterion is met then the recorded angular spectrum can be thought of as a decomposition of the received wavefield into the propagating pipe modal solutions. This is entirely analogous to the decomposition of the recorded wavefield along a linear array on a plate into plane waves which formed the basis of the imaging algorithms discussed in the previous chapter. Therefore, the imaging algorithms whose implementation was outlined in section 3.5 for plate geometry can be directly applied to the pipe geometry of interest here. Each component of the recorded angular spectrum must be backprojected axially along the pipe as was the case for the plane wave components for plate imaging. The only change is that the x direction (lateral direction) is now termed the circumferential direction.

Firstly, the imaging response of the algorithms will be tested using a simple finite element model with no defects present in the pipe. After evaluating the end-wall response from this model, a decision as to the most suitable of the three algorithms

for pipe imaging using a circumferential array of transducers can be made.

Following this decision, the chosen algorithm is tested using data from a simple analytic model for a point scatterer assuming the plate-like behaviour investigated in section 2.3.4. The circumferential Point Spread Function (PSF) is evaluated as a function of inspection frequency, axial distance from the array and pipe diameter.

The lateral defect response for plate imaging was investigated in the previous chapter. In this chapter, the circumferential defect response will be evaluated for circumferentially oriented cracks in 8 inch diameter pipes modelled with finite elements. The analysis will be extended beyond the scope of the plate imaging work to include part depth cracks and part depth notches. The finite element results will then be generalised to different axial defect locations, frequency of inspection and pipe size.

4.2 Imaging response to a pipe end wall

A 3D pipe model was made using Abaqus version 6.5 [89]. The pipe modelled was an 8 inch schedule 40 mild steel pipe (internal diameter= 202.7 mm, external diameter= 219.1 mm). The mild steel is defined by its Young's Modulus, $E = 216.9\ GPa$, its Poisson ratio, $\nu = 0.2865$ and its density, $\rho = 7932\ kgm^{-3}$.

The model was run with no features present in a 1.2m long pipe in order to test the response of the imaging algorithms to a pipe end. 2 elements through the pipe wall thickness, 360 elements around the circumference and 480 elements along the length were used. The element size was therefore around 4mm thick, 3.5mm circumferentially and 2.5mm axially. Solid brick 8 node linear elements were used.

The input is a 5 cycle Hanning-windowed toneburst centred at 50 kHz. The toneburst and its temporal frequency spectrum were shown in figure 3.18. The smallest wavelength is the shear wavelength, which at the highest frequency with significant energy (70 kHz) is 46mm. Therefore, the largest element dimension is around one twelfth of the smallest wavelength present. In order to sample the pipe circumference adequately ($\Delta < \lambda_{SH}/2$) at 50 kHz, 20 transducer locations are required. However,

due to the bandwidth of the toneburst, 24 transducer nodes were used which were evenly spaced every 15^o around the outside of the pipe wall satisfying the spatial sampling criterion (3.24) up to 60 kHz. This also mimics the actual hardware setup which was available for experiments.

The defect-free pipe model is symmetric about the pipe axis (axisymmetric) and so the backscattered response would be identical from each transducer node. Therefore, excitation of only one transducer node is necessary. The backscattered reflections are then monitored at all transducer nodes. The full data matrix which is required for the Total Focusing Method (see figure 3.2) can subsequently be filled by taking advantage of the the axial symmetry of the situation. The SAFT data set is the leading diagonal of the full matrix. The CSM data set can be found by summing the full data set over the transmitter dimension. This synthetic summation is equivalent to firing all of the transmitters simultaneously.

The forced excitation was applied in a circumferential direction at the single transduction node. This has a similar effect to the excitation of the plate finite element model described in section 3.6. The loading produces a shear-horizontal (SH) probing wave packet whose principal direction is axial ($\alpha = 0$) and a compressional (S) wave packet whose principal direction is circumferential ($\alpha = 90^o$). The circumferential signals will travel around the pipe circumference and will be received at the other transducer locations and at the excitation transducer after an integer number of circumferential passes. The backscattered wavefield is also monitored in a circumferential direction at all of the 24 transducer nodes.

Figure 4.1 shows the pulse-echo time trace which will be used by SAFT from the finite element model with amplitude normalised to that of the input toneburst. Marked on the figure are the excitation toneburst, the first and second circumferential signals and the end wall reflection. Note that the circumferential signals are larger than the end wall reflection.

Figure 4.2 shows the time trace recorded at transducer 5 with excitation at transducer 1 as an example of the data used by TFM. The direct pass circumferential

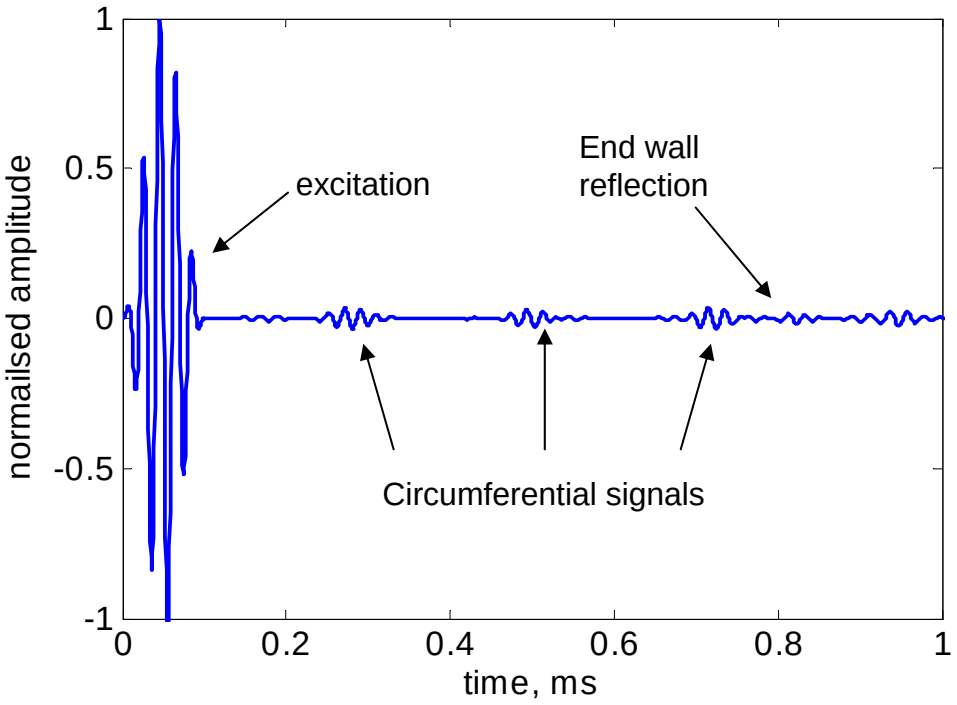

Figure 4.1: *Pulse-echo time trace with pipe end at 1.2m.*

toneburst is visible but subsequently the end wall reflection is masked by the many different circumferential signals.

Figure 4.3 shows the time trace recorded at one transducer from excitation at all 24 transducers, as would be the case for CSM. The amplitude is normalised to that of the excitation signal. Note that there are no circumferential signals, just the end wall reflection being visible. The end wall reflection is 1/24 of the input signal amplitude, as expected from monitoring at just one of the 24 firing transducers. The effect of firing all of the transducers simultaneously is to excite only the T(0,1) axisymmetric torsional mode. This is effectively a plane wave propagating perpendicular to the array, as was the case for the infinite aperture CSM plate case discussed in section 3.2.1.

Note that the phase velocity of the propagating T(0,1) mode can be evaluated using the time trace shown in figure 4.3. The finite element phase velocity in the axial direction was found to be 3230 ms^{-1} showing a 0.8% variation from the theoretical phase velocity of 3260 ms^{-1}. This is comparable to the velocity errors found by

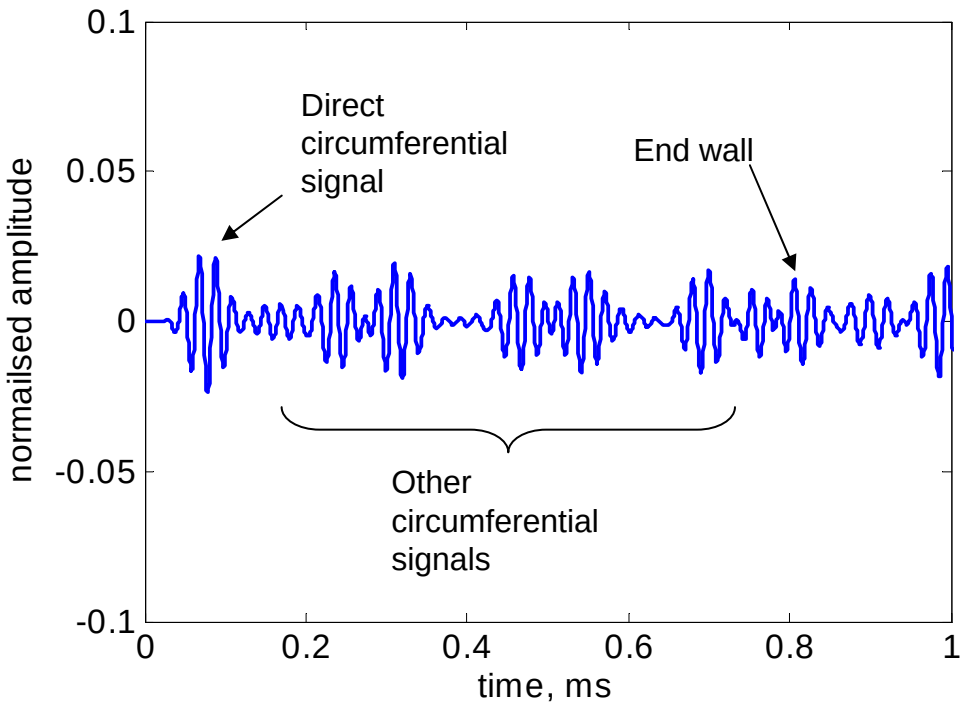

Figure 4.2: *Time trace recorded at transducer 5 from excitation at transducer 1 with pipe end at 1.2m.*

Drozdz [91] in a detailed analysis of such finite element modelling errors. This value of phase velocity will be used for all subsequent imaging of finite element data.

The finite element time traces from the defect-free model were processed using the three imaging algorithms that were described in section 3.5. Temporal frequencies of 40-60 kHz were processed, roughly corresponding to the $-6\ dB$ bandwidth of the excitation toneburst (figure 3.18b). Figure 4.4 shows the CSM image of the pipe with an end wall at 1.2m, figure 4.5 shows the SAFT image and figure 4.6 shows the TFM image. The images are scaled to the image peak amplitude.

The axial slices through the CSM, SAFT and TFM images are shown in figure 4.7a, 4.7b, 4.7c respectively. The amplitude scale has been normalised to that of the input signal.

The CSM image of figure 4.4 shows the end wall in the correct location and of the same amplitude as the input probing signal. This amplitude would be expected since all of the T(0,1) transmitted mode is reflected by the pipe end. The first axial

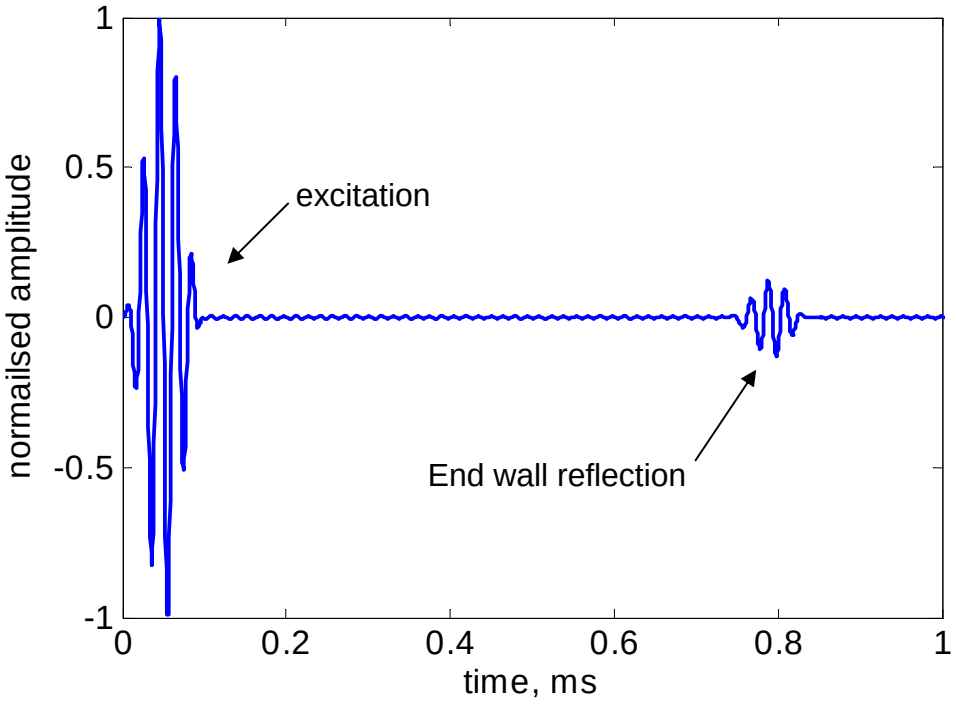

Figure 4.3: *CSM time trace with pipe end at 1.2m.*

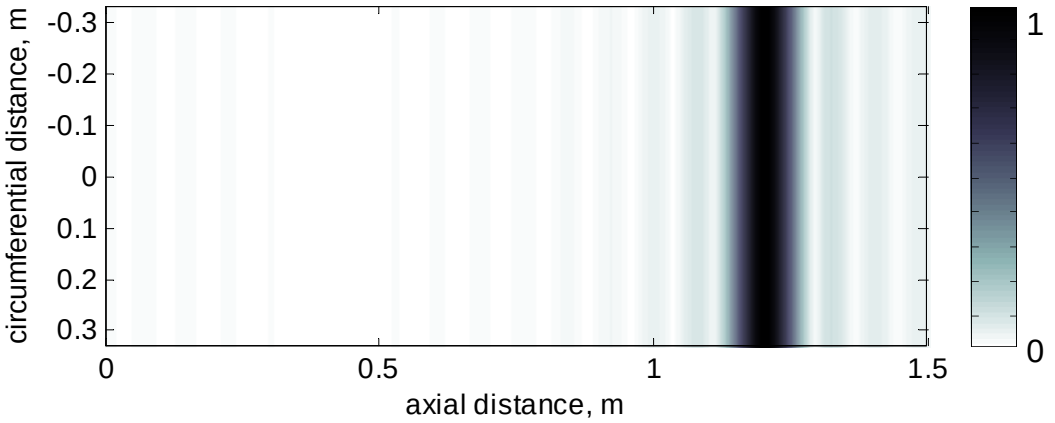

Figure 4.4: *CSM image of pipe end at 1.2m.*

sidelobes are around -17dB in amplitude and occur at axial positions of 1.08m and 1.32m. These are 0.12m ($1.85\lambda_{SH}$ at 50 kHz) axially from the end wall image peak.

It is clear that the circumferential signals observed in figures 4.1 and 4.2 are seriously detrimental to the quality of the images produced by SAFT and TFM for pipe imaging. The end wall amplitude of the SAFT image of figure 4.5 is masked almost entirely by the noise bands produced from the circumferential signals. The end wall

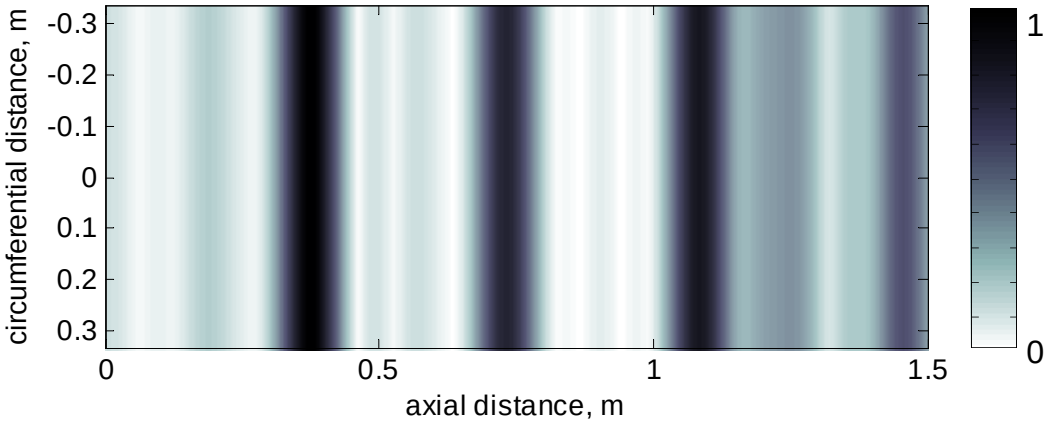

Figure 4.5: *SAFT image of pipe end at 1.2m.*

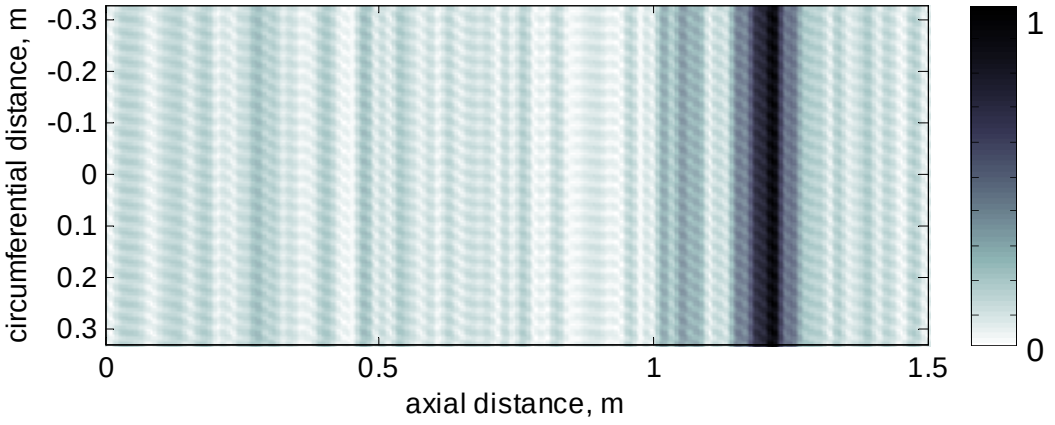

Figure 4.6: *TFM image of pipe end at 1.2m.*

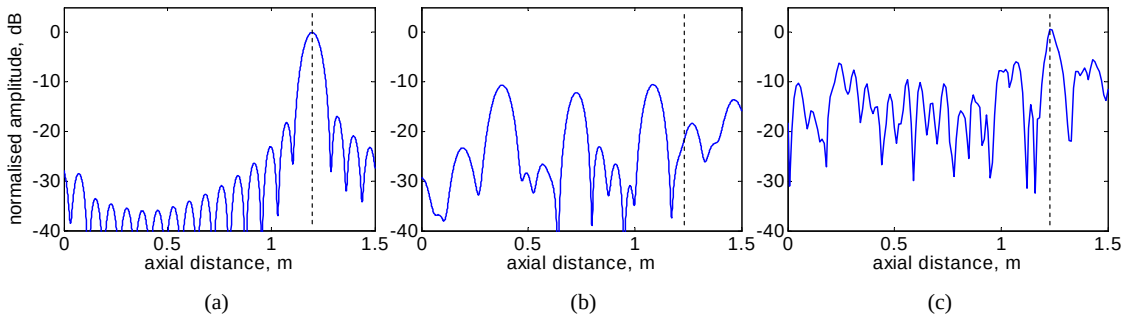

Figure 4.7: *Axial slice through image of pipe end at 1.2m in dB: (a) CSM; (b) SAFT; (c) TFM.*

amplitude of the TFM image of figure 4.6 is slightly greater than the CSM end wall amplitude but the noise in the image from the circumferential signals is still around -6dB.

Therefore, the SAFT and TFM algorithms which produced the best quality images for plate imaging, are not suitable for pipe imaging due to the unwanted excitation of circumferential signals which are received by the transducer array. These undesired signals are confused with feature reflections and hence cause coherent noise in the reconstructed SAFT and TFM images. For this reason, SAFT and TFM will no longer be investigated here for use with the proposed circumferential array. However, it may be possible to suppress the unwanted circumferential guided wave excitation using several separate circumferential arrays located at different axial positions and this is currently receiving research attention [92].

4.3 Imaging response with Synthetic Data

4.3.1 A simple synthetic scattering model

In order to further test the CSM pipe imaging algorithm, a simple analytic scattering model was used to create data for a point scatterer at some axial location z_d. The model assumes plate-like behaviour of the pipe as discussed in section 2.3.4, allowing one to unwrap the pipe and think of it as a plate. The assumption made in section 2.3.4 was that the shear horizontal wave propagation had phase velocity equal to the bulk shear velocity in all directions. In order to account for all possible helical ray paths, one must consider an infinite number of repetitions of the pipe circumference. Figure 4.8 shows the geometry of the unrolled pipe and the first two circumferential repetitions considered. The direct ray path from the defect to a single transducer, as well as the first two helical paths to the same transducer, are also shown on the figure.

The monochromatic signal U_{tr}, recorded at transducer number tr is

$$U_{tr} = e^{-\mathbf{j}k_s z_d} \sum_{p=-\infty}^{+\infty} R_{tr,p} \cdot T_{tr,p} \cdot G(k_s, d_{tr,p}) \tag{4.2}$$

where the first exponential term explains the phase shifting of the probing plane wave (T(0,1)) which occurs between the array and the defect location z_d when all transducers are fired simultaneously. $R_{tr,p}$ is the reflectivity coefficient for transducer tr and path number p. $T_{tr,p}$ is the transducer amplitude scaling factor for transducer tr and path number p. G is the Green's function describing the propagation of the backscattered waves from the defect. For the 2d case, such as this assumed plate-like behaviour, the Green's function is a Hankel function of distance travelled d and wavenumber k but can be approximated in the far-field by

$$G(k_s, d_{tr,p}) = \frac{e^{-jk_s d_{tr,p}}}{\sqrt{d_{tr,p}}} \tag{4.3}$$

where $d_{tr,p}$ is the distance from the defect to the transducer tr for the path index of p and $k_s = \frac{\omega}{c_s}$ is the bulk shear wavenumber and c_s is the bulk shear phase velocity.

The summation in (4.2) exists since all helical paths from the point scatterer back to the transducer must be considered. The index p refers to the number of times the ray path considered has traveled around the pipe circumference, in a clockwise (p is positive) or anticlockwise (p is negative) direction, as illustrated in figure 4.8. The distance travelled by each respective ray path from the defect back to the transducer tr for path number p is

$$d_{tr,p} = \sqrt{z_d^2 + (circ_{tr} + 2\pi r \cdot p)^2}. \tag{4.4}$$

where $circ_{tr}$ is the circumferential position of transducer number tr and $2\pi r$ is the pipe circumference. The angle which the returning ray path from the point scatterer makes to the axial direction is

$$\beta_p = \arctan(\frac{circ_{tr} + 2\pi r \cdot p}{z}). \tag{4.5}$$

In the limits, the returning angle will be $\beta_{-\infty} = -\pi/2$ and $\beta_{\infty} = \pi/2$.

The reflectivity model R used here is a simple function of the angle β of the backscattered ray path to the axial direction

$$\begin{aligned} R &= \cos(\beta \frac{\pi/2}{\beta_{max}}) \quad \text{for} \quad |\beta| < \beta_{max} \\ R &= 0 \quad \text{for} \quad |\beta| > \beta_{max} \end{aligned} \tag{4.6}$$

where β_{max} is the maximum angle of backscattered reflection from the defect and is predefined in the model. This model is a simple approximation to the reflection observed experimentally from small defects in a plate with plane wave incidence normal to the crack face [76, 77]. Using the plate-pipe analogy, the reflectivity function R can be thought of as a model for mode conversion from the probing plane wave (T(0,1)) to higher order torsional-flexural modes (F(n,2), $n = 1, 2..$) which propagate with angles defined by (2.33). The reflectivity function R is plotted against backscatter angle β for a maximum backscatter angle of $\beta_{max} = \frac{\pi}{4}$ in figure 4.9.

The transducer amplitude scaling factor T accounts for the ability of the transducers to measure in a circumferential direction only. The transducer will measure shear waves which are incident perpendicular to the array $\beta = 0$ with no amplitude scaling since the shear waves have motion perpendicular to their direction of propagation. Shear waves propagating in a circumferential direction $\beta = \pi/2$ around the pipe will not be measurable at all. The transducer amplitude scaling factor is defined by

$$T = \cos(\beta). \tag{4.7}$$

The transducer scaling factor T_p is plotted against the returning ray path angle β in figure 4.9. Note that, in theory, all helical paths from $p = -\infty$ to $p = +\infty$ should be considered in (4.2) but the limits are practically constrained by the reflectivity function R (4.6) since any path where R_p is zero need not be considered. Clearly, the number of paths that must be considered will increase for a given pipe size with increasing β_{max} or axial defect distance z_d.

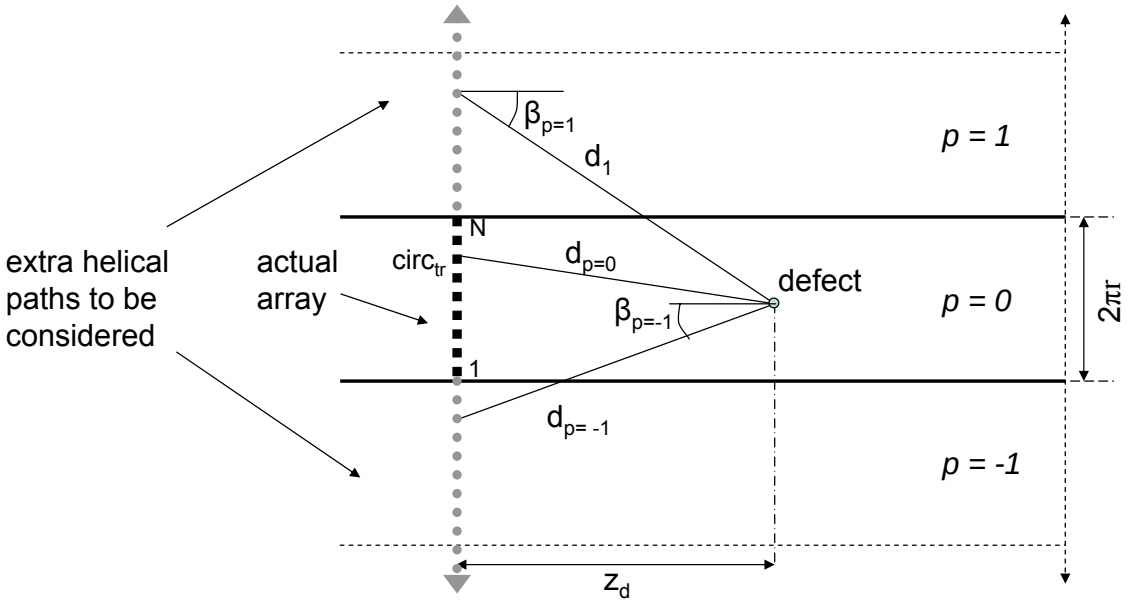

Figure 4.8: *Geometry of the unrolled pipe used for synthetic data model showing extra paths to be considered.*

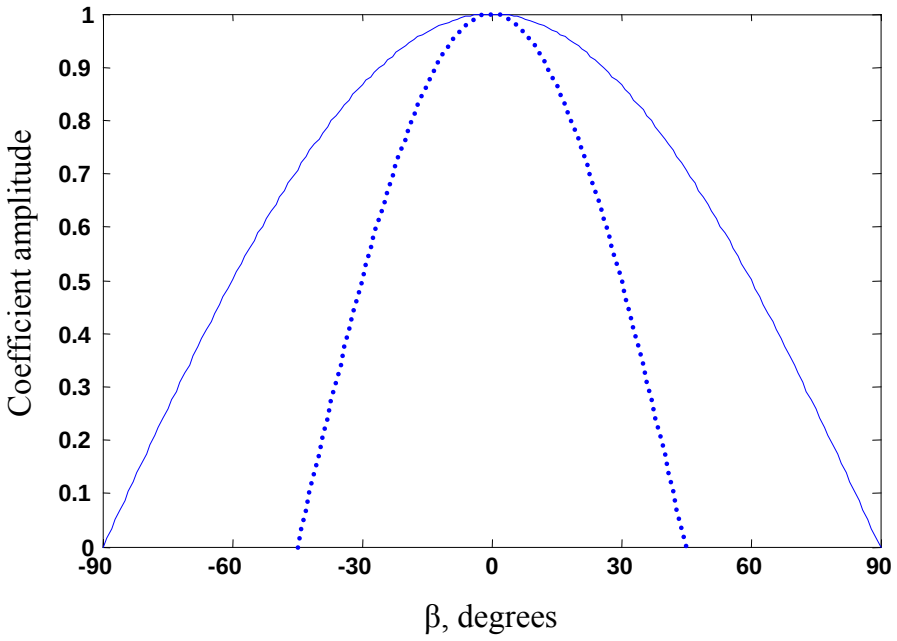

Figure 4.9: *Directional windows plotted against angle of propagation. solid line: Transducer directionality coefficient T; dotted line: Reflection coefficient R for $\beta_{max} = 45^o$.*

4.3.2 Imaging response with varying maximum backscatter angle

The synthetic data model described in the previous section was first used to create CSM data sets for a single point scatterer at a fixed axial location $z_d = 1m$ but varying the maximum angle of backscatter β_{max}. The angle of backscatter was varied from 5^o up to the maximum possible 90^o. The radius of the pipe was set to $r = 0.10545m$ (8 inch schedule 40). The number of transducers was chosen so that the Nyquist sampling criterion was satisfied for the highest frequency of interest around the pipe circumference. This is equivalent to being able to measure the highest order mode without aliasing effects, as discussed above. Data was synthesized using (4.2) for frequencies in the range of 40 kHz to 60 kHz requiring 24 transducer locations around the pipe circumference. The temporal frequency bandwidth was amplitude windowed using a Hanning window in order to synthesize some form of time domain windowed input toneburst centred at 50kHz.

The synthetic data were then processed using CSM as described in section 3.5. Note that the recorded angular spectrum will have components for the propagating pipe modes only, as was discussed in the introduction of this chapter. Figure 4.10 shows an example image created from the synthetic data set with $\beta_{max} = 45^o$. Figure 4.11 shows the circumferential slice through the defect axial location ($z = z_d = 1m$). Also shown on the figure is the circumferential slice through the defect axial location using (4.2) with no reflector direction dependence ($R = 1$ for all β). This PSF is almost identical to the PSF derived for the infinite aperture plate case of section 3.2.1, having FWHM of 42mm (0.64λ) and sidelobe amplitude of 0.18 (-15dB). The main lobe is slightly wider than the PSF plate prediction (3.13) since the transducer directionality function T has reduced the effect of the higher circumferential spatial frequencies $k_{circ} = k_s \sin\beta$. The effect of the directionally dependent backscatter function R (4.6) is extra windowing of circumferential spatial frequencies k_{circ} which further reduce the sidelobe amplitude but with a broadening of the main lobe. The FWHM for the case of $\beta_{max} = 45^o$ shown in figure 4.11 is 72mm (1.11λ).

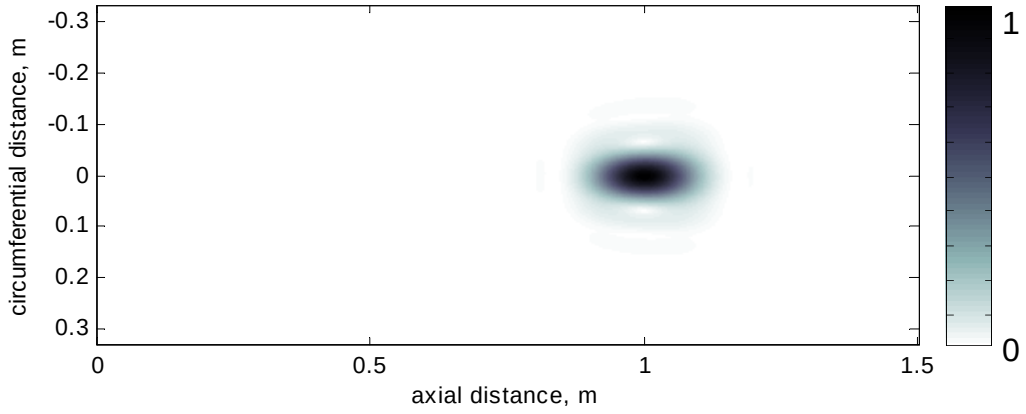

Figure 4.10: *CSM image from synthetic data with $\beta_{max} = 45^o$ in 8 inch pipe.*

Figure 4.12 shows the FWHM, measured from the image at the axial location of the defect, against the maximum angle of backscatter, β_{max}. It is clear that a defect which backscatters over a large range of angles will appear in the reconstructed CSM image with a smaller circumferential extent than a defect which only backscatters over a small range of angles. Note that an axially symmetric feature will reflect only the probing plane wave (T(0,1)) and no mode conversion will occur. The image will also be axisymmetric since no circumferential spatial frequencies are available for image reconstruction. This is equivalent to $R = a$ for $\beta = 0$ and $R = 0$ for all other β, where a is the reflectivity of the axisymmetric feature. The reflectivity will depend on the temporal frequency and the depth and axial extent of the feature.

4.3.3 Imaging response with varying axial distance

The synthetic data model (4.2) was then used to create data sets for point scatterers at varying axial distances z_d of 0.1m to 8m from the array. It was found that the PSF were identical for any defect distance tested for a constant maximum backscatter angle β_{max}. The FWHM is plotted against axial defect distance in figure 4.13 for $\beta_{max} = 30^o, 45^o$ and 60^o. Therefore, figure 4.12 is valid for defects at any axial location.

The axial invariability of the defect response for pipe imaging contrasts with that of the plate imaging case evaluated in chapter 3. The PSF for the plate case (3.31)

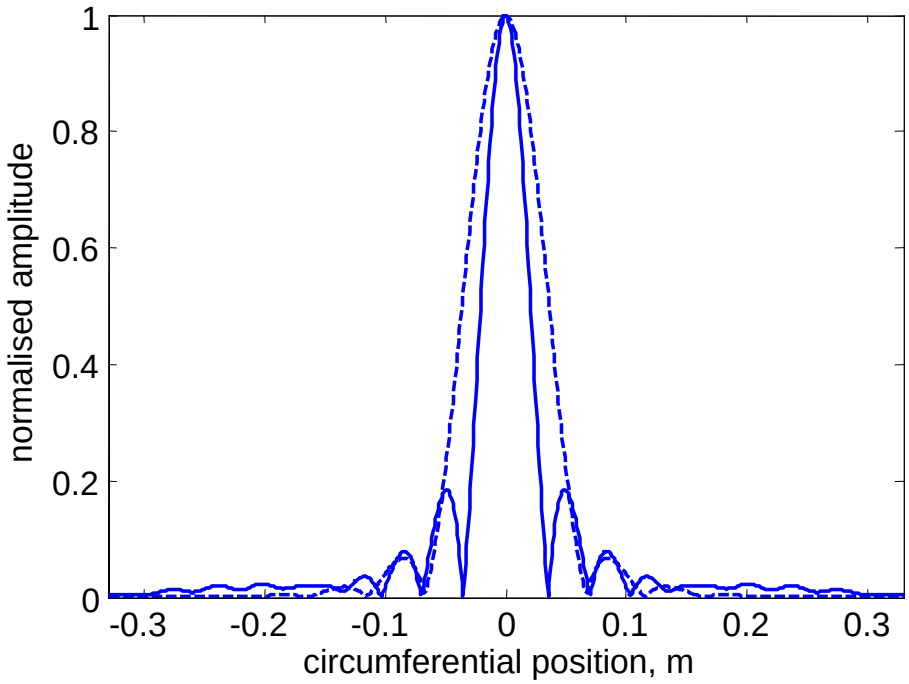

Figure 4.11: *Circumferential image slice through defect location using synthetic data model; dashed line: from figure 4.10 with* $\beta_{max} = 45^o$ *in 8 inch pipe; solid line: with no reflector directionality.*

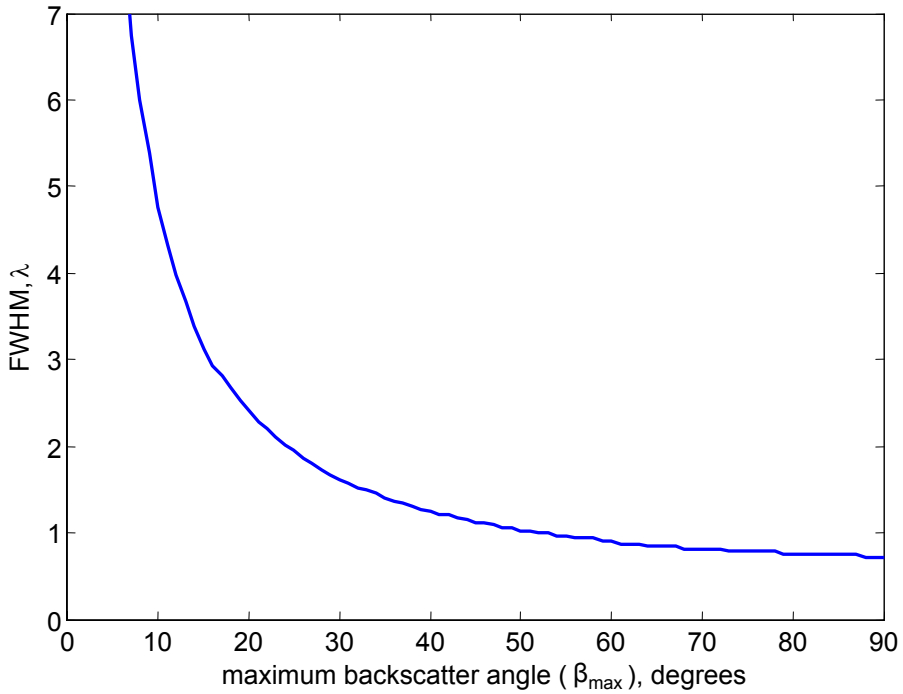

Figure 4.12: *FWHM against maximum backscatter angle,* β_{max} *for a defect at 1m from the transducer array on an 8 inch pipe with 50 kHz excitation.*

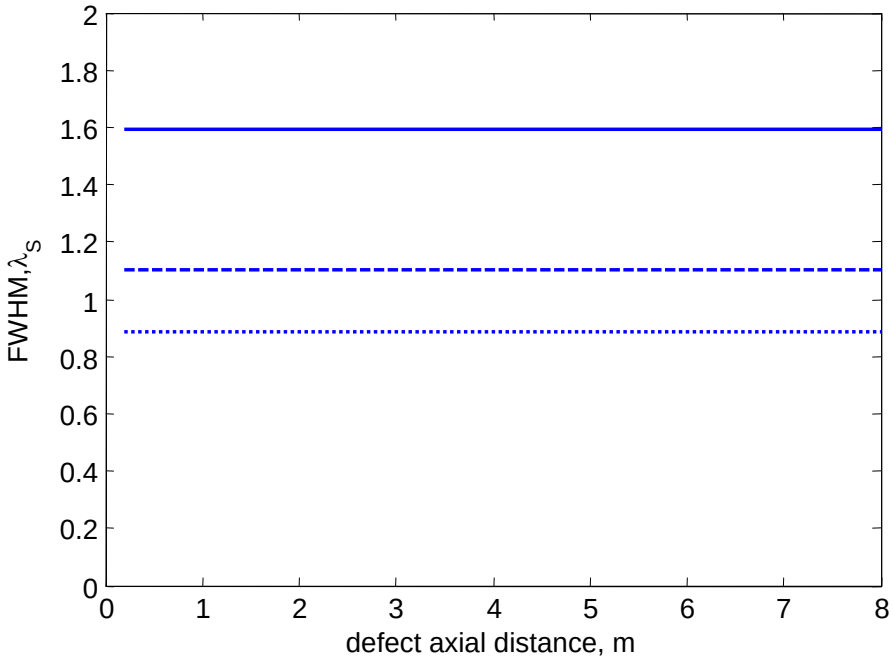

Figure 4.13: *FWHM against axial distance of defect from transducer ring. Solid line:* $\beta_{max} = 30^o$*; dashed line:* $\beta_{max} = 45^o$*; dotted line:* $\beta_{max} = 60^o$*.*

was dependent on the axial distance of the scatterer and the array aperture which limited the maximum recordable backscattered angle. The pipe geometry allows all of the backscattered information from the defect to be received by the array and this can be subsequently used for image reconstruction. This allows the best possible PSF for any axial defect location. The pipe array itself is the length of one pipe circumference but the unwrapping of the pipe as a plate gives an infinite number of aperture repetitions (see figure 4.8). This effective infinite aperture allows all of the helical paths from the defect to the array to be received for a defect at any axial location in the pipe.

4.3.4 Generalisation of synthetic data results to different pipe sizes and excitation frequencies

Synthetic data was then created using (4.2) for point scatterers at a fixed axial location, $z = 2m$ whilst varying the maximum angle of backscatter, α for 8 inch

($r = 0.10545m$), 16 inch ($r = 0.2m$) and 24 inch ($r = 0.305m$) pipes with excitation centred at frequencies of both 25kHz and 50kHz.

The measured FWHM of the defect images produced against maximum backscatter angle from all six cases are shown in figure 4.14. It is clear that the pipe size does not affect the FWHM. In contrast, the frequency of excitation greatly affects the FWHM; doubling the frequency halves the FWHM for all pipe sizes tested.

The measured FWHM are plotted in shear wavelengths (λ_s) against maximum backscatter angle in figure 4.15 and all of the curves are almost identical. The small discrepancies between the curves are most likely due to the way in which the data is synthesized by summing contributions from discrete paths. The similarity of the curves means that the FWHM, measured in wavelengths of the input signal (λ_{SH}), does not depend on pipe size, axial defect location or frequency of excitation but only on the backscatter characteristics of the particular defect. However, it is important to note that some defects will have a frequency dependent backscatter characteristic. This will be investigated in more detail with finite element modelling later in this chapter.

4.4 Finite Element modelling of circumferential cracks and slots in 8 inch Pipe

In order to further test the performance of CSM for pipe imaging a 3D pipe model was made using Abaqus version 6.5 [89] similar to that used to test the response to an end wall in section 4.2. The pipe modelled for this study was an 8 inch schedule 40 mild steel pipe. An 8 inch pipe was chosen since the prototype imaging system which was already under construction was to be an 8 inch transducer ring. The model had axial length= 2.2 m, internal diameter= 202.74 mm and external diameter= 219.1 mm. The mild steel is defined by its Young's Modulus, $E = 216.9\ GPa$, its Poisson ratio, $\nu = 0.2865$ and its density, $\rho = 7932\ kgm^{-3}$. Excitation and reception was carried out at 24 nodes equally spaced around the outside edge at one end of

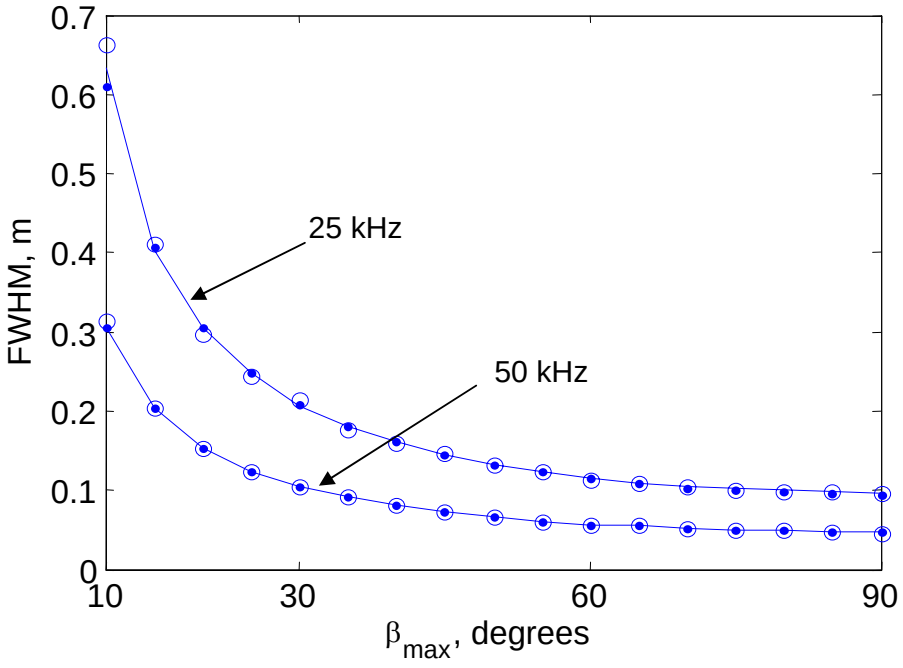

Figure 4.14: *FWHM (in metres) against maximum backscatter angle β_{max} at 25kHz and 50kHz. Circles: 8 inch cases; Lines: 16 inch cases; Dots: 24 inch cases.*

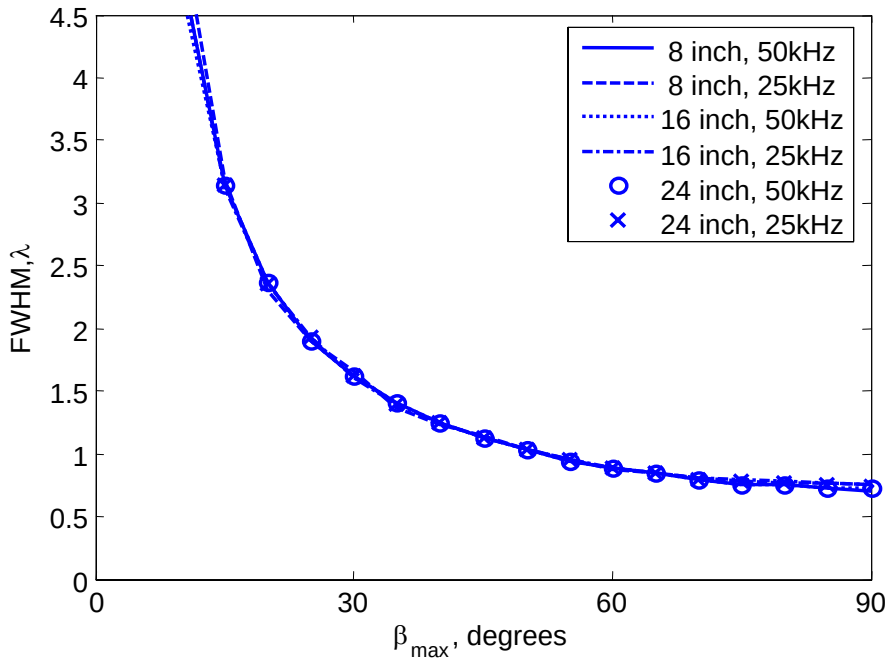

Figure 4.15: *FWHM (in λ_S) against maximum backscatter angle β_{max} for 8,16 and 24 inch pipes at 25kHz and 50kHz.*

Table 4.1: Circumferential extent of the cracks modelled

degrees	mm	λ_{SH}	% circumference
10	18.4	0.28	2.8
20	36.8	0.56	5.6
40	73.6	1.13	11.1
60	110.4	1.69	16.7
90	165.6	2.54	25.0
130	239.3	3.67	36.1

the pipe.

The axial element size was $2.5mm$, giving 880 elements along the $2.2m$ length. The model was circumferentially divided into 360 elements giving a circumferential element length of around $1.8mm$. 6 elements modelled through the pipe wall thickness giving an through-thickness element length of $1.36mm$. Solid brick 8 node linear elements were used.

4.4.1 Circumferential cracks at 1.2m in 8 inch Pipe

The aim of this finite element study was to test the response of CSM to circumferentially oriented cracks in the pipe wall. The cracks were formed by disconnecting adjacent elements in the pipe wall at 1.2m from the transduction end of the pipe. The 3D model allowed variation of the crack size in both circumferential extent, l_{crack} and depth, d_{crack}. Crack depths from one-sixth wall thickness on the outside surface of the pipe to through-wall thickness were possible since the model had six elements through the wall thickness. Crack circumferential extents of 10^o, 20^o, 40^o, 60^o, 90^o and 130^o were modelled for each of the six possible depths giving a total of 36 separate defect models. The circumferential extents of the cracks that were modelled in FE and subsequently imaged are shown in table 4.1.

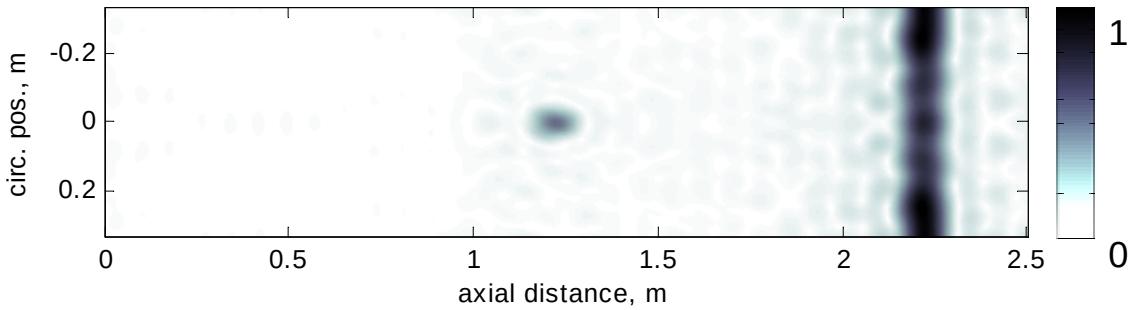

Figure 4.16: *CSM image of 20 degree through-thickness slot at 1.2m, end wall at 2.2m.*

The input wave signal was excited in the model by applying a time varying circumferential force to the 24 transduction nodes on the outer pipe surface at the end of the pipe length. The input signal was a five-cycle Hanning-windowed toneburst centred at 50 kHz. The displacements were monitored in a circumferential direction at all of the 24 transducer locations independently for each finite element run giving 24 time traces for each of the 36 finite element models. This time domain finite element data from each model was then processed with CSM as described in section 3.5.

An example image produced from the finite element data set of a through-thickness crack of 20^o circumferential extent using CSM is shown in figure 4.16. The image shows the defect in the correct location at 1.2m and the end wall at 2.2m. The end wall axial sidelobes, as seen for the end wall only case of figure 4.4, are still visible but are no longer axially symmetric due to wave interaction with the crack.

The defect amplitude and Full Width at Half Maximum (FWHM) were recorded from each image produced for all of the 36 defect cases. The defect amplitude is the peak in the circumferential profile of the image at the defect axial location. The circumferential profile through the defect axial location of 1.2m for the 20^o through-thickness crack using CSM of figure 4.16 is shown in figure 4.17. The defect amplitude and the FWHM are marked on the figure. Also shown is the circumferential profile through the end wall axial location. Note that the end wall circumferential profile is not axisymmetric. This is due to the interaction of the probing wave with the defect and the subsequent interaction of the defect reflection

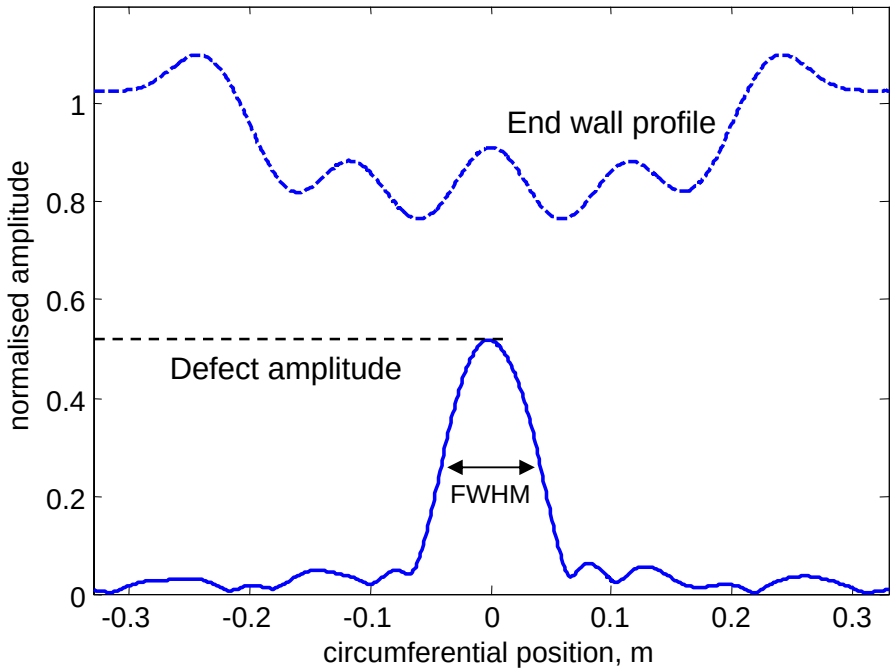

Figure 4.17: *Circumferential profiles through CSM image of 20 degree through-thickness crack at 1.2m; solid line: through defect location; dashed line: through end wall location.*

with the end wall reflection. These multiple interactions are not accounted for by the imaging algorithm which operates under the Born approximation [93] and leads to an image which is not simply the linear combination of the two separate features. The corresponding axial profile through the defect peak of figure 4.16 is shown in figure 4.18.

Figure 4.19 shows the defect amplitude normalised to the input signal amplitude against crack circumferential extent for all of the defect cases using CSM. For all crack depths, the defect image amplitude exhibits two distinct regimes. In the small circumferential extent regime below around 1.5λ, the defect amplitude increases from zero to an amplitude peak at around 1.5λ. Above this peak the amplitude remains relatively constant for each crack depth tested. The image defect amplitude of more than unity for the through-thickness cracks of circumferential extent around the transition between the two regimes can be explained by the interaction of crack tip diffraction with the crack face reflection. These phenomena have been investigated in detail by Rajagopal [76] for cracks in plates. The interaction of the tip diffractions

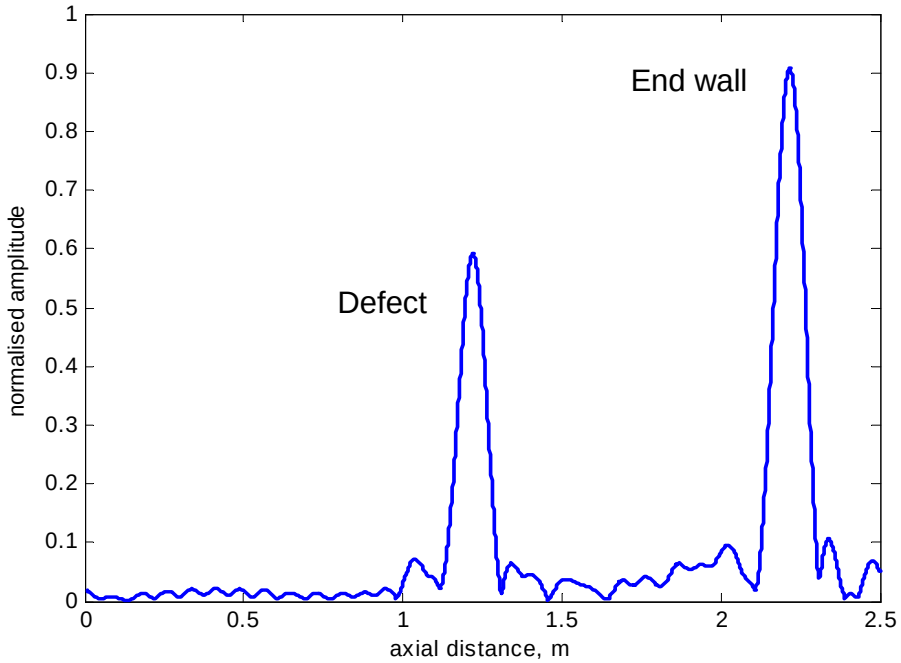

Figure 4.18: *Axial profile through defect location of CSM image of 20 degree through-thickness crack at 1.2m.*

with the backscattered reflection from the crack face itself also explains the non linear increase in amplitude for cracks of small circumferential extent and the rippling effect observed in the crack image amplitudes for larger circumferential extent cracks.

The reflection of the torsional axisymmetric T(0,1) mode from cracks in pipes has been thoroughly investigated by Demma *et al.* [19]. The T(0,1) reflection ratio from through-thickness cracks was found to be equal to the crack circumferential extent as a fraction of the pipe circumference. The T(0,1) reflection amplitude is plotted against crack circumferential extent for the through-thickness crack sizes modelled along with the through-thickness crack CSM image amplitudes in figure 4.20. The focused image amplitude is larger than those of the unfocused system (T(0,1) for transmission and reception) for all crack sizes modelled. The ratio of the focused image amplitude to the unfocused T(0,1) reflection amplitude for the 8 inch pipe studied is plotted in figure 4.21. The greatest improvement in image amplitude over the unfocused system is around 18 dB for this pipe case and occurs for cracks of circumferential extent between $0.5\lambda_S$ and $1\lambda_S$. For cracks above this circumferential extent, the amplitude ratio will gradually decrease to unity for a pipe end wall,

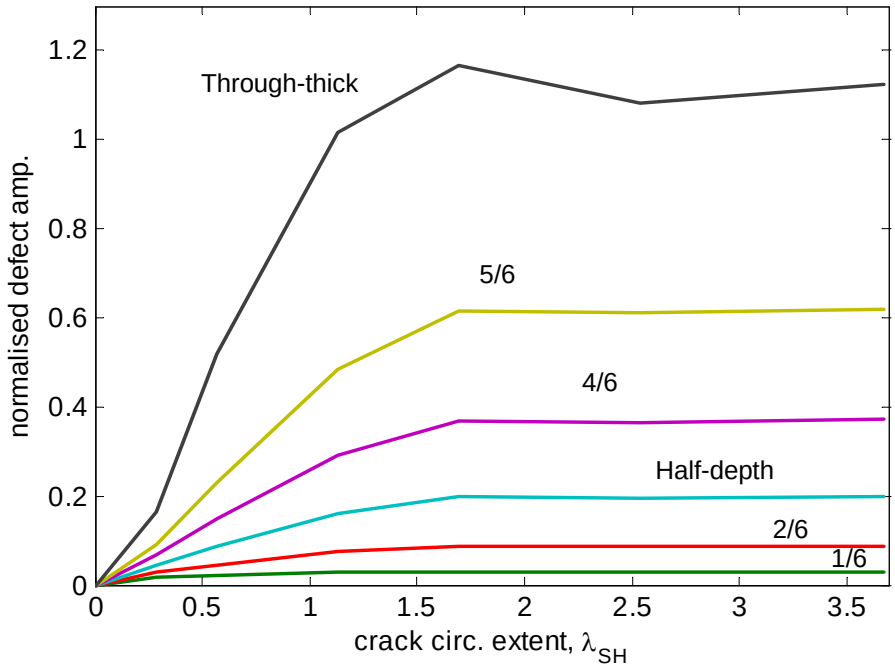

Figure 4.19: *CSM defect amplitude against crack length for all crack depths. Defects at 1.2m.*

where there is no advantage of focusing since no mode conversion from T(0,1) to higher circumferential order modes occurs.

The actual defect amplitude improvement from focusing will depend on the crack size (which affects the backscatter characteristics), pipe radius and wavelength of the probing wave λ_S. For a through-thickness crack of circumferential extent $1\lambda_S$, the defect image amplitude is around unity and the T(0,1) reflection ratio would be $\frac{\lambda_S}{2\pi r}$ where r is the pipe radius. The greatest improvement in defect sensitivity is

$$G_{amp} = \frac{Amp_{focused}}{Amp_{T(0,1)}} \approx \frac{2\pi r}{\lambda_S} \tag{4.8}$$

The gain from focusing will therefore increase with pipe size and frequency of inspection. However, larger pipes and higher frequencies will require more transducers around the pipe circumference in order to satisfy the $\lambda/2$ circumferential sampling criterion. Lower frequencies are also preferred practically due to the greater propagation distances attainable as discussed in the thesis introduction.

The defect image FWHM against crack circumferential extent using CSM are shown

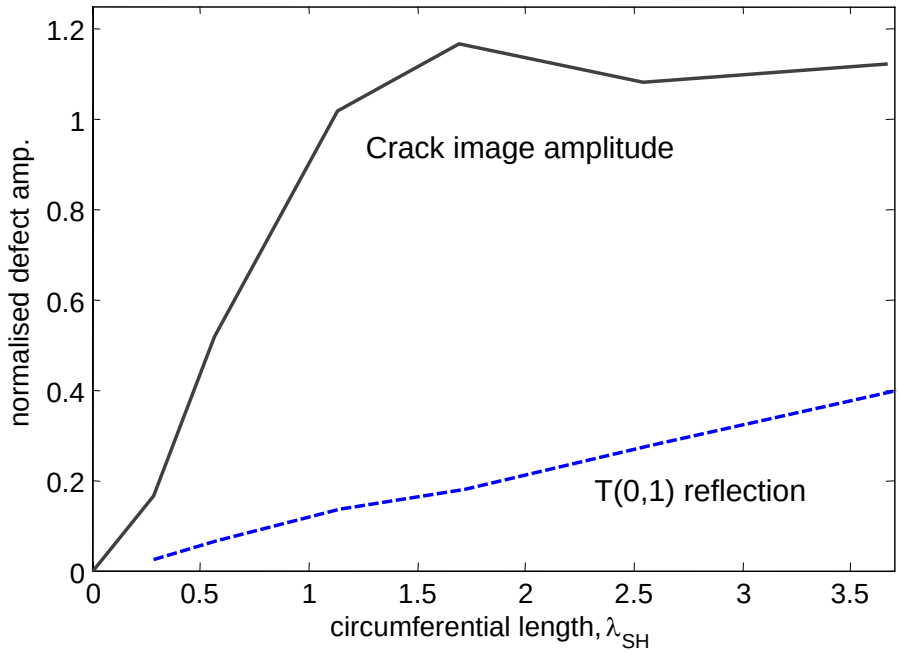

Figure 4.20: *T(0,1) defect reflection amplitudes and CSM defect amplitudes against crack length for through-thickness cracks.*

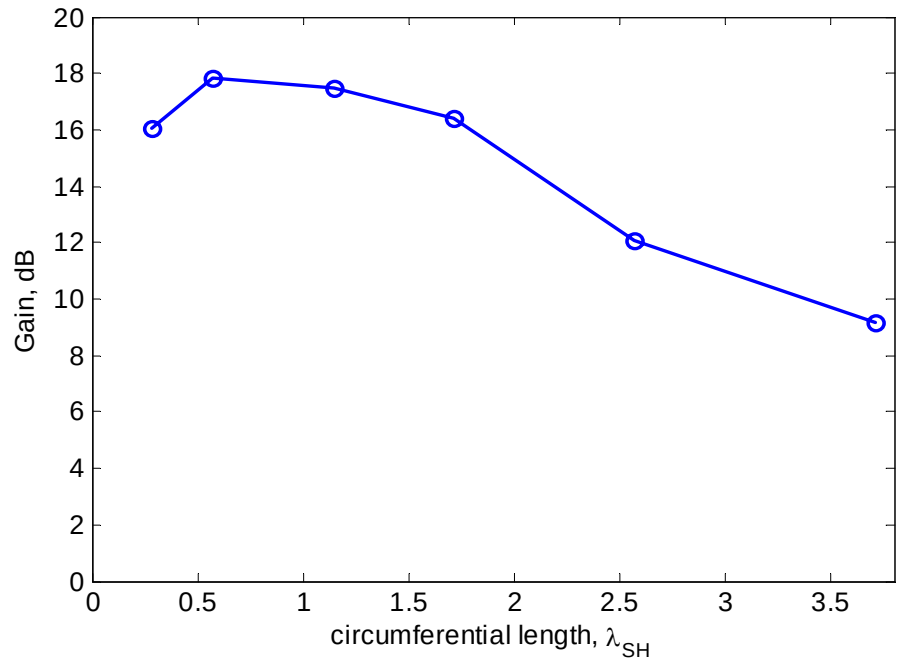

Figure 4.21: *The ratio of the focused image amplitude to the T(0,1) defect reflection amplitudes for an 8 inch pipe with 50 kHz excitation.*

in figure 4.22. The FWHM curves also exhibit two distinct regimes. For circumferential extents larger than about 1.5 λ_{SH}, the FWHM is a good estimate of the actual circumferential extent of the crack for all cracks modelled with the exception of the one sixth depth cracks whose image amplitudes are comparable to the axial sidelobe amplitude of the end wall, making their FWHM unreliable. This is also the case for the smallest of the two sixths depth cracks, and this case is not shown on the figure. In the low circumferential extent regime below 1.5λ, the FWHM is constant at around 1.4λ and hence cannot be used to estimate the actual crack circumferential extent for any depth cracks.

The circumferential extent at which it becomes possible to measure crack circumferential extent from the image is therefore the resolution limit for the CSM system below which the circumferential extent of cracks cannot be sized directly from the image. This resolution limit of the pipe imaging system derives from the limited plane wave backscattering characteristics of the defects, as was predicted using synthetic data in the preceding section of this chapter. Using figure 4.12 for synthetic data, the maximum backscatter angle β_{max} which gave a FWHM of 1.5λ for the simple synthetic data model was around 35^o. This corresponds to the scattering of plane waves from small defects in plates which has been observed in the literature [77].

The pipe imaging circumferential sizing limit of 1.5λ is larger than that of the infinite aperture plate case which has a theoretical minimum lateral sizing limit of around 0.6λ for CSM (from the PSF of (3.13)). However, this theoretical plate imaging limit was not validated with finite element models or experiments. It is unlikely that this limit is practically obtainable due to the limited angles of backscattering observed from cracks in pipes here.

It should be noted that, using an unfocused system (T(0,1) transmission and reception only), circumferential sizing is not possible and reliable depth estimation is only possible for axisymmetric defects. The improvement in circumferential sizing ability is therefore

$$G_{circ} = \frac{2\pi r}{1.5\lambda_S} \tag{4.9}$$

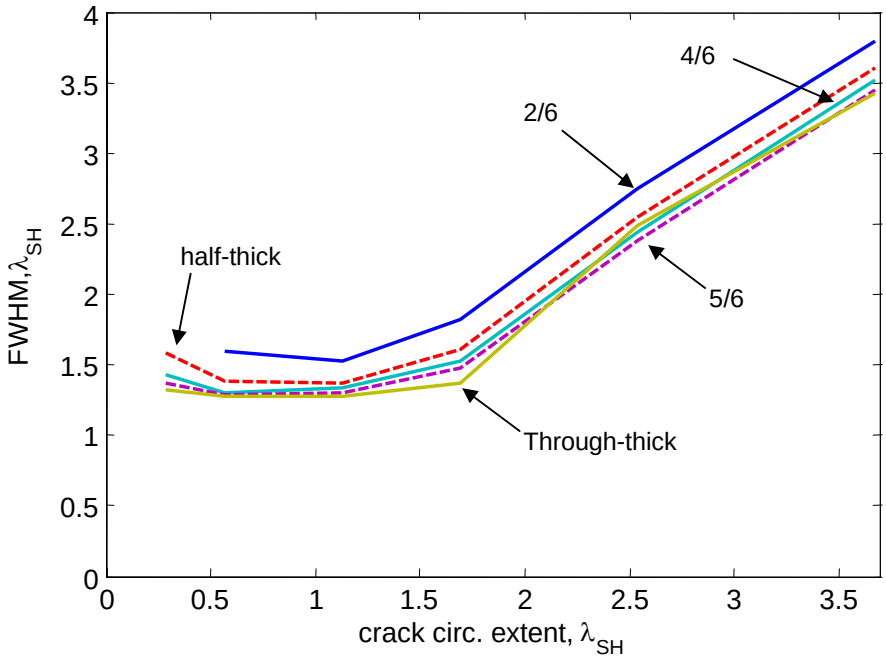

Figure 4.22: *CSM FWHM against crack length for crack depths of two sixths to through-thickness. Cracks at 1.2m. One sixth depth cracks not shown since off the vertical scale.*

where r is the pipe radius and λ_S is the wavelength of the probing signal. The gain in using the focused system will increase with pipe size and frequency of inspection as was the case for the improvement in sensitivity (7.1). For the 8 inch pipe with 50 kHz excitation studied here, the gain in resolution is 6.8 or 16.6 dB.

The circumferential image profiles for the different depth cracks of 60^o circumferential extent are shown in figure 4.23. The shape of the circumferential profile is very similar for all of the different depths but the peak amplitude varies significantly.

Figure 4.24 shows the defect amplitude normalised to the input amplitude against the crack depth for all of the six circumferential extents modelled. This is the same information as was shown in figure 4.19. The defect amplitude increases with increasing crack depth for all crack circumferential extents. Note that the amplitude against crack depth curve is comparable for all circumferential extents above $1.5\lambda_{SH}$. This would have been expected given the plateau in amplitude for larger circumferential extents observed in figure 4.19. This means that if the crack has circumferential extent larger than around 1.5λ then the crack depth can be esti-

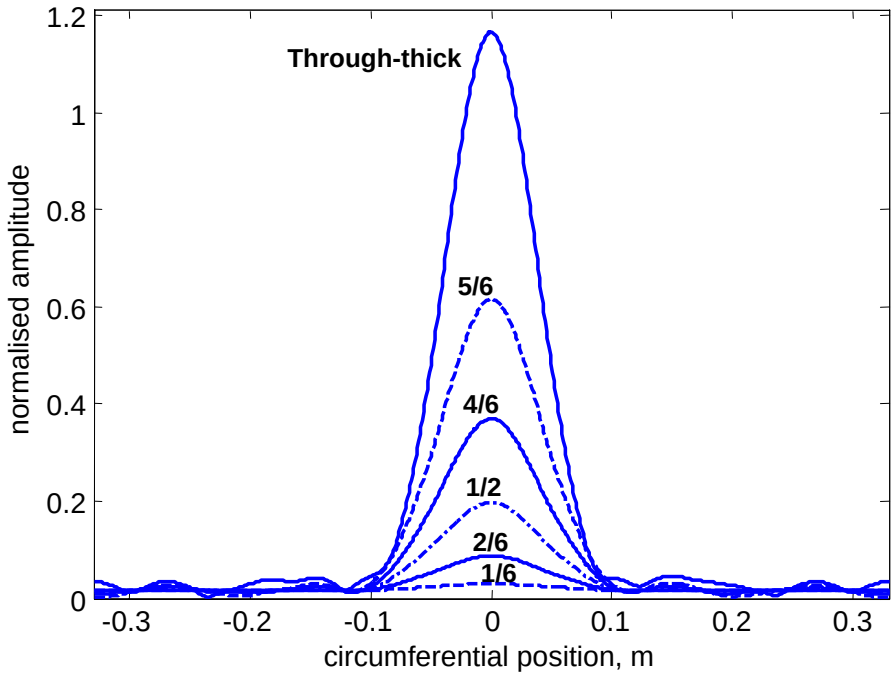

Figure 4.23: *CSM circumferential profiles at defect location for* 60^o *(*1.7λ*) circumferential extent cracks of various depths at 1.2m with excitation at 50 kHz.*

mated directly from the defect image amplitude. Figure 4.25 shows the crack depth plotted against the measured image defect amplitude for the 2.5λ circumferential extent crack and this curve can be used to estimate the defect depth using the image amplitude for any cracks of circumferential extent larger than 1.5λ. This curve is comparable to the reflection amplitudes observed from axisymmetric cracks with T(0,1) mode incidence [19] and L(0,2) mode incidence [18].

In addition to the increased sensitivity to small defects, imaging of the pipe using synthetic focusing also means that the simple curve of figure 4.25 can be used to estimate the defect depth for any circumferential extent larger than the 1.5λ limit. Using an unfocused system, this is only possible for axisymmetric defects. For cracks of circumferential extent less than the 1.5λ limit the measured defect amplitude is a function of both defect depth and circumferential extent. Therefore, they cannot be directly estimated from either image defect amplitude or the FWHM, as is the case for non-axisymmetric defects using an unfocused system.

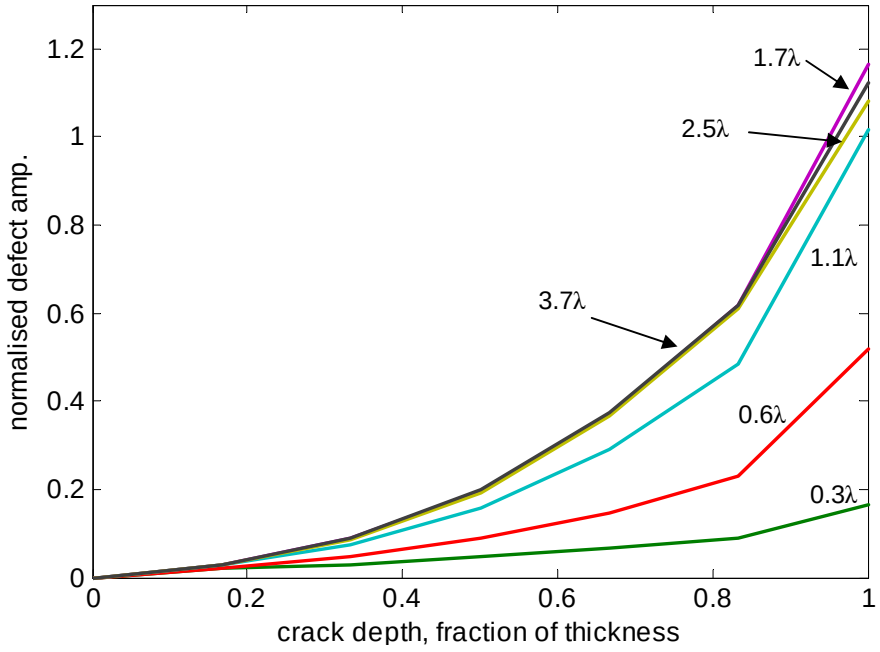

Figure 4.24: *CSM defect amplitude against crack depth for different crack lengths expressed in shear wavelengths. Defects at 1.2m with excitation at 50 kHz.*

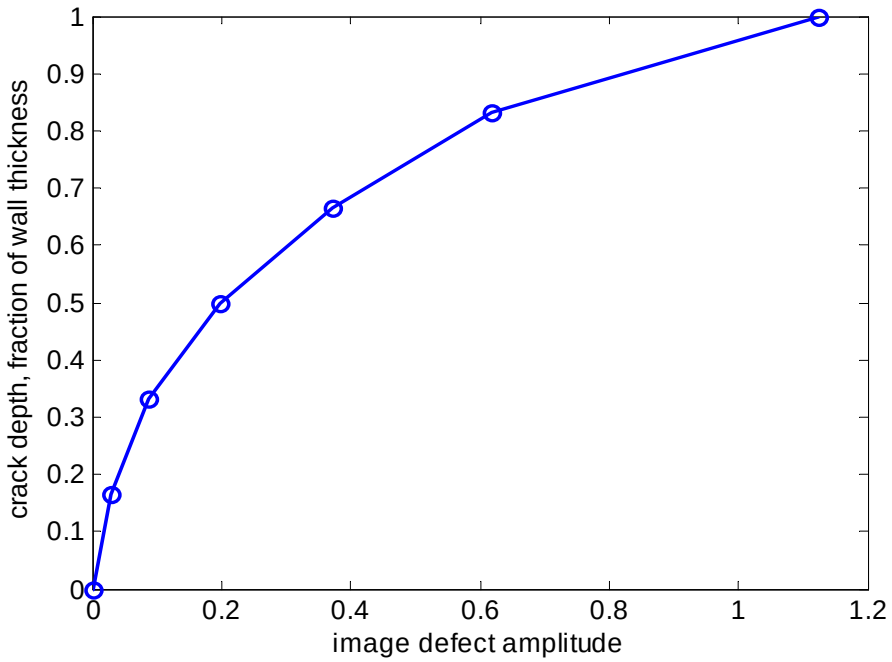

Figure 4.25: *Crack depth against defect image amplitude for crack lengths larger than* 1.5λ. *Defects at 1.2m.*

4.4.2 Imaging Response to Half-Depth Slots at 1.2m in 8 inch pipe

It has been shown that the axial extent of part-depth defects in pipes has a significant effect on the reflection amplitudes of the T(0,1) mode [14, 19]. This is due to the interaction of reflections from the front and back sides of the defects. The effect of defect axial extent on the imaging response will not be evaluated in detail here. However, a validation case of half-depth slots of 3mm axial extent will be investigated in order to compare with the previous work on T(0,1) reflectivity [19]. This axial extent was chosen since a 3mm cutter was to be used to mill defects for the validation experiments of chapter 6.

Half-depth slots were formed in the 8 inch finite element pipe model by removing elements instead of simply disconnecting elements as for the crack cases modelled previously. Half-depth (4.1mm) slots of 3mm axial extent were modelled for a range of circumferential extents. The models were excited with a 5 cycle Hanning-windowed toneburst centred at 50 kHz. At this frequency of excitation, the axial extent of the slot is $0.046\lambda_s$. The time domain finite element data from each slot model was then processed with CSM as described in section 3.5.

Figure 4.26 shows the defect image amplitude against the slot circumferential extent. Also shown on the figure is the defect amplitudes of the half-depth cracks from the previous finite element modelling study. It can be seen that the slot image amplitudes are around double the half-depth crack image amplitudes for all circumferential extent modelled. This is comparable to the increase in reflection amplitudes of the T(0,1) mode from axisymmetric slots of similar axial extent ($0.046\lambda_s$) over those from axisymmetric cracks reported by Demma [14,19]. Note that through-thickness slots would have the same defect image amplitudes as through-thickness cracks since there is no transmission past the front of the slot and hence no subsequent reflection from the back of the slot.

Figure 4.27 shows the FWHM measured from the CSM slot images against the slot circumferential extents. Also shown in the figure are the FWHM for the half-

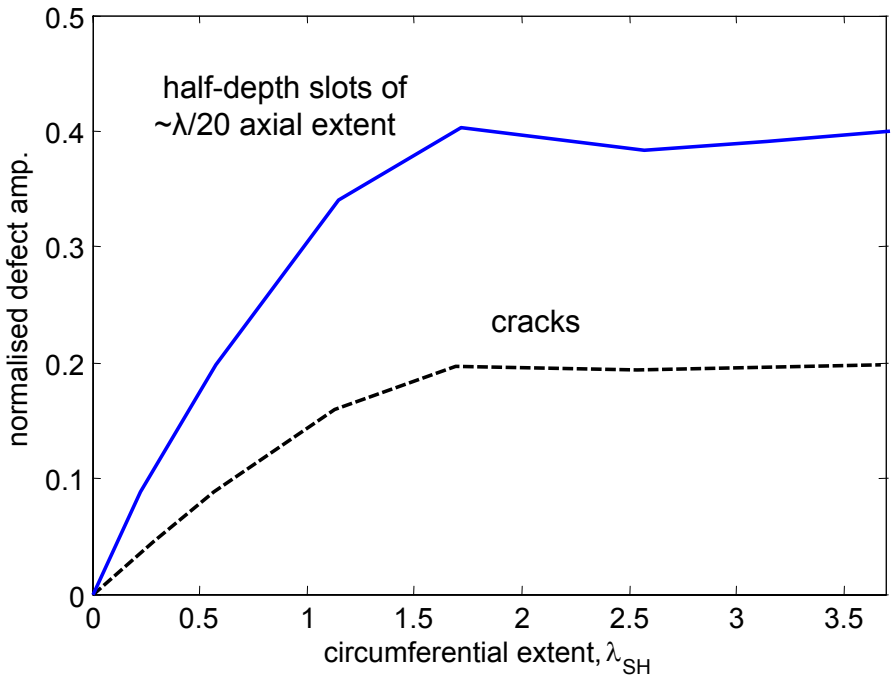

Figure 4.26: *Image defect amplitude against circumferential extent. Solid line: half-depth slots of* 0.046λ *axial extent; dashed line: half-depth cracks..*

depth cracks from the previous modelling results. The crack cases and the slot cases have comparable FWHM for all circumferential extents modelled. The smaller circumferential cracks have slightly larger FWHM than the slot cases and this is due to the FWHM being affected by the end wall axial sidelobes because of the smaller amplitude crack response.

4.4.3 Imaging through a weld cap

A simple finite element model was created to test the imaging performance through a weld cap. A through-thickness slot of circumferential extent 45 degrees (1.27λ at 50kHz) was modelled by removing elements from the pipe model at 1.2m from the transduction end. A crude model of a weld cap was created by adding an extra layer of elements onto the outside surface of the pipe at 1m from the transduction end of the 8 inch pipe model. The weld cap was 3mm thick and of 12mm axial extent. The reflection from this crude square profile model is likely to be more severe than a real

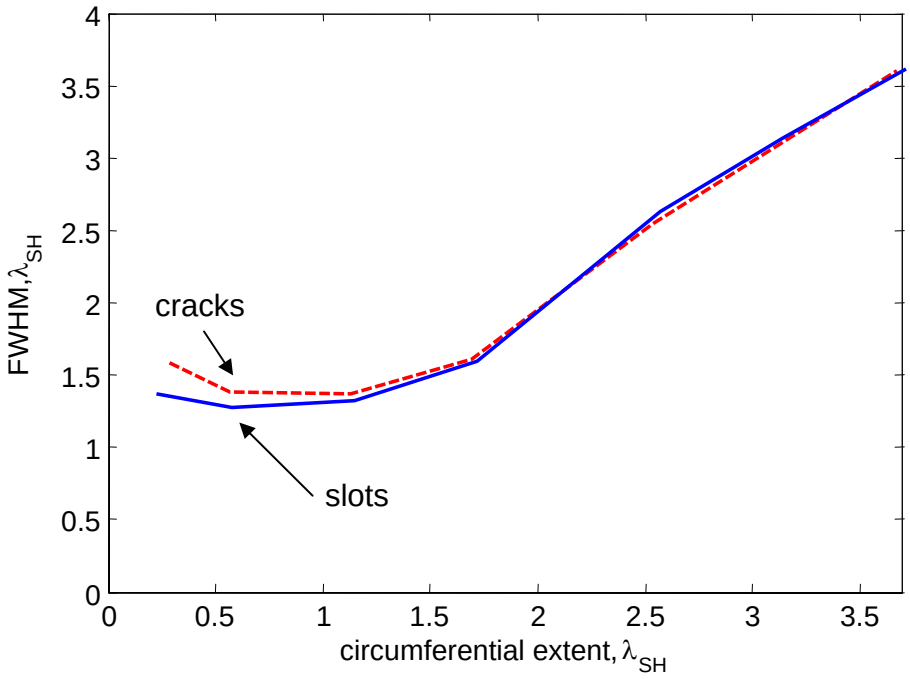

Figure 4.27: *FWHM against circumferential extent. Solid line: half-depth slots of* 0.046λ *axial extent; dashed line: half-depth cracks..*

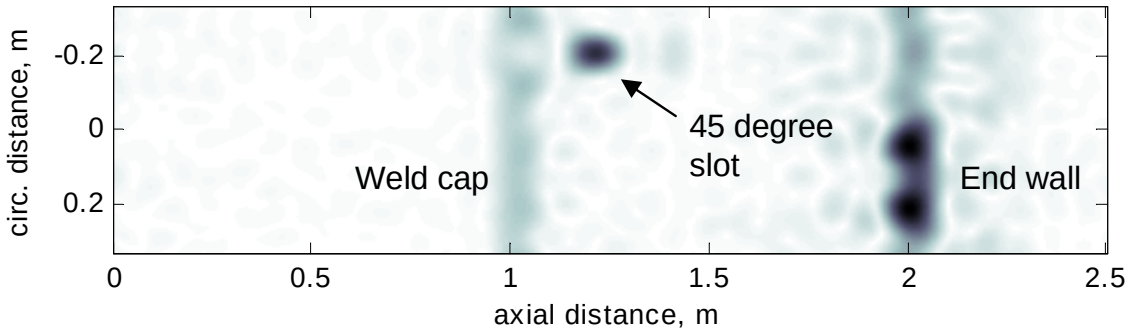

Figure 4.28: *CSM image of* 45^o *circumferential slot at 1.2m with weld cap at 1m.*

weld cap which would have a rounded profile. However, the aim here is to investigate the performance of imaging beyond the weld cap, not to study the reflections from weld caps themselves. Another model, with the weld cap directly in front of the slot at 1.2m, was also run. Figure 4.28 shows the CSM image produced from the model with the slot placed behind the weld cap and figure 4.29 shows the CSM image for the slot located at the weld cap. Note that there is quite significant distortion of the end wall image due to the large slot.

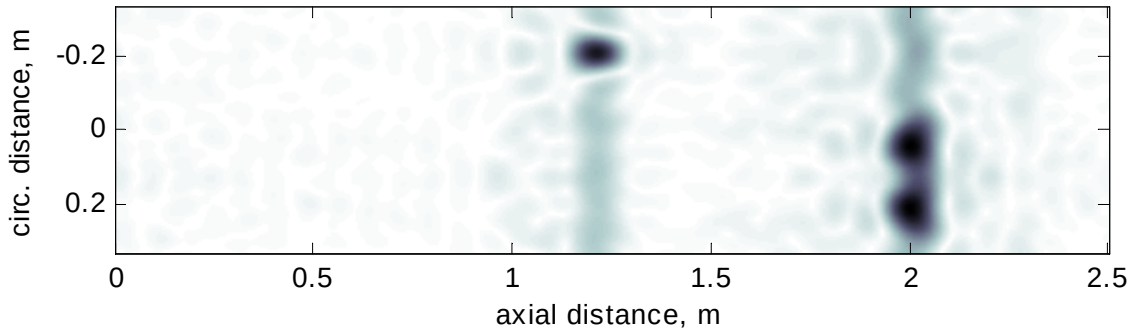

Figure 4.29: *CSM image of* 45^o *circumferential slot at 1.2m with weld cap also at 1.2m.*

Table 4.2: Imaging results for slot with weld cap finite element data

FE case	Defect Amp.	FWHM, λ_{SH}
no weld cap	1.11	1.32
slot at weld cap	1.14	1.21
slot after weld cap	1.01	1.32

Figure 4.30 shows the circumferential slices through the image at the defect locations for the case of the slot with no weld cap, the slot behind the weld cap and the slot at the weld cap. The weld cap gives around a 30% reflection, or -10.5 dB. The defect image response is very similar for all three cases. The FWHM and normalised defect image amplitudes are shown in table 4.2. The case with no weld cap has FWHM and defect amplitude as would be expected from the results of section 4.4.1. There is a slight narrowing of the defect response when the slot is just behind the weld cap location and a 3% increase in amplitude. The FWHM for the case with the slot after the weld cap is identical to the case with no weld cap but there is a 9% amplitude reduction due to the weld cap. These results are encouraging since the defect response is changed very little by the presence of the severe weld cap in the finite element model.

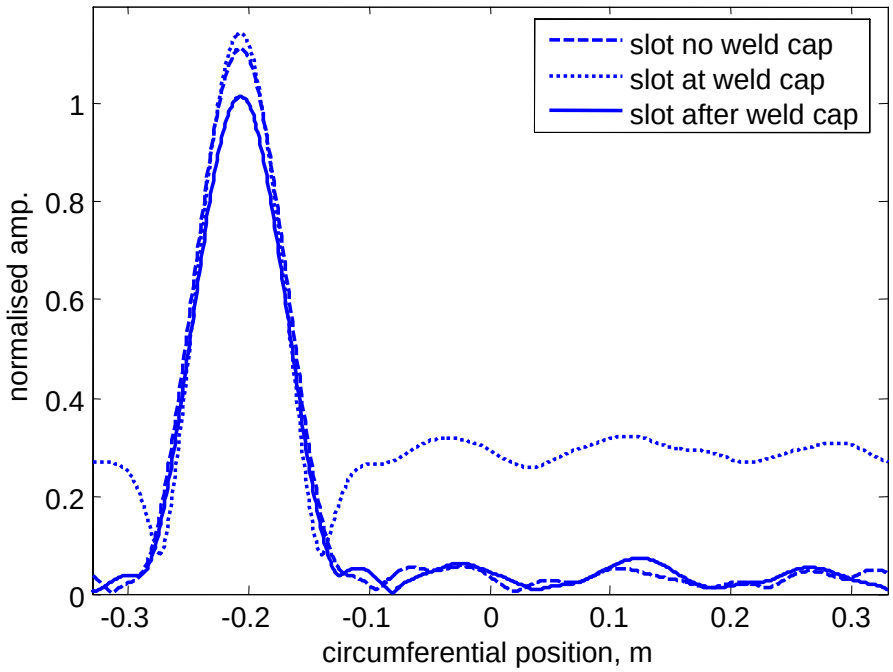

Figure 4.30: *Circumferential image slice through defect location. Solid line: slot after weld cap; dashed line: no weld cap ; dotted line: slot at weld cap.*

4.5 Generalisation of Finite Element results

4.5.1 Generalisation to different Axial Locations

It was shown for synthetic data in section 4.3.3 that the imaging response of CSM was constant with varying axial defect distance from the transducers. This prediction was tested with finite element modelling of a through-thickness crack of 20^o circumferential extent (0.55λ at 50kHz) at various axial positions in an 8 inch pipe model. The probing wave was excited at the end of the pipe model at 24 nodes spaced evenly around the pipe circumference, as before. 24 time traces were recorded at the same nodes. The received data from each axial monitoring location model was then processed using CSM.

Table 4.3 shows the image defect amplitudes and FWHM of the CSM images created from the finite element data of the three axial locations modelled. The image amplitude is relatively constant around 0.46 for all axial defect locations which is

Table 4.3: Imaging results for 20^o through-thick cracks at various axial locations

Axial location, m	FWHM, λ_{SH}	Amplitude
1	1.38	0.47
2	1.41	0.46
3	1.44	0.45

the value expected from the previous finite element studies at an axial defect location of 1.2m of section 4.4.1. However, there is a slight decrease in amplitude with increasing axial defect location. The FWHM is relatively constant around 1.4λ with axial defect location as expected from the earlier finite element case at 1.2m shown in figure 4.22. However, there is a slight increase in FWHM with increasing axial defect location.

The increasing FWHM and corresponding decrease in image defect amplitude with increasing axial defect location can be explained by small velocity errors in the finite element models. The axial phase velocity error discussed previously was -0.8% but there are additional phase velocity errors which are directionally dependent due to the cubic elements used in the finite element model. As the direction of wave propagation varies, so does the apparent element length, and this varies the velocity error. The worst velocity error is in the direction of the element diagonal, where the apparent element length is largest. For elements of the sizes used here, Drozdz [91] who has analysed these phenomena in detail, has reported velocity errors of up to around -2% across the element diagonal.

The assumption made by the imaging algorithm is that the phase velocity is constant in all directions of propagation. The velocity errors introduced by finite element modelling are significantly larger than those due to the pipe-plate analogy of section 2.3.4. This means that the higher order mode components of the recorded angular spectrum are processed with a velocity slightly different to their velocity of propagation in the finite element model. Therefore, the coherent summation of all the components of the recorded angular spectrum at the defect location will be

reduced. This means that the higher circumferential spatial frequencies (the higher order modes) have less effect in the image reconstruction for larger axial defect locations since any velocity error has an increased effect with increasing propagation distance. This reduction of higher spatial frequencies explains the decreasing amplitude and increasing FWHM with increasing axial defect location. The robustness of the imaging system to systematic errors, such as velocity errors, will be investigated in more detail in the following chapter.

The velocity errors introduced by the plate-pipe analogy of section 2.3.4 are small. However, the errors increase for situations with smaller frequency-radius product (2.36). For these situations, the imaging algorithms of section 3.5 could be implemented with an angularly dependent phase velocity. The phase velocity of any received mode at the frequencies of interest could be found using DISPERSE and subsequently used for backprojection of the received modes to build the final image.

In addition to the finite element cases above, more extensive finite element studies were carried out with various cracks at 0.3m and 1m from the transducer array. Half-depth and through-thickness circumferential cracks of circumferential extents up to 90^o (2.6λ at 50kHz) were modelled firstly at 0.3m ($4.6\lambda_S$ at 50kHz) axially from the transducer ring position and then at 1m ($15.4\lambda_S$) from the transducer position.

The resulting CSM image defect amplitudes are plotted against crack circumferential extent for all defect cases in figure 4.31. The amplitude curves are very similar at both axial defect positions for both through and half-depth cracks.

Figure 4.32 shows the measured FWHM against crack circumferential extent for both defect axial locations. The FWHM curves are comparable for both through-thickness and half-depth cracks at both axial locations as predicted with synthetic data processing. The slight differences between the results at the two different axial locations are most likely due the small finite element velocity errors discussed above.

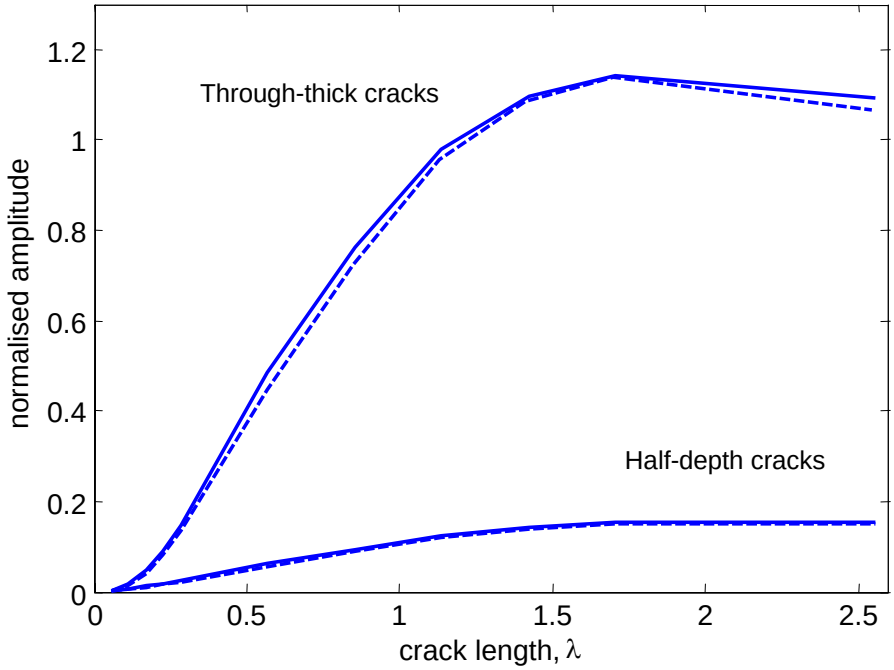

Figure 4.31: *Defect amplitude against crack circumferential extent. Solid lines: cracks at 1m; dashed lines: cracks at 0.3m.*

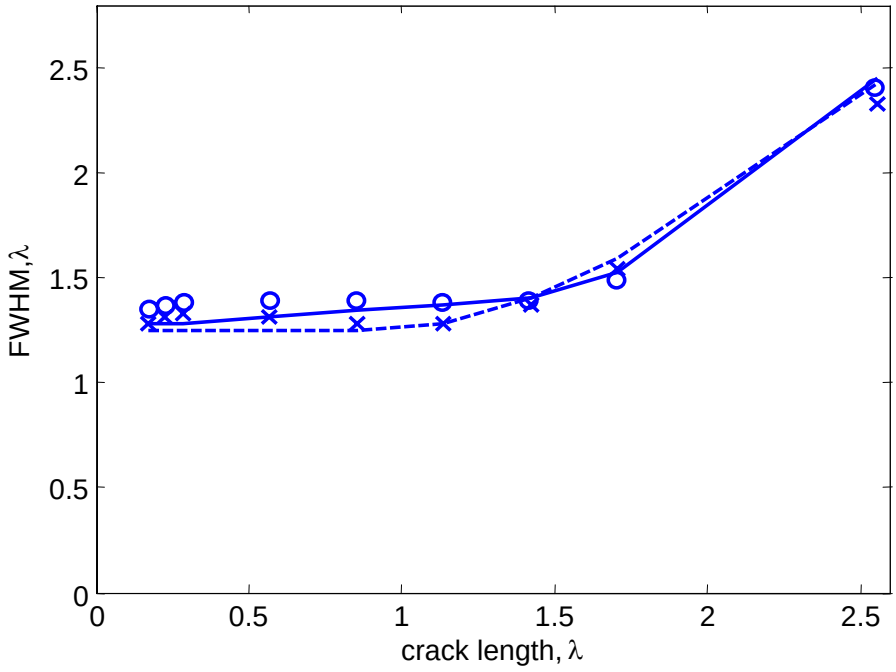

Figure 4.32: *FWHM against crack circumferential extent. Solid line: through-thickness cracks at 1m; dashed line: half-depth cracks at 1m; circles: through-thickness cracks at 0.3m; crosses: half-depth cracks at 0.3m.*

4.5.2 Generalisation to different frequencies of excitation

The 8 inch pipe finite element model was then excited using a five cycle Hanning-windowed toneburst centred at 25 kHz. Cracks were modelled by disconnecting elements at 1m, as above. Eleven different crack circumferential extents were modelled for both half-depth and through-thickness cracks. The image defect amplitude and the FWHM were recorded from the resulting CSM images produced from the finite element data.

Figure 4.33 shows the measured image defect amplitude against crack circumferential extent in degrees for the 25 kHz excitation. Also shown are the image defect amplitudes from the previous finite element study with 50 kHz excitation. It can be seen that the 25 kHz defect amplitude is smaller than the 50 kHz defect amplitude for both the half-depth and through-thickness cracks at all circumferential extents.

However, if the crack circumferential extents are scaled by the wavelength of the input excitation, as shown in figure 4.34, then the through-thickness amplitude curves are comparable for both excitation frequencies. The 25 kHz half-depth crack cases have half the amplitude of the 50 kHz half-depth cracks. This is because the reflection amplitude from part depth cracks is dependent on the crack depth as a fraction of the incident wavelength and as a fraction of the wall thickness [78]. In this case, the half-depth crack image amplitudes at 50 kHz are double those at 25 kHz.

Figure 4.35 shows the FWHM measured in metres against crack circumferential extent for both 25 kHz excitation and 50 kHz excitation. The FWHM are larger for the 25 kHz cases than the 50 kHz cases. Figure 4.36 shows the same data as figure 4.35 but with both the FWHM and crack circumferential extent scaled by the input wavelength. The curves are now comparable for both frequencies of excitation as was predicted using the synthetic data model in section 4.3.4. The small differences in FWHM between the two excitation frequencies can be explained by the interaction of the defect response sidelobes which wrap around the pipe circumference and add to the actual defect response. Also, the velocity errors in the finite element model will be slightly different at each frequency since the number

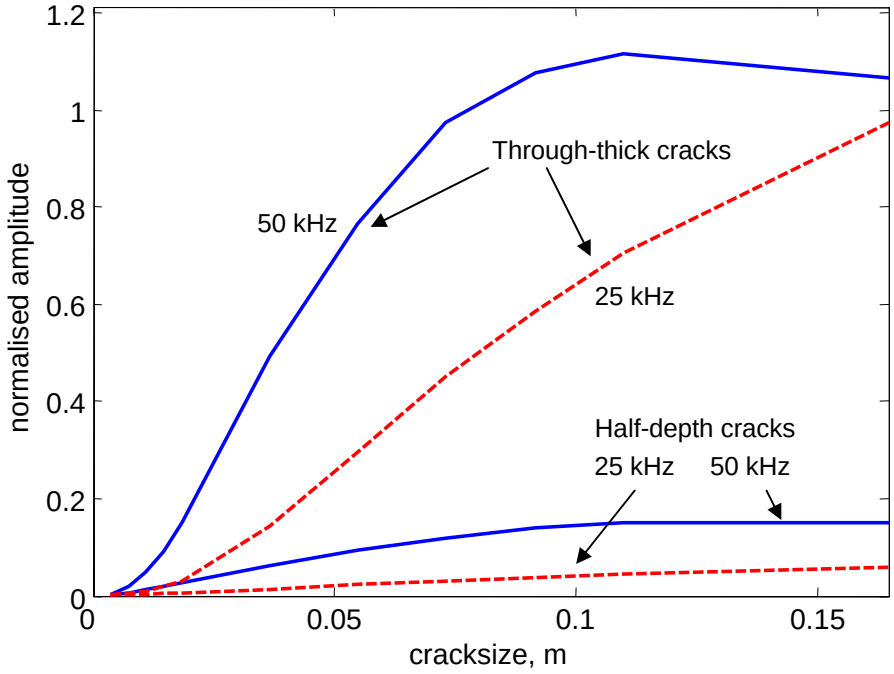

Figure 4.33: *Image defect amplitude against crack circumferential extent in metres for both through-thickness and half-depth cracks. Solid lines: excitation at 50 kHz; dashed lines: excitation at 25 kHz.*

of elements per wavelength is varying. The crack circumferential extent at which circumferential sizing is possible is around $1.5\lambda_{SH}$, as was found with previous finite element modelling studies.

4.5.3 Generalisation to different Pipe Sizes

In order to test the imaging response with different pipe sizes, finite element models were built for a 16 inch schedule 40 (centre radius $r_c = 0.19847m$, wall thickness $h = 9.53mm$) mild steel pipe and a 24 inch schedule 40 (centre radius $r_c = 0.30024m$, wall thickness $h = 9.53mm$) mild steel pipe. Through-thickness cracks were modelled with comparable physical circumferential extents of around 1.1 λ_{SH} at 50 kHz. The cases modelled are shown in table 4.4. All of the models had defects at the same axial location of 1.2m apart from the second 24 inch model which had the same defect but at an axial location of 2m.

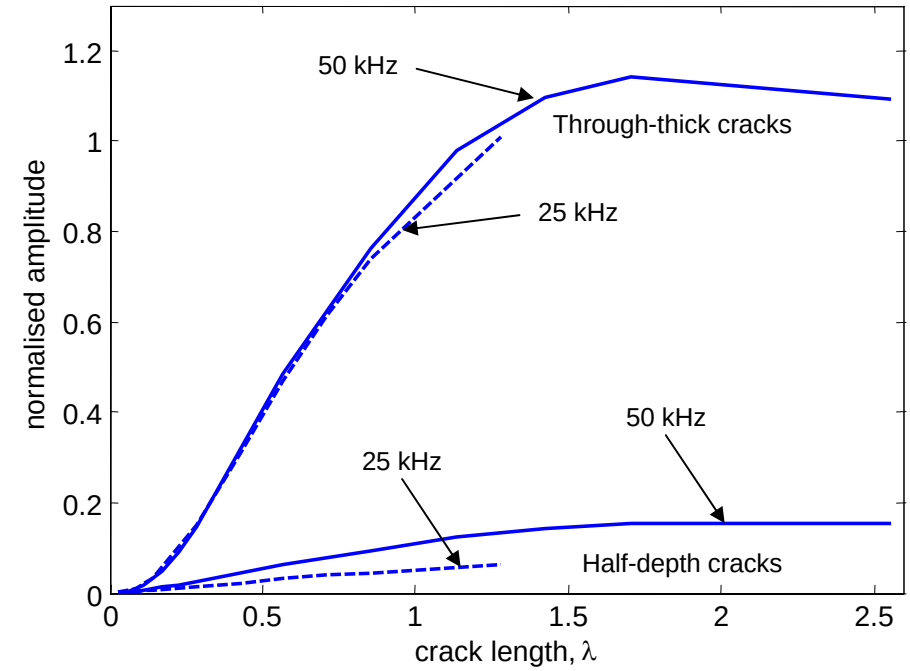

Figure 4.34: *Image defect amplitude against crack circumferential extent in λ_S for both through-thickness and half-depth cracks. Solid lines: excitation at 50 kHz; dashed lines: excitation at 25 kHz.*

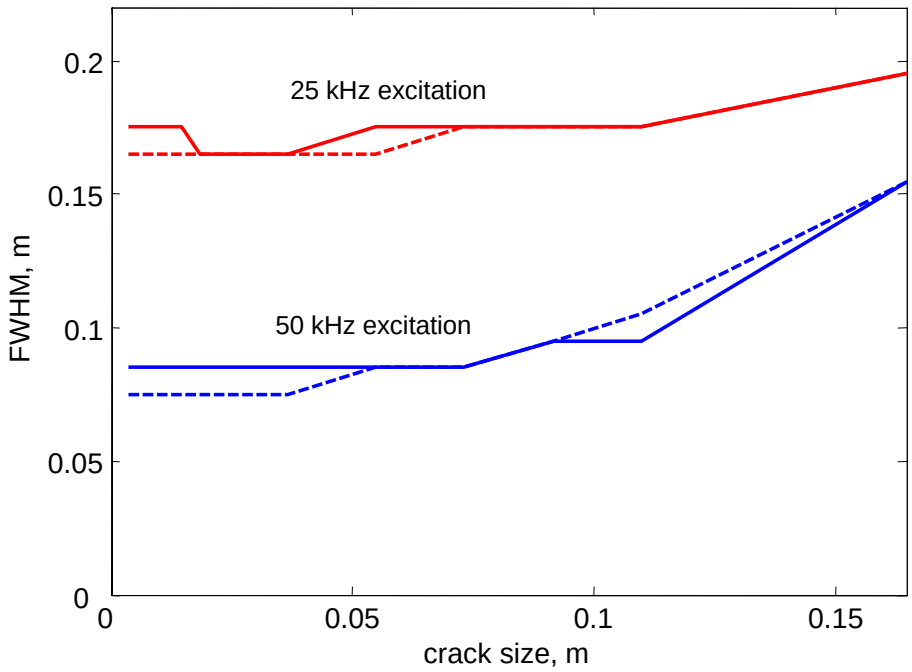

Figure 4.35: *FWHM against crack circumferential extent in meteres for excitation at 25 kHz and 50 kHz. Solid lines: through-thickness cracks; dashed lines: half-depth cracks.*

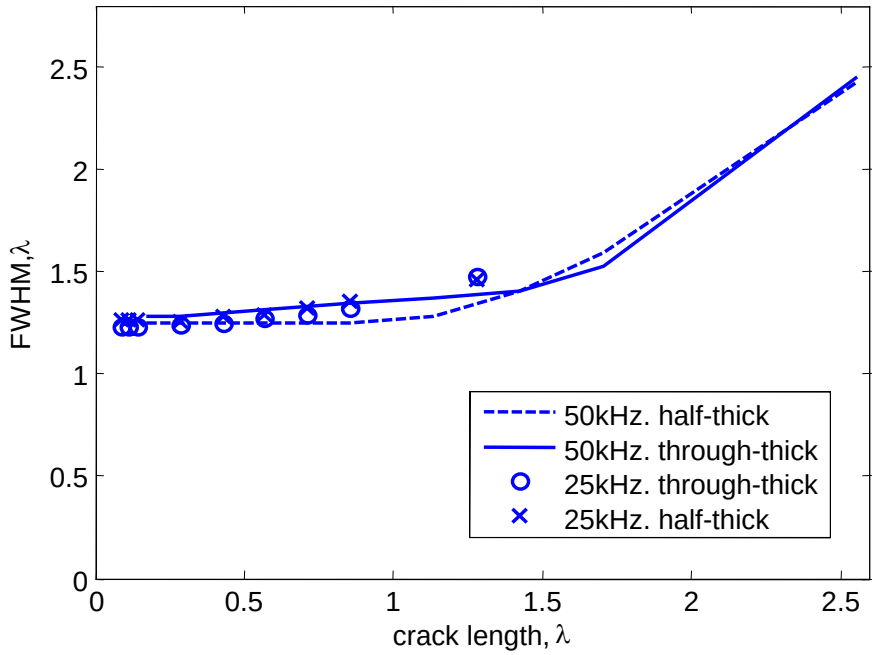

Figure 4.36: *FWHM against crack circumferential extent (in λ_{SH}). Solid line: through-thickness cracks at 1m with 50 kHz excitation; dashed line: half-depth cracks with 50 kHz excitation; circles: through-thickness cracks with 25 kHz excitation; crosses: half-depth cracks with 25 kHz excitation.*

The finite element models were excited with a 5 cycle Hanning-windowed toneburst centred at 50 kHz. The 16 inch model had 48 transduction locations around the pipe circumference and the 24 inch model had 72. Table 4.4 shows the modelled pipe geometry, the circumferential extent of the modelled defects and the measured image defect amplitude and FWHM. The image defect amplitude and FWHM (measured in *mm* or λ) are nearly identical for all pipe sizes as would have been expected from the synthetic data results of section 4.3. The amplitude gain G_{amp} over the unfocused system increases with pipe size as predicted using (7.1). There is around a 5% variation in FWHM for the three pipe cases which is most likely due to varying interaction with the end wall. There will also be small differences arising from the velocity errors of the finite element models since the element size and curvature is different for each pipe size model.

The results from the two 24 inch pipe models with the same defect at two different axial locations are extremely similar as can be seen from table 4.4. This shows that,

not only is the image response unaffected by pipe size, but also unaffected by axial defect position in the larger pipe size, as was previously shown for 8 inch pipes. Note that the FWHM is very slightly larger for the finite element case when the defect is further from the array. This can be explained by blurring resulting from small phase velocity errors as was discussed above.

The assumption made by the imaging algorithm is that the phase velocity is equal for all angles of propagation. It was shown in section 2.3.4 that the error of this assumption decreased with larger pipe diameters. Therefore, one would expect the imaging algorithm to backproject each circumferential spatial frequency component of the recorded angular spectrum with more accuracy for larger pipe cases. This would have the effect of better focusing since all of the backprojections would coherently sum exactly at the defect location and the defect image amplitude would be increased and FWHM reduced. However, the velocity errors introduced when making the plate-like assumption for the pipe are small as was demonstrated in section 2.3.4 and the effect on the final image is negligible for the pipe sizes studied here. The effects of finite element modelling exhibit larger velocity errors than those of making the plate-like assumption, as was discussed earlier.

Figure 4.37 shows the circumferential crack image profile at the defect axial location for all the pipe sizes modelled. It is clear that, despite the varying pipe circumference, the defect response is comparable. This is a very important result which shows that the defect amplitude and FWHM are dependent on the absolute size of the defect rather than the proportion of the circumference that the defect occupies. However the improvements gained by focusing in defect sensitivity (7.1) and sizing resolution (7.2) are dependent on the pipe size and frequency of inspection. The gain in amplitude for the crack case studied over the unfocused system is 19 dB for the 8 inch pipe and 28 dB for the 24 inch pipe case.

Table 4.4: Geometry and FE results for all pipe sizes

Pipe size, inches	8	16	24 I	24 II
inner radius, mm	101.37	193.70	295.47	295.47
wall thickness, mm	8.18	9.53	9.53	9.53
circumference, m	0.662	1.247	1.886	1.886
number of tran.	24	48	72	72
z_d, m	1.2	1.2	1.2	2.0
end wall	2.2	2.2	2.2	3.0
defect size, degrees	40	22	14	14
defect size, % circ.	11.1	6.1	3.9	3.9
defect size, mm	73.6	76.2	73.3	73.3
defect size, λ_{SH}	1.13	1.17	1.13	1.13
T(0,1) refl.	0.11	0.06	0.04	0.04
Defect amp.	1.00	1.01	0.98	0.98
G_{amp}, dB	19.2	24.4	28.0	28.0
FWHM, degrees	47.9	26.9	17.3	17.7
FWHM, % circ.	13.3	7.6	4.8	4.9
FWHM, mm	88.0	93.2	92.1	92.5
FWHM, λ_{SH}	1.35	1.43	1.41	1.42

4.6 Conclusions for predicted pipe imaging response

In this chapter, the imaging algorithms which were introduced in chapter 3 for the imaging of plates have been tested for their suitability for pipe imaging. The Synthetic Aperture Focusing Technique (SAFT) and Total Focusing Method (TFM) were found to be unsuitable for pipe imaging due to the excited waves in the circumferential direction which lead to unwanted artifacts in the final reconstructed image.

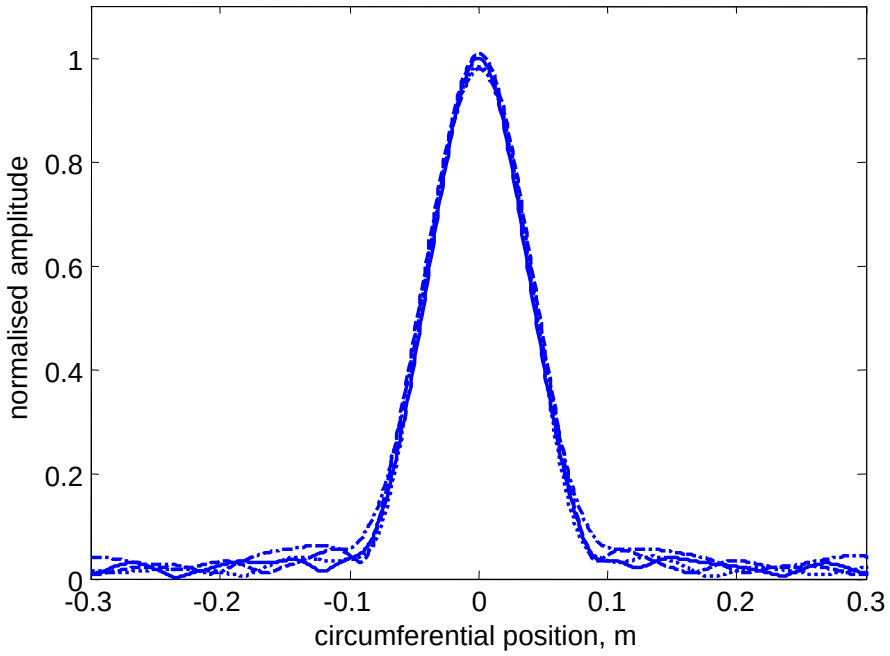

Figure 4.37: *Circumferential slice through defect axial location for all pipe sizes. Solid line: 8 inch pipe; dashed line: 16 inch pipe; dotted line: 24 inch pipe, defect at 1.2m; dash-dot line: 24 inch pipe, defect at 2m.*

The Common Source Method (CSM) was found not to suffer from such circumferential signals since all of the transducers are fired simultaneously. If the transduction is in the circumferential direction this excites the axisymmetric torsional mode T(0,1) only. CSM has been thoroughly tested in this chapter, firstly with synthetic data and then with detailed finite element studies.

The CSM was used to process data created using an analytic wave propagation and scattering model. The scattering model assumed that the backscattered reflection of the probing plane wave was limited to a fixed range of backscatter angles upon plane wave insonification, with a maximum reflection amplitude in the axial direction. This model is a simple approximation to the plane wave backscattering observed from cracks in plates [77]. It was found that the Full Width at Half Maximum (FWHM) of the defect image is a function of the maximum angle of backscatter from the defect using this simple defect scattering model. The image response was found to be invariant with axial distance from the transducer ring to the defect. The response was also found to be independent of pipe diameter and frequency of

excitation if measured in wavelengths of the probing signal.

Using data from 3D finite element models, the imaging response to circumferentially oriented cracks was tested. The aim of the finite element study was to test the limits of reliably estimating both the depth and circumferential extent of the cracks directly from the reconstructed image. The results were found to be independent of pipe size, inspection frequency and axial distance of the defect from the transducer array.

In all finite element models, at all crack depths, the amplitude of the defect image increased to a peak amplitude at a circumferential extent of around 1.5 λ_S, before plateauing in amplitude for circumferential extents larger than 1.5 λ_S (figure 4.19). For circumferential extents larger than 1.5 λ_S, the crack depth can be estimated from the image defect amplitude using figure 4.25.

The FWHM against circumferential extent curves (figure 4.22) also exhibit two distinct regimes and the boundary between the two is 1.5 λ_S which is comparable to that observed for the amplitude curves (figure 4.19). For defects with circumferential extent less than 1.5 λ_S, the FWHM is around 1.4 λ_S. For cracks with circumferential extents larger than 1.5 λ_S, the FWHM provides a reliable estimate of the actual defect circumferential extent. The limit for circumferential crack sizing is comparable to the limit for depth sizing and is around 1.5 λ_S. The FWHM could not, however, reliably estimate the circumferential extent of the shallow (one sixth depth) cracks due to their image amplitude being of comparable amplitude to the end wall axial sidelobes.

For cracks of circumferential extent smaller than 1.5 λ_S, neither the circumferential extent nor the crack depth can be reliably estimated independently since the FWHM does not significantly vary in this regime and the amplitude is a function of both crack depth and circumferential extent.

The amplitude response of part-depth defects is also dependent on axial extent of the defect as a fraction of probing wavelength. Some basic validation finite element models were run using circumferentially oriented half-depth slots with 3mm axial extent instead of cracks. The defect image amplitude of the half-depth slots were

roughly double the amplitudes observed from the images of cracks of comparable depth and circumferential extent which agrees well with previous work of T(0,1) incident on axisymmetric defects [19].

Other pipe finite element models were run in order to verify the results from the synthetic data study. It was found, using finite element data, that the image response was almost independent of axial defect position and pipe radius, as was predicted from processing analytic synthetic data. The image response was found to worsen very slightly as the defect was moved further from the transducer array. This was due to small directionally dependent velocity errors in the finite element model. These errors affect the ability of the imaging algorithm to coherently sum all of the backscattered waves at the defect location. The velocity errors have a greater effect for further axial defect locations, since the waves have propagated larger distances. The robustness of the imaging system to these systematic errors will be investigated in more detail in the following chapter.

The imaging response was then tested using two different excitation frequencies of 25 kHz and 50 kHz. The image response at the lower excitation frequency generally had smaller amplitude and larger FWHM than the higher frequency response of the same defect. However, it was found that if the crack length and FWHM are scaled to the wavelength of the excitation signal, λ_S, then the FWHM curves are comparable for both excitation frequencies. The amplitude response of the through-thickness cracks was comparable for both excitation frequencies if the crack length is scaled to the input wavelength. However, the reflection amplitude from part-depth cracks is also dependent on the crack depth as a fraction of the incident wavelength [78] and this was observed here.

It has been shown that the ability to estimate the depth and circumferential extent of defects using synthetic focusing is significantly greater than that of an unfocused system. An unfocused system, which can receive only the axisymmetric torsional mode T(0,1) cannot estimate the circumferential defect extent and can only estimate the defect depth for axisymmetric defects. In contrast, the focused system can reliably estimate both crack depth and circumferential extent independently, providing

the crack has circumferential extent larger than $1.5\lambda_S$. This result is valid for any frequency of inspection below the T(0,2) cutoff and in any pipe size. The result is also valid for any axial defect location but any errors in the wave propagation model used by the imaging algorithm, for instance, phase velocity errors, will have a more detrimental effect at larger axial defect locations.

The improvements of using the focused system in both circumferential resolution and defect sensitivity are around 17 dB in an 8 inch pipe with 50 kHz excitation. The gain in resolution (7.2) and defect sensitivity (7.1) increase for larger pipe diameters and higher inspection frequencies. However, larger pipes will require more transducer elements to sample the larger circumference in order to attain the focusing improvements.

Chapter 5

Robustness of the System

Three imaging algorithms, which were initially investigated for plate imaging in chapter 3, were tested for use with pipe imaging in the previous chapter. It was found that the algorithm most suitable for imaging of pipes was the Common Source Method (CSM) where the probing wave is axisymmetric since all transducers are excited simultaneously. Estimates of defect circumferential extent and defect depth could be made by measuring the Full Width at Half Maximum (FWHM) and amplitude of the defect image response respectively. In order for defect sizing to be reliable, the circumferential extent of the defect must be larger than 1.5λ, where λ is the wavelength of the probing signal which, for the low frequency torsional system investigated here, is the bulk shear wavelength $\lambda_S = c_S/f$.

In this chapter, the robustness of the CSM pipe imaging system to possible setup errors will be tested. The methodology will be to synthetically corrupt finite element data and then to compare the imaging results of the corrupted data set with those of the initial uncorrupted data set. The synthetic model used to corrupt the finite element data will depend on the type of setup errors under investigation.

There are two types of setup error that may occur and these are random and systematic errors. Random errors are effects that appear to varying random extents around the pipe transducer ring, for instance random coupling errors or random phase errors. Systematic errors arise when the transducer ring is not aligned per-

fectly and is tilted with respect to the pipe axis. Another form of systematic error arises from attempting to process the received data set with incorrect pipe dimensions or material properties, which result in image reconstruction using incorrect phase velocities, and these will also be briefly investigated here.

5.1 Random Coupling errors

5.1.1 Robustness against coupling variation

Random coupling errors arise since not all of the transducer elements will be perfectly coupled to the pipe. Variation of coupling around the pipe circumference will mean that a non-perfect T(0,1) mode will be excited into the pipe. This means that small amounts of other torsional flexural modes (F(n,2)) may also be excited into the system in addition to the desired T(0,1) probing wave.

The reception of the reflected wave modes will also be corrupted by coupling variations. Therefore, each complex component in the angular spectrum may have an incorrect amplitude and phase.

In order to test the robustness of the system to coupling errors, synthetic coupling variations are added to the finite element data set. The full data set is needed with all transmit-receive combinations since the coupling has an effect on the excitation of the probing wave and on the reception of the backscattered waves.

A coupling coefficient was synthesized for each transducer. For the n^{th} transducer, the coupling coefficient $coup_n$ was randomly generated using a normal variation of mean $\mu = 1$ and pre-defined standard deviation, σ_{coup}.

$$coup_n = N(1, \sigma_{coup}), \tag{5.1}$$

where N denotes the normal probability distribution. Each time trace of the full data set which was excited or received by the n^{th} transducer must be multiplied by $coup_n$. For example, the time trace received by transducer n after firing with

transducer m must be multiplied by the coupling coefficient $coup_n.coup_m$ in order to take account of the coupling variation on both transmission and reception. The full data set is then summed over all the transmitters to produce the data set used by CSM. This summation has the effect of synthetically creating a data set where all of the transducers, each with an individual coupling coefficient $coup_n$, were fired simultaneously.

The finite element model used was an 8 inch schedule 40 mild steel pipe model with a through-thickness crack of 40^o (1.15λ at 50 kHz) circumferential extent at 1.2m. The model was excited using a 5 cycle Hanning-windowed toneburst centred at 50 kHz. Note that, at this frequency, the modelled crack size is smaller than the resolution limit of 1.5λ defined in section 4.4.1. The CSM image amplitude for this defect case without any data corruption was 1.02 times that of the input amplitude and the FWHM was 1.3λ.

The coupling standard deviation σ_{coup} was varied from 0.05 to 0.55 with steps of 0.05. For larger standard deviations, some of the coupling coefficients are negative. For these situations, it was necessary to set the negative coupling coefficient to zero to simulate complete loss of coupling for that transducer.

For each value of coupling standard deviation used, 50 sets of coupling coefficients were randomly generated to corrupt the data. The means of the maximum and minimum coupling coefficients from each run are plotted against the respective coupling standard deviation in figure 5.1.

Figure 5.2a shows an example set of coupling coefficients for 24 transducers with a coupling standard deviation of 0.2. The maximum coupling coefficient is 1.5 and the minimum is 0.5. This level of coupling variation is typical of that observed experimentally, as will be demonstrated in the following chapter. Figure 5.2b shows an example with a coupling standard deviation of 0.55, the maximum tested in this study. In this example transducer 16 has zero coupling and transducer 22 has nearly zero coupling. Transducers 7 and 10 have coupling coefficients of over 2. This is clearly a very severe coupling situation and is unlikely to occur in reality.

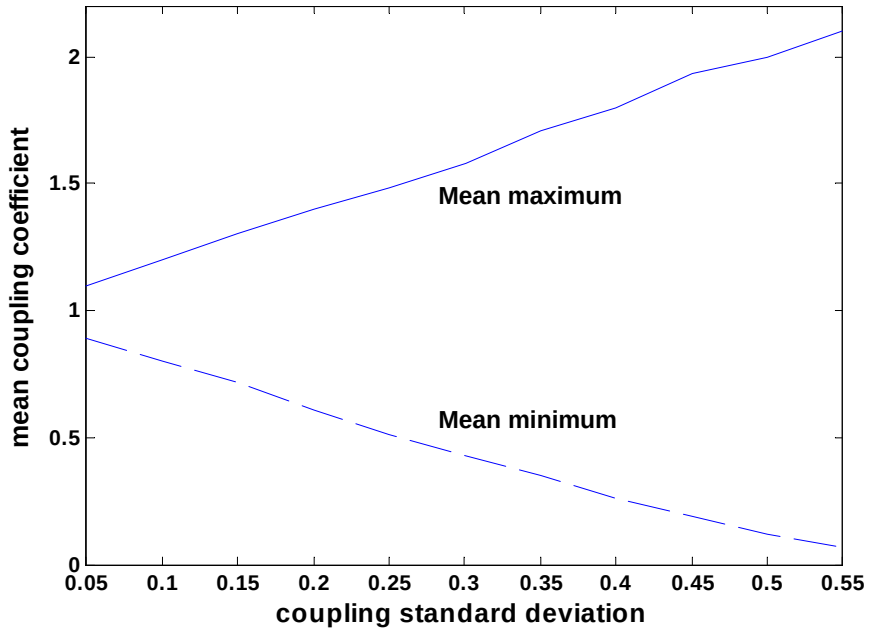

Figure 5.1: *Maximum and minimum coupling coefficients averaged over 50 runs for each coupling standard deviation.*

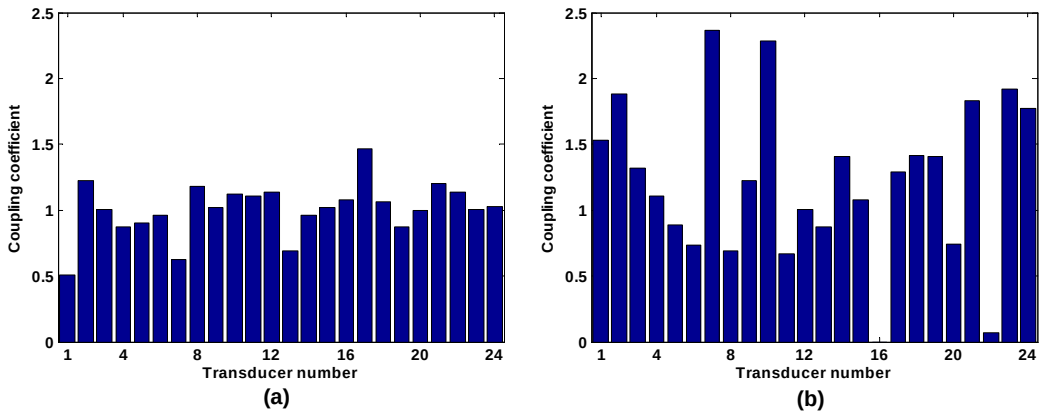

Figure 5.2: *Coupling variations across the 24 transducers in the ring. (a) coupling standard deviation = 0.2. (b) coupling standard deviation = 0.55.*

For each of the 50 runs, the data was imaged using CSM. The defect amplitude and FWHM were measured directly from the images. Also measured from the image were the peak noise and the RMS noise. The peak noise is the maximum pixel value in the image in a featureless region of the pipe and the RMS noise is the mean pixel value in this region. The noise estimate region was between 0.2m and 0.8m. This region is sufficiently far from the defect region so that the defect axial sidelobes are

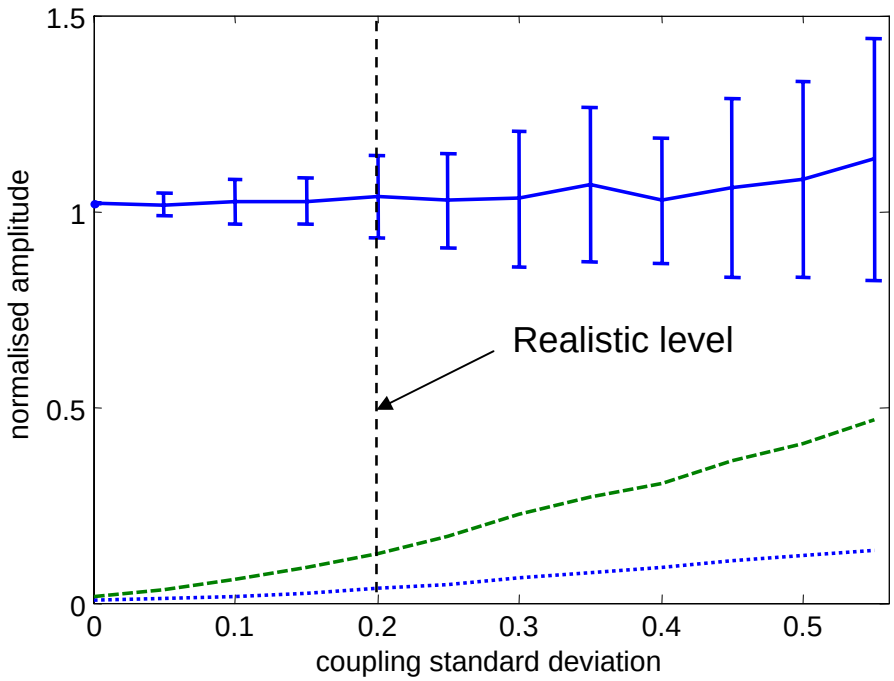

Figure 5.3: *Measured defect amplitude with* 1σ *error bars against coupling standard deviation. Also, dashed line: mean peak image noise; dotted line: mean RMS noise.*

very small as was observed in figure 4.18. The mean and standard deviation of each of the measured values across the 50 runs were then recorded.

Figure 5.3 shows the mean defect amplitude with 1σ error bars against the coupling standard deviation. The mean maximum noise and the mean RMS noise in the featureless region are also plotted on the same figure. The mean defect amplitude remains relatively constant with increasing coupling variation, with increasing standard deviation, as would be expected since the coupling coefficients have mean $\mu = 1$. The increase in mean defect amplitude at very high coupling standard deviations occurs due to the minimum coupling coefficient being limited to zero whereas there is no upper limit for coupling coefficient. The peak noise and RMS noise both increase with increasing coupling errors to 47% of the input amplitude and 14% of the input amplitude respectively for a coupling standard deviation of 0.55.

Figure 5.4 shows the mean measured FWHM with 1σ error bars against the coupling standard deviation. The mean FWHM remains relatively constant for all levels of coupling errors, with the FWHM standard deviation increasing minimally with

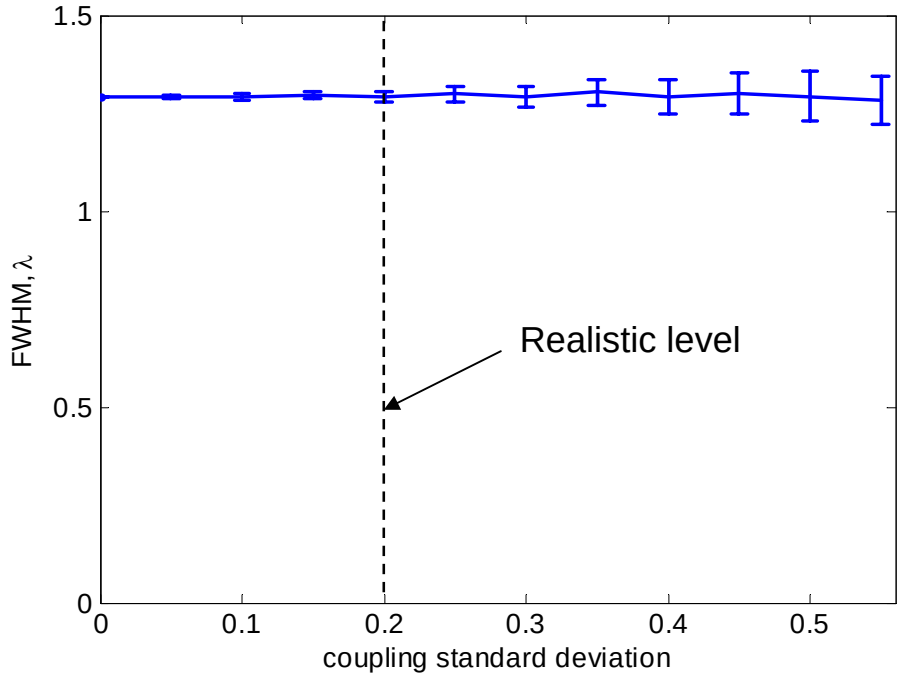

Figure 5.4: *Measured FWHM with* 1σ *error bars against coupling standard deviation.*

increasing coupling standard deviation. The system is clearly easily capable of dealing with coupling variations of the order seen in real experiments, with a standard deviation of 0.2.

5.1.2 Robustness against transducer dropouts

The situation may arise whereby an individual transducer does not make physical contact with the pipe wall. In this case that transducer will have a coupling coefficient of zero. This would also be the case should the transducer or some part of the electronic drive and reception circuitry be faulty, although this would easily be detected by simple pre-inspection checks. The situation where there is no coupling for a transducer is referred to as a transducer dropout.

In order to simulate transducer dropouts, some coupling coefficients were set to zero. Up to seven transducer dropouts out of the possible 24 in the transducer ring were tested. For each number of dropouts, the dropout transducers were chosen randomly 50 times. Each corrupted data set was then imaged with CSM. As with

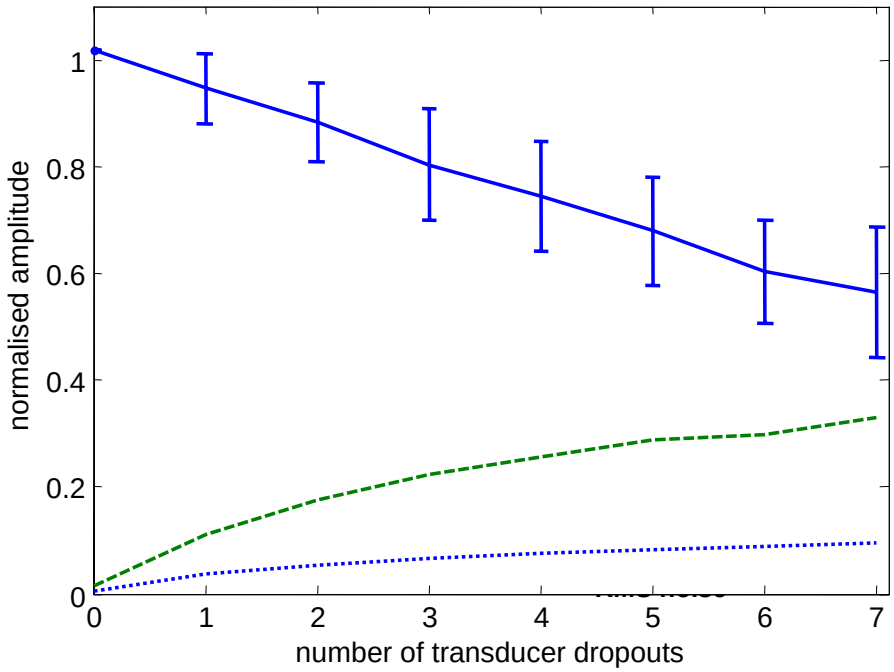

Figure 5.5: *Measured defect amplitude against number of transducer dropouts. Also, dashed line: mean peak image noise; dotted line: mean RMS noise.*

the coupling variation study, the defect amplitude, FWHM, noise mean and noise maximum were recorded from each image and then averaged over the 50 runs for each number of transducer dropouts.

Figure 5.5 shows the mean defect amplitude with 1σ error bars against the number of transducer dropouts. The mean maximum noise and the mean RMS noise are also plotted on the same figure. The measured defect amplitude decreases from 102% of the input amplitude with no transducer dropouts to 56% with 7 transducer dropouts. This is because less energy is coupled into the pipe with increasing transducer dropouts. Also, not all of the backscattered modes will be correctly received by the transducer ring. The peak noise increases from 1.6% with no dropouts to 37% with 7 dropouts. However, it is important to note that it is unlikely that there would be even a single transducer dropout, since they should be detected and fixed prior to inspection.

Figure 5.6 shows the mean FWHM with 1σ error bars against the number of transducer dropouts. The mean FWHM is relatively constant but the FWHM standard

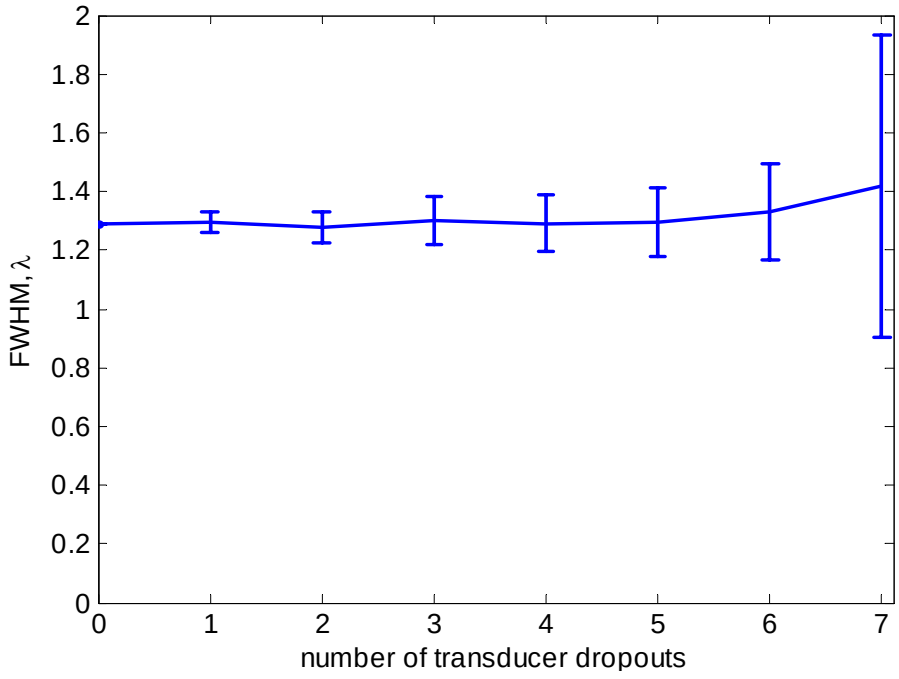

Figure 5.6: *Defect image FWHM against number of dropouts with* 1σ *error bars.*

deviation becomes large for the case of 7 transducer dropouts. Nevertheless, the FWHM is much less affected by transducer dropouts than the image defect amplitude (figure 5.5).

5.2 Random Phase Errors

5.2.1 Robustness against phase errors

Phase errors could occur either from incorrect mechanical axial placement of the transducers or from varying delays in the electronic drive/reception circuitry. The phase error may be positive or negative since any timing error may be an advance or a delay. A delay of time, τ_n for the n^{th} transducer will give a phase error of

$$\theta_n(\omega) = \omega\tau_n \tag{5.2}$$

A transducer axial misplacement of Δz_n will produce a time delay of $\Delta z_n/c$, where c is the phase velocity and the subsequent phase error for that transducer will be

$$\theta_n(\omega) = \omega(\Delta z_n/c) \tag{5.3}$$

A 1mm axial misplacement will produce a $0.3\mu s$ time shift and this is a realistic level of maximum axial deviation. It is clear that both types of phase error can be synthesized using the same error model. As with the coupling error model, a normal distribution with mean $\mu = 0$ and standard deviation of σ_τ was used to generate random time delays for each transducer.

$$\tau_n = N(0, \sigma_\tau) \tag{5.4}$$

The phase errors are then calculated subject to equation (5.2) for each frequency of interest and subsequently applied to the finite element data. The standard deviations tested range from $0.1\mu s$ to $2\mu s$ in steps of $0.1\mu s$. These time standard deviations correspond to axial misalignment standard deviations up to 6.5mm which is significantly larger than the realistic setup scenario.

For each standard deviation tested, the normal distribution is used 50 times. The corrupted data is then imaged using CSM for each of the 50 corrupted data sets. As before, the defect chosen is a through-thickness crack of 40^o circumferential extent. The defect amplitude and FWHM are measured directly from the image as well as the mean and maximum noise in the featureless region of the pipe, between 0.2m and 0.8m.

Figure 5.7 shows the measured defect amplitude of the 40^o through-thickness crack with 1σ error bars against the input time error standard deviation σ_τ. The mean maximum noise and the mean RMS noise over the 50 runs are also plotted on the same figure. The mean defect amplitude reduces with increasing phase errors from 1.02 to 0.88 for a time error standard deviation of $2\mu s$. The mean peak noise value increases from 1.6% of the input amplitude with no phase errors to 47% with a time error standard deviation of $2\mu s$. Note that the case studied employed excitation centred at 50 kHz. The observed detrimental effects are likely to be worse at higher inspection frequencies since a given time shift τ will cause a larger phase shift 5.2.

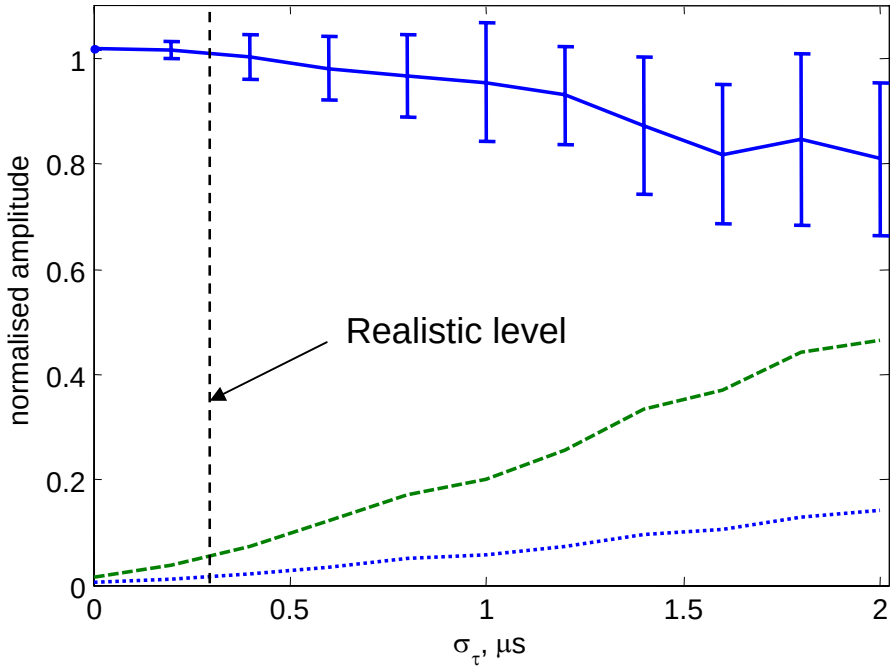

Figure 5.7: *Measured defect amplitude with* 1σ *error bars against time delay standard deviation. Also, dashed line: mean peak image noise; dotted line: mean RMS noise.*

Figure 5.8 shows the mean FWHM with 1σ error bars against the time error standard deviation. The mean FWHM remains roughly constant around 1.3λ for all levels of time error standard deviations. The FWHM standard deviation increases with increasing time error standard deviations as expected. The system is clearly easily capable of dealing with the expected maximum time shift error of $0.3\mu s$ which has little effect on either the FWHM or defect amplitude.

5.2.2 Robustness against reversed transducers

There is a possibility that one or more of the transducers may be assembled into the transducer ring backwards. This is unlikely and would easily be picked up by quality control and fixed prior to inspection. However, the effect of having one or more reversed transducers is investigated here for completeness.

The effect of reversing a transducer is equivalent to introducing a phase error of 180^o across all frequencies or applying a coupling coefficient of -1.

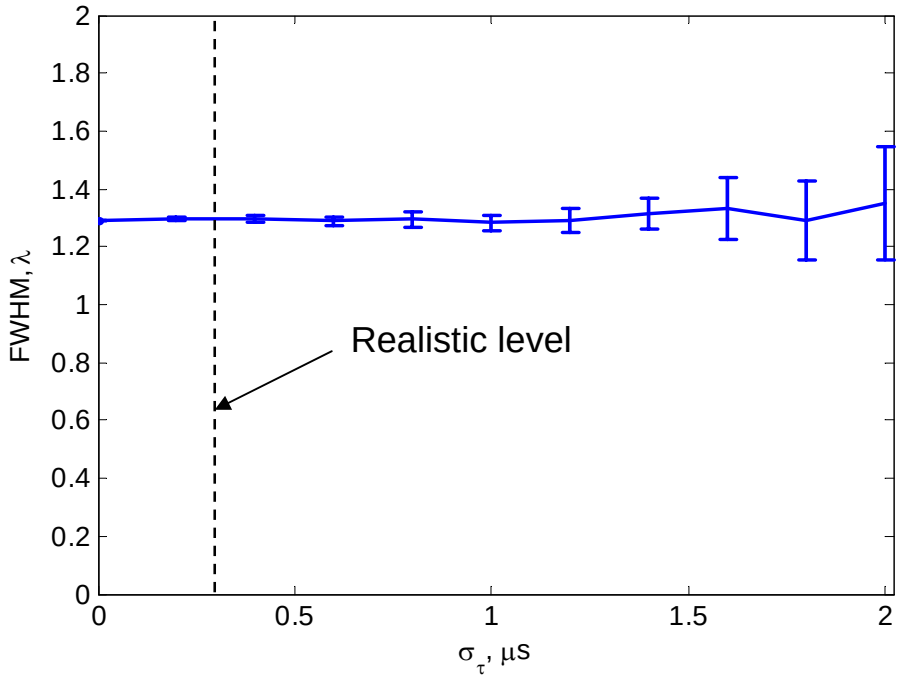

Figure 5.8: *FWHM with* 1σ *error bars against time delay standard deviation.*

Up to five transducers out of the 24 in the ring were reversed synthetically in the full finite element data set. The finite element case used was again the through-thickness crack of 40^o circumferential extent. The transducers to be reversed were randomly chosen. The corrupted data was then imaged using CSM. The defect amplitude, FWHM and noise estimates were recorded from the image, as with the previous setup error studies. For each number of transducers reversed this process was repeated 50 times. The recorded parameters were then averaged over the 50 runs.

Figure 5.9 shows the defect amplitude and the noise values against the number of reversed transducers. The defect amplitude is reduced as more transducers are reversed. The mean peak noise increases quickly and for three or more reversed transducers, the peak pixel value in the featureless region of the pipe has comparable image amplitude to that of the defect. At this point the defect amplitude to noise ratio is unity and hence the system becomes useless since defects are not detectable above the noise in the image.

Figure 5.10 shows the mean measured FWHM with 1σ error bars against the num-

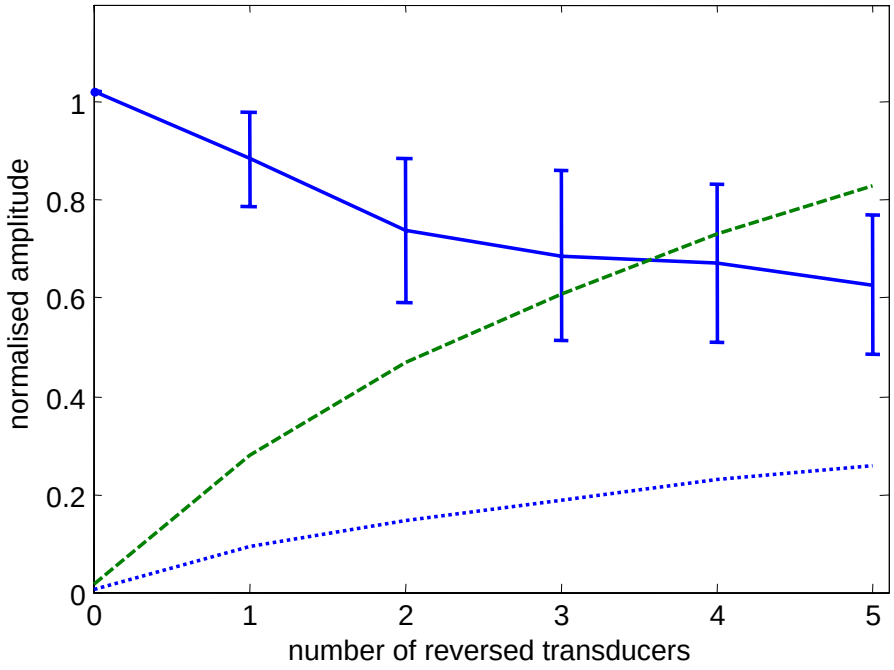

Figure 5.9: *Measured defect amplitude with* 1σ *error bars against number of reversed transducers. Also, dashed line: mean peak image noise; dotted line: mean RMS noise.*

ber of reversed transducers. The FWHM increases drastically with more than two reversed transducers but, as mentioned above, this is an extremely unlikely situation.

5.3 Tilting of the transducer ring

The correct setup for the transducer ring would be for all of the transducers to be at the same axial position around the pipe circumference, i.e. on a plane normal to the pipe axis (Figure 5.11a). However, incorrect manual setup may result in tilting of the transducer ring meaning that some of the transducers will not be at the desired axial location (Figure 5.11b). These deviations from the desired axial transduction location will cause phase shifts in a similar way to the random axial transducer misalignment discussed in the previous section. The phase shift is relative to the axial deviation of the transducer from the desired location (5.2). The axial position deviation δz increases with the distance of the transducer from the tilt axis

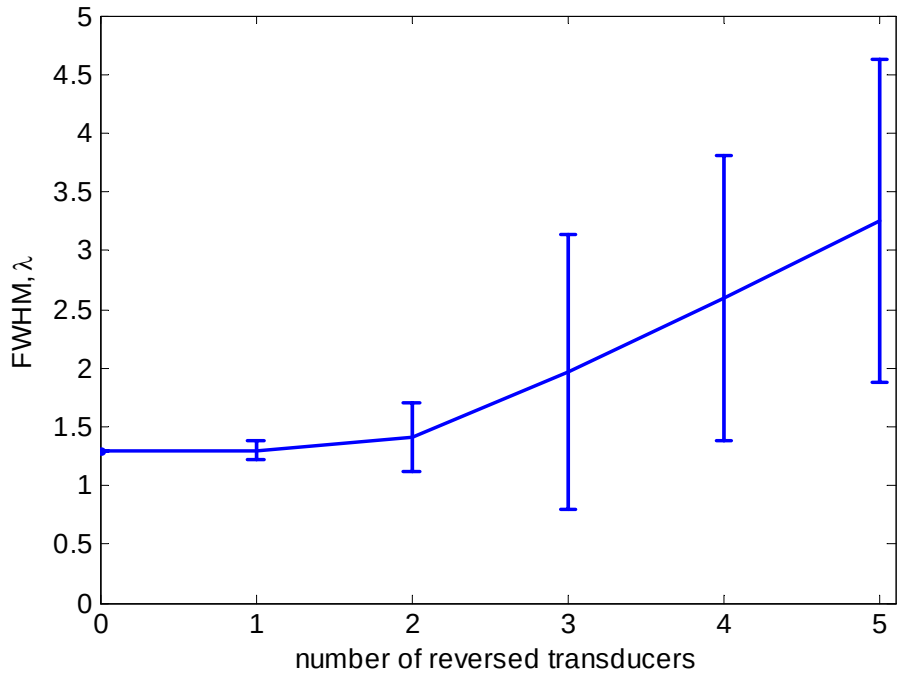

Figure 5.10: *FWHM with* 1σ *error bars against number of reversed transducers.*

y (marked in figure 5.11c)

$$\delta z = y \sin \gamma, \tag{5.5}$$

where γ is the tilt angle in radians. The resulting phase error θ_{tilt} is

$$\theta_{tilt}(\omega) = \frac{\omega y \sin \gamma}{c_S}, \tag{5.6}$$

where c_S is the bulk shear velocity. These phase errors can be applied to the full matrix data set, in the same manner as the previous study for random phase errors.

5.3.1 Effect of tilting on end wall response

The above analysis was applied to the full matrix finite element data set from an end wall only model of an 8 inch pipe, in order to apply synthetic tilt to the transducer ring, prior to imaging the corrupted data. The circumferential image slice through the end wall location, from the corrupted data set with end at 1.2m are shown in figure 5.12. It is clear that tilting of the transducer ring has a strong effect on the end wall circumferential image profile. However, a tilt angle of 1^o gives a maximum axial

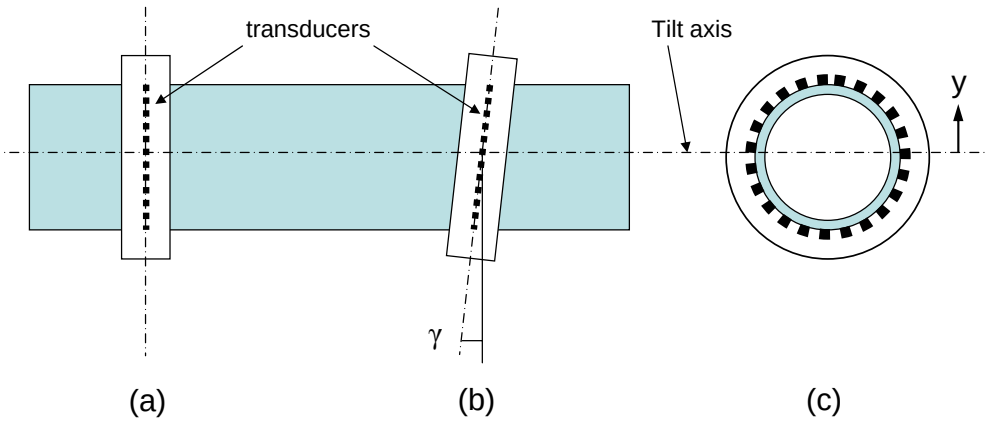

Figure 5.11: *Setup of the transducer ring on the pipe: a) correct setup; b) transducer ring by γ; c) view along the pipe axis .*

misplacement $\delta_{max} \pm 1.8mm$ and a tilt of 4^o tilt gives a maximum axial misplacement of $\delta_{max} \pm 7.3mm$ on an 8 inch pipe (5.5). These axial deviations from the desired axial transducer location would be noticeable and set up axial deviations of more than a few millimetres would be unlikely. Therefore, a transducer ring tilt of 2^o is a sensible maximum likely error. This situation creates a variation in the circumferential end wall image profile of ± 0.3 from the correct untilted value of unity.

5.3.2 Tilting effect on the defect response

Synthetic tilt phase errors were then applied to the full matrix finite element data set used for the previous random error robustness studies of this chapter. The model of an 8 inch pipe has a through-thickness crack of 40^o circumferential extent at 1.2m from the transduction end of the pipe.

Firstly, synthetic tilt was applied to the finite element data with the tilt axis through the defect circumferential location as shown in figure 5.13a. Figure 5.14 shows the circumferential image profiles through the crack axial location for various tilt angles. The effect of tilting the transducer ring in this fashion is to reduce the defect image amplitude accompanied by an increase in sidelobe amplitude. The circumferential profiles also become non-symmetric due to the tilting. The effect of a 2^o tilt in the 8

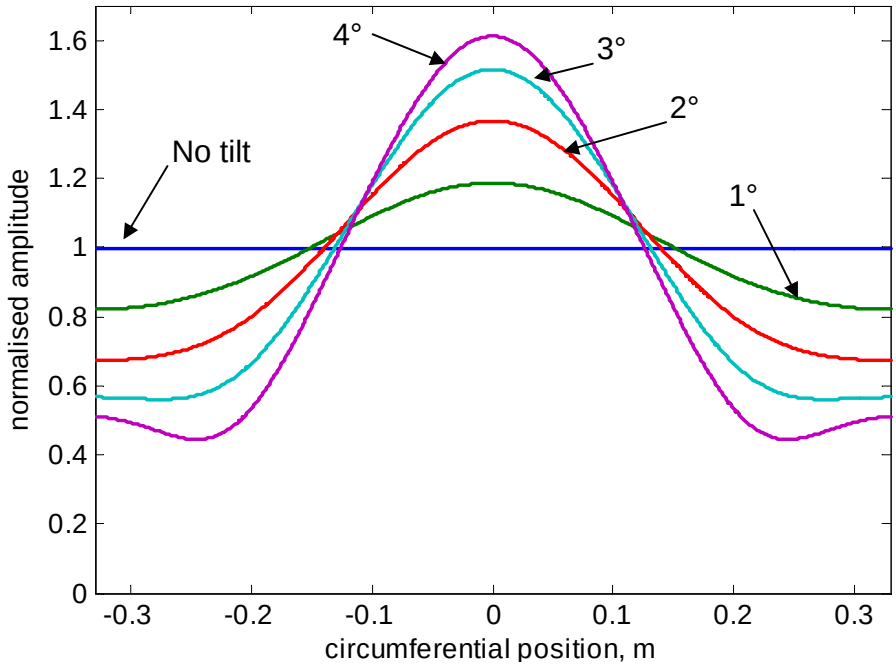

Figure 5.12: *Circumferential image slices at the end wall location of 1.2m with various transducer ring tilt angles.*

inch pipe model is a 7.3% amplitude reduction and an increase in maximum sidelobe amplitude from 0.06 to 0.21.

The same 8 inch pipe finite element data was then corrupted using the above method for tilting of the transducer ring towards (positive tilt angles) and away (negative tilt angles) from the 40^o circumferential extent crack, as shown in figure 5.13b. Circumferential slices at the defect axial location through the reconstructed images of the corrupted finite element data for tilt angles of -2^o and $+2^o$ are shown along with the non-corrupted image slice are shown in figure 5.15. Note that only half of the pipe circumference is plotted since the profiles are symmetric through the centre of the defect. The image defect amplitude is reduced for negative tilt angles and increased for positive tilt angles. For a tilt of $+2^o$, towards the defect, the amplitude is increased by 18% and the sidelobe amplitude is increased to 0.2 from 0.06. For a tilt of -2^o, away from the defect, the amplitude is decreased by 20% from the untilted value and the sidelobe amplitude is increased to 0.15. Therefore, the effects of tilting the transducer ring towards and away from the defect (figure 5.13b) are more severe than tilting the ring on an axis through the defect (figure 5.13a).

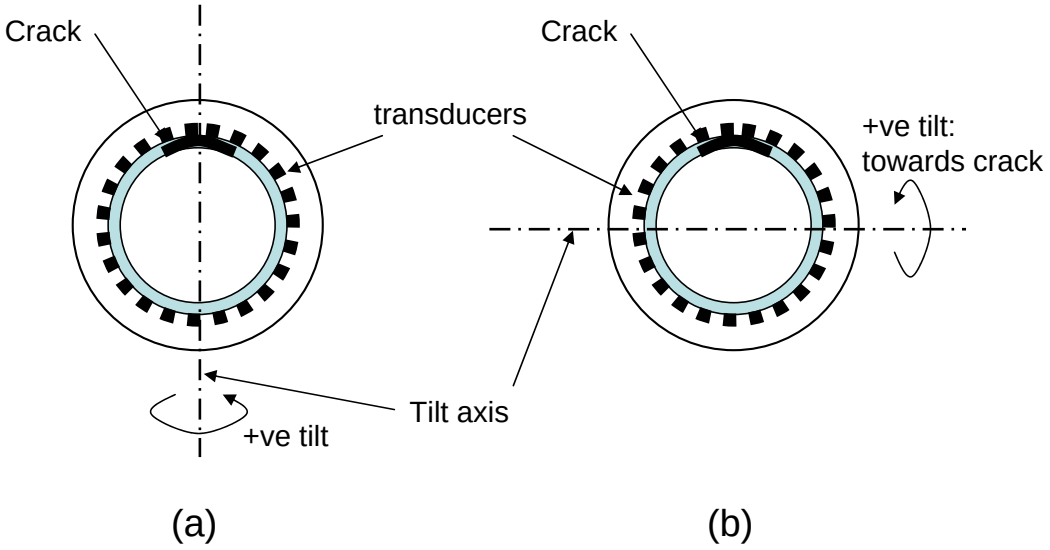

Figure 5.13: *Titling of the transducer ring with a defect present, the rotational direction indicates a positive tilt angle; (a) tilt axis through the defect location; (b) tilt towards the defect.*

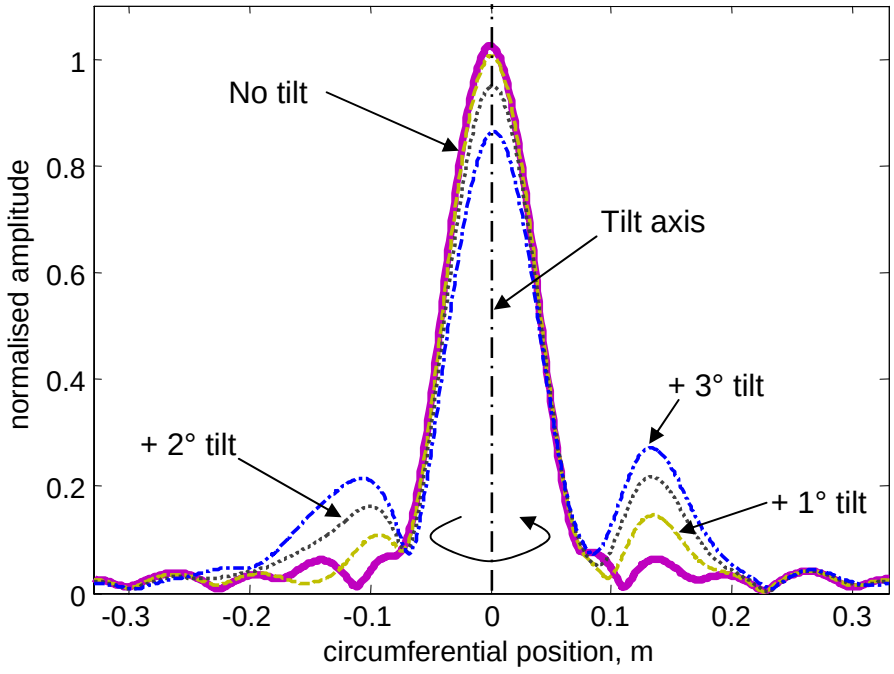

Figure 5.14: *Circumferential image profiles through crack location for tilting of the transducer ring on an axis through the defect as shown in figure 5.13a.*

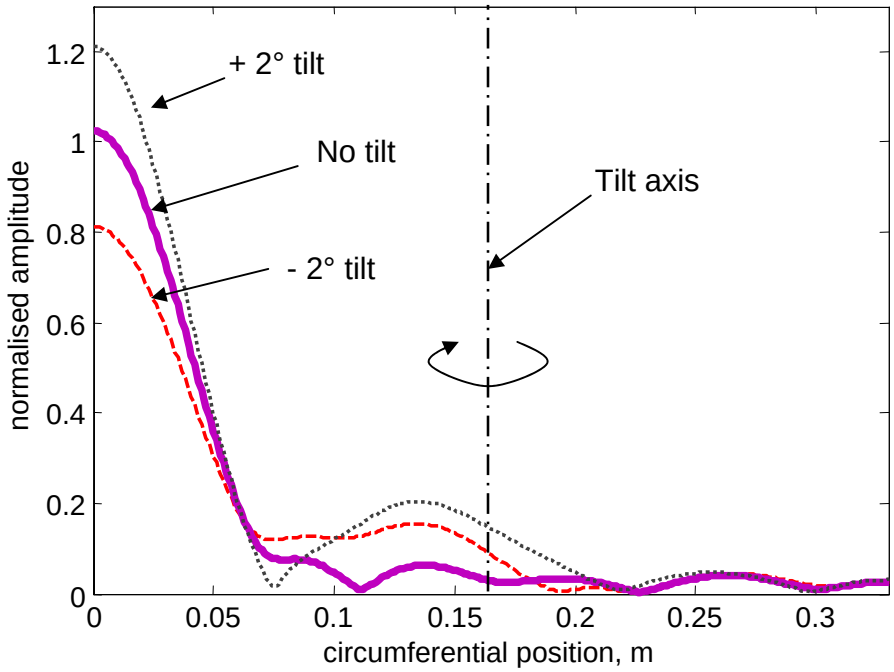

Figure 5.15: *Circumferential image profiles through crack location for tilting of the transducer ring towards and away from the defect as shown in figure 5.13b.*

It should be noted that the above case of tilting of the transducer ring on an 8 inch pipe with a crack at 1.2m, with excitation centred at 50 kHz is only one scenario and different size pipes, different axial defect locations or inspection frequencies would produce varying results. Notably, the effects of axial misplacement become more severe with increasing inspection frequency 5.6. Nevertheless, the results from the case studied show that tilting of the transducer ring affects the image response more severely than the random errors which were tested in the previous sections of this chapter.

5.4 Robustness to incorrect input parameters

5.4.1 Effect of incorrect velocity

If the phase velocity used for image reconstruction is different from the actual phase velocity of the material under inspection then this will affect the ability to coherently

sum all of the backscattered information in the correct defect location. If there are no defects present in the pipe then the end wall reflection will be purely T(0,1) which travels with an axial phase velocity equal to the bulk shear velocity c_S. The effect of image reconstruction using an incorrect phase velocity will be that the end wall image will appear at the wrong axial location.

Defects which are not axisymmetric, such as the cracks modelled with finite element simulations in the previous chapter, will backscatter to higher circumferential order modes. The axial phase velocities of these higher order modes, assuming the plate-like behaviour of the pipe as discussed in section 2.3.4, can be evaluated using (2.32). The error in bulk shear velocity c_S used for image reconstruction will affect the axial phase velocity $c_{z,n}$ of each mode differently. Therefore, the backprojection of each mode will not necessarily create coherent summation at the correct axial defect location.

The phase velocity of the T(0,1) pipe mode in the finite element model was found previously to be 3330 ms^{-1}, showing a 0.8% error from the expected 3360 ms^{-1}. This velocity was extracted from a pipe finite element model with no defects. A T(0,1) probing wave was excited into the model and this was reflected by the pipe end. The group velocity was found by dividing the total distance travelled by the time taken. For the nondispersive T(0,1) mode, the phase velocity is equal to the group velocity [59]. This phase velocity was used for processing the finite element data in the previous chapter. Note that the higher order modes are likely to have a greater velocity error since they propagate at angles across the finite element mesh [91].

Here, the data from the finite element case of a through-thickness crack of 60^o circumferential extent (1.7λ at 50 kHz) at 1.2m from the transducer ring in an 8 inch pipe was processed using CSM with deliberately incorrect bulk shear velocities. The bulk shear velocities used for image reconstruction ranged from 3100 ms^{-1} to 3400 ms^{-1} in steps of 10 ms^{-1}. The axial position error of the peak defect response was recorded along with the peak defect image amplitude and FWHM at the peak axial location.

Figure 5.16 shows the axial position error of the defect image peak against the shear phase velocity used for image reconstruction. Lower processing velocities move the defect image peak closer to the transducer ring and higher processing velocities move the peak further from the transducers in a roughly linear fashion, as expected. The defect image peak occurs at the correct axial location of 1.2m for a reconstruction phase velocity of 3220 ms^{-1}. This is slightly less than the axial phase velocity of 3230 ms^{-1} found from the T(0,1) reflection from an end wall only finite element model. This is because the defect response here is formed for the summation of all of the backscattered modes. The higher order modes have slightly slower velocities in the finite element model since they propagate across different directions across the finite element mesh. These effects agree with those observed by Drozdz [91] in his detailed study of such finite element phenomena. This means that the contributions from higher order backscattered modes appear slightly behind the actual defect location which has the effect of moving the defect image peak slightly farther from the array than the actual defect axial location. Therefore, a slightly slower processing phase velocity of 3220 ms^{-1} puts the defect peak at the exact axial defect location in the image.

The peak image amplitude normalised to that of the input signal is plotted against the shear phase velocity used for image reconstruction in figure 5.17. The maximum defect image amplitude occurs for a processing shear velocity of $3230ms^{-1}$ which is the T(0,1) finite element phase velocity used for the finite element data image reconstruction in the previous chapter. Processing with an incorrect shear phase velocity has the effect of decreasing the defect amplitude response.

The FWHM at the peak defect axial location is plotted against the shear phase velocity used for image reconstruction in figure 5.18. The smallest FWHM occurs for a processing shear velocity of $3230ms^{-1}$ which is the T(0,1) finite element phase velocity. Processing with an incorrect shear phase velocity shows the defect peak at an incorrect axial location with an increased FWHM and reduced amplitude. These detrimental effects will worsen with increasing axial defect location since the propagation distances, and hence errors, are increased.

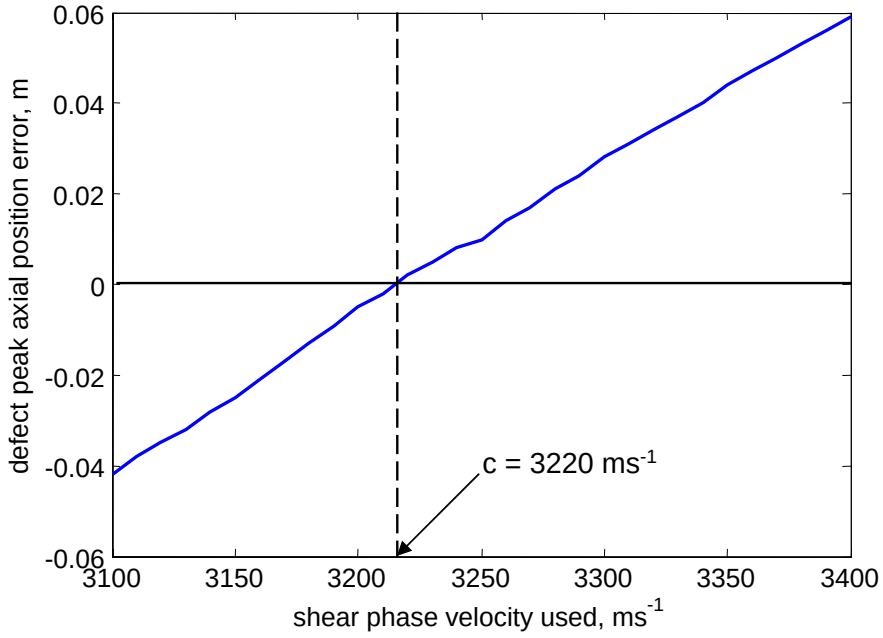

Figure 5.16: *Axial position error of the image defect peak against shear phase velocity used for image reconstruction.*

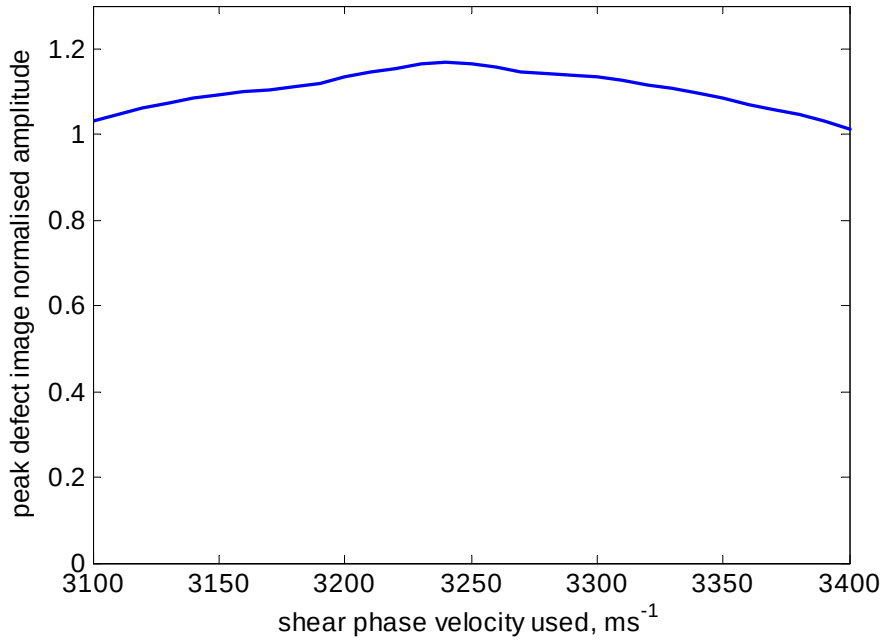

Figure 5.17: *Normalised defect image amplitude against shear phase velocity used for image reconstruction.*

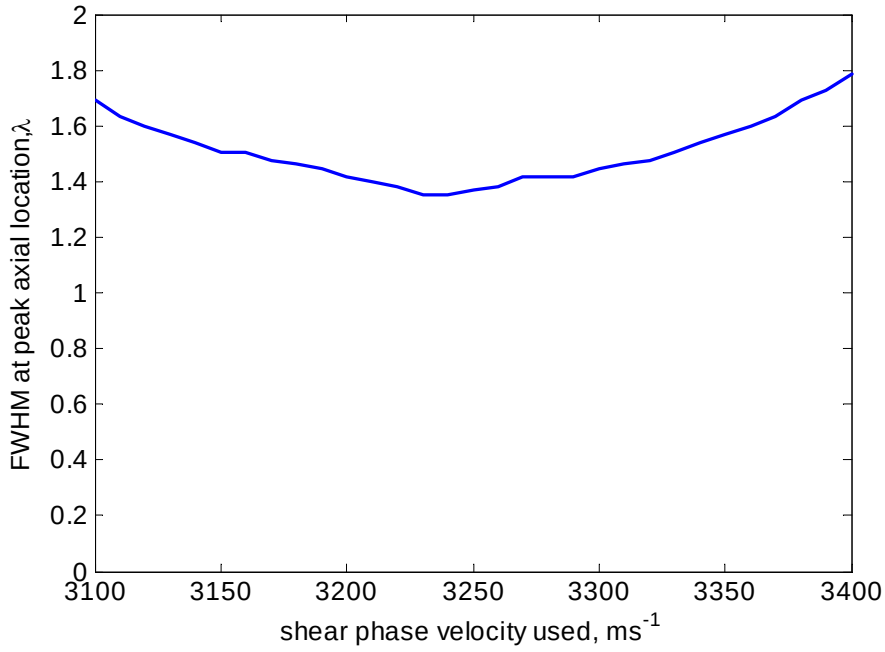

Figure 5.18: *FWHM against shear phase velocity used for image reconstruction.*

5.4.2 Effect of incorrect pipe dimensions

In addition to shear phase velocity, the other input parameter for the pipe imaging algorithm is the pipe radius. The effect of processing with an incorrect pipe radius was first investigated using the synthetic data model defined in section 4.3. Data was synthesised for a range of axial defect locations using a maximum backscatter angle $\beta_{max} = 35^o$ with a temporal bandwidth of 40 to 60 kHz. The pipe radius used for data synthesis was $r = 0.10545\ m$ which is the central radius of an 8 inch schedule 40 pipe. Each synthetic data set was then processed with CSM using pipe radii ranging from $0.95r$ to $1.05r$. The inner and outer radii of the 8 inch pipe are 101.4 mm and 109.5 mm. These correspond to $0.96r$ $1.04r$ respectively.

The peak image amplitude at the axial defect location is plotted against axial defect position for all radii processed in figure 5.19. If the synthetic data is processed using the correct pipe radius then the defect image amplitude is constant with axial position, as was found in the previous chapter. If the data is processed using an incorrect pipe radius then the amplitude decreases with increasing axial defect position. The decrease in defect response amplitude is worse for larger radius errors

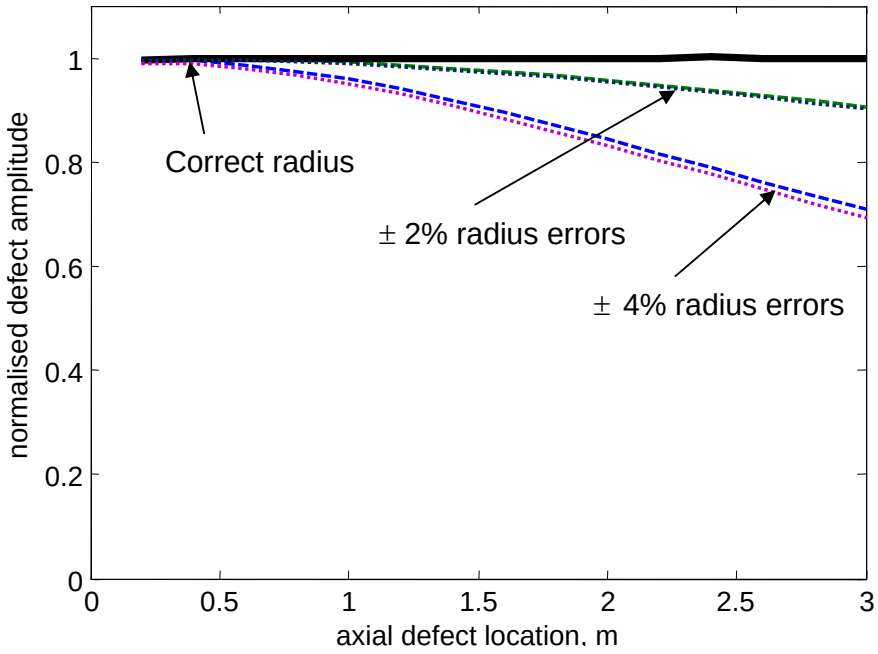

Figure 5.19: *Defect image amplitude against axial defect position processed with different pipe radii.*

but is comparable for positive or negative radius errors.

Figure 5.20 shows the FWHM at the defect axial position plotted against axial defect position for all radii processed. Once again, the FWHM is constant with axial defect position if the correct radius is used for image reconstruction. If the data are processed using an incorrect radius then the FWHM increases with increasing axial defect position. Larger errors are observed for larger radius errors.

The effects of processing with an incorrect pipe radius can be explained by the subsequent errors in axial phase velocities used for image reconstruction (2.32). If the wrong radius is used then the calculated axial phase velocities which are used to backproject each received mode are affected in different ways. The error in the axial phase velocity caused by an incorrect pipe radius is worse for higher order modes. These phase velocity errors cause imperfect coherent summation of backprojected modes at the defect location. The effect of this is that the defect response will decrease in amplitude and the FWHM will increase. The diminished performance will worsen with increased axial defect position.

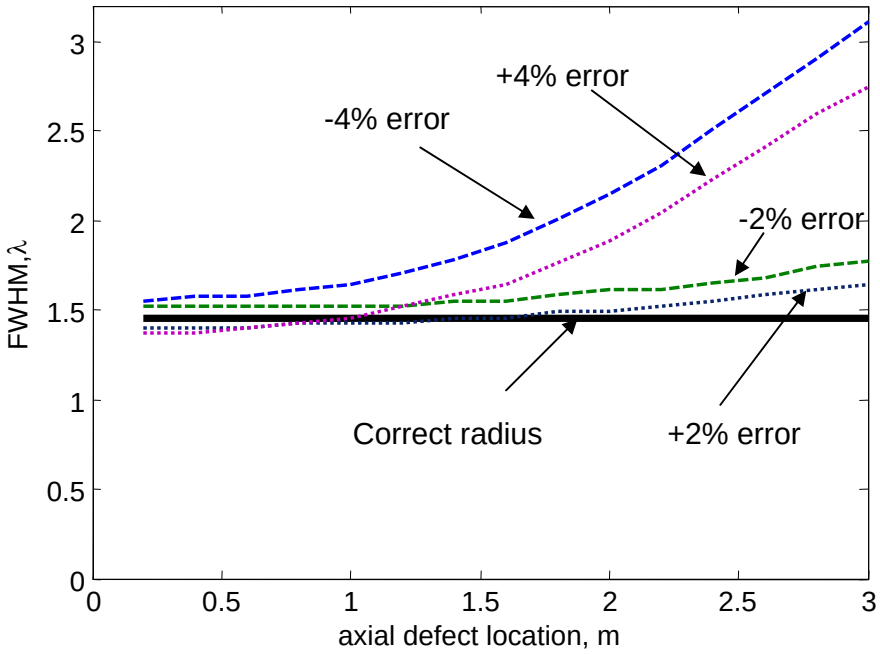

Figure 5.20: *FWHM against axial defect position processed with different pipe radii.*

In order to validate the errors observed using synthetic data, finite element data was processed with incorrect pipe radii. The model case was a through-thickness crack of 60^o circumferential extent in an 8 inch pipe at 1.2m. The defect image amplitude is plotted against the pipe radius used for image reconstruction in figure 5.21. The peak image defect amplitude occurs when processing using the correct central pipe radius. The defect image FWHM is plotted against the pipe radius used for image reconstruction in figure 5.22. The smallest FWHM also occurs when processing with the correct central pipe radius. Processing with a radius equal to the pipe internal radius ($0.96r$) reduces the defect image amplitude by 4.3% and increases the FWHM by 21%. Processing with a radius equal to the external radius of the pipe ($1.04r$) reduces the defect image amplitude by 14% and increases the FWHM by 23%.

It should also be noted that the image reconstruction algorithm is not dependent on the pipe wall thickness and this is not a required input parameter. However, the inspection frequency must be lower than the cutoff frequency for the T(0,2) mode. Also, the pipe wall thickness will need to be known in order to estimate the defect depth using the analysis of section 4.4.1.

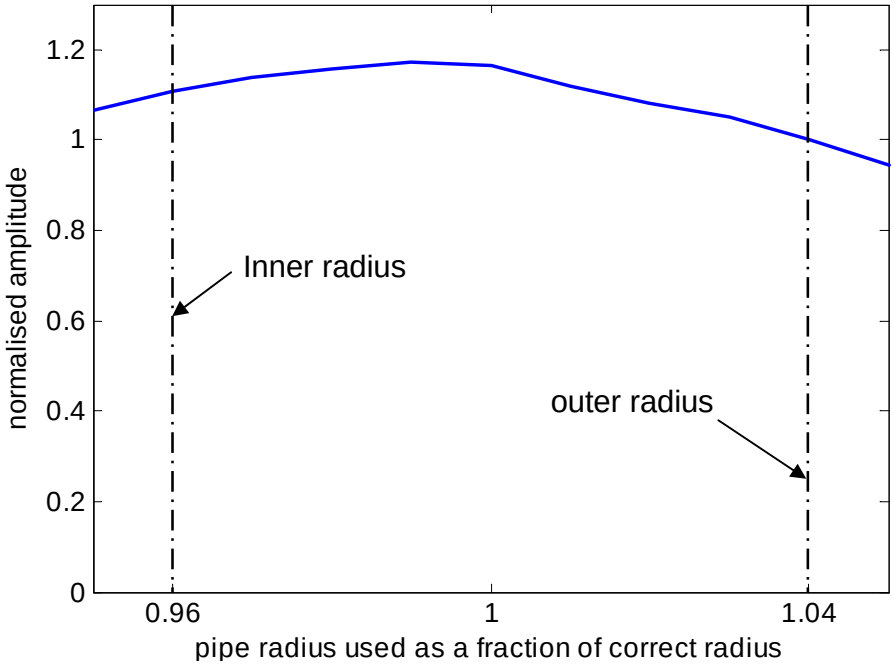

Figure 5.21: *Defect image amplitude for 60^o through-thickness finite element crack against pipe radius used for image reconstruction.*

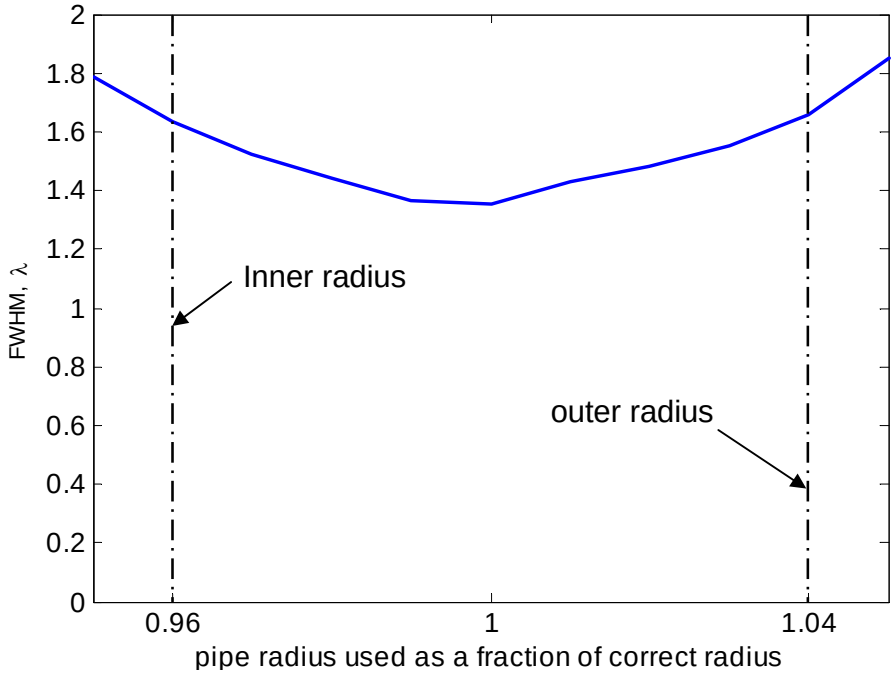

Figure 5.22: *Defect image FWHM for 60^o through-thickness finite element crack against pipe radius used for image reconstruction.*

5.5 Robustness conclusions

In this chapter, the robustness of the CSM pipe imaging system has been investigated. The method was to intentionally corrupt finite element data and then to process the resulting corrupted data. The errors caused by random setup errors, such as coupling variation and axial misplacement of the transducers in the transducer ring, were evaluated. For all types of random error, the defect image amplitude was decreased and the FWHM was increased for increasingly severe errors. However, the system was found to be very robust against random setup errors even those larger than those likely to be encountered in the real system.

The imaging response to systematic errors was also investigated. Tilting of the transducer ring on the pipe caused reasonably severe variations of the order of $\pm 20\%$ in the defect image amplitude and FWHM. The effect of processing data with incorrect phase velocities was that the image defect amplitude was decreased and the FWHM increased. The decrease in performance was found to worsen with increasing axial defect location from the transducers, for a given level of velocity error.

The system has shown to be extremely robust against random errors but less robust against systematic errors from testing with finite element data. It is important to note that entering an incorrect pipe size or bulk shear velocity of the material could be avoided with vigilance on behalf of the operator. The tilting of the transducer ring could also be reduced by careful operator setup.

Chapter 6

Laboratory Experiments with Circumferential Slots

The pipe imaging system which utilises the Common Source Method (CSM) for image reconstruction was thoroughly tested using data from finite element simulations in chapter 4. It was found that the circumferential extent and depth of cracks could be estimated from the Full Width at Half Maximum (FWHM) and amplitude of the defect image. Reliable crack sizing was possible for cracks of circumferential extent larger than $1.5\lambda_S$, where λ_S is the wavelength of the probing T(0,1) guided wave mode at the frequency of inspection. The imaging response was found to be independent of axial defect location, pipe radius and inspection frequency, provided the amplitude is scaled by the excitation amplitude and the FWHM is scaled by the probing wavelength λ_S.

In this chapter, the results from the extensive finite element studies will be validated with laboratory experiments on 8 inch schedule 40 mild steel pipe. The defects will be circumferentially milled slots of both half-depth and through-wall thickness. The experimental data will be processed using CSM and the imaging results will be compared to the finite element predictions of chapter 4. The coupling variation will also be evaluated and compared to the synthetic analysis of the previous chapter.

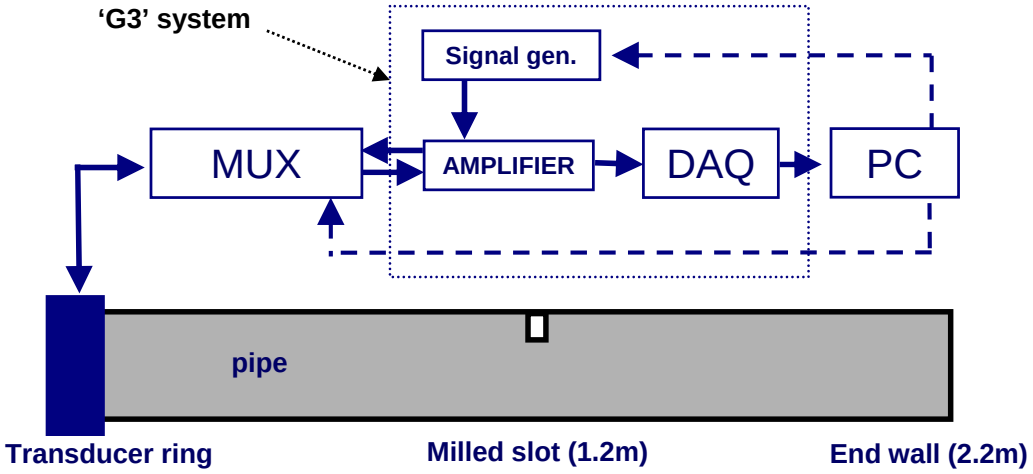

Figure 6.1: *Experimental setup.*

6.1 Experimental setup

The experimental apparatus is shown in figure 6.1. The hardware consists of 4 distinct units; the transducer ring, a multiplexer box, a personal computer and a Guided Ultrasonics Limited [24] G3 unit. Figure 6.2 shows a photograph of the transducer ring, clamped to the end of a pipe sample, the multiplexer unit and the portable PC. The G3 unit contains an onboard signal generator to generate the required input toneburst, a power amplifier for excitation and a receiver amplifier for reception. The G3 unit and the multiplexer unit are controlled via the PC so that data acquisition is automatic.

The transducer ring used was an 8 inch inflatable ring manufactured by Guided Ultrasonics Limited. The transducer ring comprises two separate rows of 24 dry-coupled piezoelectric shear transducers. The two rows of transducers are required for directionality control. The transducers are forced onto the pipe sample with an inflatable bladder which is clamped around the outside of the pipe circumference. The transducers make a point contact with the pipe surface. The standard commercial equipment has transducers that are grouped into segments and hence no external multiplexer stage is necessary for normal testing. The ring used here was modified so that each of the 48 transducer elements is individually wired so that each

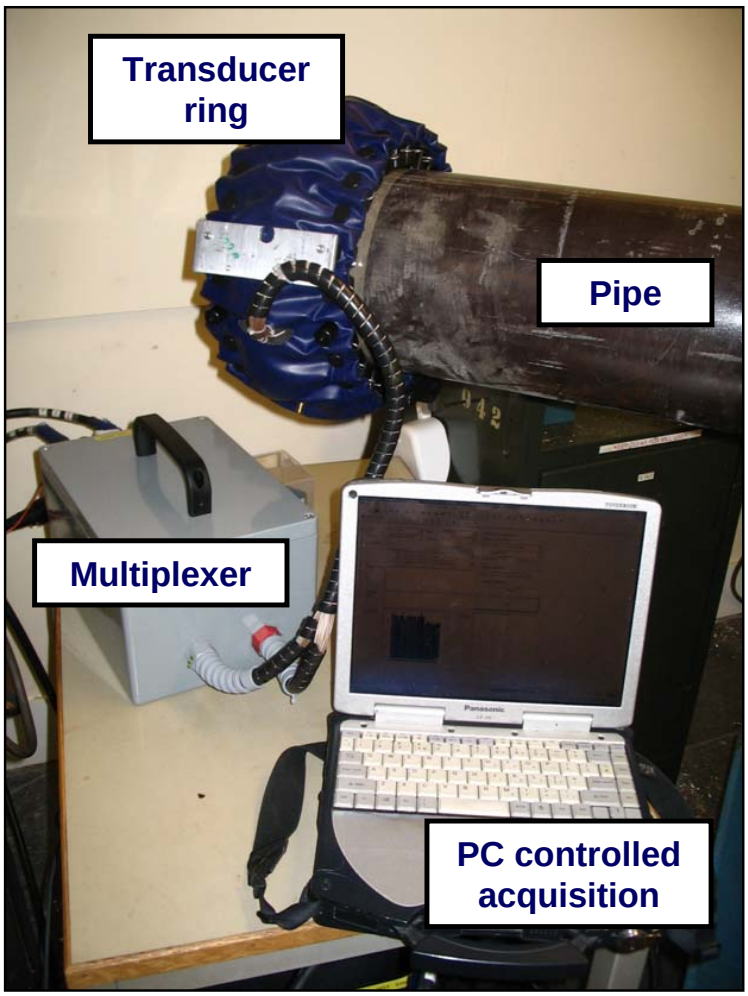

Figure 6.2: *Photograph of experimental setup.*

transd+ucer can be individually addressed. By using an external multiplexer stage, the hardware setup is capable of recording the full data set (FMC) as required for TFM. However, both TFM and SAFT were shown to be unsuitable for pipe imaging in section 4.2 and hence will not be evaluated experimentally here.

Two 8 inch schedule 40 mild steel pipe samples were used and circumferential slots were made in the pipe samples using a milling machine with a 3mm cutter. The pipe samples were both 2.2m long. This length was chosen due to spatial constraints around the milling machine. The first pipe sample had through-thickness slots milled into it and the second pipe sample had half wall-thickness slots milled into it. The first experiment on each pipe sample was with no milled features present. The

transducer ring was then left clamped to the pipe while defects were milled at 1.2m from the transducer ring. The pipe samples were rotated about the pipe axis and circumferential slots were cut. After each new larger slot had been cut, data was acquired using the experimental hardware. The slot circumferential extent was then further increased up to a maximum of 90^o (166 mm) circumferential extent for both the half-depth and the through-thickness pipe samples.

The ring was clamped onto the pipe test samples so that one row of transducer elements was as near to the end of the pipe length as possible. By clamping the transducer ring in this location, there is no need for directionality control since the probing wave can only propagate in one direction. Therefore, only the row of transducers located at the pipe end were used. This means that $24^2 = 576$ time traces were recorded. The data required for CSM were created by summing time traces from the full data set, thus creating 24 time traces for each experimental defect case. This has the effect of synthetically firing all of the 24 transducer elements simultaneously.

6.2 Experimental results

6.2.1 Experiments on clean pipe

Prior to milling any slots in the pipe samples, data was acquired for the featureless pipe samples. The excitation was an 8 cycle Hanning-windowed toneburst centred at 50 kHz. The reflections for the featureless pipe around the circumference should be of similar amplitude since the pipe end is axisymmetric. The variation in reflection amplitudes gives an indication of the variation in coupling coefficients around the pipe circumference. The amplitudes of the reflections at 50 kHz from the pipe end wall for the CSM data set are shown in figure 6.3. The reflected amplitudes vary between around 0.5 and 1.5. This is comparable to the synthetic coupling study with a coupling standard deviation of 0.2 which was shown in figure 5.2a. Coupling variations of this severity gave a defect amplitude standard deviation of

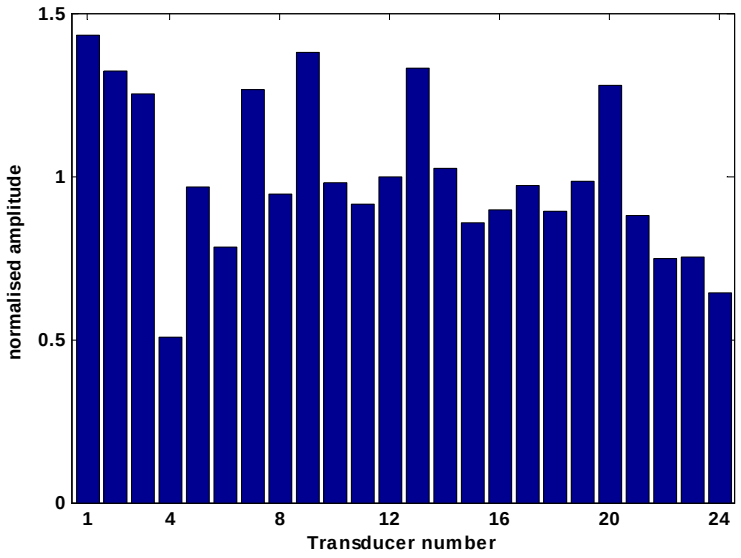

Figure 6.3: *Experimental reflection amplitudes at 50 kHz normalised to the mean reflection amplitude from the pipe end at the different transducers upon firing all transducers.*

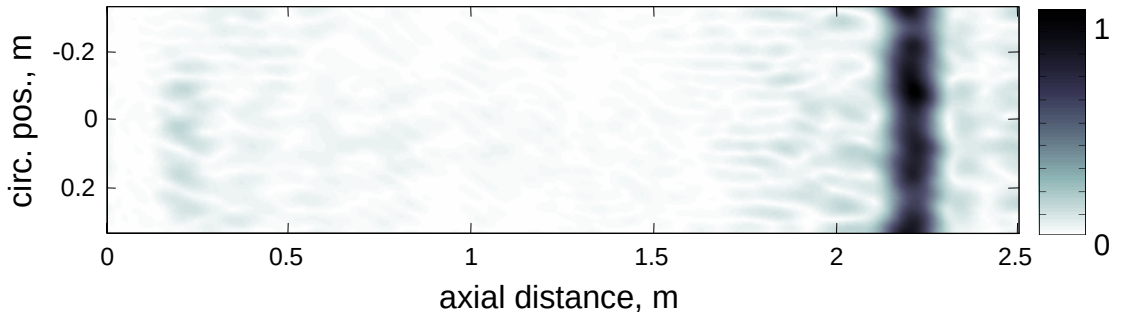

Figure 6.4: *Experimental CSM image of pipe end wall at 2.2m.*

0.1, a FWHM standard deviation of 0.02λ and a peak image noise value of 0.13 for the synthetically corrupted finite element case study of section 5.1. Note that no attempt to correct for these coupling variations will be done here though this is done in practice by the commercial Guided Ultrasonics Limited system.

The reconstructed CSM image for the featureless pipe is shown in figure 6.4. The CSM image shows the end wall in the correct axial location with no other major features in the image. The peak noise in the featureless region up to 1.7m was 0.13 which is the same as the finite element study with synthetic coupling errors with a standard deviation of 0.2.

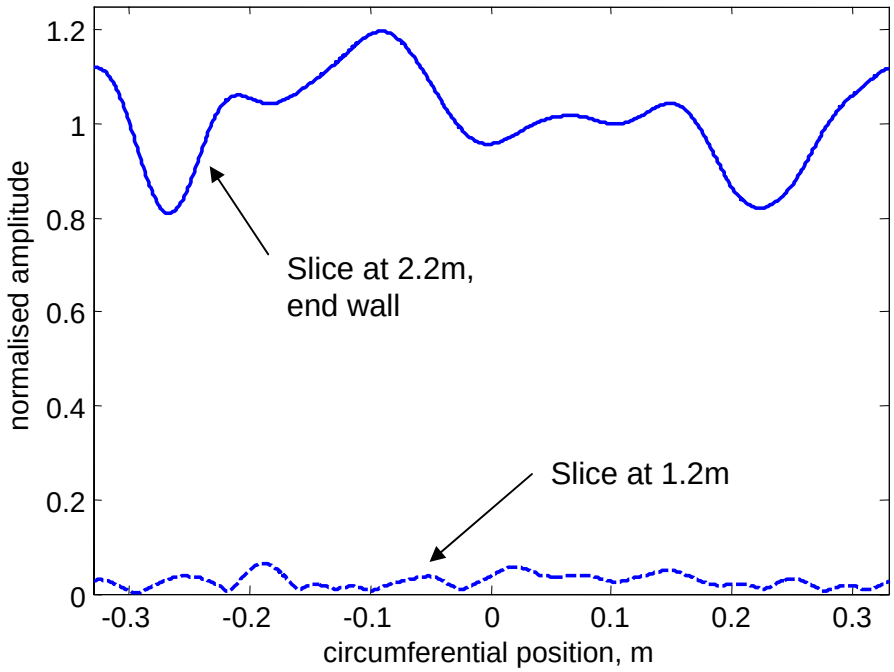

Figure 6.5: *Experimental CSM circumferential image profile through pipe end axial location for featureless pipe sample.*

The circumferential image profile through the CSM image (figure 6.4) at the pipe end axial location is shown in figure 6.5. The circumferential profile at the featureless axial location of 1.2m is also shown. The amplitude scale has been normalised to the mean end wall amplitude. The pipe end wall image normalised amplitude varies between 0.8 to 1.2. This variation is most likely due to the observed coupling variation of the transducers around the pipe circumference (figure 6.3).

Figure 6.6 shows an axial image slice through the end wall only image of figure 6.4. The axial slice was taken at a circumferential position of 0, i.e. through the centre of figure 6.4. The largest axial sidelobe of the end wall image is 0.19 (-14.4 dB). The end wall sidelobe of the finite element image of an end wall at 1.2m shown in figure 4.4 was -17 dB.

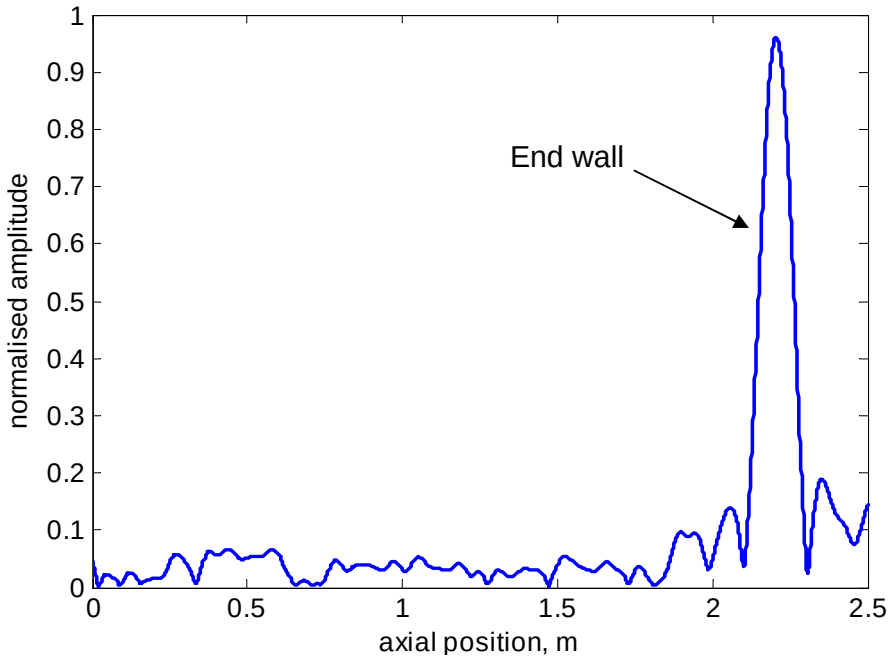

Figure 6.6: *Experimental CSM axial image profile for featureless pipe sample, end wall at 2.2m.*

6.2.2 Experiments with milled circumferential slots at 50 kHz

The data from all the slot experiments were imaged with CSM using a temporal bandwidth of 40 to 60 kHz. The defect amplitude and the FWHM were measured directly from the resulting images. An example image of the 20^o through-thick slot case is shown in figure 6.7. The circumferential image slices through the defect and end wall axial locations are shown in figure 6.8. The defect image appears at the correct axial and circumferential position as was observed in the finite element image of figure 4.16 and its circumferential profile (figure 4.17).

The defect image in figure 6.7 has an amplitude of 0.68. The peak noise value in the image is 0.08. Therefore, the signal to noise ratio (SNR) in this particular focused image is 18.5 dB. The unfocused trace is shown in figure 6.9. The unfocused defect amplitude is 0.11 and the peak noise value in the T(0,1) trace is 0.04. Therefore the SNR the unfocused system is 9.5 dB, meaning that there is a 9 dB improvement in the practical SNR with the focused system.

The defect image amplitudes are plotted against the circumferential extent of the slot

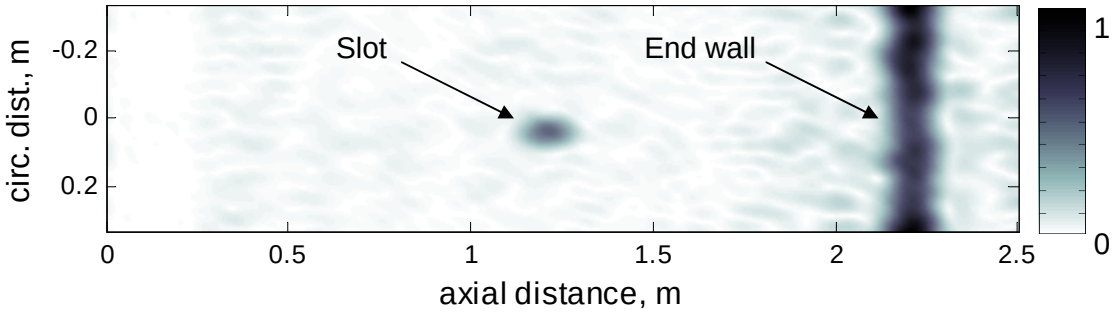

Figure 6.7: *CSM experimental image for the case of a through-thickness slot of* 20^o *circumferential extent at 1.2m.*

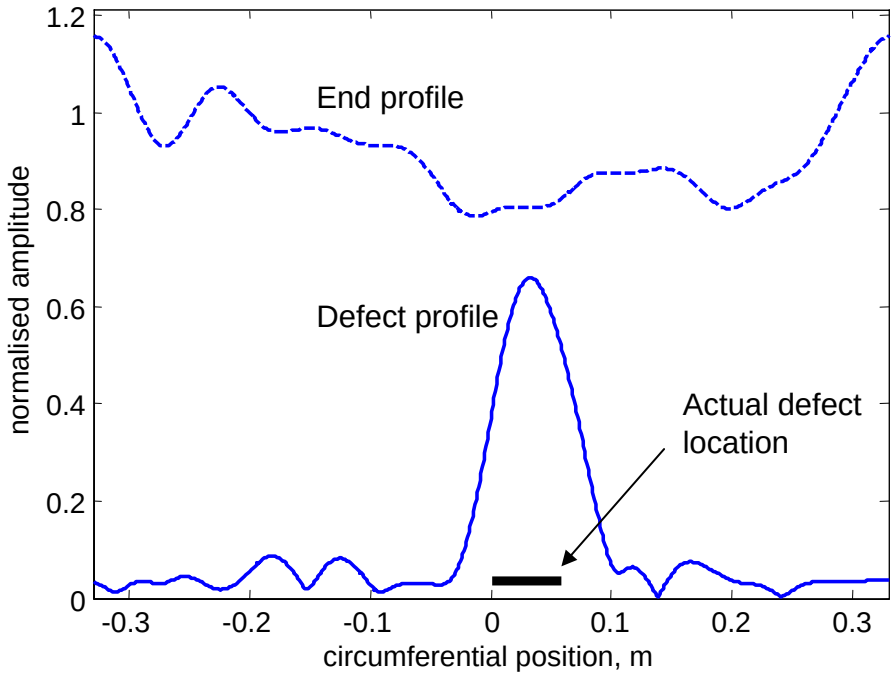

Figure 6.8: *Circumferential image slices at the defect axial location (solid line) and the end wall location (dashed line) for the case of a through-thickness slot of* 20^o *circumferential extent.*

in figure 6.10 for the through-thickness experiment and the finite element predictions of section 4.4 are also shown. The experimental amplitudes are scaled to the end wall amplitude of the featureless pipe experiment of the previous section. The theoretical and experimental T(0,1) slot reflection amplitudes are also shown. It can be seen that the experimental amplitudes are slightly larger than the predictions for all experimental slot lengths. This is likely to be due to 'bedding in' of the transducers

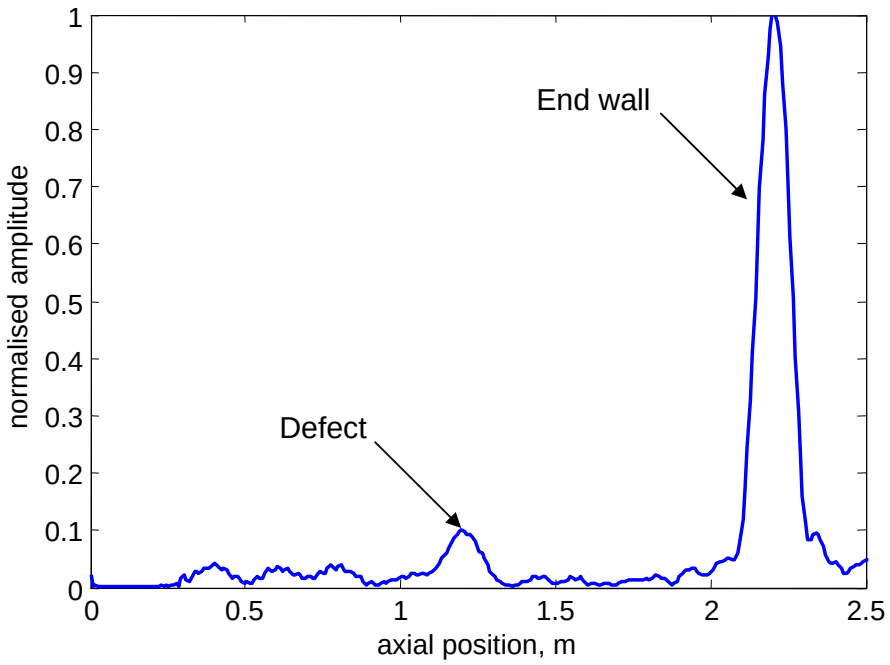

Figure 6.9: *Unfocused trace for 20 degree through-thickness crack at 1.2m, end wall at 2.2m.*

after the first featureless pipe experiment which increases the coupling of energy into the pipe and results in slightly higher image amplitudes for later experiments.

The defect image amplitudes for the half-depth slot experiments are shown in figure 6.11. The experimental amplitudes agree extremely well with the finite element predictions of section 4.4 which are also plotted on the figure for comparison with the exception of the largest slot where the image amplitude of the experiment was slightly higher than the FE prediction.

The gain in amplitude of using the focused system over the unfocused system (T(0,1) reception only) is shown in figure 6.12. The maximum gain achieved was 17 dB for the through-thickness slot experiment and was 18.4 dB for the half-depth experiment. The largest gains in amplitude are achieved for slot lengths of around 0.5 to 1λ which is where the focused amplitude is near the maximum attainable but the T(0,1) reflection is still small. Note that all of the gains will reduce to unity for slot lengths equal to the circumference of the pipe (10.6λ for this 8 inch pipe at 50 kHz). The experimental gains achieved were slightly lower than the gains observed from

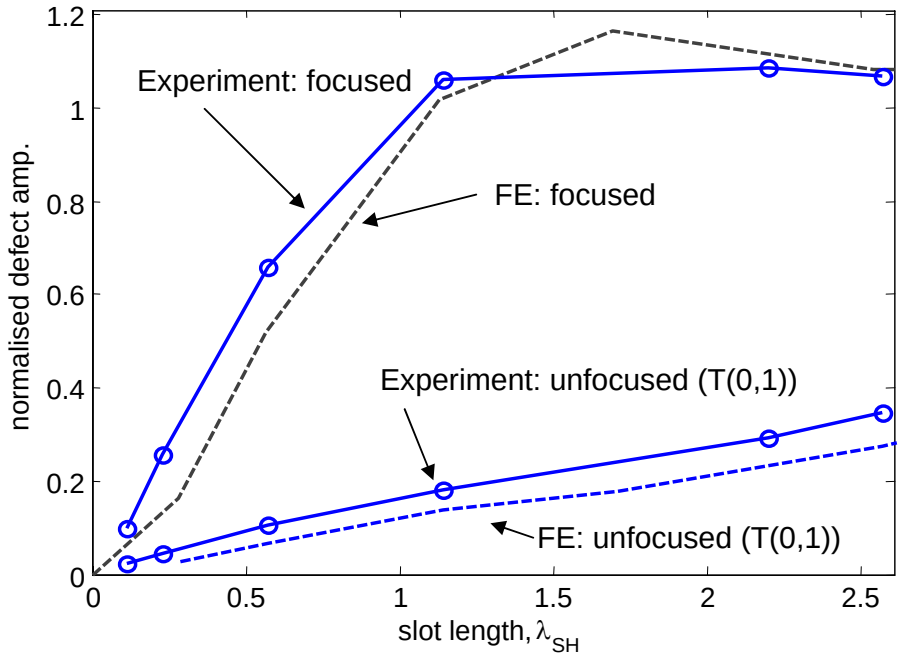

Figure 6.10: *Through-thickness slot image amplitudes and unfocused (T(0,1)) reflection amplitudes; solid lines with circles: Experiment amplitudes; dashed lines: Predicted amplitudes.*

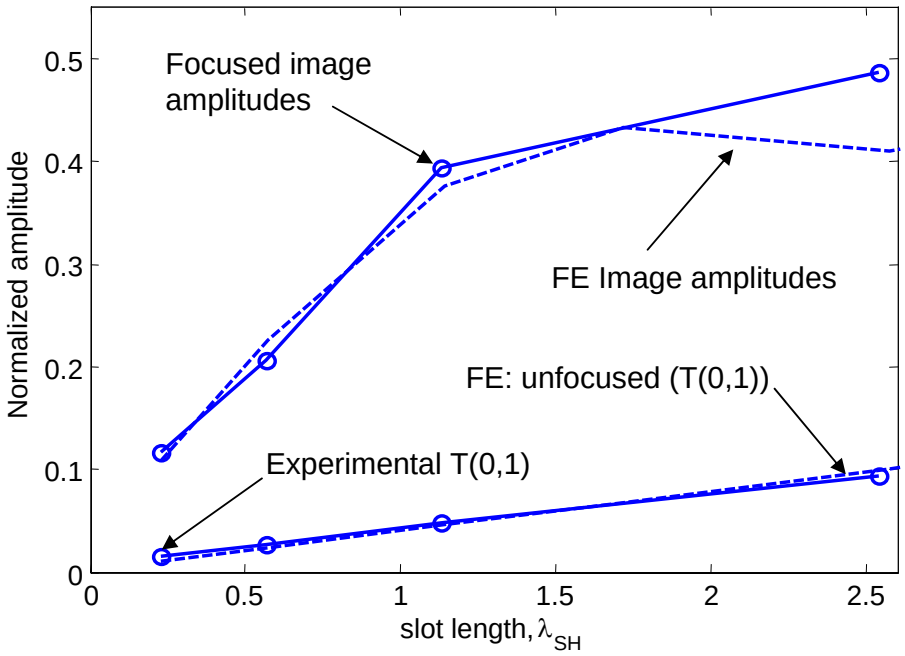

Figure 6.11: *Half-depth slot image amplitudes and unfocused (T(0,1)) reflection amplitudes; solid line with circles: Focused experimental amplitudes; dotted line with circles: Experimental unfocused amplitudes; dashed line: slot finite element predictions.*

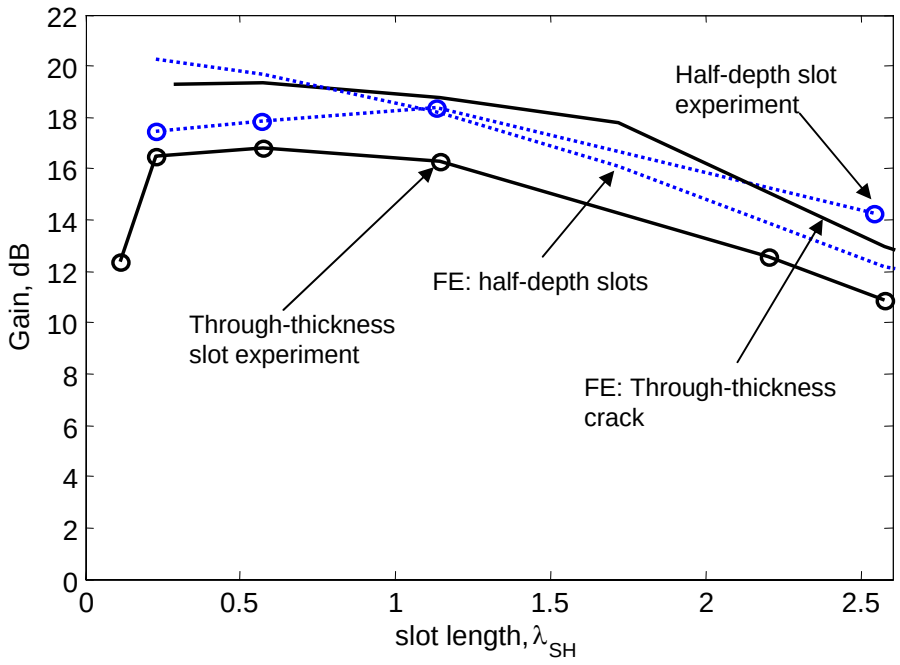

Figure 6.12: *Gain in amplitude of focused system over unfocussed system; solid line with circles: experiment with through-thickness slots; dashed line with circles: experiment with half-depth slots; dotted line: finite element predictions for through-thickness cracks.*

finite element data, which are also shown in the figure.

The FWHM of the defect images are plotted against the circumferential extent of the slots in figure 6.13 for both the through-thickness and half-depth experiments. The experimental FWHM compare well with those of the through-thick crack finite element study of section 4.4 and the half-depth slot finite element study of section 4.4.2. In fact, for small through-thickness slots, the experiments produced a FWHM which was smaller than the finite element predictions. The variations in FWHM from the finite element predictions are most likely to be due to the coupling variations around the transducer ring. The experimental FWHM curves exhibit the two separate regimes that were observed in the finite element studies of chapter 4. The first regime, for slot lengths below around 1.5λ, has a constant FWHM of around 1.3λ. In this region, estimation of the circumferential extent of the slot is not possible. The second regime, for slot lengths above 1.5λ have FWHM which are reliable estimates of the actual physical slot lengths.

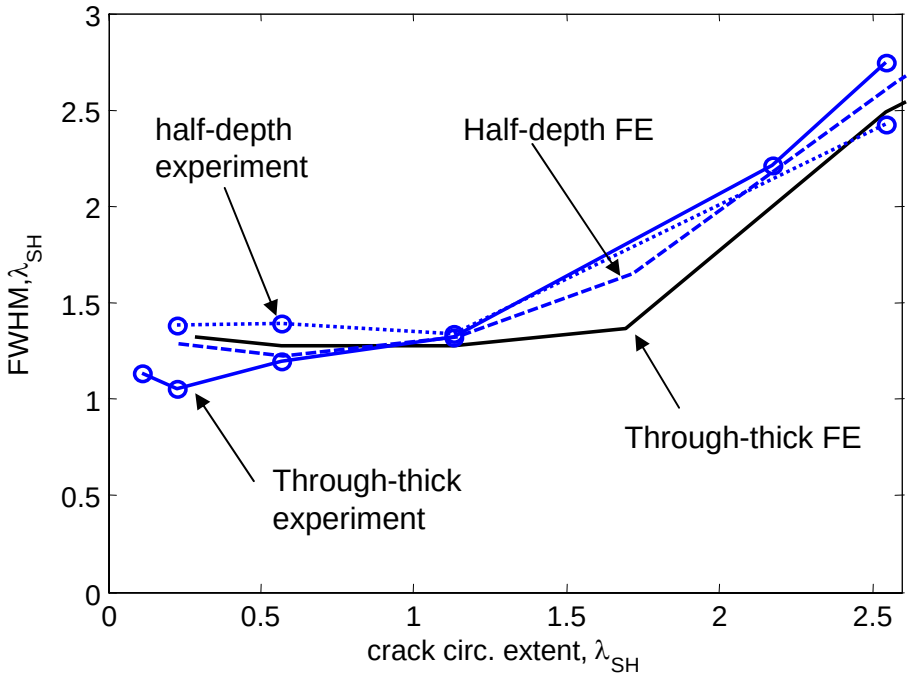

Figure 6.13: *FWHM measured from the experimental CSM images. solid line with circles: through-thickness slots; dashed line with circles: half-depth slots; dotted line: through-thick FE predictions.*

6.2.3 Through-thickness experiments at different inspection frequencies

In addition to the data recorded from excitation centred at 50 kHz, which were processed in the previous section, data was also recorded with excitation centred at 30 kHz for the through-thickness slot cases. The excitation signal was an 8 cycle Hanning-windowed toneburst centred at 30 kHz. The resulting experimental data were processed with CSM employing a temporal bandwidth of 20 to 40 kHz. The data are processed raw and hence are already frequency domain windowed due to the frequency spectrum of the excitation toneburst.

The defect image amplitude is plotted against the slot length expressed in wavelengths of the probing signal in figure 6.14. The defect image amplitudes from the 50 kHz experiments and the 50 kHz finite element study are also shown for comparison. The imaging response to through-thickness cracks was found to be independent

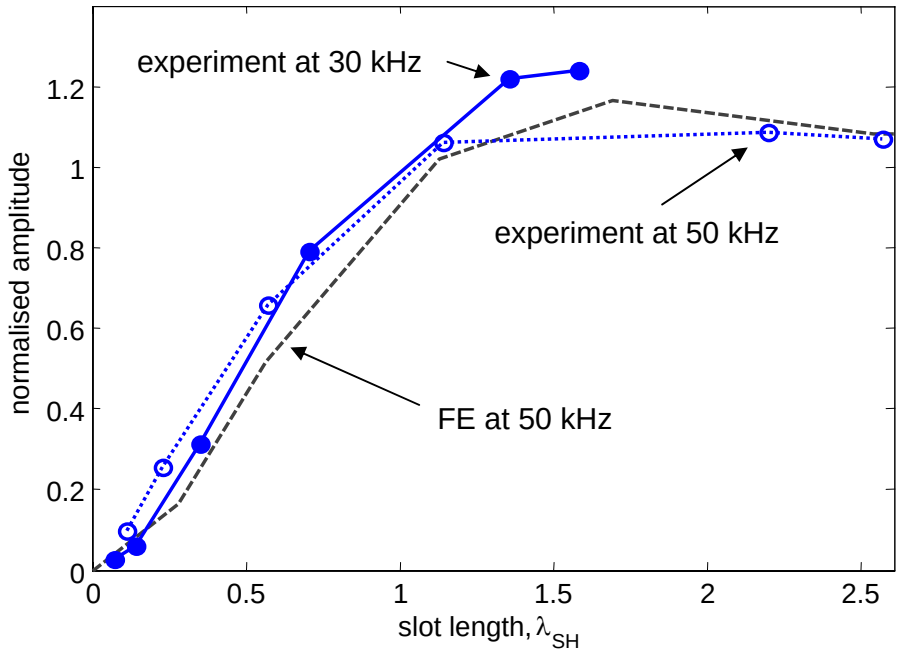

Figure 6.14: *Defect image amplitude against through-thickness slot length; solid line with circles: experiment with 30 kHz excitation; dotted line with circles: experiment with 50 kHz excitation; dashed line: finite element predictions with 50 kHz excitation.*

of inspection frequency for the finite element study of section 4.5.2. Here, the experimental curves for the different inspection frequencies both agree well with the finite element predictions, exhibiting a peak amplitude for a slot length of around 1.5λ. This means that the through-thickness defect image amplitude response is independent of inspection frequency if the defect circumferential extent is expressed in wavelengths of the probing signal. This agrees with the finite element findings of section 4.5.2.

Figure 6.15 shows the defect image FWHM for the through-thickness slot experiment with excitation centred at 30 kHz plotted against the slot length expressed in wavelengths of the probing signal. It was shown in section 4.5.2 that the defect FWHM was independent of inspection frequency for finite element cracks. The experimental FWHM from the 30 kHz experiments agree very well with the experimental and finite element predictions at 50 kHz. This means that the experimental defect FWHM are independent of inspection frequency, agreeing with the finite element predictions of section 4.5.2. The discrepancy for very small slot lengths occurs

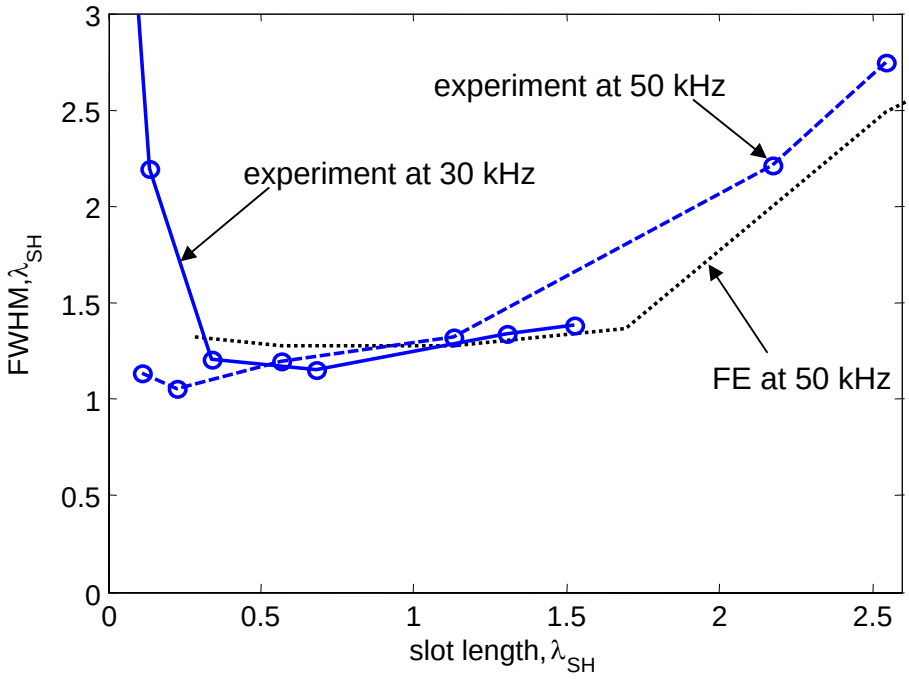

Figure 6.15: *Defect image FWHM against through-thickness slot length; solid line with circles: experiment with 30 kHz excitation; dashed line with circles: experiment with 50 kHz excitation; dotted line: finite element predictions with 50 kHz excitation.*

because the defect image amplitude are comparable to the image noise levels, rendering the FWHM unreliable.

6.3 Experimental conclusions

Laboratory experiments were carried out on an 8 inch schedule 40 mild steel pipe. The defects were milled circumferential slots of 3mm width. Two pipe samples were used; one for through-thickness slots and the other for half-depth slots (4.1 mm deep). The hardware employed for data capture was based on modified commercial equipment manufactured by Guided Ultrasonics Limited [24].

Imaging of a featureless pipe gave an estimate of the experimental coupling variations of the transducer ring. The peak noise (peak pixel value in the image) in the featureless pipe experimental image was comparable with the peak noise observed in

the previous chapter when synthetically corrupting finite element data with similar levels of coupling variation. The system was shown to be robust against these levels of coupling variation with finite element data in the previous chapter and this has now also been proved experimentally.

The experimental defect image amplitudes and FWHM showed excellent agreement with the finite element predictions of chapter 4 for both through-thickness and half-depth slots. Two regimes were observed in the experimental imaging response, as was predicted with the finite element studies. The first regime, for slot lengths below 1.5λ have increasing defect image amplitude with increasing slot lengths but constant FWHM of around 1.3λ. The maximum defect image amplitudes then occur for slot lengths of around $1.5\lambda_S$. The second regime, for slot lengths above 1.5λ exhibits defect image amplitudes which remains relatively constant with increasing slot length for both through-thickness and part-depth slots. For slots of circumferential extent greater than around $1.5\lambda_S$, the defect image FWHM provides a reliable estimate of the actual slot length for all experimental slot depths. This means that reliable defect sizing is possible for slots of circumferential extent larger than 1.5λ, as predicted in section 4.4.1.

The experimental gain in amplitude of the focused system over the unfocused (T(0,1) reception only) system for the 8 inch pipe case with an inspection frequency of 50 kHz was of the order of 17 dB for through-thickness slots which is comparable to the finite element prediction of 18 dB, found in section 4.4.1. The half-depth slot experiment achieved gains of 19 dB. The largest gains occurred for slot lengths of between 0.3λ and 1λ where the focused image amplitudes rise very quickly but the unfocused T(0,1) reflection amplitudes are still very small. Note that the gain will decease to unity for axisymmetric defects, when there is no mode conversion of the probing T(0,1) wave. There was also a 9 dB improvement in signal to noise ratio.

Experiments carried out at different excitation frequencies proved the finite element prediction of section 4.5.2 that the imaging response is not affected by excitation frequency if the the slot lengths and measured FWHM are normalised to the probing wavelength λ_S at the frequency of inspection.

Chapter 7

Conclusions

7.1 Main findings of this thesis

The aim of the work presented in this thesis was to develop a high-resolution pipe testing system that is able to detect and size defects from a remote axial location. Guided waves are already an established tool for the screening of long sections of pipe from a single inspection location. The strategy proposed was to use guided waves for imaging of the pipe features. Information about the location and severity of defects could then be seen clearly in the reconstructed image. The decision was made to use torsional type excitation since this had proved very successful in the commercial pipe screening tools.

In order to achieve the goal of pipe imaging, several stages of research were carried out. Firstly, in chapter 2, the similarity between guided wave propagation in pipes and plates was analysed. The flexural modes F(n,2) which tend to the bulk shear velocity, c_S at higher frequencies were investigated in detail since it was this mode family which were relevant to the chosen torsional type inspection.

It was proposed that the propagation of the torsional-flexural (F(n,2)) mode family in a pipe is comparable to the fundamental Shear-Horizontal (SH0) plate mode propagating in different helical directions. The finite number of modes at a given

frequency is accounted for by the boundary condition along the axial cut made in the pipe wall in order to 'unwrap' it. Each mode, of circumferential order n, can be thought of as a plane wave propagating in a direction at a fixed angle α_n to the axial direction, having phase velocity equal to the bulk shear velocity, c_S. The phase velocity error introduced by this plate-like assumption was evaluated and was found to be proportional to $(\frac{1}{fr})^2$, where fr is the frequency-radius product. The maximum error for likely inspection frequencies in 8 inch pipe were of the order of 1%.

Given the similarity between guided wave propagation in pipes and plates, synthetic focusing imaging algorithms were investigated and tested for the imaging of plates in chapter 3. Three imaging algorithms were introduced which differed in their transmit-receive geometries (see figure 3.2). The Common Source Method (CSM) transmits from all array elements simultaneously and records time traces across the array. The Synthetic Aperture Focusing Technique (SAFT) uses a pulse-echo data set and the Total Focusing Method (TFM) uses every transmit-receive combination available. The performance of the three algorithms was investigated theoretically for the case of a point scatterer in the object space. The lateral image response of a point scatterer is the Point Spread Function (PSF) and it was found that, for a given array aperture, SAFT produced the narrowest PSF, half that of the CSM, and hence achieved the best two-point resolution. However, SAFT and CSM both suffer from substantial sidelobes in the image. The TFM has significantly smaller sidelobes and FWHM between those of CSM and SAFT. However, TFM requires significantly more complex data acquisition than either CSM or SAFT.

The lateral crack sizing ability of the imaging algorithms was evaluated using data from a finite element model with cracks parallel to the array aperture and using the SH0 guided wave mode for inspection. It was found that all of the algorithms were capable of reliably estimating the crack length so long as the crack size was larger than the width of the theoretical PSF. The width of the theoretical PSF can therefore be used to define the smallest sizable crack. Here, the width of the PSF was measured using the Full Width at Half Maximum (FWHM). The width of

the PSF was finite because of spatial frequency windowing effects caused by wave propagation in the background medium. In addition, there is further filtering of high spatial frequencies caused by the finite sized aperture of the array. This means that the resolution of the plate algorithms gets worse for locations further from the array aperture.

Several plate experiments using the A0 guided wave mode at 50 kHz were carried out. The imaging results from the experimental data showed excellent agreement with the theory and the finite element study using the SH0 mode. It was found that broadband processing slightly reduced the sidelobe amplitude. The experimental results also showed the ability of the imaging techniques presented to deal with dispersion effects.

Following the encouraging plate imaging results, the same three synthetic focusing algorithms that were introduced for plate imaging were tested for their suitability for pipe imaging in chapter 4. No modifications to the implementation of the imaging algorithms of chapter 3 was necessary following the results of chapter 2. The Synthetic Aperture Focusing Technique (SAFT) and Total Focusing Method (TFM) were found to be unsuitable for pipe imaging with a circumferential array of transducers due to the excited waves in the circumferential direction which led to unwanted artifacts in the final reconstructed image. The decision was made to concentrate on CSM for pipe geometries.

The Common Source Method (CSM) was found not to suffer from such circumferential signals since conceptually all of the transducers are fired simultaneously. If the transduction is in the circumferential direction (shear transducers) this excites the axisymmetric torsional mode T(0,1) only as a probing wave.

The CSM was tested vigorously by imaging data from finite element models of circumferential cracks of varying depth and circumferential extent. The defect image amplitude increased roughly linearly with increasing circumferential extent of the crack, for any fixed crack depth, until a maximum amplitude was reached at a circumferential extent of around $1.5\lambda_{SH}$ (see figure 4.19). Here, λ_{SH} is the wavelength

of the probing T(0,1) guided wave mode and is equal to the SH0 wavelength in a plate. For cracks of circumferential extent larger than $1.5\lambda_{SH}$, the defect image amplitude remained relatively constant for a given crack depth. In this region, the depth of the crack can be reliably estimated from the defect image amplitude (see figure 4.25).

The proposed method for circumferential sizing of defects was to measure the circumferential extent of the defect image. The Full Width at Half Maximum (FWHM) of the circumferential image profile was used for this purpose. The FWHM was found to remain roughly constant at around $1.4\lambda_{SH}$ for cracks of circumferential extent less than $1.5\lambda_{SH}$ (see figure 4.22). For cracks of circumferential extent larger than around $1.5\lambda_{SH}$, the FWHM can be used to reliably estimate the circumferential extent of the crack. For cracks of circumferential extent below the $1.5\lambda_{SH}$ limit, the defect image amplitude is affected by both defect depth and circumferential extent, and the FWHM remains constant. Therefore, the depth and circumferential extent cannot be extracted from the image independently.

The resolution limit of $1.5\lambda_{SH}$ is due to the limited backscatter angles observed from small cracks. The resolution limit observed here suggests a maximum plane wave backscatter angle of around 42^o, which agrees well with detailed finite element studies on the backscatter of fundamental shear-horizontal plane waves incident on cracks in plates [77].

It was found that the resolution limit of $1.5\lambda_{SH}$ is independent of the inspection frequency, as long as the crack size and FWHM are expressed in wavelengths of the probing wave, λ_{SH}. The image defect response was found to be unaffected by pipe size or axial defect position; the defect image response is only dependent on the backscatter characteristics of the defect. This is because all of the backscattered signals from the defect are received at the array, via higher order mode propagation, regardless of the defect axial position or the array size (pipe circumference). This result is in contrast to plate imaging with a linear array, where the resolution limit is greatly affected by the array aperture.

The robustness of the proposed focused system was tested in chapter 5. The method of testing was to synthetically corrupt data from a finite element model and then to attempt imaging of the corrupted data. Random transducer coupling variations were applied to the finite element data and it was found that the system was robust against coupling variations larger than those observed experimentally. The system was also shown to be robust against realistic levels of random axial transducer misplacement (which are equivalent to phase errors) and even one or two faulty transducers. However, the system was not robust against reversed transducers, but this is an extremely unlikely situation and would be easily diagnosed and fixed prior to inspection.

The robustness of the system to systematic errors was also investigated. Tilting of the transducer ring on the pipe caused variations in the defect image amplitude and FWHM of the order of $\pm 20\%$. The effect of processing data with incorrect phase velocities was that the image defect amplitude was decreased and the FWHM increased. The decrease in performance was found to worsen with increasing axial defect location from the transducers, for a given level of velocity error. However, it is important to note that entering an incorrect pipe size or bulk shear velocity of the material could be avoided with vigilance on behalf of the operator. The tilting of the transducer ring could also be reduced by careful operator setup.

The results from the finite element studies of chapter 4 were validated experimentally using modified Guided Ultrasonics Limited [24] hardware in chapter 6. The defects were milled circumferential slots of both half-thickness and through-thickness depths. The experimental results agreed very well with the finite element results. The observed experimental sizing limit was around $1.5\lambda_{SH}$ at two different experimental inspection frequencies (30 and 50kHz) in 8 inch pipe.

7.2 Summary of Pipe Imaging performance improvements

The ability to estimate the depth and circumferential extent of defects using synthetic focusing is significantly greater than that of an unfocused system, which can excite and receive the axisymmetric torsional mode T(0,1) only. The unfocused system cannot estimate the circumferential defect extent and can only estimate the defect depth reliably for axisymmetric defects. In contrast, the focused system can reliably estimate both crack depth and circumferential extent independently using the image defect amplitude and its FWHM respectively, providing the crack has circumferential extent larger than $1.5\lambda_S$, which can be observed from the image FWHM. This result is valid for any axial defect location, in any pipe size and for any frequency of inspection below the T(0,2) cutoff. The sizing limit of $1.5\lambda_S$ is around 100 mm at 50 kHz in mild steel pipes.

The maximum amplitude gain occurs for cracks of circumferential extent around $1\lambda_{SH}$ where the focused image amplitude is near its maximum but the unfocused amplitude is still very small. For axisymmetric defects, the focused amplitude is equal to the unfocused amplitude since the backscattered signal consists of only the axisymmetric T(0,1) mode. In this case, the amplitude gain is unity. The greatest sensitivity improvement for through-thickness cracks is

$$G_{amp} = \frac{Amp_{focused}}{Amp_{T(0,1)}} \approx \frac{2\pi r}{\lambda_S} \tag{7.1}$$

where r is the pipe radius and λ_S is the wavelength of the probing signal. The amplitude gain achieved increases for larger pipes and higher inspection frequencies. For example, the gain at 50 kHz for an 8 inch pipe is around 18 dB but is 28 dB for 24 inch pipes at the same frequency. The amplitude gains observed experimentally in 8 inch pipe at 50 kHz were around 17 dB.

The gain in resolution arises since the unfocused system cannot circumferentially size defects. The focused system is capable of reliable circumferential sizing of defects

with circumferential extents greater than $1.5\lambda_S$. The resolution improvement is therefore

$$G_{circ} = \frac{res_{T(0,1)}}{res_{focused}} \approx \frac{2\pi r}{1.5\lambda_S} \tag{7.2}$$

The gain in resolution will increase in larger pipes and at higher inspection frequencies, as was the case for the sensitivity gain above. The resolution gain at 50 kHz in 8 inch pipe is around 16 dB but would be 25 dB in 24 inch pipe. However, it should be noted that more transducer elements would be required to sufficiently sample the pipe circumference for larger pipes or higher frequencies of inspection. The resolution gain observed experimentally in 8 inch pipe at 50 kHz was 16 dB.

7.3 Future work

The reflection from part-depth defects has been shown to be frequency dependent in section 4.4.2 and [19]. Therefore, the curve of crack depth against image amplitude shown in figure 4.25 is only valid for cracks (zero axial extent) and an inspection frequency of 50 kHz. This curve can be used to estimate the crack depth for any pipe size with inspection at 50 kHz. However, this curve will vary with inspection frequency since the crack depth as a fraction of the probing wavelength will vary.

The effect of the axial extent of the defect was briefly investigated in section 4.4.2. The reflection from defects with finite axial extent is also frequency dependent since the reflection depends on the axial extent expressed as a fraction of the probing wavelength. Therefore, further work is needed to assess the frequency dependent image response from part-depth defects with finite axial extent. It may be possible to inspect over a range of frequencies and hence the frequency varying response could be used to give more information about the defect shape.

The resolution of the proposed focused system is limited by the backscatter characteristics of the cracks and slots studied here. A detailed study into different shaped defects may lead to different defect backscatter characteristics which may, in turn,

lead to better resolution. Field trials and testing of the focused system with real defects would also be beneficial.

The conventional imaging techniques presented here will always be limited by the filtering of spatial frequencies by propagation in the background medium [83]; in this case, the undamaged pipe wall. This spatial frequency filtering leads to difficulties in imaging sub-wavelength features and gives rise to the 'diffraction limit' [83], see section 3.2.1. Imaging techniques which break this conventional resolution limit are known as super resolution algorithms [94], for example, the MUltiple SIgnal Classification (MUSIC) method [95,96]. These super resolution techniques have not yet been developed for hollow cylinder geometries such as the pipes of concern here. However, they have shown promising results for imaging using bulk ultrasonic waves and some experimental work on guided wave imaging in plates [97]. They may yet prove a valuable tool for sizing of small defects in pipes.

Appendix A

The Angular Spectrum of Plane Waves

A.1 The Physical Interpretation of the Angular Spectrum

If a 2 dimensional monochromatic wave field is incident on a line (x,z=0) then let the complex field across the z=0 line be represented as U(x,z=0). The spatial Fourier transform over x is

$$A(f_x; z=0) = \int_{-\infty}^{+\infty} U(x, z=0) e^{-j2\pi f_x x} dx \tag{A.1}$$

The Fourier transform is a decomposition of a complicated function into a collection of simple complex exponentials. The inverse Fourier transform of (A.1) is

$$U(x, z=0) = \int_{-\infty}^{+\infty} A(f_x; z=0) e^{j2\pi f_x x} df_x \tag{A.2}$$

In order to explain the significance of the functions in the integrand above, consider a simple plane wave propagation with wavevector $\mathbf{k}$ whose magnitude is $2\pi/\lambda$ and has

directional cosines (α, β). Such a plane wave has standard complex representation

$$p(x, z, t) = e^{j(\mathbf{k}\cdot\mathbf{r}-\omega\mathbf{t}})} \tag{A.3}$$

where $\mathbf{r} = x\hat{x}+z\hat{z}$ is a position vector ($\hat{x}$ and $\hat{z}$ are unit vectors), and $\mathbf{k} = \frac{2\pi}{\lambda}(\alpha\hat{x}+\beta\hat{z})$. Omitting the time dependence, the complex phasor amplitude of the plane wave across a line of constant z is

$$P(x, z) = e^{j\mathbf{k}\cdot\mathbf{r}} = e^{j\frac{2\pi}{\lambda}\alpha x}e^{j\frac{2\pi}{\lambda}\beta z} \tag{A.4}$$

Noting that the directional cosines are related by

$$\beta = \sqrt{1-\alpha^2} \tag{A.5}$$

Thus across the z=0 line, the complex exponential function $\exp(j2\pi f_x x)$ can be regarded as a plane wave propagating with directional cosines

$$\alpha = \lambda f_x \quad \beta = \sqrt{1-\alpha^2} \tag{A.6}$$

In the Fourier decomposition of U, the complex amplitude of the plane-wave component of spatial frequency f_x is simply $A(f_x, z = 0)df_x$, evaluated at $f_x = \alpha/\lambda$. For this reason the function

$$A(\frac{\alpha}{\lambda}; z = 0) = \int_{-\infty}^{+\infty} U(x, z = 0)e^{-j2\pi\frac{\alpha}{\lambda}x}dx \tag{A.7}$$

is called the *Angular Spectrum* of the complex disturbance $U(x, z = 0)$ whose components represent plane waves travelling away from the z=0 line.

A.2 Propagation of the Angular Spectrum

Having decomposed the recorded wavefield $(U(x, z = 0))$ across the line $z = 0$ into plane waves using the Angular Spectrum, it is useful to see how the angular

spectrum at a parallel line at $z = d$ relates to the angular spectrum at $z = 0$. The angular spectrum at $z = d$ is defined by

$$A(\frac{\alpha}{\lambda}; z = d) = \int_{-\infty}^{+\infty} U(x, z = d)e^{-j2\pi\frac{\alpha}{\lambda}x}dx \tag{A.8}$$

whose inverse Fourier transform is

$$U(x, z = d) = \int_{-\infty}^{+\infty} A(\frac{\alpha}{\lambda}; z = d)e^{j2\pi\frac{\alpha}{\lambda}x}d\frac{\alpha}{\lambda} \tag{A.9}$$

In addition, U must satisfy the Helmholtz equation,

$$\nabla^2 U + k^2 U = 0 \tag{A.10}$$

in the absence of any sources. Applying this condition directly to (A.8) gives the differential equation

$$\frac{d^2}{dz^2}A(\frac{\alpha}{\lambda}; z = d) + (\frac{2\pi}{\lambda})^2[1 - \alpha^2]A(\frac{\alpha}{\lambda}; z = d) = 0. \tag{A.11}$$

The solution to (A.11) is of the form

$$A(\frac{\alpha}{\lambda}; z = d) = A(\frac{\alpha}{\lambda}; z = 0)e^{j\frac{2\pi}{\lambda}\sqrt{1-\alpha^2}d}. \tag{A.12}$$

Therefore, the effect of propagation over a distance d is simply a change of the relative phases of the components of the angular spectrum. Since each plane-wave component propagates at a different angle, each travels a different distance between the two parallel lines, and relative phase delays are thus introduced. The exponential term in (A.12) is termed the *propagator* of the angular spectrum and can be shown to be a linear space-invariant transfer function.

References

[1] D. C. Gazis. Three dimensional investigation of the propagation of waves in hollow circular cylinders. *J. Acoust. Soc. Am.*, 31(5):568–578, 1959.

[2] J.L. Rose. A baseline and vision of ultrasonic guided wabe inspection potential. *Journal of Pressure Vessel Technology*, 124:273–282, 2002.

[3] W. Mohr and P. Holler. On inspection of thin-walled tubes for transverse and longitudinal flaws by guided ultrasonic waves. *IEEE Trans. Sonics Ultrason.*, SU-23:369–378, 1976.

[4] R. B. Thompson, G.A. Alers, and M.A. Tennison. Application of direct electromagnetic lamb wave generation to gas pipeline inspection. *1972 Ultrasonics Symposium*, pages 91–94, 1972.

[5] R. B. Thompson, R.K. Elsley, W.E. Petersen, and C.F. Vasille. An emat system for detecting flaws in steam generator tubes. *1979 Ultrasonics Symposium*, pages 246–249, 1979.

[6] M. G. Silk and K. F. Bainton. The propagation in metal tubing of ultrasonic wave modes equivalent to Lamb waves. *Ultrasonics*, 17(1):11–19, 1979.

[7] W. Bottger, H. Schneider, and W. Weingarten. Prototype emat system for tube inspection with guided ultrasonic waves. *Nuclear Eng. Design*, 102:356–376, 1987.

[8] J.L. Rose, J.J. Ditri, A. Pilarski, K. Rajana, and F. Carr. A guided wave inspection technique for nuclear steam generator tubing. *NDT & E Int.*, 27:307–310, 1994.

[9] D. N. Alleyne, B. Pavlakovic, M. J. S. Lowe, and P. Cawley. Rapid, long range inspection of chemical plant pipework using guided waves. *Insight*, 43:93–96,101, 2001.

[10] P.J. Mudge. Field application of the teletest (r) long-range ultrasonic testing. *Insight*, 43:74–77, 2001.

[11] J. Barshinger, J.L. Rose, and M.J. Avioli Jr. Guided wave resonance tuning for pipe inspection. *Journal of Pressure Vessel technology*, 124:303–310, 2002.

[12] Y.Y. Kim, C.I. Park, S.H. Cho, and S.W. Han. Torsional wave experiments with a new magnetostrictive transducer configuration. *J. Acoust. Soc. Am.*, 117(6):3459–3468, 2005.

[13] M. J. S. Lowe, D. N. Alleyne, and P. Cawley. Defect detection in pipes using guided waves. *Ultrasonics*, 36:147–154, 1998.

[14] A. Demma, P. Cawley, M. Lowe, A. G Roosenbrand, and B. Pavlakovic. The reflection of guided waves from notches in pipes: a guide for interpreting corrosion measurements. *NDT&E International*, 37:167–180, 2004.

[15] D. N. Alleyne and P. Cawley. Long range propagation of Lamb waves in chemical plant pipework. *Materials Evaluation*, 55:504–508, 1997.

[16] D. N. Alleyne, M. J. S. Lowe, and P. Cawley. The reflection of guided waves from circumferential notches in pipes. *Journal of Applied Mechanics*, 65:635–641, 1998.

[17] M. J. S. Lowe, D. N. Alleyne, and P. Cawley. The mode conversion of a guided wave by a part-circumferential notch in a pipe. *Journal of Applied Mechanics*, 65:649–656, 1998.

[18] P. Cawley, M. J. S Lowe, F. Simonetti, C. Chevalier, and A. G. Roosenbrand. The variation of the reflection coefficient of extensional guided waves in pipes from defects as a function of defect depth, axial extent, circumferential extent and frequency. *Journal of Mechanical Engineering Science*, 216(C):1131–1143, 2002.

[19] A. Demma, P. Cawley, M. Lowe, and A. G Roosenbrand. The reflection of fundamental torsional mode from cracks and notches in pipes. *J. Acoust. Soc. Am.*, 114(3):611–625, 2003.

[20] D. N. Alleyne, B. Pavlakovic, M. J. S. Lowe, and P. Cawley. The use of guided waves for rapid screening of chemical plant pipework. *Journal of the Korean Society doe Nondestructive Testing*, 22(6):589–598, 2002.

[21] R. Long, M. Lowe, and P. Cawley. Attenuation characteristics of the fundamental modes that propagate in buried iron water pipes. *Ultrasonics*, 41:509–519, 2003.

[22] M. J. S. Lowe. Matrix techniques for modelling ultrasonic waves in multilayered media. *IEEE Trans. Ultrason. Ferroelectr. Freq. Control*, 42:525–542, 1995.

[23] D. N. Alleyne and P. Cawley. The excitation of Lamb waves in pipes using dry coupled piezoelectric transducers. *J NDE*, 15:11–20, 1996.

[24] *http://www.guided-ultrasonics.com/.*

[25] H. Kwun, Y. Kim, Sang, and G.M. Light. The magnetostrictive sensor technology for long range guided wave testing and monitoring of structures. *Materials Evaluation*, 61(1):80–84, 2003.

[26] T. Hayashi and M. Murase. Defect imaging with guided waves in a pipe. *J. Acoust. Soc. Am.*, 117(4):2134–2140, 2005.

[27] J.J. Ditri, J.L. Rose, and A. Pilarski. Generation of guided waves in hollow cylinders by wedge and comb type transducers. *Review of Progress in Quantitative Nondestructive Evaluation*, 12A:211–218, 1993.

[28] J. Li and J.L. Rose. Excitation and propagation of non-axisymmetric guided waves in a hollow cylinder. *J. Acoust. Soc. Am.*, 109(2):457–464, 2001.

[29] T.R. Hay and J.L. Rose. Flexible pvdf comb transducers for excitation of axisymmetric guided waves in pipes. *Sensors and Actuators*, 100:18–23, 2002.

[30] J. Li and J.L. Rose. Implementing guided wave mode control by use of a phased transducer array. *J. Acoust. Soc. Am.*, 109(2):457–464, 2001.

[31] J. J. Ditri. Utilization of guided elastic waves for the characterization of circumferential cracks in hollow cylinders. *J. Acoust. Soc. Am.*, 96(6):3769–3775, 1994.

[32] W. Zhu. An fem simulation for guided elastic wave generation and reflection in hollow cylinders with corrosion defects. *Journal of Pressure Vessel technology*, 124(1):108–117, 2002.

[33] D. N. Alleyne, P. Cawley, A.M. Lank, and P.J. Mudge. The lamb wave inspection of chemical plant pipework. In D. O. Thompson and D. E. Chimenti, editors, *Review of Progress in Quantitative NDE*, volume 16, pages 1269–1276. Plenum Press, New York, 1997.

[34] H.J. Shin and J.L Rose. Guided waves by axisymmetric and non-axisymmetric surface loading on hollow cylinders. *Ultrasonics*, 37:355–363, 1999.

[35] Z. Sun, L. Zhang, and J.L. Rose. Flexural torsional guided wave mechanics and focusing in pipe. *Journal of Pressure Vessel Technology*, 127:471–478, 2005.

[36] J. Li and J.L. Rose. Angular-profile tuning of guided waves in hollow cylinders using a circumferential pahsed array. *IEEE trans. Ultrasonics, Ferroelectrics and Freq. Control*, 49(12):1720–1729, 2002.

[37] J. Li and J.L. Rose. Natural beam focusing of non-axisymmetric guided waves in large-diameter pipes. *Ultrasonics*, 44:35–45, 2006.

[38] T. Hayashi, K. Kawashima, Z. Sun, and Rose J.L. Analysis of flexural mode focusing by a semianalytical finite element method. *J. Acoust. Soc. Am.*, 113(3):1241–1248, 2003.

[39] T. Hayashi, K. Kawashima, Z. Sun, and Rose J.L. Guided wave focusing mechanics in pipe. *Journal of PRessure Vessel Technology*, 127:317–321, 2005.

[40] J. Li. On circumferential disposition of pipe defects by long-range ultrasonic guided waves. *Journal of Pressure Vessel Technology*, 127:530–537, 2005.

[41] C. Ennaceur, P. Mudge, M. Kayous, and T.H. Gan. Application of the time reversal technique to the focusing of long-range ultrasound in pipelines. *Insight*, 49(4):217–223, 2007.

[42] P.D. Corl, P.M. Grant, and G.S. Kino. A digital synthetic focus acoustic imaging system for nde. *1978 Ultrasonics Symposium*, pages 263–268, 1978.

[43] M. Karaman, P.-C. Li, and M. O'Donnell. Synthetic aperture imaging for small scale systems. *IEEE Trans. Ultrason. Ferroelect. Freq. Contr.*, 42(3):429–442, 1995.

[44] J.T. Ylitalo and H. Ermet. Ultrasound synthetic aperture imaging: Monostatic approach. *IEEE Trans. Ultrason. Ferroelectr. Freq. Control*, 41(3):333–339, 1994.

[45] J.C. Curlander and R.N. McDonough. *Synthetic aperture radar - Systems and signal processing.* John Wiley and Sons, New York, 1991.

[46] M.P. Hayes and P.T Gough. Broad-band synthetic aperture sonar. *IEEE Journal of Oceanic Engineering*, 17(1):80–94, 1992.

[47] C. Holmes, B.W. Drinkwater, and P.D. Wilcox. Post-processing of the full matrix of ultrasonic transmit-receive array data for non-destructive evaluation. *NDT&E*, 38:701–711, 2005.

[48] P.D. Wilcox. Omni-directional guided wave transducer arrays for the rapid inpsection of large areas of plate structures. *IEEE Trans. Ultrason. Ferroelectr. Freq. Control*, 50(6):699–709, 2003.

[49] P.D. Wilcox, M. Lowe, and P. Cawley. Omnidirectional guided wave inspection of large metallic plate structures using an emat array. *IEEE Trans. Ultrason. Ferroelectr. Freq. Control*, 52(4):653–665, 2003.

[50] P. Fromme, P. Wilcox, and P. Cawley. Remote monitoring of plate-like structures using guided wave arrays. In D. O. Thompson and D. E. Chimenti, editors, *Review of Progress in Quantitative NDE*, volume 22A, pages 157–164, 2003.

[51] R. Sicard, J. Goyette, and D. Zellouf. A saft algorithm for lamb wave imaging of isotropic plate-like structures. *Ultrasonics*, 39:487–494, 2002.

[52] R. Sicard, A. Chahbaz, and J. Goyette. Guided Lamb waves and L-SAFT processing technique for enhanced detection and imaging of corrosion defects in plates with small depth-to-wavelength ratio. *IEEE Trans. Ultrason. Ferroelect. Freq. Contr.*, 51(10):1287–1297, 2004.

[53] L.J. Busse. Three-dimensional imaging using a frequency-domain synthetic aperture focusing technique. *IEEE Trans. Ultrason. Ferroelect. Freq. Contr.*, 39(2):174–179, 1992.

[54] Lord Rayleigh. On the free vibrations of an infinite plate of homogeneous isotropic elastic matter. *Proceedings London Mathematical Society*, 20(357):225–237, 1888-1889.

[55] H. Lamb. On waves in an elastic plate. *Proceedings Royal Society*, 93:114–128, 1916-1917.

[56] R. Stonely. Elastic waves at the surface of separation of two solids. *Roy. Soc. Proc. London*, 106(Series A):416–428, 1924.

[57] B. A. Auld. *Acoustic Fields and Waves in Solids*, volume 1. Krieger Publishing Company, Malabar, Florida, 1990.

[58] K. F. Graff. *Wave motion in elastic solids*. Clarendon Press, Oxford, 1975.

[59] J. L. Rose. *Ultrasonic Waves in Solid Media*. Cambridge University Press, Cambridge, UK, 1999.

[60] B. A. Auld. *Acoustic Fields and Waves in Solids*, volume 2. Krieger Publishing Company, Malabar, Florida, 1990.

[61] B. N. Pavlakovic, M. J. S. Lowe, D. N. Alleyne, and P. Cawley. Disperse: A general purpose program for creating dispersion curves. In D. O. Thompson and D. E. Chimenti, editors, *Review of Progress in Quantitative NDE*, volume 16, pages 185–192. Plenum Press, New York, 1997.

[62] I. Mirsky. Wave propagation in transversely isotropic circular cylinders, part 1: Theory. *J. Acoust. Soc. Am.*, 37(6):1016–1021, 1965.

[63] J. Zemanek. An experimental and theoretical investigation of elastic wave propagation in a cylinder. *J. Acoust. Soc. Am.*, 51(1):265–283, 1972.

[64] B.N. Pavlakovic. *Leaky Guided Ultrasonic Waves in NDT*. PhD thesis, University of London, 1998.

[65] B. N. Pavlakovic and M. J. S. Lowe. A general purpose approach to calculating the longitudinal and flexural modes of multi-layered, embedded, transversely isotropic cylinders. In D.O. Thompson and D.E. Chimenti, editors, *Review of Progress in Quantitative NDE*, volume 18, pages 239–246. Plenum Press, New York, 1999.

[66] L. Knopoff. A matrix method for elastic wave problems. *Bull. Seism. Soc. Am.*, 54:431–438, 1964.

[67] H. Schmidt and F.B. Jensen. Efficient numerical solution technique for wave propagation in horizontally stratified environments. *Comput. Math. Appl.*, 11:699–715, 1985.

[68] D. C. Gazis. Exact analysis of plane-strain vibrations of thick-walled hollow cylinders. *J. Acoust. Soc. Am.*, 30(8):786–794, 1958.

[69] K.L.J Fong. *A study of curvature effects on guided elastic waves*. PhD thesis, University of London, 2005.

[70] D. Gridin, R. V. Craster, J. Fong, M. Lowe, and M. Beard. The high-frequency asymptotic analysis of guided waves in a circular elastic annulus. *Wave Motions*, 38:67–90, 2003.

[71] A. N. Norris and C. Vemula. Scattering of flexural waves on thin plates. *J. Sound Vib.*, 181(1):115–125, 1995.

[72] J.C.P McKeon and M.K. Hinders. Lamb wave scattering from a through hole. *Journal of Sound and Vibration*, 224(5):843–862, 1999.

[73] P. Fromme and M.B. Sayir. Measurement of the scattering of a lamb wave by a through hole in a plate. *J. Acoust. Soc. Am.*, 111(3):1165–1170, 2002.

[74] A. Demma, P. Cawley, and M. Lowe. Scattering of the fundamental shear horizontal mode from steps and notches in plates. *J. Acoust. Soc. Am.*, 113(4):1880–1891, 2003.

[75] F.B. Cegla, A. Rohde, and M. Veidt. Analytical prediction and experimental measurement for mode conversion and scattering of plate waves at non-symmetric circular blind holes in isotropic plates. *Wave Motion*, 45:162–177, 2008.

[76] P. Rajagopal and M.J.S. Lowe. Short range scattering of the fundamental shear horizontal guided wave mode normally incident at a through-thickness crack in an isotropic plate. *J. Acoust. Soc. Am.*, 122(3):1527–1538, 2007.

[77] P. Rajagopal and M.J.S. Lowe. Angular influence on scattering when the fundamental shear horizontal guided wave mode is incident at a through-thickness crack in an isotropic plate. *submitted to J. Acoust. Soc. Am.*, 2008.

[78] P. Rajagopal and M.J.S. Lowe. Scattering of the fundamental shear horizontal guided wave mode by part-thickness cracks in an isotropic plate. *submitted to J. Acoust. Soc. Am.*, 2008.

[79] R. Y. Chiao and L. J. Thomas. Analytic evaluation of sampled aperture ultrasonic imaging techniques for nde. *IEEE Trans. Ultrason. Ferroelect. Freq. Contr.*, 41(4):484–493, 1994.

[80] Y. Ozaki, H. Sumatini, T. Tomoda, and M. Tanaka. A new system for real-time synthetic aperture ultrasonic imaging. *IEEE Trans. Ultrason. Ferroelectr. Freq. Control*, 35(6):828–838, 1988.

[81] R. Y. Chiao and L. J. Thomas. Aperture formation on reduced-channel arrays using the transmit-receive apodization matrix. *IEEE Ultrasonics Symposium*, pages 1567–1571, 1996.

[82] J. Johnson, M. Karaman, and P. Khuri-Yakub. Synthetic phased array image formation and restoration. In *ICASSP '02*, volume 3, pages 2885–2888. IEEE, 2002.

[83] J. W. Goodman. *Introduction to Fourier Optics*. McGraw-Hill, New York, 1996.

[84] H.J. Callow, M.P. Hayes, and P.T. Gough. Wavenumber domain reconstruction of sar/sas imagery using singletransmitter and multiple-receiver geometry. *IEEE Elecetronic letters*, 38(7):336–338, 2002.

[85] R.H. Stolt. Migration by fourier transform. *Geophysics*, 43:23–48, 1978.

[86] P. M. Morse and H. Feshbach. *Methods of theoretical physics*. McGraw-Hill Book Company, New York, London, 1953.

[87] Lord Rayleigh. Investigations in optics with special reference to the spectroscope. *Phols. Mag.*, 8:261–274, 403–411, 477–486, 1879.

[88] C.M. Sparrow. On spectroscopic resolving power. *The Astrophysical Journal*, 44:76–86, 1916.

[89] *http://abaqus.cc.ic.ac.uk/v6.5/index.html*.

[90] *http://www.polytec.com/*.

[91] M.B. Drozdz. *Efficient finite element modeling of ultrasound waves in elastic media*. PhD thesis, University of London, 2007.

[92] S. Velichko and P. Wilcox. Post-processing of the full matrix of ultrasonic transmit-receive array data for guided wave pipe inspection. In D. O. Thompson and D. E. Chimenti, editors, *Review of Progress in Quantitative NDE*, volume 28. American Institue of Physics, New York, in press.

[93] M. Born and E. Wolf. *Principles of Optics*. Cambridge University Press, Cambridge, 1999.

[94] F. Simonetti, M. J. Fleming, and E. A. Marengo. Illustration of the role of multiple scattering in subwavelength imaging from far-field measurements. *J. Opt. Soc. Am.*, 25(2):292–303, 2008.

[95] A. J. Devaney. Super-resolution processing of multi-static data using time-reversal and music. *Unpublished*, page available at www.ece.neu.edu/faculty/devaney/ajd/preprints.htm, 2000.

[96] A. J. Devaney. Time reversal imaging of obscured targets from multistatic data. *IEEE Trans. Antennas Propag.*, 53(5):1600–1610, 2005.

[97] F. Simonetti. Breaking the resolution limit: A new perspective for imaging in nde. In D. O. Thompson and D. E. Chimenti, editors, *Review of Progress in Quantitative NDE*, volume 25, pages 700–707. American Institue of Physics, New York, 2006.

List of Publications

[P1] J. Davies, F. Simonetti, M. Lowe and P. Cawley. Review of synthetically focused guided wave imaging techniques with application to defect sizing. In D. O. Thompson and D. E. Chimenti, editors, *Review of Progress in Quantitative NDE*, volume 25, pages 142-149. American Institute of Physics, Melville, New York, 2006.

[P2] J. Davies and P. Cawley. The Application of synthetically focused imaging techniques for high resolution guided wave pipe inspection. In D. O. Thompson and D. E. Chimenti, editors, *Review of Progress in Quantitative NDE*, volume 26, pages 681-688. American Institute of Physics, Melville, New York, 2007.

[P3] J. Davies and P. Cawley. Synthetic focusing for high resolution guided wave pipe inspection: Further results and robustness studies. In D. O. Thompson and D. E. Chimenti, editors, *Review of Progress in Quantitative NDE*, volume 27, pages 139-146. American Institute of Physics, Melville, New York, 2007, 2008.

[P4] J. Davies and P. Cawley. The use of imaging algorithms for improved guided wave pipe inspection. In preparation, 2008.

[P5] J. Davies and P. Cawley. The application of synthetic focusing for defect imaging in pipelines using guided waves. submitted to IEEE Ultrasonics, Ferroelectrics and Control, 2008.